Advanced Turbine Technology

ATTAP

Applications Project

DOE/NASA 0336-3
NASA CR-189142
EDR 15593

IN-37
92884
p. 156

1990 Annual Report

Allison
Gas Turbine Division
General Motors Corporation
P.O. Box 420
Indianapolis, Indiana 46206-0420

December 1991

Final

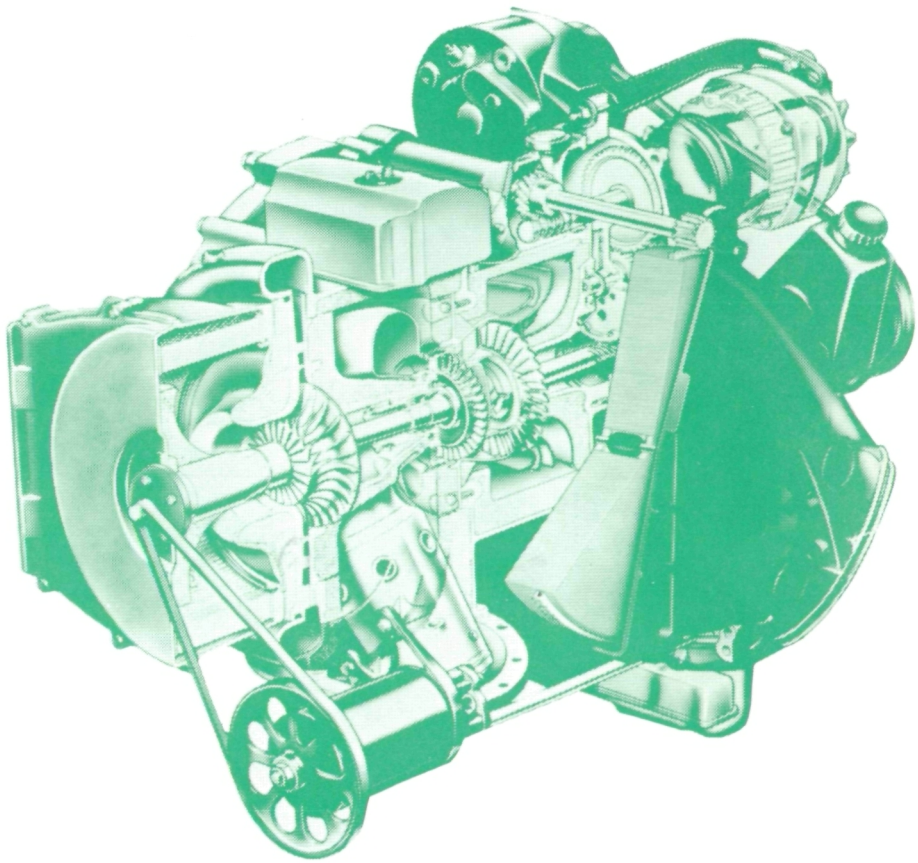

Prepared for
National Aeronautics
and Space Administration
Lewis Research Center
Cleveland, Ohio 44135
Contract DEN 3-336

For U.S. Department of Energy
Conservation and Renewable Energy
Office of Transportation Technologies

(NASA-CR-189142) ADVANCED TURBINE TECHNOLOGY APPLICATIONS PROJECT (ATTAP) Final Annual Report, 1990 (Detroit Diesel Allison) 156 p

N92-25649

Unclas
G3/37 0092884

NOTICE

This report was prepared to document work sponsored by the United States Government. Neither the United States nor its agent, the United States Department of Energy, nor any Federal employees, nor any of the contractors, subcontractors, or their employees makes any warranty, express or implied, or assumes any legal liability or responsibility for the accuracy, completeness, or usefulness of any information, apparatus, product, or process disclosed, or represents that its use would not infringe privately owned rights.

DOE/NASA 0336-3
NASA CR-189142
EDR 15593

Advanced Turbine Technology
ATTAP
Applications Project

1990 Annual Report

Allison
Gas Turbine Division
General Motors Corporation
P.O. Box 420
Indianapolis, Indiana 46206-0420

December 1991

Final

Prepared for
National Aeronautics
and Space Administration
Lewis Research Center
Cleveland, Ohio 44135
Contract DEN 3-336

For U.S. Department of Energy
Conservation and Renewable Energy
Office of Transportation Technologies

FOREWORD

This report presents a technical summary of work accomplished on the Advanced Turbine Technology Applications Project (ATTAP) under NASA contract DEN3-336 for calendar year 1990. The report is set up and arranged per the original Work Breakdown Structure (WBS). Only WBS's with activity in 1990 are reported herein.

This technology project is funded by the U.S. Department of Energy, Conservation and Renewable Energy, Office of Transportation Technologies, Office of Propulsion Systems, Advanced Propulsion Division. Project management and technical direction are provided by the NASA Lewis Research Center (LeRC), Aeronautics Directorate, Propulsion Systems Division, Terrestrial Propulsion Office.

The overall intent of the ATTAP is to bring the automotive gas turbine engine to a technology state at which industry can make commercialization decisions. Key to this goal is the development and demonstration of structural ceramic component technology as the critical high risk/high payoff element in this type of engine. Such ceramic technology is the prime ATTAP focus. Automotive gas turbine attractions include the following potential advantages:

- Significantly increased fuel economy
- Ability to meet Federal emission standards with untreated exhaust
- Ability to operate on a wide range of alternate fuels
- Inherently smooth, low-vibration operation

General Motors (GM) is addressing the ATTAP with a team that draws on:

- The extensive ceramic design, analysis, and materials data base and expertise in place at the Allison Gas Turbine Division (Allison)
- The substantial experience, design and test capabilities, automotive gas turbine technology and hardware, and test vehicle resources that were developed under GM funding as background to this project and are in place at GM's Advanced Engineering Staff (AES)
- The infrastructure of expertise and resources in place in the American ceramics industry and the working relationships between the industry and GM
- The unique capabilities and resources existing at universities and at national laboratories, such as the High Temperature Materials Laboratory (HTML) at the Oak Ridge National Laboratory (ORNL)

In this arrangement, Allison serves as prime contractor. Major ceramics industry development subcontractors to date are: The Carborundum Company; GTE Laboratories Inc; Corning Inc; Manville Corp; Ceramics Process Systems; Garrett Ceramic Components; and Norton/TRW Ceramics. A major ceramic component supplier is the Kyocera Industrial Ceramics Corporation.

TABLE OF CONTENTS

Section	Title	Page
Foreword		i
Summary		xi
Introduction		xv
I	Engine/Powertrain Design and Development, Analysis, and Materials Assessment	1-1
1.4	Test-Bed Engine Design and Development	1-1
1.4.1	Mechanical	1-1
1.4.2	Combustion Systems	1-3
1.4.3	Alternate Flow Paths	1-9
1.4.4	Engine System Integration	1-13
II	Ceramic Component Design	2-1
2.1	Design Activities	2-1
2.1.2	Gasifier Turbine Static Structure	2-2
2.1.3	Gasifier Turbine Rotor	2-12
2.1.4	Regenerator	2-36
2.1.5	Power Turbine	2-37
III	Materials Characterization and Ceramic Component Fabrication	3-1
3.1	Materials and Component Characterization	3-1
3.1.1	Material Properties and Microstructure	3-1
3.1.3	Failure Analysis	3-11
3.2	Ceramic Component Process Development and Fabrication	3-18
3.2.1	Carborundum	3-19
3.2.2	Manville	3-26
3.2.3	GTE Laboratories	3-30
3.2.4	Corning	3-34
3.2.5	Garrett Ceramic Components	3-34
3.2.6	Ceramics Process Systems	3-38
3.2.9	Norton/TRW Ceramics	3-39
IV	Component Rig Development and Test	4-1
4.1	Component Rig Development	4-1
	4.1.3.1 Rotor/Shafting System Rig Development	4-1
	4.1.3.3 Hot Gasifier Rig Development	4-1
4.2	Component Rig Testing	4-2
	4.2.3.1 Rotor/Shafting System Rig Test	4-2
	4.2.3.3 Hot Gasifier Rig Test	4-4
4.2.4	Regenerator Rigs Test	4-8
V	Performance and Durability Testing--Test-Bed Engines	5-1
5.2	Durability Testing	5-1
5.2.3	Test-Bed Engine Fabrication and Test	5-1
	5.2.3.1 Test-Bed Engine Fabrication	5-1
	5.2.3.2 Test-Bed Engine Testing	5-1
Appendix		A-1

PRECEDING PAGE BLANK NOT FILMED

PAGE ii INTENTIONALLY BLANK

LIST OF ILLUSTRATIONS

Figure	Title	Page
1	ATTAP schedule	xvi
2	Ceramic component development cycle	xvii
3	ATTAP test-bed engine--AGT-5	xvii
4	Ceramic components selected for development	xviii
5	Polyimide-graphite fiber regenerator cold side seal with pressure and leaf installation deflection	1-2
6	AGT-5 test-bed enhanced stability diffusion flame combustor	1-4
7	Comparison of measured emissions from standard, enhanced stability, and rich primary zone combustors	1-5
8	AGT-5 test-bed rich primary zone diffusion flame combustor	1-6
9	AGT-5 test-bed solid wall diffusion flame combustor	1-7
10	AGT-5 test-bed indexing head low emissions prevaporizing/premixing combustor	1-8
11	Alternative mechanisms for actuating the indexing head variable geometry	1-10
12	Campbell diagram--integral vane/hub platform aerodynamic designs	1-11
13	Gasifier rotor flow area effect on total--total stage efficiency	1-12
14	Rotor hub surface velocities: high vs. low reaction stages	1-13
15	Gasifier turbine static structure	2-2
16	Gasifier turbine static structure FEM model	2-4
17	Temperature and maximum principal stress in scroll with vane slots; maximum power	2-5
18	Temperature and maximum principal stress in scroll with vane slots; 16 seconds into transient	2-6
19	Modified scroll design (vane pockets and retaining ring removed) for use with one-piece integral vane platform	2-7
20	Temperature and maximum principal stress in scroll without vane slots; maximum power	2-8
21	Temperature and max principal stress in scroll without vane slots; 16 seconds into transient	2-9
22	Gasifier scroll/vane transient radial deflections: includes vane containment ring and uses cold start-to-maximum power transient	2-11
23	Gasifier scroll/vane transient radial deflections: does not include vane containment ring. Uses cold start-to-maximum power transient	2-11
24	Gasifier scroll-to-vane platform mount interface	2-12
25	Maximum allowable geometric tolerances applied to the gasifier scroll/vane platform interface	2-12
26	Revised gasifier vane platform geometry	2-13
27	3-D calculated maximum principal stresses, 15-airfoil rotor, SN252 silicon nitride, transient acceleration condition	2-15
28	3-D calculated maximum principal stresses, 15-airfoil rotor, airfoil suction side, SN252 silicon nitride, transient acceleration condition	2-15
29	Calculated thermal gradients, 15-airfoil rotor, SN252 silicon nitride, transient acceleration condition	2-16
30	3-D calculated radial stress components, 15-airfoil rotor, SN252 silicon nitride, transient acceleration condition	2-17
31	Maximum principal stress profile, 15-bladed CBO GT rotor, room temperature spin, 100% N_1	2-18
32	CBO hot isostatic pressed (HIPed) α-SiC rotor (FX78504) burst, N_1 = 68,000 rpm	2-18
33	CBO HIPed α-SiC rotor (FX78513) burst, N_1 = 54,800 rpm	2-18
34	CBO HIPed α-SiC rotor (FX78509) burst, N_1 = 49,900 rpm	2-19
35	New balance method for spin testing rotors	2-19

LIST OF ILLUSTRATIONS (cont)

Figure	Title	Page
36	CBO HIPed α-SiC rotor (FX78505) burst, N_1 = 78,000 rpm, new balance method utilized	2-20
37	CBO HIPed α-SiC gasifier rotor (FX78517) burst, N_1 = 79,900 rpm	2.20
38	CBO HIPed α-SiC gasifier rotor (FX78519) burst, N_1 = 31,000 rpm	2-21
39	Section of CBO HIPed α-SiC burst rotor (FX78519). Initial failure site is circular crack (see arrow)	2-21
40	CBO HIPed α-SiC rotor (FX78522) burst, N_1 = 78,900 rpm	2-21
41	CBO HIPed α-SiC rotor (FX78528) burst, N_1 = 79,600 rpm	2-21
42	GTE Si_3N_4 gasifier rotor (S/N 399) burst, N_1 = 73,400 rpm	2-22
43	GTE rotor S/N 576 at moment of burst, N_1 = 76,400 rpm	2-22
44	Failure origin of GTE rotor (S/N 576)	2-23
45	Failure site location of GTE rotor (S/N 576)	2-24
46	3-D calculated maximum principal stress distribution for GTE PY6 rotor - room temperature spin condition	2-24
47	GTE rotor (S/N 656) at moment of burst, N_1 = 66,800 rpm	2-25
48	Failure origin of GTE rotor (S/N 656)	2-26
49	Failure site location of GTE rotor (S/N 656)	2-27
50	Failure origin of GTE rotor (S/N 639)	2-29
51	GTE rotor (S/N 647) at moment of burst, N_1 = 75,500	2-30
52	GTE rotor (S/N 670) just after failure, N_1 = 56,900	2-30
53	Failure origin of GTE rotor (S/N 670)	2-31
54	GCC GN-10 rotor (S/N 126) burst, N_1 = 78,800 rpm	2-33
55	GCC GN-10 rotor (S/N 145) burst, N_1 = 21,500 rpm	2-33
56	GCC GN-10 rotor (S/N 148) burst, N_1 = 65,300 rpm	2-34
57	GCC GN-10 rotor (S/N 189) burst, N_1 = 79,500 rpm	2-34
58	GCC GN-10 rotor (S/N 191) burst, N_1 = 75,600 rpm	2-35
59	GCC GN-10 rotor (S/N 149) burst, N_1 = 67,900 rpm	2-35
60	GCC GN-10 rotor (S/N 199) burst, N_1 = 78,700 rpm	2-36
61	Ceramic regenerator matrix sizing study for recommended 2 to 1 performance to fuel economy trade-off ratio	2-38
62	FEM model of ceramic power turbine rotor assembly	2-39
63	First-stage power turbine rotor temperature and stress distributions - SN252, steady-state	2-40
64	First-stage power turbine rotor temperature and stress distributions - SN252, transient, 36 seconds after start-up	2-40
65	Second-stage power turbine rotor temperature and stress distributions - SN235, steady-state	2-41
66	Second-stage power turbine rotor temperature and stress distributions - SN235, transient, 50 seconds after start-up	2-41
67	Normal probability plot of Mode 1 frequency for AGT-5 first stage ceramic power turbine rotor airfoils	2-43
68	Normal probability plot of Mode 2 frequency for AGT-5 first stage ceramic power turbine rotor airfoils	2-44
69	Power turbine FEM heat transfer model	2-45
70	Power turbine FEM stress model	2-45
71	Transient temperature and stress distribution results at 340 seconds--power turbine first-stage vane shroud	2-46
72	Transient temperature and stress distribution results at 340 seconds--power turbine first-stage vane	2-47

LIST OF ILLUSTRATIONS (cont)

Figure	Title	Page
73	Transient temperature and stress distribution results at 340 seconds--power turbine first-stage vane hub	2-48
74	Transient temperature and stress distribution results at 340 seconds--power turbine first-stage rotor shroud	2-48
75	Transient temperature and stress distribution results at 340 seconds--power turbine second-stage vane support	2-49
76	Transient temperature and stress distribution results at 340 seconds--power turbine second-stage vane	2-49
77	Transient temperature and stress distribution results at 340 seconds--power turbine second-stage shroud clamp	2-50
78	Transient temperature and stress distribution results at 340 seconds--power turbine second-stage rotor shroud	2-51
79	Power turbine metal static component normalized transient stresses: normalized by yield strength for alternate test stand transient	2-51
80	Ceramic first-stage power turbine vane configuration	2-52
81	FEM model of ceramic first-stage power turbine vane assembly	2-53
82	Temperature and equivalent stress distributions for forward PT case at 15 second transient	2-54
83	Temperature and equivalent stress distributions for aft PT case at 15 second transient	2-55
84	Temperature and equivalent stress distributions for PT first-stage rotor shroud at 15 second transient	2-56
85	Temperature and equivalent stress distributions for PT first stage vane at 15 second transient	2-57
86	Temperature and equivalent stress distributions for PT first stage vane centerbody at 15 second transient	2-58
87	Temperature and equivalent stress distributions for PT centerbody attachment bolt at 15 second transient	2-59
88	Temperature and equivalent stress distributions for PT centerbody attachment spool at 15 second transient	2-60
89	Power turbine ceramic component transient POS; first-stage vane and rotor shroud	2-61
90	Typical fracture origin (surface flaw) observed in GCC GN-10 Si_3N_4 IEA test bars	3-2
91	Fracture origin (surface porosity) observed in GCC GN-10 Si_3N_4	3-2
92	Microstructure of Norton/TRW NT154 Si_3N_4	3-3
93	Typical fracture origin (surface flaw) observed in Norton/TRW NT154 Si_3N_4 machined bars tested at room temperature	3-4
94	Typical fracture origin (internal pore) observed in Norton/TRW NT154 Si_3N_4 machined bars tested at 1370°C (2500°F)	3-4
95	Typical fracture origin (flaw in shallow surface depression) observed in as-HIPed NT154 bars tested at room temperature	3-5
96	Typical fracture origin (surface flaw) observed in as-HIPed NT154 bars tested at 1370°C (2500°F); shell-like feature is indicative of mechanical/impact damage	3-5
97	Microstructure of Norton/TRW NT235 reaction bonded SiC	3-5
98	Microstructure of Carborundum Hexoloy SX SiC	3-5
99	Typical room temperature fracture origin (internal inclusion/pore) observed in Carborundum Hexoloy SX SiC	3-6
100	Typical fracture origin (surface pore) observed in Dow Corning sintered β-SiC test bars	3-7
101	Typical fracture origin (internal porosity) observed in Ethyl Corporation unsintered SiC test specimens	3-7

LIST OF ILLUSTRATIONS (cont)

Figure	Title	Page
102	Typical fracture origin (Si_3N_4 grain) observed in Kyocera SN252 Si_3N_4 fabricated by new forming process	3-8
103	Primary fracture origin (surface flaw) observed in GTE PY6 Si_3N_4 rotor bars	3-9
104	Fracture origin (metallic inclusion) observed in GTE PY6 Si_3N_4 rotor bars	3-9
105	Schematic of test bars cut from Carborundum SiC rotors	3-10
106	Fracture origin (internal pores) observed in Carborundum sintered SiC rotor S/N FX78523	3-10
107	Typical fracture origin (surface flaw) observed in test bars cut from Carborundum sinter/HIPed SiC rotor S/N FX78520	3-10
108	Typical fracture origins observed in CPS CM200 sialon vane platform testbars-- a) surface flaw, b) internal flaw	3-11
109	Typical fracture origin (surface flaw) observed in CPS CM200 sialon tested at 1250°C (2282°F). The bubbles are the result of oxidation	3-12
110	As-disassembled condition of combustor dome and burner cover insulation (top); black O-ring (pointed out by arrow in bottom photo)	3-13
111	Gasifier turbine rotor (P/N 5-67200, S/N 0001-4) after laboratory cleaning	3-14
112	A representative rotor airfoil exhibited dark metallic deposits at leading edge root. This is the same airfoil shown in Figure 113	3-14
113	Representative gasifier rotor airfoil impact fracture. Golden metallic marks (circles) were found on suction surface of airfoil. Magnification = 5X	3-15
114	Two pieces of combustor dome welded to I.D. of scroll inlet	3-15
115	As-disassembled condition of the shroud	3-16
116	Rubbed I.D. surface on the aft side (left) and the cross-section of the piece (right)	3-16
117	Schematic diagram of the fracture of the gasifier shroud. Arrows point to the fracture origin at the O.D. of the shroud	3-17
118	Fractographs of the shroud on the forward side. The fracture origin is pointed out by the arrow	3-17
119	The O.D. surface condition at the fracture origin (arrow)	3-17
120	Kyocera SN252 Si_3N_4 gasifier rotor (P/N 5-67200, S/N 5K25) after testing in engine S/N 11, BU25	3-17
121	Schematic of damage to Kyocera gasifier rotor S/N 5K25	3-18
122	Fracture origins in Kyocera rotor S/N 5K25 airfoils	3-18
123	Suction side of blade 10 (per Figure 121). White areas are engine insulation	3-19
124	CBO sintered α-SiC microstructures. X°C is the standard sintering temperature	3-21
125	CBO molded and sintered vane iterations	3-22
126	CBO scroll configurations	3-23
127	Effect of casting time and pressure on wall thickness; CBO low pressure slip casting	3-25
128	Length shrinkage versus colloidal silica ratio: Manville insulation	3-26
129	Width shrinkage versus colloidal silica ratio: Manville insulation	3-27
130	Thickness shrinkage versus colloidal silica ratio: Manville insulation	3-27
131	Dry density versus colloidal silica ratio: Manville insulation	3-27
132	Length shrinkage versus mixing time for both old and new polyox batches: Manville insulation	3-27
133	Width shrinkage versus mixing time for both old and new polyox batches: Manville insulation	3-28
134	Thickness shrinkage versus mixing time for both old and new polyox batches: Manville insulation	3-28
135	Dry density versus mixing time for both old and new polyox batches: Manville insulation	3-28
136	Effect of fiber milling on insulation drying shrinkage: Manville insulation	3-29

LIST OF ILLUSTRATIONS (cont)

Figure	Title	Page
137	Effect of fiber milling on insulation dry density: Manville insulation	3-29
138	Injection molded and HIPed GTE AGT-5 rotors made using monolithic PY6 (left) and PY6 +30% SiC whiskers (right)	3-35
139	CPS vane platform configuration	3-38
140	Redesigned mounting system of hot gasifier rig viewing window	4-3
141	Peak operating temperature versus speed: advanced concept ceramic scroll test	4-6
142	Temperature survey of regenerator matrix sample thermal cyclic rig (note: radial location = center of sample)	4-12
143	Regenerator test sample pressure rig	4-12
144	Haynes 230 nickel alloy after 5000 thermal cycles	4-13
145	Comparison of ceramic regenerator versus metal regenerator: pressure drop	5-2
146	AGT-5 engine--external thermocouple locations (top view)	5-3
147	AGT-5 engine--external thermocouple locations (side view)	5-4

LIST OF TABLES

Table	Title	Page
I	Comparison of RPD vehicle performance to baseline Grand Am	xviii
II	Chassis dynamometer test results of rich primary zone combustor, M85 fuel	1-7
III	Engine inlet test results	1-13
IV	Gasifier turbine static structure materials: materials utilized in the thermal/ deflection analysis of the gasifier assembly incorporating an integrally vaned platform	2-7
V	Gasifier turbine transient analysis points: all points from cold start	2-7
VI	Gasifier static structure deflection analysis with retaining ring: radial clearance summary	2-10
VII	Gasifier static structure deflection analysis without retaining ring: radial clearance summary	2-10
VIII	Calculated probabilities of survival, 15-airfoil ceramic rotor, AGT-5 engine	2-14
IX	Comparison of transient POS values for 15- & 20-airfoil rotors of Kyocera SN252 Si_3N_4	2-14
X	CBO rotor spin test results	2-20
XI	CBO rotor status	2-22
XII	GTE rotor spin test results	2-27
XIII	GTE rotor status	2-28
XIV	N/TRW rotor spin test results	2-28
XV	N/TRW rotor status	2-28
XVI	GCC rotor spin test results	2-30
XVII	GCC spin test data vs. NDE results	2-30
XVIII	GCC rotor status	2-32
XIX	Gasifier rotor status	2-32
XX	Ceramic PT rotor analysis results	2-42
XXI	First stage power turbine rotor frequency summary	2-43
XXII	Strength characteristics of Norton/TRW NT154 silicon nitride	3-4
XXIII	Strength characteristics of Carborundum Hexoloy SX SiC	3-6
XXIV	Strength characteristics of Ethyl Corporation unsintered SiC material	3-7
XXV	Strength characteristics of Kyocera SN252 silicon nitride	3-8
XXVI	Strength characteristics of GTE Labs PY6 silicon nitride gasifier turbine rotor (P/N 5-80503, S/N 420)	3-9
XXVII	Strength characteristics of CPS CM200 sialon	3-11
XXVIII	Carborundum SiC rotor sintering matrix	3-20
XXIX	Properties of CBO sintered and sinter/HIPed α-SiC rotors	3-20
XXX	Drying shrinkage comparison: desired versus measured	3-29
XXXI	Evaluation of fresh colloidal silica impact on drying shrinkage	3-29
XXXII	Strength characteristics of GTE PY6 Si_3N_4 gasifier turbine rotors	3-31
XXXIII	GCC GN-10 silicon nitride gasifier turbine rotor spin test results	3-36
XXXIV	Strength characteristics of GN-10 silicon nitride test bars cut from AGT-5 rotors	3-37
XXXV	CPS CM200 sialon vane platform dimensions	3-39
XXXVI	Mechanical properties of slip cast NT154 Si_3N_4	3-40
XXXVII	Spin test results for N/TRW NT154 silicon nitride gasifier turbine rotors	3-41
XXXVIII	Mechanical properties of NT235 SiC	3-42
XXXIX	Hot gasifier rig accumulated test time	4-5
XL	History of AGT-5 ceramic gasifier rotor; 20-blade design, Kyocera SN252, S/N 5K22	4-7
XLI	Corning MAS regenerator matrix MOR strength following cyclic testing	4-10
XLII	Corning regenerator samples (MOR) extruded MAS (26% porous) as received	4-11

SUMMARY

ATTAP activities during the past year were highlighted by test-bed engine design and development activities; ceramic component design; materials and component characterization; ceramic component process development and fabrication; component rig testing; and test-bed engine fabrication and testing. Although substantial technical challenges remain, all areas exhibited progress.

Test-bed engine design and development activity included engine mechanical design, combustion system design, alternate aerodynamic designs of ceramic gasifier scrolls, and engine system integration aimed at upgrading the AGT-5 from a 1038°C (1900°F) metal engine to a durable 1371°C (2500°F) structural ceramic component test-bed engine. A one-piece molded polyimide-graphite fiber cold side regenerator seal was designed and fabrication of a subscale seal was initiated. Design layouts for two new hot face regenerator seal concepts were also initiated. Combustion system design/development activities included testing both the enhanced stability and rich primary zone diffusion flame combustors. A solid wall diffusion flame combustor was also designed to increase combustor wall temperature, thereby reducing wall quenching of carbon monoxide (CO) and hydrocarbon (HC) burnout reactions. In addition, a mechanical design of an indexing head low emissions prevaporizing/premixing combustor was completed. The aerodynamic design of an integral vane/hub platform for an alternate scroll assembly was completed. Engine control software for durability cycle operation was completed and the AGT-5 engine was successfully tested utilizing the new control software and hardware. Comparative evaluations of starter motors have been completed and new fuel pump/motor combinations are undergoing evaluation.

ATTAP-defined ceramic and associated ceramic/metal component design activities completed include: the ceramic gasifier turbine static structure, the ceramic gasifier turbine rotor, the ceramic regenerator disk, the ceramic power turbine rotors, and the ceramic/metal power turbine static structure. A 2-D finite element method (FEM) analysis was completed for the gasifier turbine scroll utilizing DuPont/Lanxide Aluminum Titanate/Alumina. The probability of survival (POS) was unacceptable in both the individual vane and integral vane/hub platform configurations. A heat transfer and deflection analysis was performed, for material selection purposes, for the gasifier integral vane/hub platform and scroll assembly. Based upon assembly and operating clearance considerations, it was determined that the optimum material configuration consists of a Kyocera SN252 Si_3N_4 scroll and a Norton/TRW (N/TRW) NT154 Si_3N_4 vaned platform. Three-dimensional (3-D) FEM analyses were completed for the 15-blade gasifier rotor design utilizing the following Si_3N_4 materials: Kyocera SN252, GTE Laboratories (GTE) PY6, and N/TRW NT154. All three material systems exceeded the Reference Powertrain Design (RPD) POS goals at steady-state max power but failed to do so in the cold start to max power transient condition. Seven gasifier rotors successfully passed proof spin testing: two Carborundum (CBO) α-SiC 15-bladed rotors, four N/TRW NT154 20-bladed rotors, and one Garrett Ceramic Components (GCC) GN-10 20-bladed rotor. A ceramic regenerator matrix sizing study, based solely on a performance/fuel economy tradeoff, was completed specifying wall thickness and cell density combinations. The 2-D FEM analysis for both ceramic power turbine rotors was revisited using updated temperature data. Both rotors exceeded the probability of survival goals for engine operation. In addition, the first-stage power turbine rotor natural frequencies were calculated (using 3-D FEM analyses) and determined experimentally with excellent correlation between the two methods. A ceramic power turbine first-stage vane 2-D axisymmetric FEM analysis was performed. The probability of survival meets design goals at steady-state max power as well as throughout the cold start-up transient. The metal power turbine static structure was re-analyzed using a modified "test stand" transient schedule that increased the hold time at idle while keeping the baseline idle-to-max power acceleration. Material yield strengths for the metal power turbine static hardware are still exceeded locally with the modified transient schedule as

PRECEDING PAGE BLANK NOT FILMED

PAGE X INTENTIONALLY BLANK

the transient stresses are driven primarily by the idle-to-max power acceleration as opposed to the length of time spent at idle.

The materials and component characterization efforts included the testing and evaluation of seven candidate ceramic materials and three components being developed for use in the ATTAP. Material characterization activities have focused on microstructural, density, fracture toughness, and flexural strength evaluations of various candidate ceramic materials. Fracture surface analysis was also used to determine the nature and location of the strength-controlling defects. In addition, the time-dependent strength and oxidation resistance characteristics were evaluated for selected materials.

Ceramic component process development and fabrication activities are being conducted for the gasifier turbine rotor, gasifier turbine scroll, gasifier turbine vanes and vane platform, extruded regenerator disks, and thermal insulation. Major ceramic industry development subcontractors are: The Carborundum Company (CBO); Manville Corp.; GTE Laboratories Inc (GTE); Corning Inc.; Garrett Ceramic Components (GCC); Ceramics Process Systems (CPS); and Norton/TRW Ceramics (N/TRW). Carborundum optimized their sintering and hot isostatic pressing (HIP) parameters and delivered 3 sintered and 12 HIPed α-SiC rotors. CBO also delivered 113 defect free α-SiC gasifier turbine vanes. Their slip casting development efforts resulted in the delivery of 4 gasifier turbine scrolls, one of which was qualified for rig/engine testing. Manville successfully completed the initial injection molding of thermal insulation onto the gasifier housing utilizing a thin plastic film for mold release. In addition, Manville continued process/material development activities aimed at eliminating drying shrinkage and water "bleeding". GTE established their process for fabrication of PY6 Si_3N_4 gasifier turbine rotors. Twenty rotors were delivered. In addition, the final batch of PY6 Si_3N_4 rotors with 30 v/o SiC whiskers were fabricated. Due to extreme airfoil distortion during rotor densification, the whisker-reinforced rotor activity was discontinued. Corning delivered samples of a new 20% porous magnesium aluminum silicate (MAS) extruded regenerator matrix. The thermal expansion of the new MAS was found to be 62% higher than the typical expansion of Corning 26% porous MAS. Corning also confirmed an excessive projected production cost for aluminum silicate (AS) regenerator disk material with the current process. GCC completed its full-scale GN-10 Si_3N_4 rotor fabrication effort with the delivery of one proof spin tested rotor. The rotor successfully passed proof spin testing to 80,000 rpm following blade release at a lower speed. CPS completed tool modifications which successfully eliminated cracking in the vane pocket region of the gasifier vane platform. Fabrication activities were completed and components forwarded for final machining. N/TRW established processes for the fabrication of NT154 rotors and NT235 scrolls. Four proof spin tested rotors were delivered. Scroll casting/processing yields exceed 60%. Scroll fracturing in the shroud area during finish machining will be addressed by changing from NT235 to the stronger NT230 SiC material.

Component rig activities include the development of both rigs and the necessary test procedures, and conduction of rig testing of the ceramic components and assemblies. All ceramic components are rig proof tested prior to engine test-bed installation. Currently, five component rigs are being utilized: a gasifier rotor/shafting system rig, two hot gasifier rigs, a regenerator cyclic sample rig, and a regenerator matrix sample compressive pressure failure rig. Developmental issues with the gasifier rotor/shafting system rig have been resolved and the rig is fully operational. Design of a power turbine rotor/shafting system rig has been completed and hardware procurement initiated. A second hot gasifier rig was fabricated and installed in the test cell. Shakedown testing was successfully completed. Developmental hot gasifier rig evaluations were performed with an experimental air-cooled metal gasifier scroll and both 15- and 20-bladed Si_3N_4 rotors. The rotors were successfully operated to 1366°C (2491°F) @ 90% N_1, and 1395°C (2543°F) @ 98% N_1, respectively. An experimental Si_3N_4 gasifier turbine scroll and a Si_3N_4 20-bladed rotor were operated to 1401°C (2554°F) @ 100% N_1. These runs exceeded the Reference Powertrain Design (RPD) goals. A test cell was automated,

and unattended running of a hot gasifier rig on the GM Automotive Gas Turbine Durability Test Cycle was implemented. The regenerator cyclic sample rig is used to evaluate candidate ceramic and metal regenerator matrix samples by exposure to cyclic temperatures. Several candidate material samples were evaluated using a simulated engine full throttle acceleration-deceleration thermal cycle. The Corning 20% and 26% porous MAS materials, as well as the Haynes 230 nickel alloy, were found to be unsuitable regenerator materials. The Corning AS material retained-strength after 10,000 cycles was more than adequate for usage in the regenerator disk. The regenerator compressive pressure failure rig was fabricated and brought on-line. After testing Corning AS to 6.2 MPa (900 psi), it was concluded that the rectangular matrix is not subjected to cross corner compressive weakness by pressure loading.

Test-bed engine fabrication, testing, and development supported improvements in ceramic component technology that will permit the achievement of program performance and durability goals. Both long-term cyclic and steady-state engine tests are being performed. Test-bed engine testing activities included durability testing of the AGT-5 durability test-bed engine; verification testing of the "upgraded" power turbine gearbox; and initial evaluation of an intermediate temperature engine configured with a ceramic gasifier rotor. A total of 2444 hr of test and development time have been accumulated on the test-bed engines and rigs since the inception of ATTAP. The designated durability engine has accumulated 730.6 hr (371.3 hr in 1990), 485.6 of which were on the General Motors Automotive Gas Turbine Durability Test Cycle. Tests were also conducted at idle, cruise, and full power conditions.

INTRODUCTION

This is the third of a series of annual reports documenting work performed on the ATTAP. This work is being conducted by a team directed by GM, with significant activities underway at GM's Allison Gas Turbine Division (which serves as prime contractor), at GM's AES located at the General Motors' Technical Center, and at the several domestic ceramic suppliers who are under development subcontracts. The U.S. Department of Energy (DOE) sponsors this work, which is managed and technically directed by NASA under contract DEN3-336.

GOAL AND OBJECTIVES

ATTAP is intended to advance the technological readiness of an automotive ceramic gas turbine engine based on efforts begun in the Automotive Gas Turbine (AGT) Project, a DOE/NASA program executed between 1979 and 1987. This AGT project successfully demonstrated the feasibility of using structural ceramic hot-section components in automotive-sized gas turbine engines. Specifically, ATTAP aims to develop and demonstrate the technology of structural ceramics that have the potential for competitive automotive engine life cycle cost and for operating for 3500 hr (automotive engine life) in a turbine engine environment at temperatures up to 1371°C (2500°F). Project objectives are the following:

- Enhance the development of analytical tools for ceramic component design using the evolving ceramic properties data base
- Establish improved processes for fabricating advanced ceramic components
- Develop improved procedures for testing ceramic components
- Evaluate ceramic component reliability and durability in an engine environment

PROGRAM SCHEDULE AND CONTENT

Figure 1 shows the scheduled activities in the 61-month program. Materials assessment occurred at the initiation of ATTAP and resulted in the targeting of ceramic component technology goals and the identification of materials, processes, and manufacturers to address those goals. The materials assessment was updated in Year 3 and will be updated in Year 5, at which time the state of the art will be reassessed for each component and required technology improvements will be redefined. The identification and evaluation of materials, processes, and manufacturers are ongoing, continuous activities in ATTAP, and promising candidates are integrated into the program as merited. Similarly, those technologies and/or ceramic component suppliers which do not productively evolve to address program goals are truncated from ATTAP.

RPD activities include the preliminary design of a powertrain system which could meet performance, cost, and reliability design goals. Such a design was executed at the beginning of ATTAP using a high temperature derivative of the AGT-5 automotive gas turbine engine. The RPD was updated in Year 3 to reflect current ceramic component technology and goals, and will be updated again in Year 5 to provide a cost estimate of such a powertrain in production.

Test-bed engine development, shown in Figure 1 as an intermittent activity, includes those efforts aimed at ensuring the availability and functionality of the AGT-5 gas turbine engine as the test-bed for the high temperature ceramic components. Although engine development is not a primary focus of ATTAP, these activities recognize the need for continuing evolution of the engine to handle the power and thermal loads, as well as design changes resulting from the integration of a high temperature flow path.

Central to the logic of Allison's ATTAP approach is an iterative component development cycle. Three such cycles are shown in Figure 1 and include the design/fabrication/characterization/rigs/engine test sequences of activities. These three development cycles reflect anticipated improvements in ceramic materials and the associated component processing technologies, and the incorporation of laboratory characterization data and rig/engine test results into succeeding designs. The initial design activity, shown with a milestone at the end of

PAGE XIV INTENTIONALLY BLANK

PRECEDING PAGE BLANK NOT FILMED

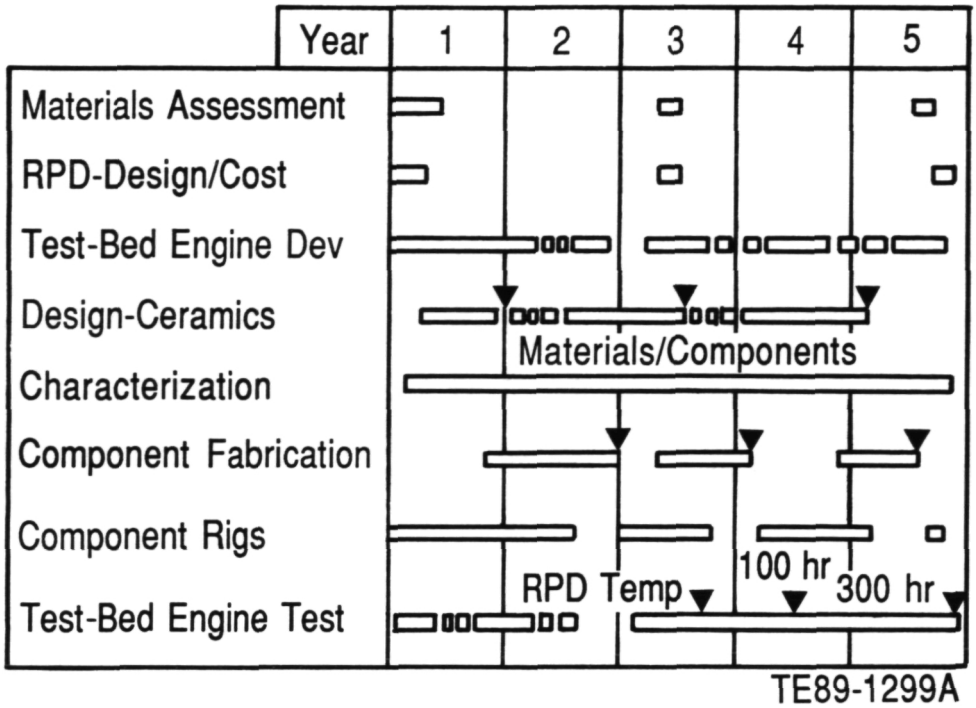

Figure 1. ATTAP schedule.

Year 1, featured then-current monolithic ceramic technology in the design of the gasifier turbine stage of the AGT-5 engine for 1371°C (2500°F) turbine inlet temperature (TIT) plus other required hot flow-path pieces. The second and third design phases incorporate toughened and advanced (e.g., from Oak Ridge's Ceramic Technology for Advanced Heat Engines [CTAHE] project) materials and processes as they become available, used in the same gasifier stage components. Additionally, these succeeding design phases include other necessary ceramic components in the high-temperature test-bed engine, notably power turbine flow-path pieces. Component fabrication includes those process development activities executed by ceramic suppliers that result in the fabrication of engine-usable components. Characterization involves those laboratory activities both at suppliers and at Allison which measure and define the various properties and qualities of ceramic materials in both test bar form and in components. Examples are microstructural evaluation and measurements of density, strength, oxidation resistance, toughness, etc. Included are the development and application of nondestructive evaluation (NDE) techniques.

Component rig activity includes the development of rigs for component verification and testing (e.g., hot gasifier turbine rigs) as well as the actual testing activities. Test-bed engine test includes those testing activities associated with test-bed engine development plus the verification and development testing of the ceramic components. Note that each of the three component development cycles begins with design, followed by component fabrication, characterization, then rig testing, and finally engine testing. This rigorous development process, shown in Figure 2, is iterative between the users and the ceramic supplier community and ensures developing an understanding of the behavior of components in service and the continuous identification of areas for improvement.

TEST-BED ENGINE AND RPD

Figure 3 shows the automotive gas turbine engine being used as the ceramic component development test-bed for the ATTAP. This GM-developed engine, the AGT-5, is a two-shaft, regenerative configuration with axial-flow gasifier and power turbines. The engine produces approximately 110 hp at its original full-power TIT of 1038°C (1900°F).

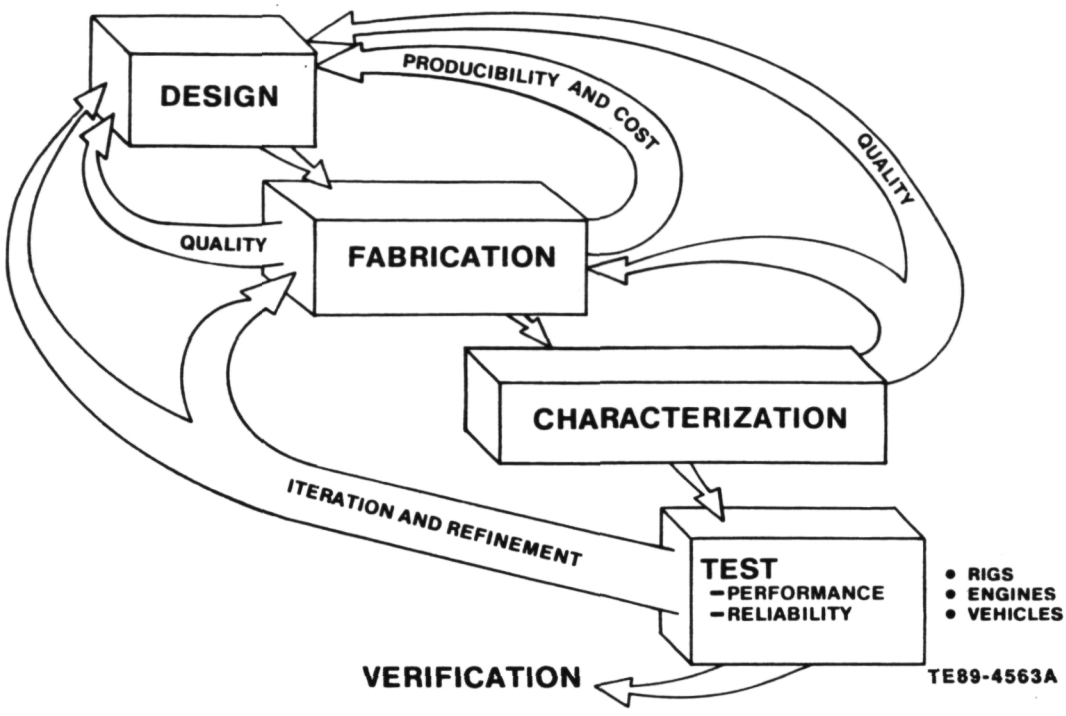

Figure 2. Ceramic component development cycle.

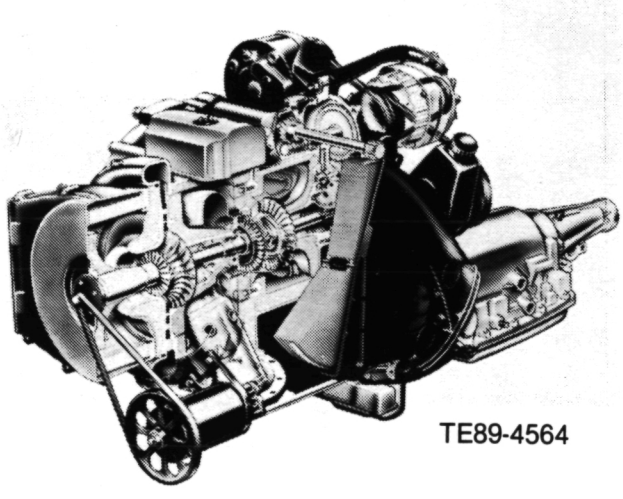

Figure 3. ATTAP test-bed engine--AGT-5 .

An RPD was completed at the outset of ATTAP in order to ensure that the AGT-5-type power plant has the potential to fulfill the overall fuel economy goals that underlie the DOE's sponsorship of automotive gas turbine technologies. This RPD is a preliminary engineering design of a powertrain system that integrates with vehicle characteristics to provide a system with the potential for meeting not only performance, but also cost and reliability goals. Specific performance goals are the following:

- 30% improvements in fuel economy over the reference 1988 Pontiac Grand Am equipped with a 2.5 ℓ, 4-cylinder, spark-ignition engine over the combined Federal Driving Cycle
- competitive vehicle drivability and performance with the reference 1988 Grand Am
- gaseous emissions and particulate levels less than the following (based on diesel fuel No. 2):

  NO_x = 0.249 gm/km (0.4 gm/mile), HC = 0.255 gm/km (0.41 gm/mile), CO = 2.11 gm/km (3.4 gm/mile), particulates = 0.129 gm/km (0.2 gm/mile)

- ability to use a variety of alternate fuels

Table I shows the results of the RPD performance simulation, based on the AGT-5-type engine, versus the baseline reference vehicle.

Table I.
Comparison of RPD vehicle performance to baseline Grand Am.

	Baseline--2.5 ℓ spark-ignition	RPD--turbine
0-96.5 kmph (60 mph) time--sec	13.5	13.1
Top gear gradability at 88.5 kmph (55 mph)--%	7.9	10.9
Composite fuel economy--ℓ/100 km (miles/gal)	7.66 (30.7)	4.87 (48.3)

Thus the simulated RPD gas turbine equivalent vehicle outperforms the reference piston engine installation in critical fuel economy, performance, and drivability parameters.

The emissions and alternate fuels goals are considered achievable based on demonstrated GM experience. For example, the AGT 100 (from AGT Project) engine's combustion system has displayed laboratory steady-state emissions of oxides of nitrogen (NO_x), CO, and unburned hydrocarbons (UHC) well within current Federal Emissions Standards using diesel fuel, jet fuel, and methanol. The AGT-5 engine has successfully run on dry powered coal. Although such systems have demonstrated the potential for low emission/alternate fuel gas turbine combustion, much work remains to achieve a fully-functional system suitable for automotive application. Such efforts are outside the scope of ATTAP. The definition of power plant cost and reliability goals, in addition to performance, is included in ATTAP.

CRITICAL COMPONENTS

Consistent with the strong ATTAP emphasis on ceramic component technology is the focus on specific gas turbine components as development/demonstration targets. Four ceramic components and the engine insulation have been identified as critical development components because: (1) their functional success is critical to the viability of the ceramic automotive gas turbine engine, and (2) each requires some further technological development to be proven reliable and durable in the automotive engine environment. These critical elements, shown in Figure 4, are the following:

- gasifier turbine rotor
- gasifier turbine vanes
- gasifier turbine scroll
- regenerator disks
- thermal insulation

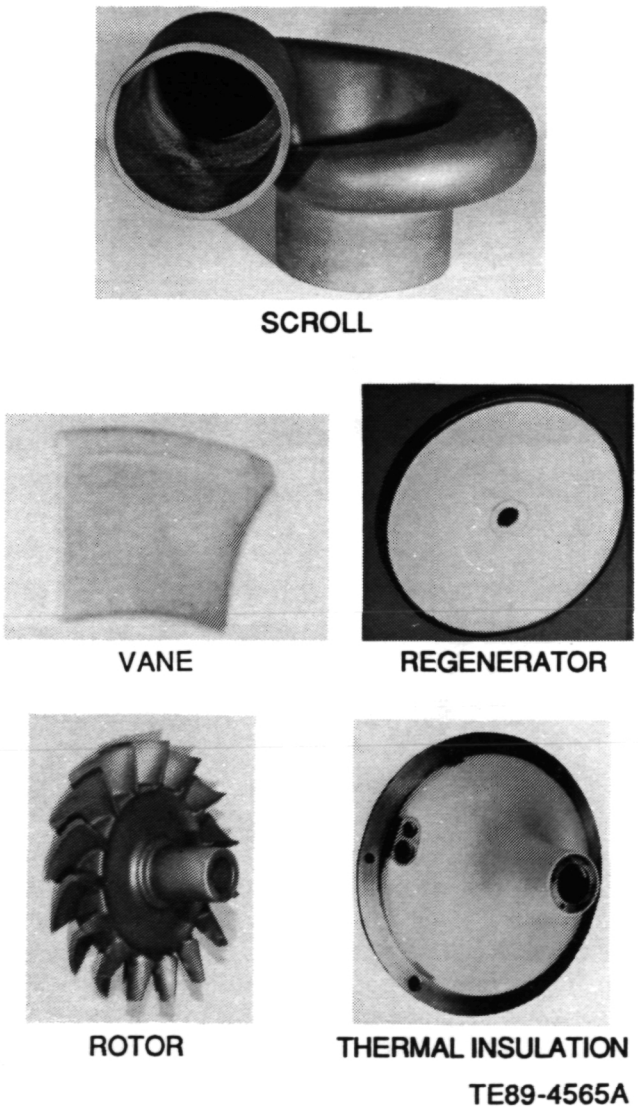

Figure 4. Ceramic components selected for development.

For each component, specific areas and parameters requiring improvement have been identified and quantified where possible.

I. ENGINE/POWERTRAIN DESIGN AND DEVELOPMENT, ANALYSIS, AND MATERIALS ASSESSMENT

1.4 TEST-BED ENGINE DESIGN AND DEVELOPMENT

The overall objective of this task is to perform the required preliminary and detail design activities to ensure that the AGT-5 ATTAP rig(s) and test-bed engine(s) can accept improved ceramic components and operate at the higher temperatures permitted by improved ceramics. Design activities are based on the RPD operating conditions. Specifically, efforts are concentrated in the following four areas:

- mechanical
- combustion systems
- alternate flow paths
- engine system integration

1.4.1 Mechanical

Objective/Approach

The objective of the mechanical design and development activity is to upgrade the AGT-5 from a 1038°C (1900°F) metal engine to a durable 1371°C (2500°F) structural ceramic component test-bed engine. Activity during 1990 primarily focused on the regenerator seal system.

Accomplishments/Results

- Evolved a one-piece molded polyimide-graphite fiber cold side regenerator seal design using stress analysis
- Designed a three-piece die for molding one-piece, subscale, polyimide-graphite fiber regenerator cold seals; initiated seal fabrication
- Obtained carbon-carbon tensile strength data from BP Chemicals (HITCO) Inc. of 47 ksi which is 4x the strength of current material (carbon-carbon is used as a combined structure and wearface for regenerator seals); obtained a production quantity quote for stronger carbon-carbon blanks for hot side regenerator seal rims
- Requested quote from APS Materials Inc. for plasma spray coating seal crossarms with Ford I112 wear coat for comparative tests
- Obtained a budgetary quote for regenerator seal wearface plasma spray powder
- Initiated design layouts for two new hot face regenerator seal concepts featuring fewer parts and simplified assembly

Discussion

The one-piece molded polyimide-graphite fiber cold side regenerator seal design was optimized (tapered sealing leaf tip reduction to 0.015 in.) to achieve acceptable deflection stresses. The resulting cross section, and radial stress distributions for combined deflection and pressure loads, are shown in Figure 5. The seal stress was calculated to be 41% of the material's ultimate flexural strength and 88% of its ultimate tensile strength. This is judged to be low enough to merit fabrication and evaluation of a subscale test piece. Stress calculations show that die deflection, due to molding forces, will be negligible and will not prevent accurate molding of the thin tapered sealing leaf for the subscale polyimide-graphite cold seal. The one-piece molded seal offers the potential of reduced leakage and lower cost.

A previous supplier of nickel oxide/calcium fluoride (NiO/CaF_2) plasma spray powder has again agreed to produce some and made a budgetary quote. A change in the oxidized state of the NiO used by the current supplier had resulted in spalling of the NiO/CaF_2 during heat treatment which has necessitated a change in powder. Spray coated seal crossarms are required for engine and turbine rig testing.

In order to improve the durability and high temperature capability of hot face regenerator seals, design layouts for two new seal concepts have been initiated. Both concepts feature fewer parts, simplified assembly, and the potential for reduced cost. A production quantity

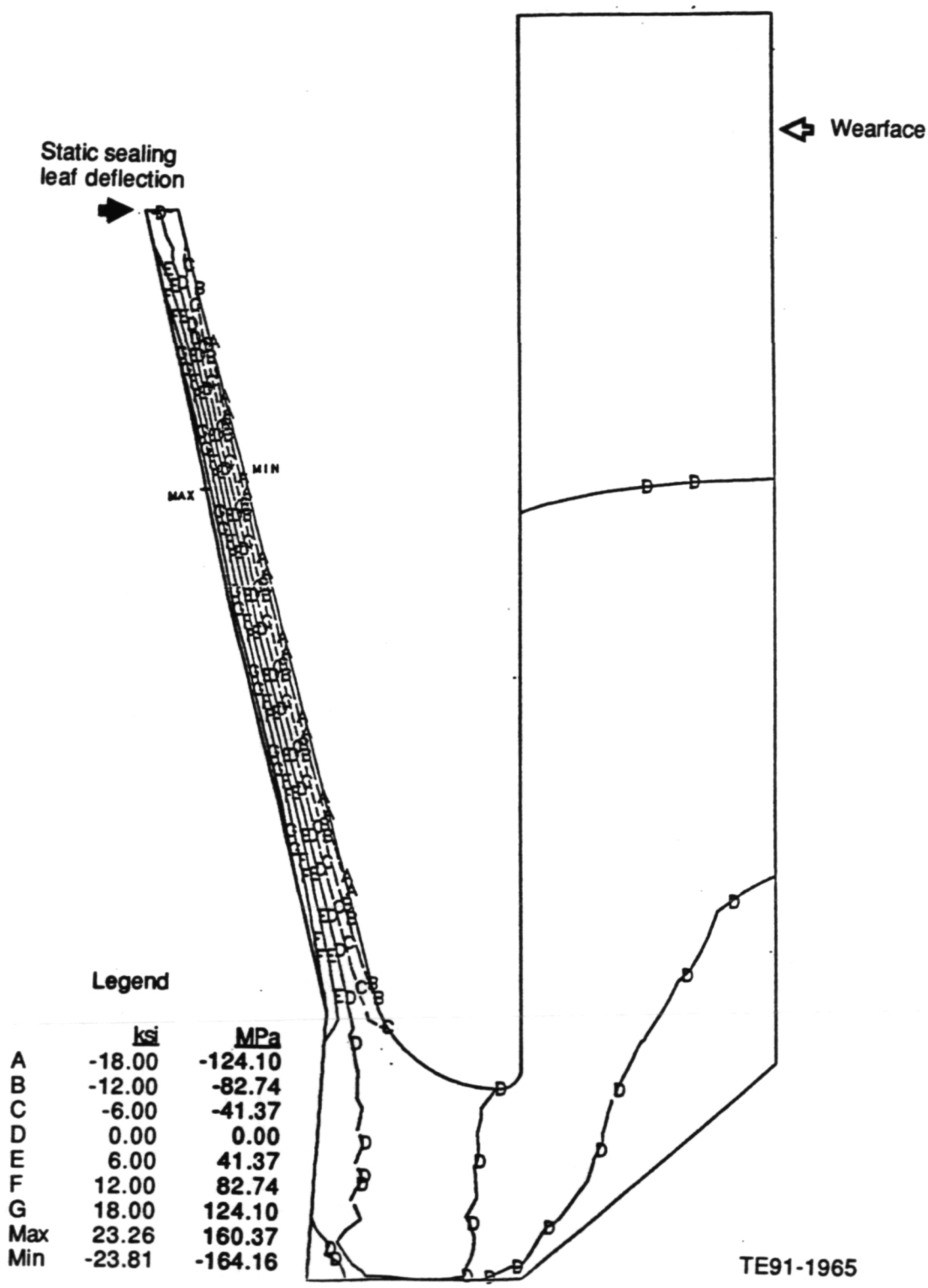

Figure 5. Polyimide-graphite fiber regenerator cold side seal with pressure and leaf installation deflection.

quote was obtained from Hitco to verify that cost would not be a show-stopper if one of their carbon-carbon materials was selected for the rim seal in one of the concepts being studied.

1.4.2 Combustion Systems

Objective/Approach

Combustion system development efforts contain both short- and long-term objectives. The short-term objective entails meeting current Federal automotive emission standards (1.0 gm/mi NO_x, 3.4 gm/mi CO, 0.41 gm/mi HC) while remaining carbon free when burning methanol fuel by making minor changes to the AGT-5 test-bed diffusion flame combustor. The long-term objective is an ultra-low NO_x combustor that will meet the lowest proposed California NO_x standard of 0.2 gm/mi while operating on diesel fuel. A prevaporizing/premixing combustor is required to achieve this goal. Other requirements include fuel flexibility, combustion stability, carbon free operation, cold start capability, driveability, and reliability. An additional long-term objective is the development of an advanced combustion system that has the potential to meet emission goals without the benefit of exhaust gas treatment.

Accomplishments/Results

- Enhanced stability and rich primary zone diffusion flame combustors were tested on an engine dynamometer stand. At steady-state conditions, emissions from the rich primary zone combustor were low enough to meet current Federal standards.

- Rich primary zone combustor was tested in Camaro Z28 turbine car on chassis dynamometer. Over the transient urban driving cycle NO_x and CO emissions were 19% and 5%, respectively, above current Federal standards.

- Solid wall diffusion flame combustor, to be tested in 1991, was designed.

- Mechanical design of indexing head low emissions prevaporizing/premixing combustor was completed.

Discussion

During 1990 two diffusion flame combustor modifications were tested and a third was designed. Also, the mechanical design of an ultra-low emissions prevaporizing/premixing combustor was completed.

Diffusion Flame Combustors. Historically, the standard AGT-5 test-bed diffusion flame combustor has met current Federal emissions standards for CO and HC when burning diesel fuel and for NO_x when burning methanol. However, all three standards have not been met simultaneously.

In the initial attempt to reduce CO and HC emissions so that all three emissions standards could be met on methanol fuel, the standard combustor was modified to improve its combustion stability. Thumbnail louvers in the combustor dome were replaced with an axial swirler, and the primary air admission jets were relocated to a plane further downstream on the combustor body. The revised burner was named the enhanced stability combustor and is depicted in Figure 6. The modifications were made to significantly increase the recirculating mass flow rate in the combustor primary zone and to eliminate combustion instability as a potential cause of high CO and HC emissions when burning methanol.

The enhanced stability combustor was installed in an AGT-5 engine and tested on an engine dynamometer stand at the General Motors' Technical Center. Emissions were measured at steady-state operating conditions over a range of gasifier speeds. Atomizing air pressure drop was also varied in the test. The fuel was M85, a mixture of 85% methanol and 15% gasoline by volume. Emissions results are compared to those of the standard combustor in Figure 7. As can be seen from this figure, the modifications had the opposite of the intended effect. NO_x emissions were reduced, but CO and HC emissions increased with respect to the standard combustor. This result indicated that combustion instability was not the cause of

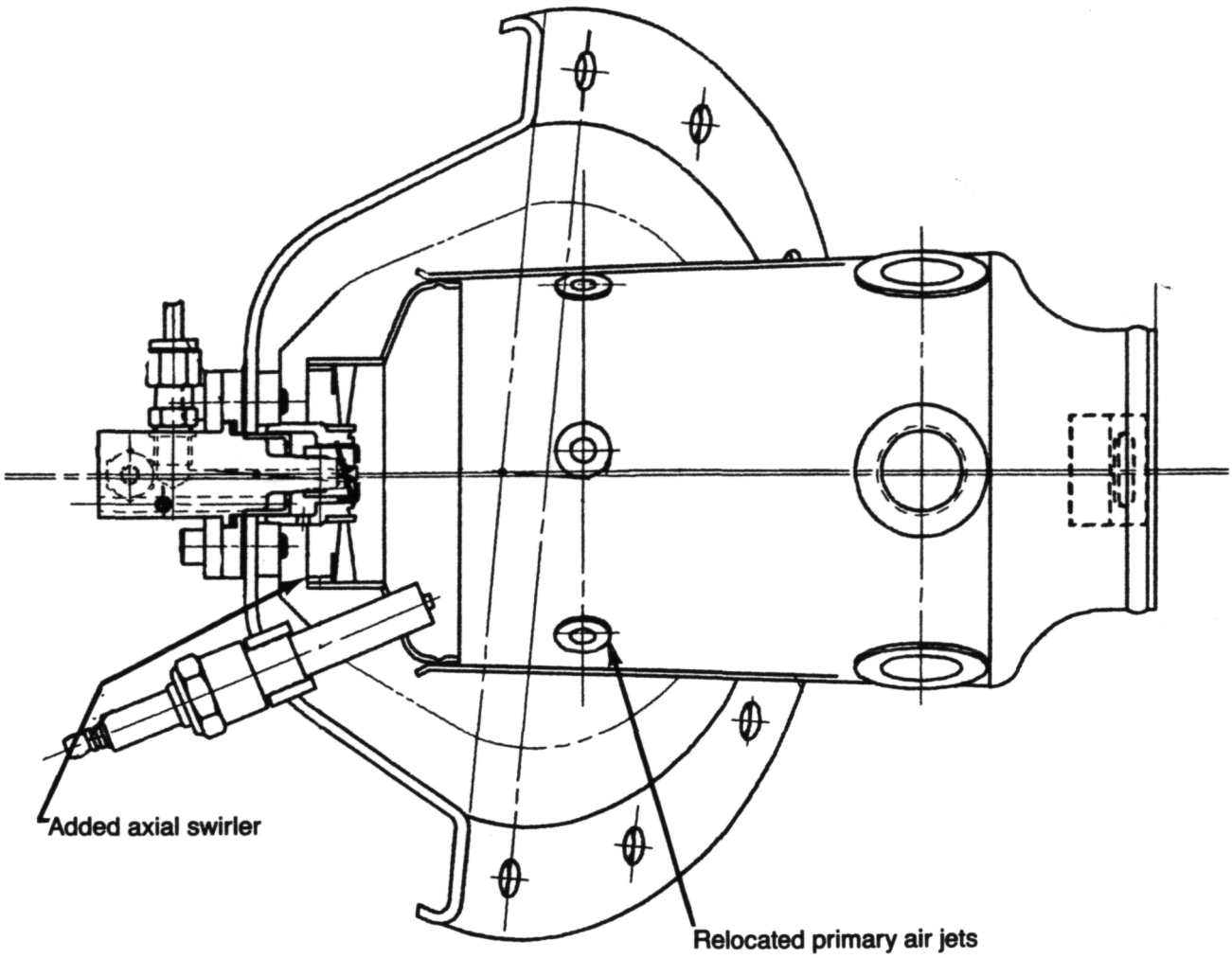

TE90-2075

Figure 6. AGT-5 test-bed enhanced stability diffusion flame combustor.

high CO and HC emissions, but that primary zone stoichiometry might be since the enhanced stability combustor has a leaner primary zone. Figure 7 also shows the significant effect of atomizing air pressure drop on CO and HC emissions.

The next modification tested was designed to have less air in the primary zone than the standard combustor and was, therefore, called the rich primary zone combustor. The only difference between the two burners is that thumbnail louvers on the standard combustor dome are blocked in the rich primary zone combustor as shown in Figure 8. Emissions results with the rich primary zone combustor are shown in Figure 7. Very significant reductions in CO and HC were achieved without an increase in NO_x. In fact, emissions were low enough to meet current Federal standards if converted to a gm/mi basis. However, this result was not obtained over the formal urban driving cycle since the test was performed on an engine dynamometer stand under steady-state conditions.

The next step was to install the rich primary zone combustor in a Chevrolet Camaro Z28 turbine car for test on a chassis dynamometer to evaluate the effect of transient operation on emissions. Test results over the Federal Urban Driving Cycle are listed in Table II. In the initial test NO_x and CO emissions exceeded the standard by 19% and 5%, respectively. The test was repeated because data acquisition problems

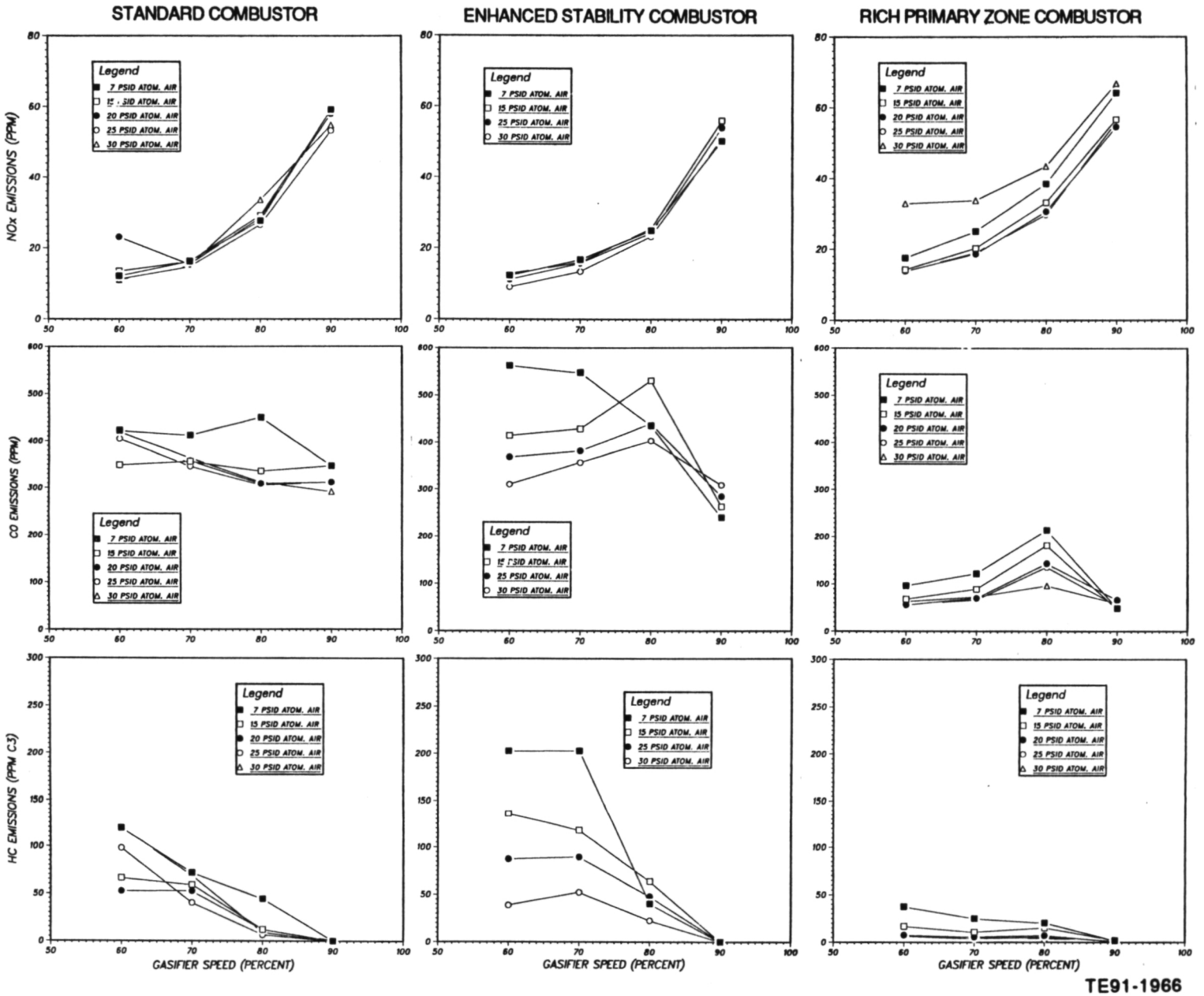

Figure 7. Comparison of measured emissions from standard, enhanced stability, and rich primary zone combustors.

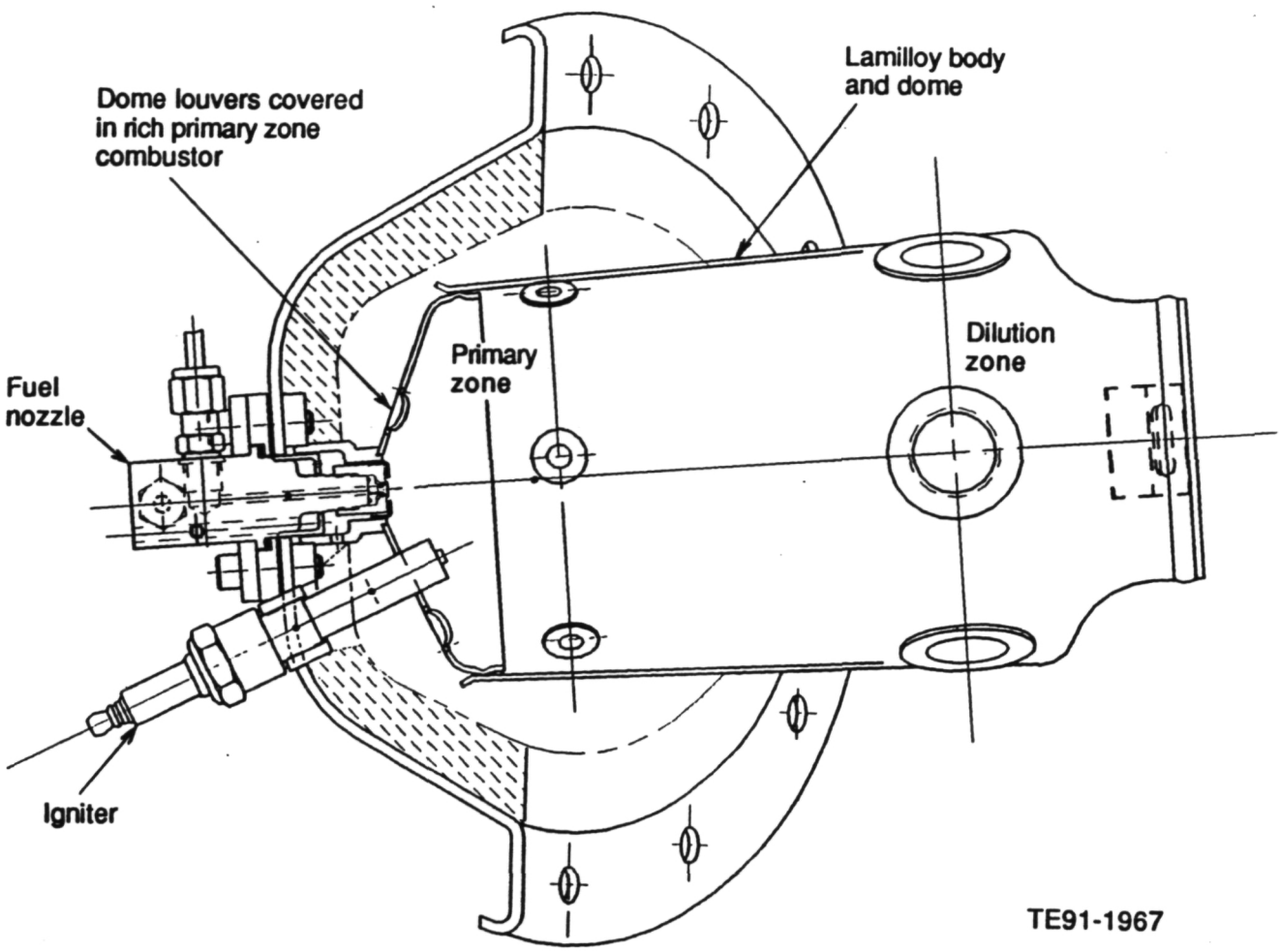

Figure 8. AGT-5 test-bed rich primary zone diffusion flame combustor.

prevented the recording of HC emissions. In the second test, HC emissions met the Federal standard, NO_x emissions remained virtually unchanged, and CO emissions increased significantly. The combustor was removed from the engine and several of the strips covering the dome louvers were found to have fallen off, explaining the increase in CO emissions from one test to the next. Although the rich primary zone combustor did not pass the transient test, progress was achieved in addressing NO_x, CO, and HC standards simultaneously.

The standard, enhanced stability, and rich primary zone combustors are all fabricated from Lamilloy*, a porous, transpiration-cooled wall structure. In another modification, the Lamilloy body and dome were replaced by solid sheet metal as shown in Figure 9. This was done to increase combustor wall temperature, thereby reducing wall quenching of CO and HC burnout reactions. Also, an intermediate zone was added to quench NO_x formation at high power. Design of the solid wall combustor was completed in 1990 with testing scheduled to begin in early 1991.

*Lamilloy is a registered tradename of the General Motors Corporation.

Table II.
Chassis dynamometer test results of rich primary zone combustor, M85 fuel.

	Current Federal standard	Test No. 1	Test No. 2
NO_x gm/km (gm/mi)	0.62 (1.00)	0.74 (1.19)	0.75 (1.21)
CO gm/km (gm/mi)	2.11 (3.40)	2.22 (3.58)	2.80 (4.50)
HC gm/km (gm/mi)	0.25 (0.41)	– –	0.078 (0.126)

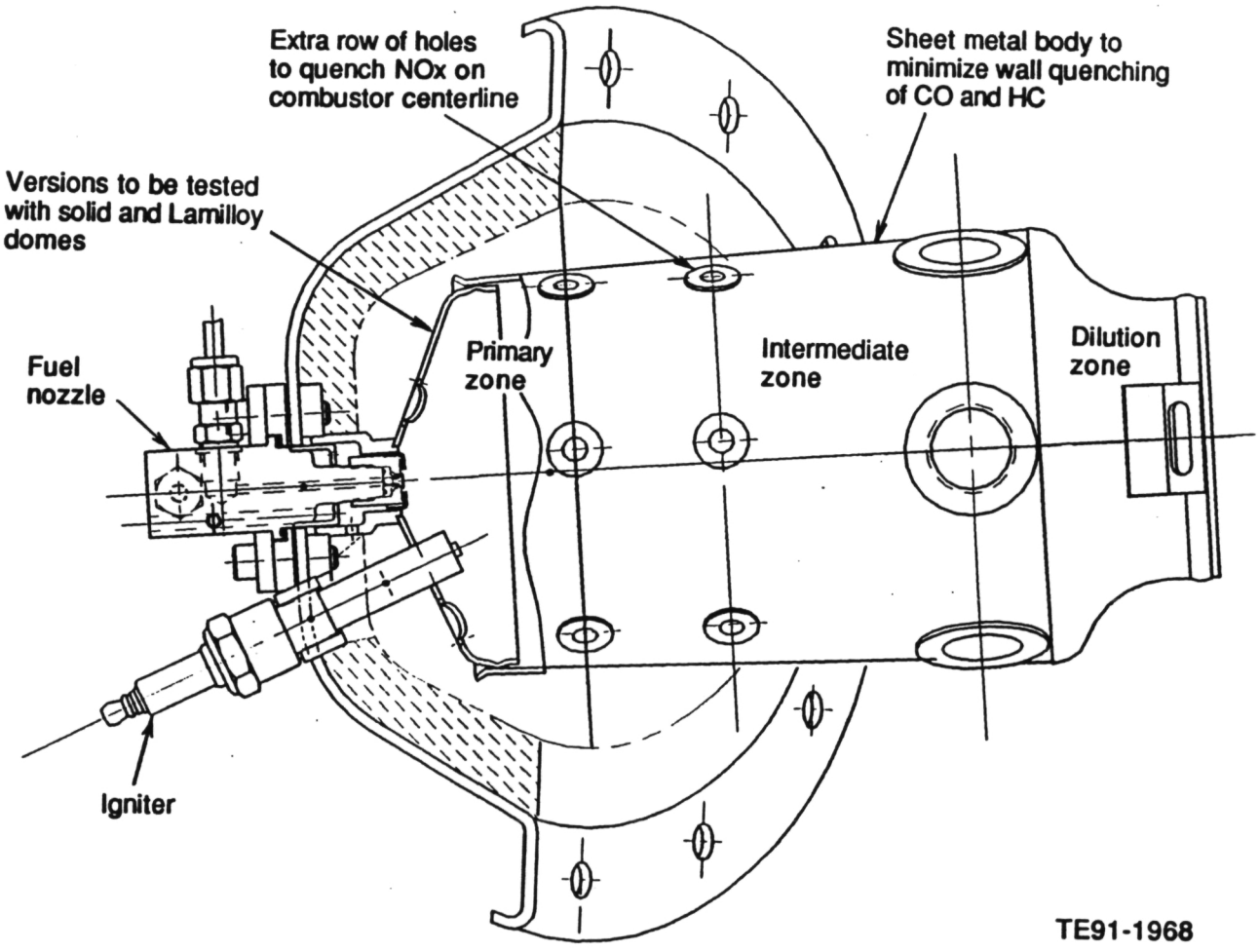

Figure 9. AGT-5 test-bed solid wall diffusion flame combustor.

Low Emissions Prevaporizing/Premixing Combustors. A prevaporizing/premixing combustor will be required to meet the California Ultra Low Emissions Vehicle (ULEV) NO_x standard of 0.124 gm/km (0.2 gm/mi). The aerothermodynamic analysis of such a combustor was described in the 1989 ATTAP Annual Report. Mechanical design of this combustor, called the indexing head combustor, was completed in 1990.

The indexing head combustor (Figure 10) derives its name from the rotatable cover which controls the airflow split between two concen-

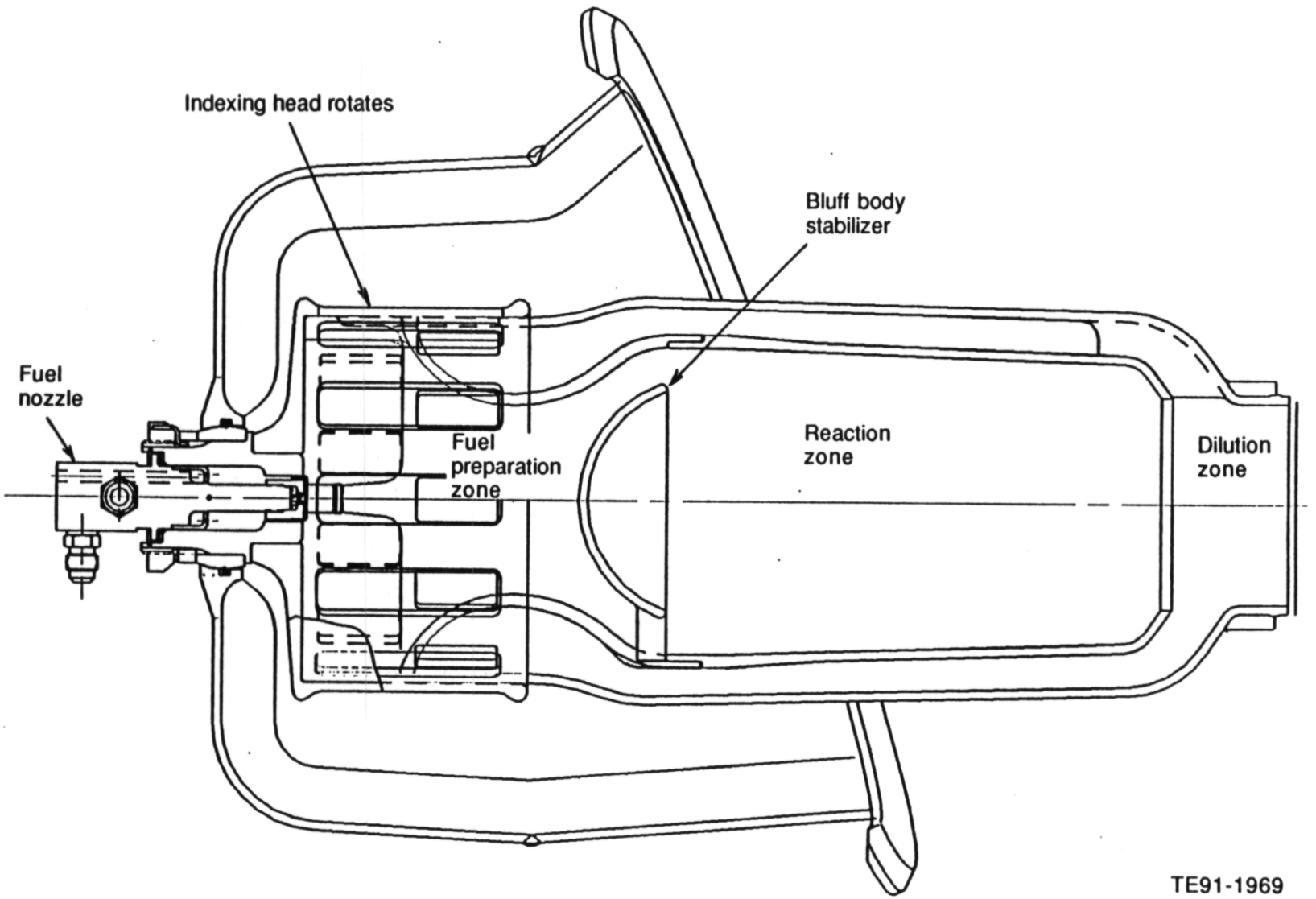

Figure 10. AGT-5 test-bed indexing head low emissions prevaporizing/premixing combustor.

tric paths. The inner path contains the fuel preparation and reaction zones. The outer annular path channels dilution air around the reaction zone for mixing with combustion products just prior to entering the turbine scroll. The indexing head covers two rows of rectangular slots which open and close as the head indexes. As combustion airflow is increased, dilution airflow is decreased. Total flow area remains constant.

Upon entering the fuel preparation zone, combustion air mixes with the fuel spray. To achieve ultra-low NO_x operation, the fuel preparation zone must provide sufficient residence time for vaporization of the fuel and mixing of the fuel and combustion air. Although residence time is beneficial for evaporation and mixing, excessive residence time within this region will result in autoignition. This must be avoided as it can cause increased NO_x emissions and possibly damage the combustor.

Flame stabilization in the indexing head combustor is accomplished via a bluff body stabilizer. Premixed fuel and air flow around this dome-shaped obstruction which separates the fuel preparation and reaction zones. Hot combustion products recirculate behind this bluff body and continuously ignite the incoming fresh mixture. Since the overall fuel/air ratio varies considerably over the operating envelope of the engine, variable geometry is required to maintain fuel/air ratios and flame temperatures in the reaction zone within a narrow window which will ensure both low CO and NO_x emissions. Carbon formation is precluded by the lean premixing approach. The ceramic inner liner surrounding the reaction zone is uncooled except for external convection driven by dilution air passing around it.

Two alternative methods of actuating the variable geometry mechanism are shown in Figure 11. The first method utilizes a linear actuator attached to a crank which in turn is clamped directly to the fuel nozzle body. In this design, the fuel nozzle rotates with the indexing head. The fuel nozzle body is mounted in a spherical nut which permits rotation and allows for slight misalignment with the turbine scroll.

In the second design, the indexing head is rotated by means of a reciprocating rod which passes through the combustor case. One end of the rod is attached to the actuator and the other to a crank which is cast as part of the indexing head. This approach avoids the moving fuel line of the first design but requires an additional seal and may be more likely to bind.

1.4.3 Alternate Flow Paths

Objective/Approach

Turbine aerodynamic development efforts are required to upgrade the existing 1038°C (1900°F) metal AGT-5 test-bed flow path to meet the requirements of the 1371°C (2500°F) RPD operating conditions. Activities during 1990 focused on developing alternate ceramic gasifier vane set designs, refining the existing metal engine aerodynamics, and cold flow testing the all-ceramic gasifier scroll assembly.

Accomplishments/Results

- The concept of an integrally vaned ceramic hub platform was evaluated. The design was considered too risky due to unaccepted natural frequency excitation intersections
- Assessed the flow characteristic of the existing engine gasifier turbine set and determined the optimum rotor tip diameter
- Completed the cold flow testing of the all-ceramic gasifier scroll assembly

Discussion

Airfoils, along with the hub and tip shroud, were designed for a one-piece ceramic integrally vaned gasifier hub platform. The airfoil shapes were created to utilize a two-piece axially-pullable die. The die required a low solidity vane; the vane pitch was larger than the tangential chord of the vane. Viewing the vane row straight on, a slight gap was required between each of the vanes. This gap allowed the two-piece airfoil tool to create each blade shape. Unfortunately, the vanes were found to have high aerodynamic loading, with the possibility of flow separation. Due to the poor aerodynamics, the ceramic integrally

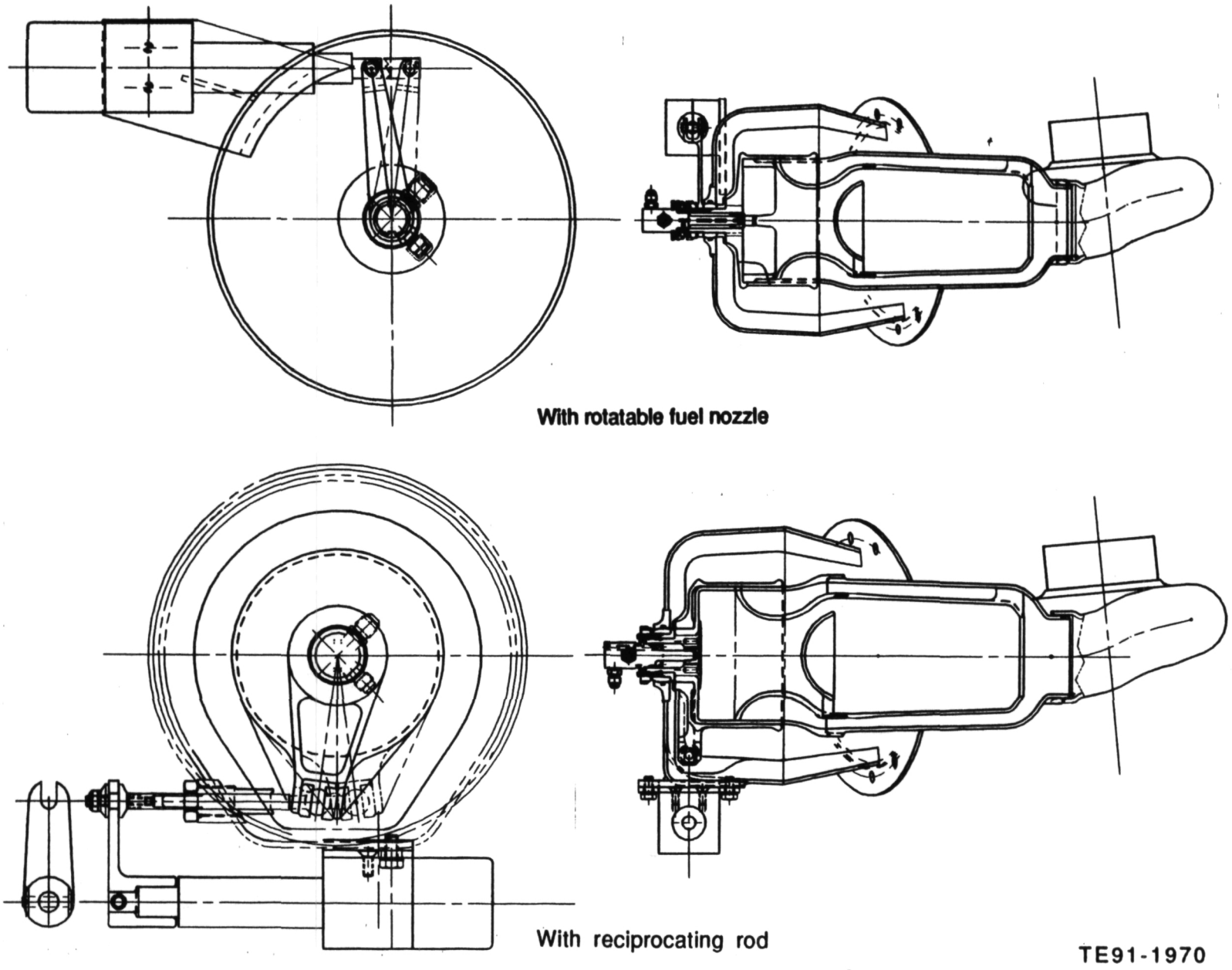

Figure 11. Alternative mechanisms for actuating the indexing head variable geometry.

vaned hub platform design molded with a two-piece axially-pullable die was rejected.

An alternate ceramic integrally vaned hub platform was designed which utilized existing ceramic rotor molding techniques and a radially-pullable die. Conceptually, the integrally vaned hub platform would slide into the existing scroll with minimal clearance between the vane tips and scroll inner diameter (I.D.). A matrix of vane designs was examined. The number of vanes was varied from 14 to 10, and the taper ratio was varied from 115% to 64%. Taper ratio is defined as the ratio of the tip cross-sectional area compared to the hub cross-sectional area.

The frequency results for four vane sets are illustrated in the Campbell diagram in Figure 12. The axial length of the 10-vane design was too long to fit in the present gasifier scroll. The aerodynamic performances of vane sets with taper ratios less than 75% were considered poor, requiring highly loaded tip sections and lightly loaded hub sections.

Of the acceptable designs evaluated in the matrix, a 12-vane design with a 85% taper ratio had the highest calculated frequencies. Unfortunately, as illustrated in Figure 12, the 1st mode frequency intersects the 20 engine-order excitation (bow wake of the gasifier rotor) just past the engine's design point and is considered too risky. It was concluded that all of the one-piece integrally vaned gasifier hub platform designs evaluated had unacceptable natural frequency excitation intersections. This design is on hold while other alternatives are examined.

A series of engine builds was completed in an attempt to enhance the gasifier turbine stage efficiency and increase the engine airflow. The gasifier rotor tip diameter was increased from the standard area (BU29) to a tip diameter with a 8.5% increase in throat area (BU31). The large diameter rotor had a 2 point increase in stage efficiency at 100% gasifier speed. At the low speed conditions, the efficiency of the large rotor was 1.5 points lower than the small diameter rotor (see Figure 13).

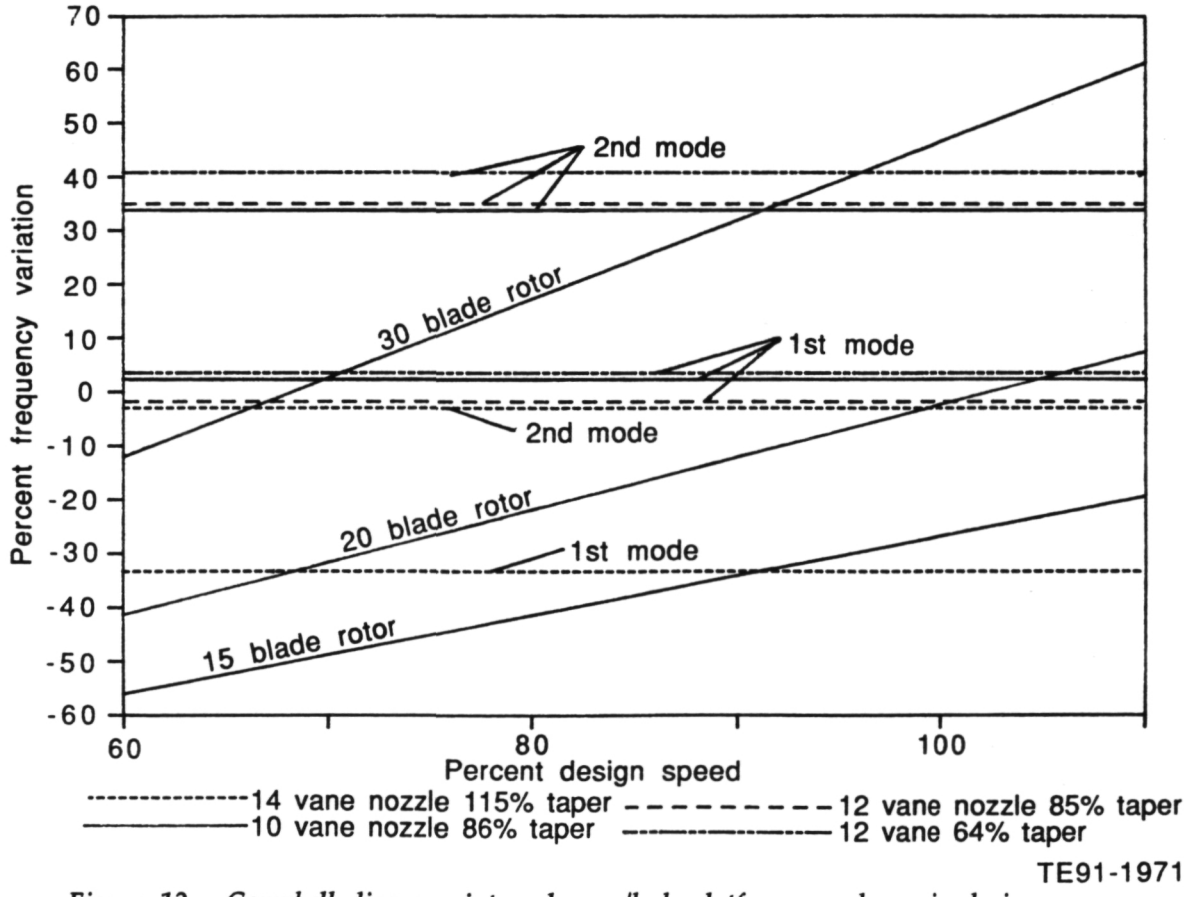

Figure 12. Campbell diagram--integral vane/hub platform aerodynamic designs.

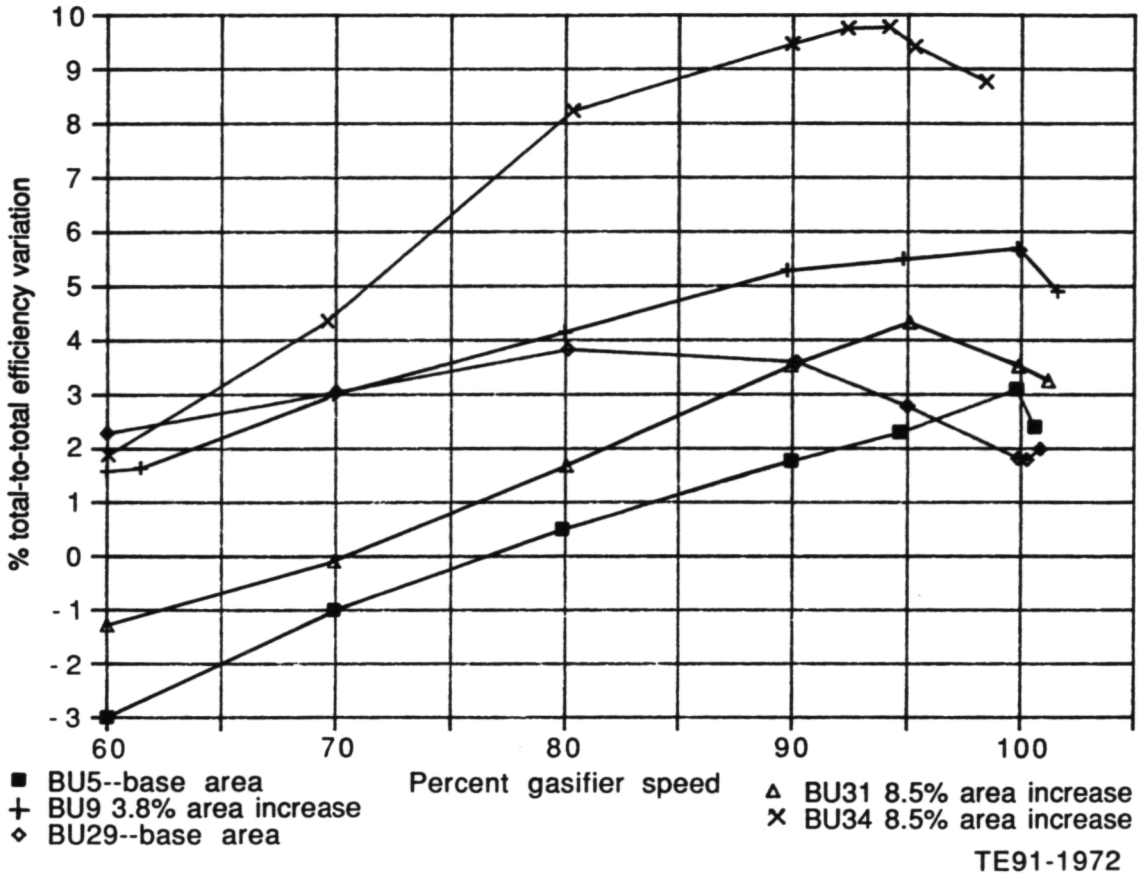

Figure 13. Gasifier rotor flow area effect on total–total stage efficiency.

At the low speed conditions, a free vortex model of the larger tip diameter rotor (a low reaction stage) calculated a relative rotor hub inlet Mach number of 0.48 and a relative exit Mach number of 0.41. The smaller tip diameter rotor (a higher reaction stage) had a calculated relative inlet Mach number of 0.465 and the exit relative Mach number of 0.444. The hub surface velocities were calculated for each of the above cases and as expected the surface velocities on the suction surface of the large tip diameter rotor (low reaction stage) dropped off at a greater rate than the suction surface velocities of the small diameter rotor (high reaction stage). The surface velocity comparison is illustrated in Figure 14. The adverse decrease in surface velocities on the large tip diameter rotor (low reaction stage) is suspected to induce separation, thereby lowering stage efficiency.

The gasifier efficiencies from a number of previous engine builds were also plotted on Figure 13. It should be noted that engine operating conditions were similar from build to build with minor variations. Qualitative conclusions were drawn, but direct quantitative comparisons are not valid between later and earlier builds. The gasifier stage mass flow rate used to calculate stage efficiency varies from build to build. A best compromise rotor having a 3.8% increased throat area over the baseline case was chosen. At the low speed conditions, the stage efficiency for the 3.8% increase area rotor did not drop off as rapidly as the large tip diameter rotor. At 100% speed, the efficiency of the 3.8% increased area rotor did not drop as rapidly as the small diameter rotor.

In conjunction with the gasifier rotor changes made between BU29 and BU34, the engine air inlet conditions were varied in an attempt to increase engine air flow and surge margin. It was suspected that the existing automotive inlet air filters were inducing compressor preswirl and decreasing the airflow. Test results are shown in Table III.

Table III.
Engine inlet test results.

BU No.	Inlet condition	Rotor area increase--%	Flow increase at $90N_1$--%	Comments
BU29	Auto inlet with auto filters	Baseline	Baseline	
BU31	Auto inlet with auto filters	8.5	3.4	
BU32	Auto inlet with auto filters	8.5	4.6	New compressor diffuser
BU33	Axial inlet with plenum filters	8.5	(surge)	
BU34	Axial inlet without filters	8.5	8.9	

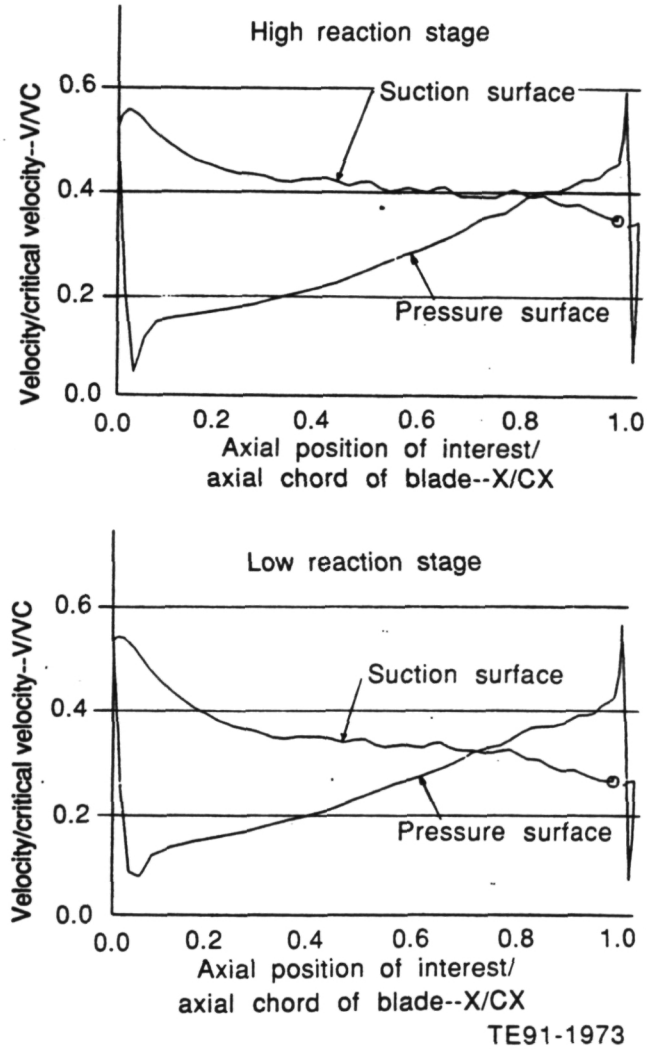

Figure 14. Rotor hub surface velocities: high vs. low reaction stages.

The straight axial engine inlet produced the best engine results. The airflow rate increased by 4% from BU32 to BU34. The experimental plenum inlet was found to induce engine surge. The axial inlet without the filter, BU34, was found to have the greatest airflow and stage efficiency.

The all-ceramic gasifier scroll assembly was flow tested on a carburetor flow bench. Air at 24°C (75°F) and 101 kPa (14.7 psi) was pulled through the scroll and expansion ratio versus equivalent flow was measured. The inlet conditions allowed the design Reynolds number to be matched as well as the design expansion ratio. The assembly was found to flow at the design flow rate.

1.4.4 Engine System Integration

Object/Approach

Development efforts on automatic control systems, fuel pumps, and starter motors are required to integrate ceramic components and 1371°C (2500°F) temperature capabilities into the AGT-5 rigs and test-bed engines. Activity during 1990 focused on modification and development of engine control software, procurement and checkout of a new generation of engine control system, (Engine Development Module (EDM-800) and Remote Display System (RDS-1000)) and development of a high capacity fuel

pump and automotive starter motor for the AGT-5 test-bed engine operating at RPD conditions.

Accomplishments/Results

- Comparative evaluation of starter motors was completed. The Delco-Remy PG-150 with a 3.4 pulley ratio appears to offer the best compromise between time to starter drop and minimum battery voltage during the start.
- Evaluation of a Gerotor fuel pump showed that the existing spur gear pump is superior to the Gerotor fuel pump at high back pressures.
- Evaluation of two different cammed vane type fuel pump/motor combinations was completed. The first sample pump stalled before reaching minimum flow while the second pump/motor combination appears to satisfy the required range of flow rates.
- All hardware parts for the I/O board of the EDM-800 controller, whose function is to control the operation of all the gasifier rigs and engines, are now in. The main engine control software routines have been translated into the proper form for compiling, using the RDS-1000. The EDM-800 will replace the current Function Control Module (FCM) controller. It is smaller, faster, and performs many more functions than the FCM.
- Completed an engine computer control program for durability testing which takes N_1 commands from a Hewlett-Packard (HP) master computer and regulates the engine to that speed as well as provides for automatic start-up and shut-down.
- The input/output (I/O) board was designed and the control software rewritten and tested for the engine control routines. These essential components were needed for compatability with the EDM-800.
- Successfully ran an AGT-5 engine using the new EDM-800.

Discussion

Starter Motors. The PG-150 Delco-Remy starter motor was installed on a test-bed engine for cold and hot start testing. The independent variables in the test were: (1) motor, (2) pulley ratio, and (3) resistance drop due to wire gage to the starter motor. The primary dependent variables were: (1) voltage drop at the battery, (2) time to starter drop, and (3) maximum current draw. For a given motor, pulley ratio, and gage wire, the voltage drop at the battery, time to starter drop, and maximum current draw were recorded. Comparisons were made with the PG-100 and the PG-200 starter motors.

A minimum battery voltage of approximately 9 volts was chosen as being an acceptable value for the engine controllers. The PG-100 starter motors always stayed above 9 volts; however, they do not have acceptable start times. The PG-200 starter motors have acceptable start times; however, they cause an excessive voltage drop. The PG-150 starter motors have acceptable start times and also have acceptable minimum battery voltages.

Of the other parameters tested, using a higher gage wire keeps the minimum battery voltage higher, but extends the time to starter drop. Using a 3.4 pulley ratio, instead of 3.0, decreases time to starter drop and causes a negligible change in minimum battery voltage. The best choice appears to be using the PG-150 starter motor with a 3.4 pulley ratio.

Fuel Pumps. Current work with fuel pumps centers around finding a pump that can provide sufficient fuel during maximum engine acceleration and is also capable of providing a steady idle fuel flow. The pump/motor must also handle the wide range of back pressures which the engine fuel nozzle requires. Current spur gear fuel pumps have not been able to satisfy all of the above criteria.

Evaluation of a Gerotor fuel pump was conducted. Testing consisted of varying the side clearance between the Gerotor mechanism and the spacer plate. The results of this test showed that, regardless of the side clearance, the Gerotor's high tip leakage rate at high back pressure conditions more than offset its po-

tentially higher flow rate. At high back pressures, the existing spur gear pump is superior to the Gerotor pump.

The manufacturer of a cammed vane fuel pump and motor supplied a unit for evaluation. At low pump speeds/low flow rates which simulated idle and deceleration fuel flows, the pump stalled when the motor voltage fell below 1.5 volts. The flow rate achieved at maximum motor voltage was also slightly less than required for the 2500°F RPD design point.

The vendor proposed a second pump and motor. The new pump was similar to the first; however, the motor had a higher torque rating. With the higher torque rating the motor was able to operate at lower voltages before stalling. It also gave the motor more torque for operating at high back pressure.

In testing this pump and motor, it was found that the voltage at the motor was lower than that previously recorded. The fuel controller uses a power transistor that suffers a voltage drop due to current flow. With the original motor, the voltage dropped from 13.8 to 11 volts. The new motor voltage drop was from 13.8 to 9 volts. This voltage drop slightly reduced the maximum flow and back pressure capability; however, the flow range is still thought to be acceptable.

A second power transistor with a lower voltage drop was tested. This new transistor increased the maximum flow rate; however, its nonlinearity caused the flow to go unstable at the low end. The voltage drop through the transistor needs to be reduced, and future activities will investigate the best method to accomplish this.

Engine Control. The function control module (FCM) continues to be used for all engine and rig control tasks while its replacement, the EDM-800, is developed. All hardware parts for the I/O board are now in. Also, the EDM-800 unit with a special microprocessor has been delivered. This processor has the capability of allowing a logic analyzer to read all bus transactions and data being manipulated with protection from overwrite. This will aid in software and hardware debugging. The main routines have been translated into the proper form for compiling using the RDS-1000. Debugging of the program will be followed by I/O board testing.

Durability testing has been performed in the test cell by using the FCM with cycles stored in memory. However, data logging during the test could not be coordinated with the various cycle points. Now the HP computer in the cell, which performs data logging, will also send commands to the FCM or EDM to control the timing and prescribe the operating values for the durability cycle as well as provide for cell safety and shut down. This system has been validated.

All of the I/O circuits needed to run the various rigs and engines have been redesigned and verified using the new I/O boards for the EDM-800. Future plans for additional I/O have been taken into account. There are approximately 14 discrete inputs, 4 pulse timing measurement inputs, 11 analog inputs, and 1 pulse accumulation input. There are 21 discrete outputs, 1 wave form generator output, and 3 analog outputs. The entire EDM-800 package, including software, I/O, and computer board, fits within a box of 20 x 6 x 14 cm.

The successfully tested EDM-800 and its operator display/interface, the VMS-1000, will become the primary engine controller, replacing the FCM. The EDM is capable of handling more systems and signals with faster and more advanced calculations. It is based on a Motorola 68HC11 chip and a Universal Pulse Processor. Smaller size, lighter weight, and greater reliability are also strong advantages. Furthermore, the program is now free to be edited and compiled on a desktop PC, or in the VMS-1000 display interface and an IBM-XT compatible computer. The compiled program can then be downloaded to the EDM to which it is connected. This was impossible to do with the FCM.

II. CERAMIC COMPONENT DESIGN

2.1 DESIGN ACTIVITIES

The AGT-5 ATTAP test-bed engine is a two shaft regenerative engine designed to operate at RPD operating conditions, specifically at 1371°C (2500°F) turbine inlet temperature. Engine operation at this TIT requires heat resistant structural ceramic materials in the engine hot section. The overall objective of the ceramic component design activity is to create ceramic component designs that permit successful operation of the AGT-5 engine at the RPD operating conditions.

Specifically, the objectives of this activity are to do the following:

- Complete designs of the defined ATTAP ceramic development components; turbine components include the gasifier scroll, gasifier vane(s) and vane platform, gasifier vane retaining ring, and the gasifier rotor
- Complete design of associated ceramic and metal components necessary to permit evaluation of the ATTAP development ceramic components in rig and engine environments at RPD operating conditions; included are the combustor body (ceramic) and associated components, two power turbine rotors (ceramic) and associated components, two power turbine rotor blade tip shrouds (ceramic), and the two power turbine nozzle assemblies and associated components
- Prepare and present design reviews of selected components
- Incorporate into the ceramic design activity "simultaneous engineering" which integrates component performance and reliability and related design activities, and component vendor fabrication technology development, to enhance the successful manufacture of cost-effective components

The overall approach utilized to design the ATTAP/AGT-5 test-bed ceramic components includes the following steps:

- Establish operating conditions(s) and reliability goals for ceramic engine components
- Prepare conceptual designs of components
- Complete detailed linear elastic, fast fracture probabilistic design analysis based on: certified material characteristics, i.e., two parameter characteristic strength and Weibull parameters generated from test bar fracture data; design reliability goals established from engine system reliability goals
- Iterate design configuration, materials, and operating requirements to achieve satisfactory preliminary component design
- Iterate component design details with ceramic manufacturer(s) to correlate component requirements with processing capabilities
- Finalize design layout and detail drawings

After progressing through further steps of the development cycle, as shown in Figure 2, the design function reviews component performance, cost, and reliability results and updates or modifies component designs, as appropriate, to achieve overall design goals.

In addition to those ceramic components identified as requiring considerable development under ATTAP (i.e., the gasifier turbine assembly, regenerator disks, and engine insulation) the engine assembly also includes a ceramic combustor assembly and selected ceramic power turbine components (rotors and shrouds). The gasifier turbine static structure, shown in Figure 15, consists of a scroll that guides the gas flow from the combustor to the turbine vane (nozzle) row. This row consists of loosely mounted vanes that act to accelerate the flow to rotor inlet conditions; a retaining ring surrounds the scroll outer shroud and covers slots within this shroud through which the vanes are inserted into the gas path. A vane platform forms the inner gas path boundary and positions the hub end of the vanes within machined pockets contained in this structure. The gasifier turbine rotor completes the gasifier turbine assembly. The gasifier turbine static structure is mounted to the engine structure by a combination insulating/locating subassembly, which inhibits heat flow from the gas path into the engine structure. Cross key features are utilized to accu-

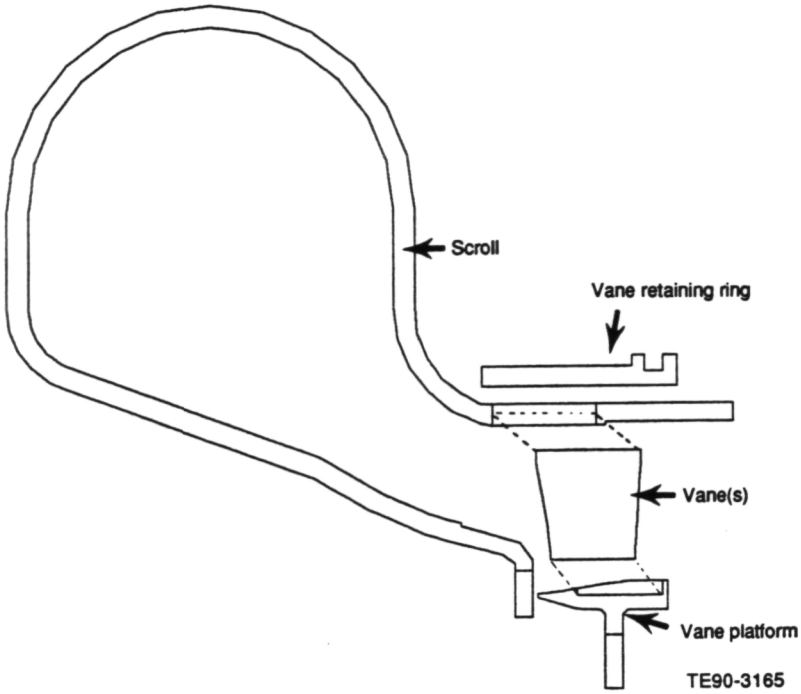

Figure 15. Gasifier turbine static structure.

rately locate the static structure relative to the rotor blade tips while allowing free movement between ceramic and metallic components as unequal thermal expansion occurs.

The power turbine vane assemblies are attached to the engine housing by a bolted flange which maintains concentricity between the vane assemblies and the power turbine rotors. The ceramic rotor tip shrouds are radially located in the vane assemblies by cross keys. The power turbine rotors are individually attached to metal shaft segments, which are in turn bolted together to form the turbine rotor assembly.

Overall engine design requirements impacting ceramic (and metal) turbine and combustor design are as follows:

- Duty cycle: 100,000 miles life of which 55,000 miles operate on an urban cycle and the remainder (45,000 miles) is considered highway operation
  - 3,500 hr life
  - 12,000 starts
  - 33,600 low cycle fatigue (LCF) cycles
- Gasifier turbine inlet temperature of 1371°C (2500°F)
- Rotor containment at maximum burst speeds
- Adherence to automotive environmental, maneuver, and attitude requirements
- Reliability goals to have fewer than 0.25 major engine system failures in 100,000 miles

Detail design and analyses of the turbine assemblies are described in the following subsections. Further, the POS design goal for each ceramic engine component is based on the number of failure sites for that component in relation to the total number of failure sites in the complete engine assembly. The POS design goal for each ceramic component is also listed in those subsections describing that component.

2.1.2 Gasifier Turbine Static Structure

Objective/Approach

The objective of this activity is to design ceramic components in the gasifier turbine static structure that operate satisfactorily at ATTAP RPD turbine inlet temperature (1371°C, [2500°F]) conditions and achieve assigned POS

criteria. Design concepts are prepared, FEM models created, heat transfer and stress analyses performed, and calculations of POS completed for each ceramic component of the gasifier turbine static structure.

Accomplishments/Results

- 2-D axisymmetric finite element heat transfer and stress analyses were performed for a gasifier turbine scroll of DuPont/Lanxide Aluminum Titanate/Alumina (Al_2TiO_5/Al_2O_3) material. The minimum POS is unacceptably low (zero) for the individual or "loose vane" configuration. The scroll POS improves to 0.5821 when the vane slots and retaining ring are eliminated (integrally vaned hub platform configuration).

- 2-D axisymmetric finite element heat transfer and deflection analyses were performed for an integrally vaned hub platform and gasifier turbine scroll assembly. A matrix of candidate scroll and platform materials were examined. The design is acceptable from a radial deflection standpoint. Based upon assembly and operating clearance considerations, it was determined that the optimum material configuration consists of an SN252 Si_3N_4 scroll with an NT-154 Si_3N_4 vaned platform.

- Gasifier vane platform design modifications were identified and implemented to ensure proper mating and radial clearance at the platform-to-scroll flange interface.

Discussion

A 2-D axisymmetric finite element analysis was conducted to determine if a gasifier turbine scroll fabricated of Aluminum Titanate/Alumina material would meet design goal probability of survival. The scroll geometry selected was the current ceramic design configured to position 14 individual "loose" vanes in slots as illustrated in Figure 15. The finite element model used for the scroll analysis is shown in Figure 16. Material properties were provided by DuPont and are considered preliminary. The Aluminum Titanate/Alumina material exhibits a low elastic modulus, low strength, and a unique thermal expansion characteristic. Thermal expansion does not commence until the material temperature reaches 600°C (1112°F).

Operating temperatures, stresses, and POS were calculated for maximum power and cold start-up transient conditions. Temperatures and stresses in the scroll at maximum power steady-state are shown in Figure 17. The scroll POS at maximum power is 0.9985. Temperatures and stresses in the scroll at 16 seconds into the start-up transient are shown in Figure 18. Sixteen seconds is the time at which the scroll has the minimum probability of survival; in this case zero. The maximum principal stresses in the scroll occur between vane slots.

An alternate scroll design, Figure 19, was analyzed to determine if the Aluminum Titanate/Alumina scroll POS could be improved. In this configuration, the vanes are an integral part of the platform, and the vane slots and retaining ring have been eliminated. The existing vane retaining ring is required in the current design as a part of a piston ring seal at the gasifier-to-power turbine interface. Operating temperatures and stresses were calculated for the alternate scroll design at maximum power and throughout the cold start-up transient. Scroll temperatures and stresses at maximum power steady-state are shown in Figure 20. Temperatures and stresses for the 16 second transient time point are shown in Figure 21. Elimination of the vane slots and retaining ring improves the scroll minimum POS to 0.5821 at the 16 second transient condition; however, this POS is still significantly below the design goal of 0.9826. The corresponding maximum power POS is in excess of 0.999.

2-D axisymmetric finite element analyses of the alternate scroll configuration (integrally vaned platform) were performed in order to quantify relative radial thermal growths between vane tips and the scroll shroud for a variety of candidate ceramic materials. Temperatures and deflections were generated for the cold start-up transient. The matrix of configurations examined includes five scroll materials and three platform materials as

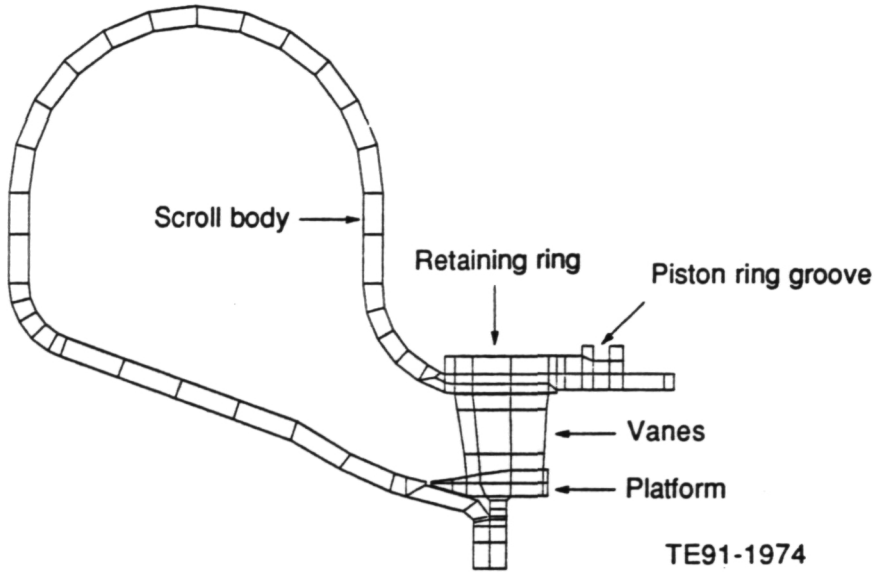

Figure 16. Gasifier turbine static structure FEM model.

listed in Table IV. In addition, each material combination was analyzed with and without a vane retaining ring of the same material as the scroll. The vane retaining ring was included in the analysis because it also positions the piston ring seal at the gasifier-to-power turbine interface. As future designs evolve, the seal would be redesigned and the retaining ring eliminated. Deflections were evaluated at eight time points during the accel transient as listed in Table V. Transient radial deflections for the optimum material combination (SN252 Si_3N_4 scroll/NT154 Si_3N_4 vaned platform) are illustrated in Figure 22 and Figure 23, respectively. Radial expansion characteristics of the other materials investigated are similar to those shown in Figures 22 and 23, but differ in magnitude. Resulting build and operating clearances for the configurations utilizing a retaining ring are summarized in Table VI. Build clearances were selected in 0.03 mm (0.001 in.) increments and are the minimum radial clearances required to prevent interference between the vane tips and the scroll shroud. Note that minimum operating clearances occur during the cold start-up transient. Operating clearances at steady-state maximum power vary depending on the scroll and vane material combination. Similar clearance results for the configurations without a retaining rig are summarized in Table VII. Results indicate that the vane-to-scroll operating clearances are relatively insensitive to the presence of the vane retaining ring. In addition, the required radial build clearances are relatively small; they range from one to seven thousandths of an inch. Based upon considerations of minimum vane-to-scroll steady-state operating clearance and a reasonable assembly clearance, it was found that the optimum material configuration consists of the SN252 Si_3N_4 scroll with an NT154 Si_3N_4 vaned platform.

A pretest assembly of ceramic gasifier turbine static hardware revealed an interference between the vane platform and scroll mount flanges as illustrated in Figures 24 and 25. This interference allowed the platform to rock on the scroll flange rather than lying flush against it. A detailed review of the platform geometry and allowable tolerances exposed two potential problems: (1) the radial clearance between the scroll inner flow-path wall and the platform leading edge I.D. was minimal when extreme tolerances and thermal growths were applied, and (2) the axial location of the flange cast surface was not tied directly to the machined mount surface "datum C", thereby allowing the cast surface to float 0.89 mm (0.035 in.) axially. The indicated rocking of the platform against the scroll flange was attributed to the second item. Item 1 was corrected by opening the platform leading edge I.D. by 0.13 mm (0.005 in.) radially. Item 2 was corrected by redimensioning the platform and associated

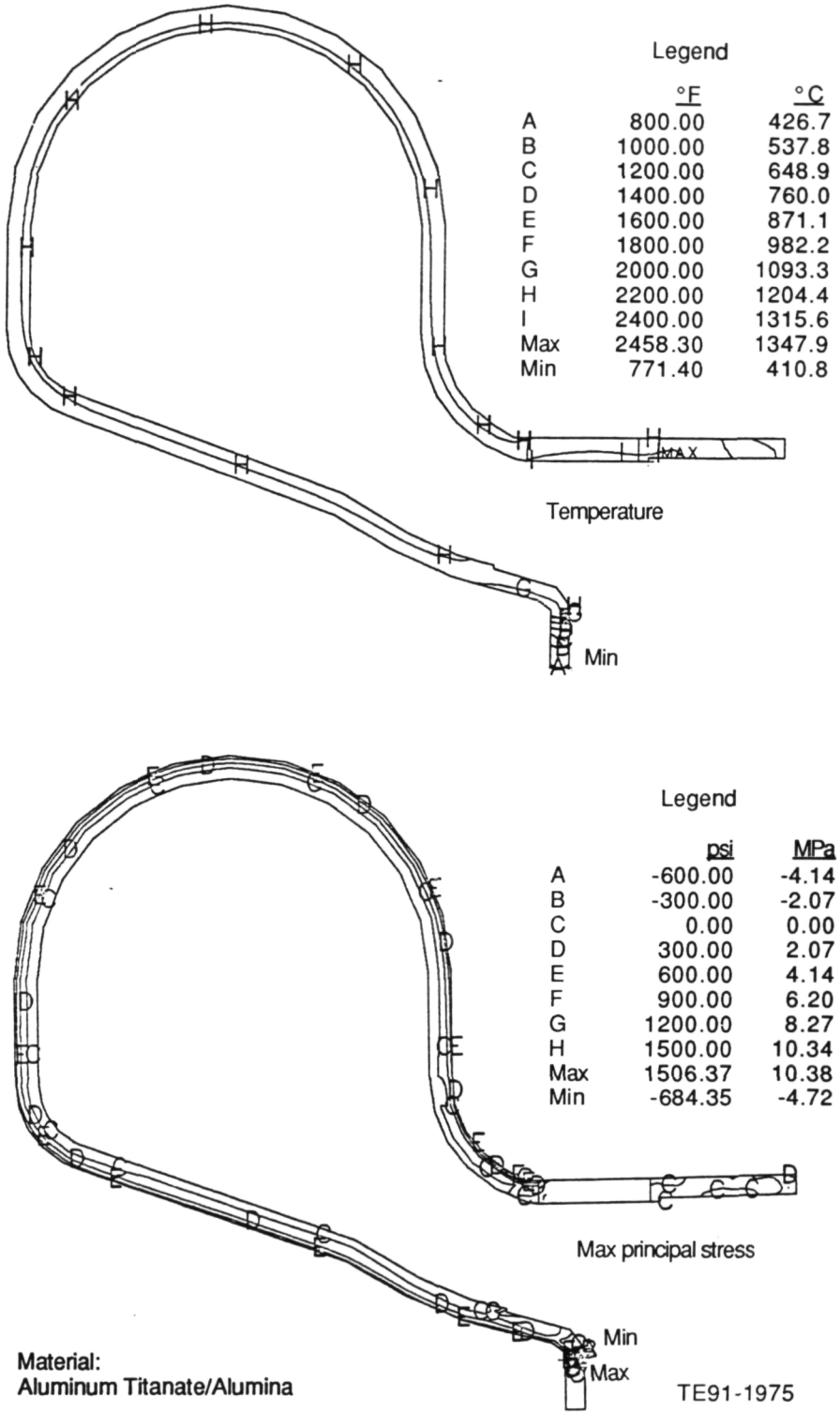

Figure 17. Temperature and maximum principal stress in scroll with vane slots; maximum power.

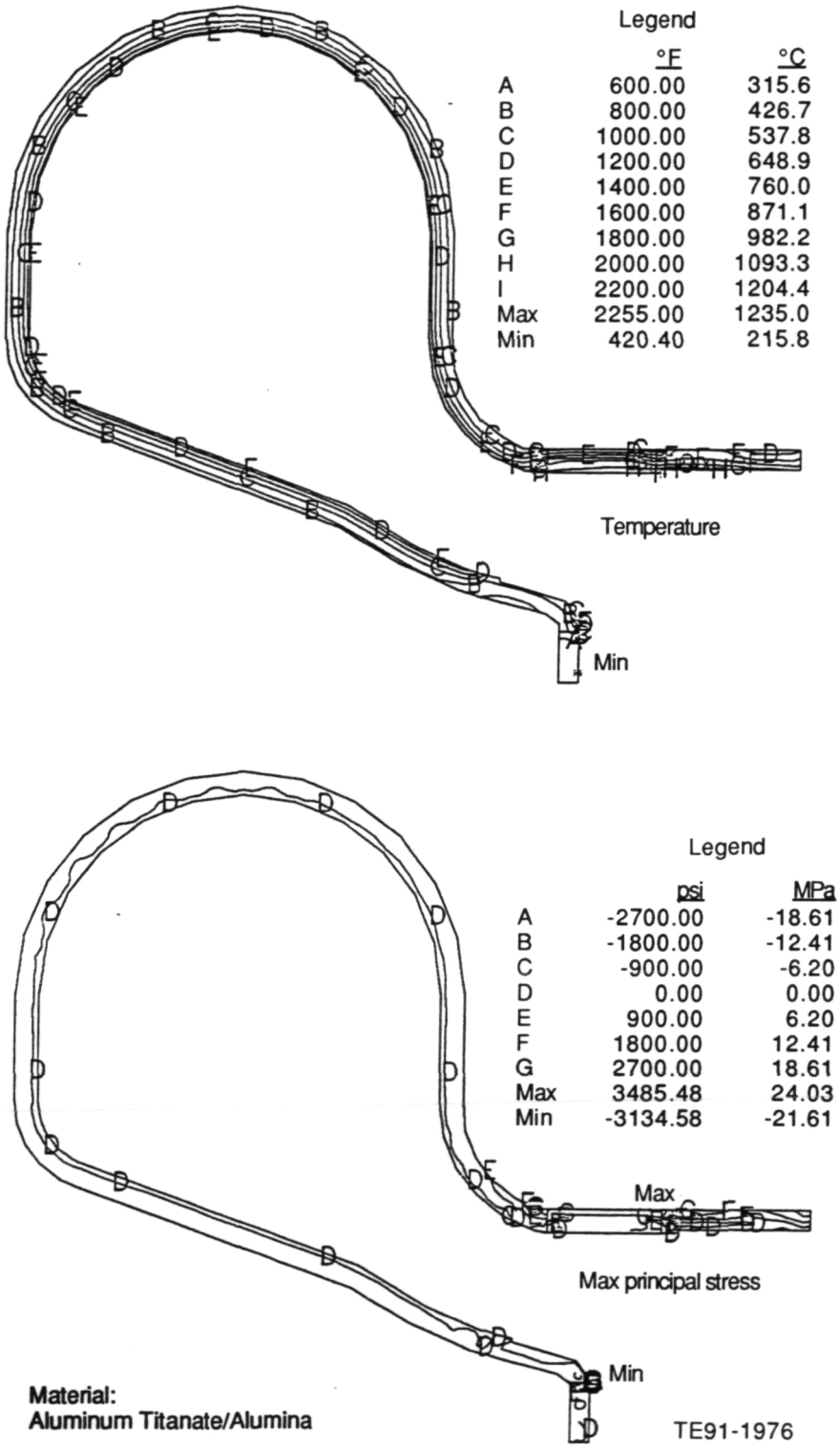

Figure 18. Temperature and maximum principal stress in scroll with vane slots; 16 seconds into transient.

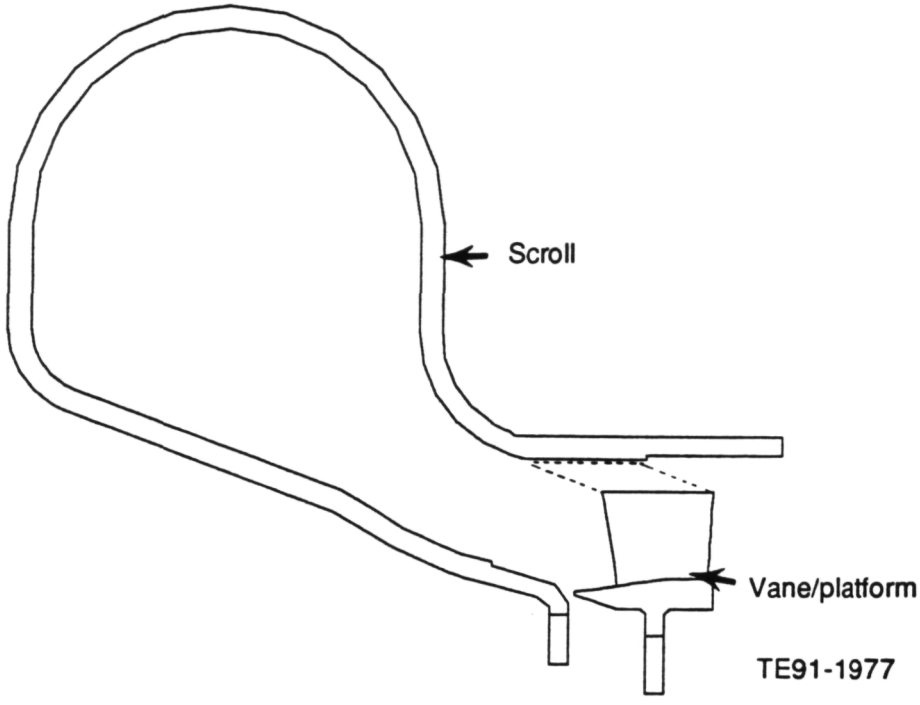

Figure 19. Modified scroll design (vane pockets and retaining ring removed) for use with one-piece integral vane platform.

Table IV.
Gasifier turbine static structure materials: materials utilized in the thermal/deflection analysis of the gasifier assembly incorporating an integrally vaned platform.

Scroll/ring material	Vane/platform material
Carborundum α–*SiC*	Kyocera SN252 Si_3N_4
Norton/TRW NC430 *SiC*	Norton/TRW NT154 Si_3N_4
Dupont/Lanxide *Aluminum Titanate/Alumina*	GTE PY6 Si_3N_4
Dupont/Lanxide *SiC/Alumina*	
Kyocera SN252 Si_3N_4	

Table V.
Gasifier turbine transient analysis points: all points from cold start.

Time–sec	Operating condition
8.0	Engine idle
12.0	Maximum power
16.0	Maximum power
20.0	Maximum power
25.0	Maximum power
30.0	Maximum power
60.0	Maximum power
300.0	Maximum power steady-state

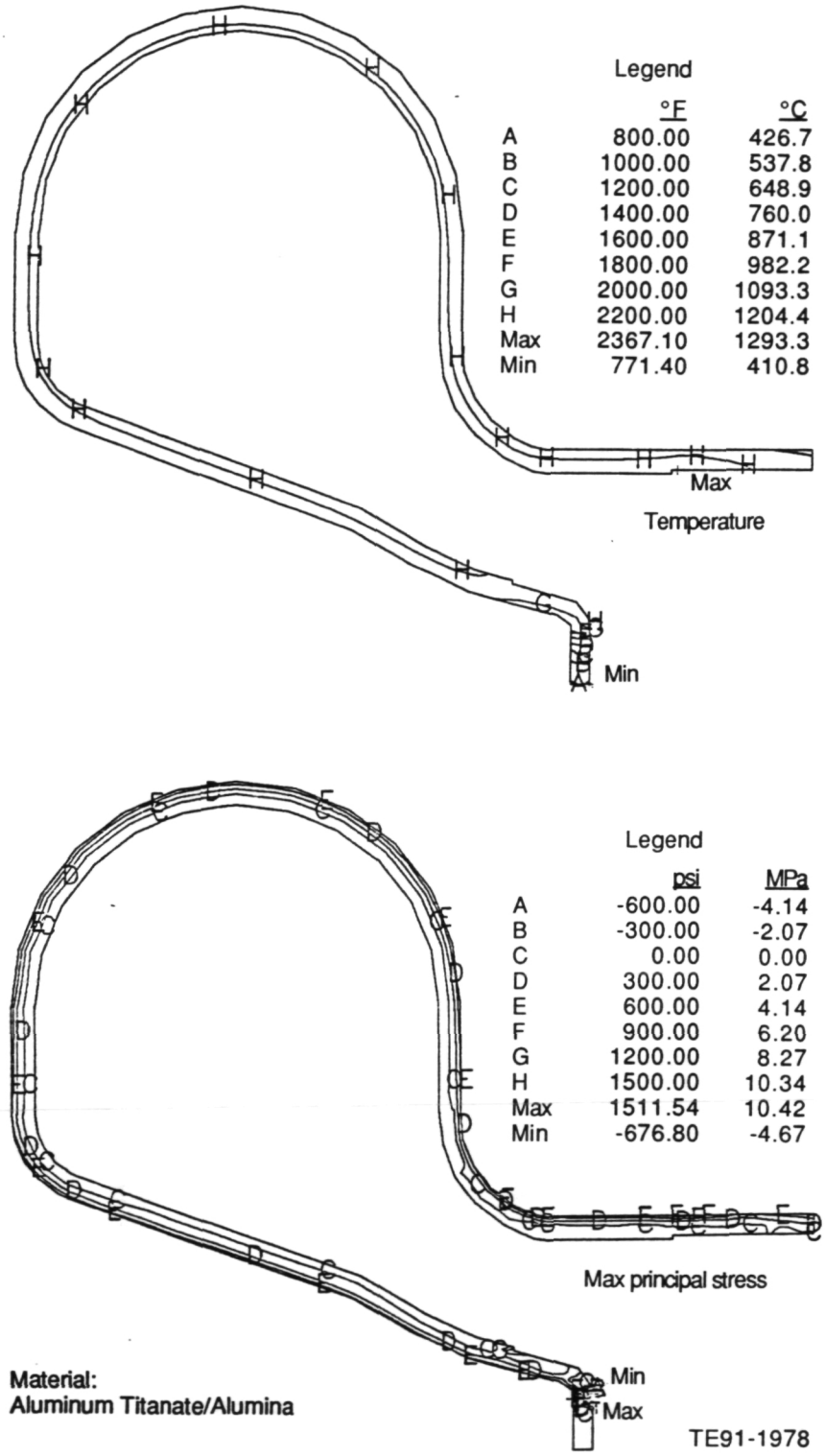

Figure 20. Temperature and maximum principal stress in scroll without vane slots; maximum power.

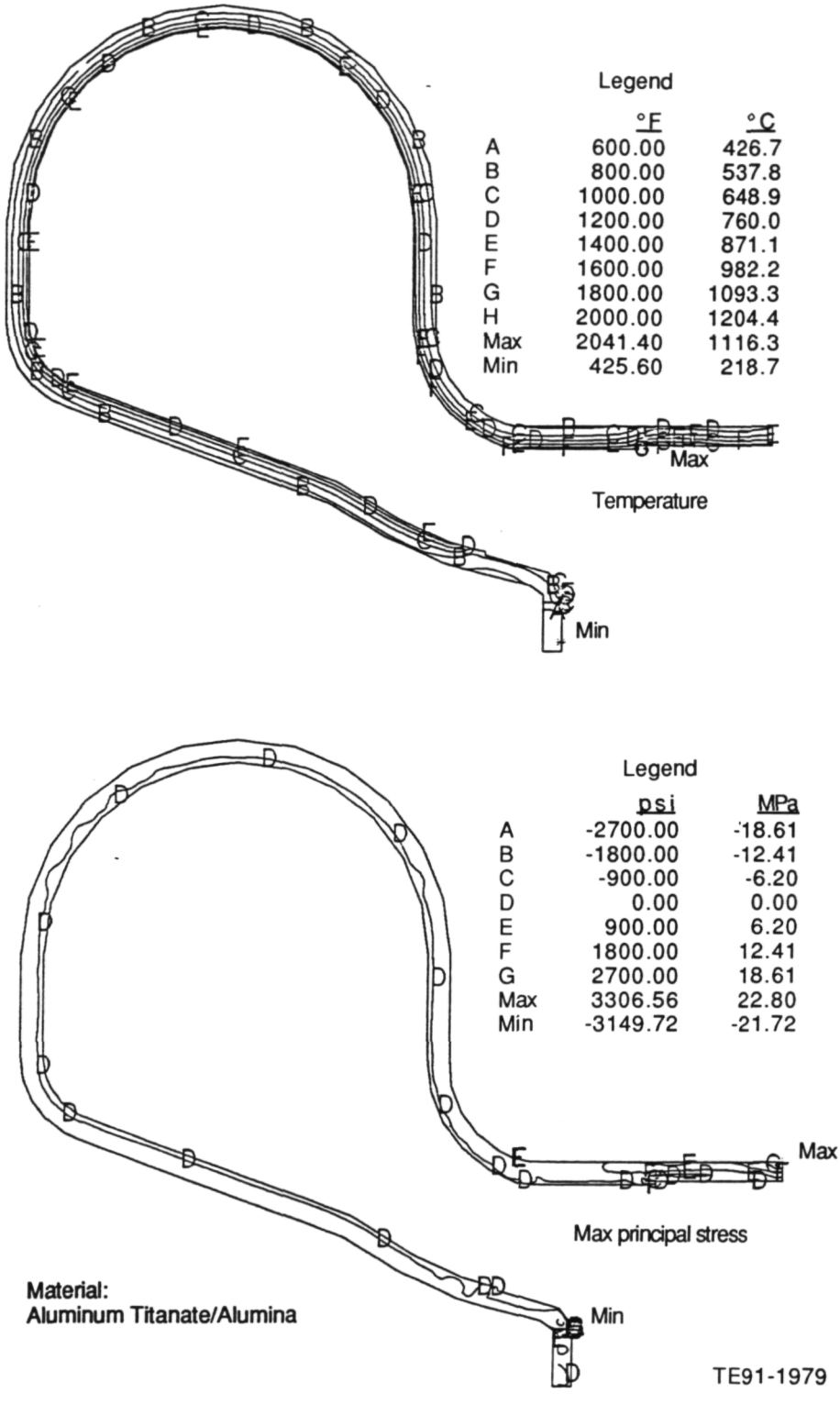

Figure 21. Temperature and max principal stress in scroll without vane slots; 16 seconds into transient.

Table VI.
Gasifier static structure deflection analysis with retaining ring: radial clearance summary.

Scroll/ring material	Vane/platform material	Build clearance δR- *mm*-(in.)	Minimum transient clearance δR mm--(in.)	Maximum power steady-state clearance δR mm--(in.)
α-*SiC*	SN252 Si_3N_4	0.025 (0.0010)	0.008 (0.0003)	0.117 (0.0046)
α-*SiC*	NT154 Si_3N_4	0.051 (0.0020)	0.020 (0.0008)	0.097 (0.0038)
α-*SiC*	PY6 Si_3N_4	0.025 (0.0010)	0.005 (0.0002)	0.094 (0.0037)
NC430 *SiC*	SN252 Si_3N_4	0.025 (0.0010)	0.013 (0.0005)	0.117 (0.0046)
NC430 *SiC*	NT154 Si_3N_4	0.051 (0.0020)	0.015 (0.0006)	0.097 (0.0038)
NC430 *SiC*	PY6 Si_3N_4	0.051 (0.0020)	0.023 (0.0009)	0.117 (0.0046)
Aluminum Titanate/Alumina	SN252 Si_3N_4	0.152 (0.0060)	0.015 (0.0006)	0.135 (0.0053)
Aluminum Titanate/Alumina	NT154 Si_3N_4	0.178 (0.0070)	0.010 (0.0004)	0.114 (0.0045)
Aluminum Titanate/Alumina	PY6 Si_3N_4	0.051 (0.0020)	0.000 (0.0000)	0.117 (0.0046)
SiC /Alumina	SN252 Si_3N_4	0.025 (0.0010)	0.020 (0.0008)	0.191 (0.0075)
SiC /Alumina	NT154 Si_3N_4	0.025 (0.0010)	0.020 (0.0008)	0.191 (0.0075)
SiC /Alumina	PY6 Si_3N_4	0.025 (0.0010)	0.015 (0.0006)	0.165 (0.0065)
SN252 Si_3N_4	SN252 Si_3N_4	0.076 (0.0030)	0.020 (0.0008)	0.061 (0.0024)
SN252 Si_3N_4	NT154 Si_3N_4	0.102 (0.0040)	0.023 (0.0009)	0.043 (0.0017)
SN252 Si_3N_4	PY6 Si_3N_4	0.076 (0.0030)	0.015 (0.0006)	0.038 (0.0015)

Table VII.
Gasifier static structure deflection analysis without retaining ring: radial clearance summary.

Scroll material	Vane/platform material	Build clearance mm δR--(in.)	Minimum transient clearance δR mm--(in.)	Maximum power steady-state clearance mm δR--(in.)
α-*SiC*	SN252 Si_3N_4	0.025 (0.0010)	0.005 (0.0002)	0.119 (0.0047)
α-*SiC*	NT154 Si_3N_4	0.051 (0.0020)	0.020 (0.0008)	0.102 (0.0040)
α-*SiC*	PY6 Si_3N_4	0.025 (0.0010)	0.003 (0.0001)	0.097 (0.0038)
NC430 *SiC*	SN252 Si_3N_4	0.051 (0.0020)	0.023 (0.0009)	0.142 (0.0056)
NC430 *SiC*	NT154 Si_3N_4	0.051 (0.0020)	0.013 (0.0005)	0.099 (0.0039)
NC430 *SiC*	PY6 Si_3N_4	0.051 (0.0020)	0.015 (0.0006)	0.099 (0.0039)
Aluminum Titanate/Alumina	SN252 Si_3N_4	0.152 (0.0060)	0.015 (0.0006)	0.150 (0.0059)
Aluminum Titanate/Alumina	NT154 Si_3N_4	0.178 (0.0070)	0.015 (0.0006)	0.132 (0.0052)
Aluminum Titanate/Alumina	PY6 Si_3N_4	0.152 (0.0060)	0.008 (0.0003)	0.127 (0.0050)
SiC /Alumina	SN252 Si_3N_4	0.025 (0.0010)	0.015 (0.0006)	0.196 (0.0077)
SiC /Alumina	NT154 Si_3N_4	0.025 (0.0010)	0.008 (0.0003)	0.152 (0.0060)
SiC /Alumina	PY6 Si_3N_4	0.025 (0.0010)	0.010 (0.0004)	0.173 (0.0068)
SN252 Si_3N_4	SN252 Si_3N_4	0.076 (0.0030)	0.020 (0.0008)	0.064 (0.0025)
SN252 Si_3N_4	NT154 Si_3N_4	0.076 (0.0030)	0.003 (0.0001)	0.020 (0.0008)
SN252 Si_3N_4	PY6 Si_3N_4	0.076 (0.0030)	0.015 (0.0006)	0.041 (0.0016)

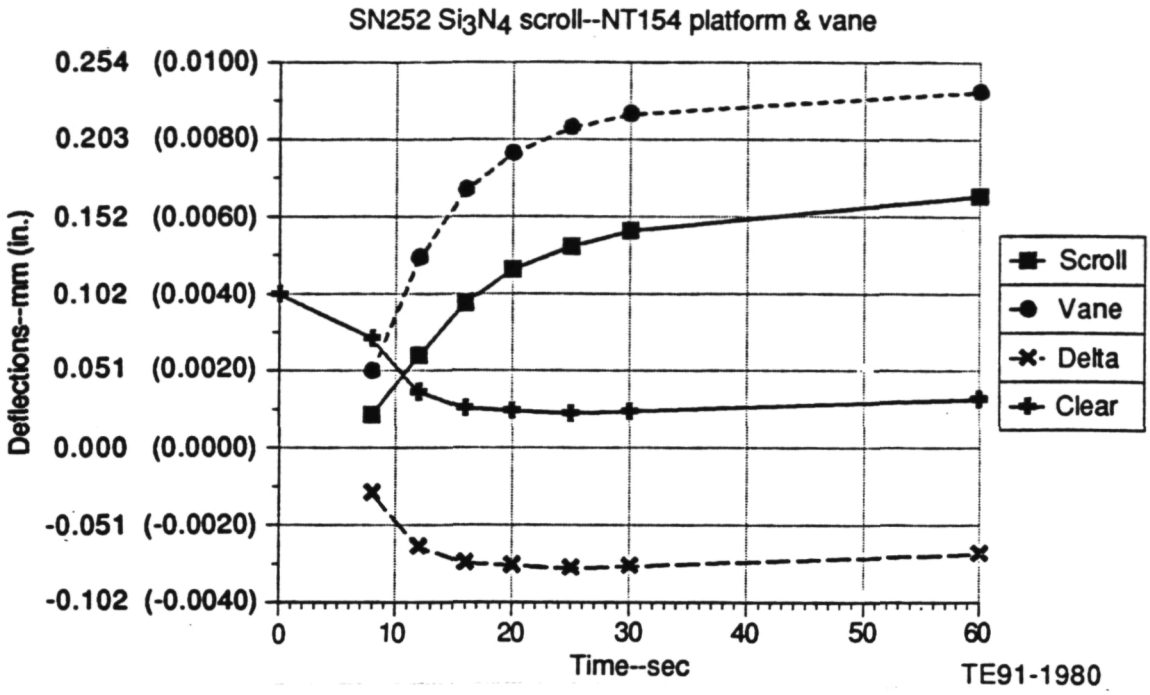

Figure 22. Gasifier scroll/vane transient radial deflections: includes vane containment ring and uses cold start-to-maximum power transient.

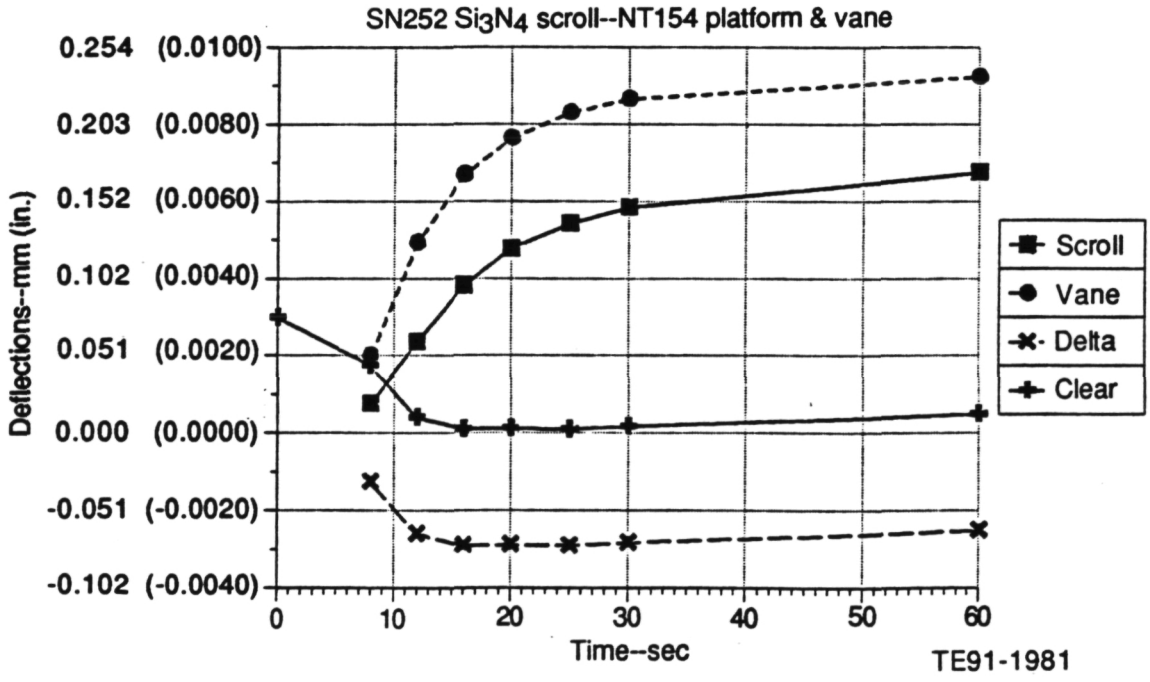

Figure 23. Gasifier scroll/vane transient radial deflections: does not include vane containment ring. Uses cold start-to-maximum power transient.

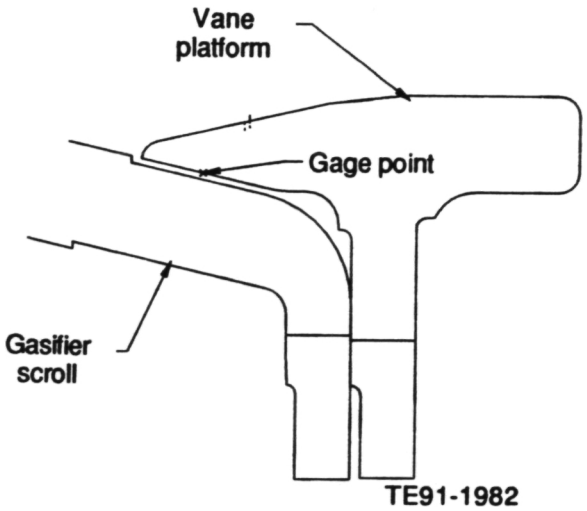

Figure 24. Gasifier scroll-to-vane platform mount interface.

datums to more closely tie the cast surface to datum C and by redefining the leading edge I.D. fillet so that the circular ridge no longer exists. The modified vane platform geometry is illustrated in Figure 26. All detail drawings and engine quality hardware have been updated to reflect the prescribed design modifications.

2.1.3 Gasifier Turbine Rotor

Objective/Approach

This activity is focused on designing structural ceramic rotors for the gasifier turbine that meet performance, mechanical strength, and dimensional criteria for operating in the AGT-5 hot gasifier rigs and test-bed engines at RPD operating conditions. Efforts include the analytic assessment of the structural reliability (statistical basis) of gasifier rotor designs considering various ceramic material systems. The rotor design reliability goal is 0.9797. Twenty- and fifteen-airfoil designs utilizing silicon carbide and several varieties of silicon nitride have been considered. Critical points in the engine operating cycle are analyzed, including 1371°C (2500°F) TIT maximum power steady-state and a cold start to maximum power transient. Prior to hot gasifier rig evaluation, all ceramic rotors are subjected to room temperature spin testing.

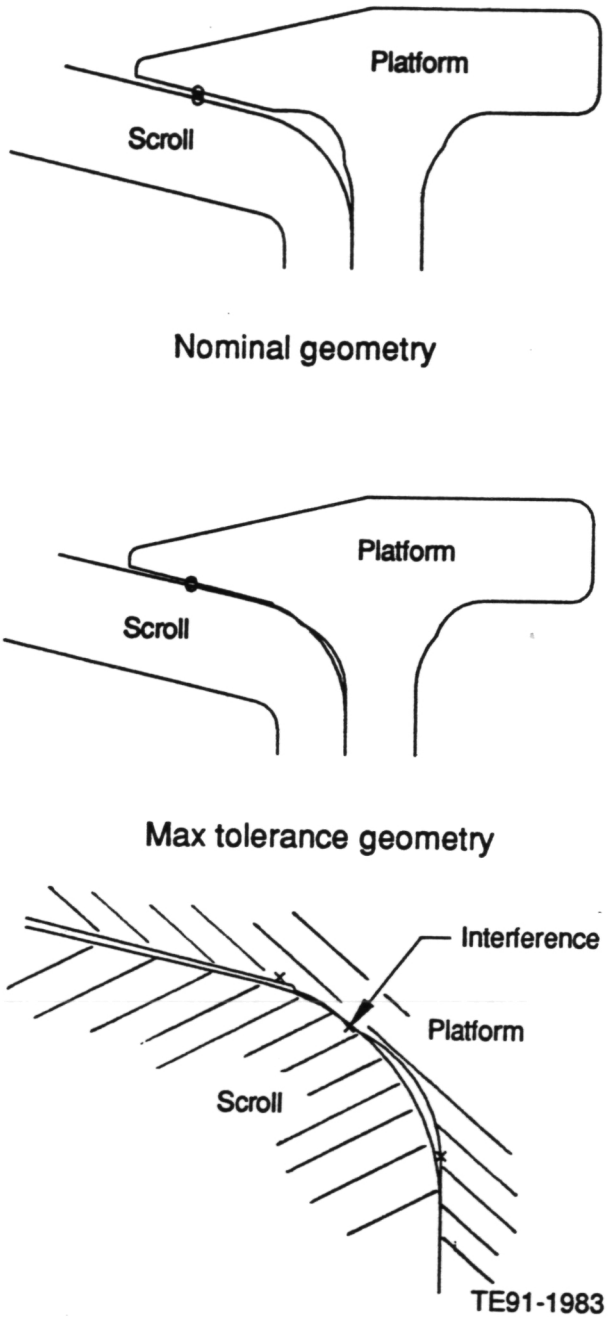

Figure 25. Maximum allowable geometric tolerances applied to the gasifier scroll/vane platform interface.

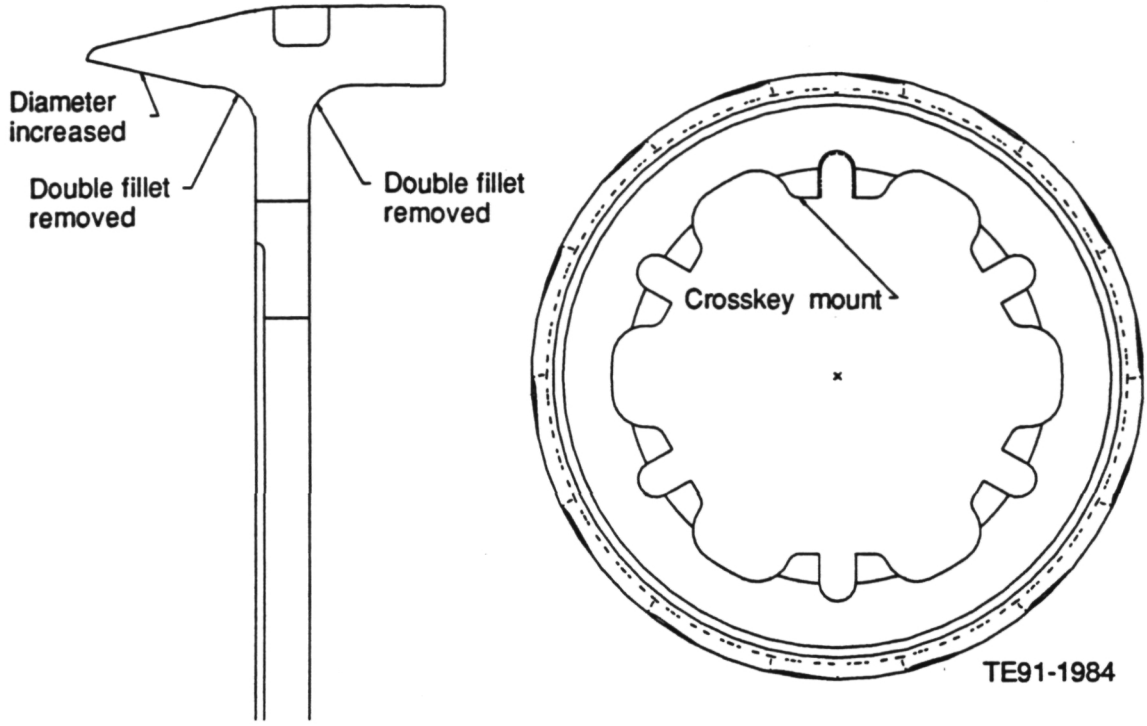

Figure 26. Revised gasifier vane platform geometry.

Accomplishments/Results

- 3-D analyses of the following 15-airfoil gasifier rotor designs were completed:
  - Kyocera SN252 Si_3N_4
  - GTE PY6 Si_3N_4
  - Norton/TRW NT154 Si_3N_4
- Two out of eleven α–SiC rotors were successfully proof spin tested to 80,000 rpm.
- Eight GTE PY6 Si_3N_4 rotors burst during proof spin testing prior to the 80,000 rpm required speed.
- Four out of seven N/TRW NT154 Si_3N_4 rotors were successfully proof spin tested to 80,000 rpm.
- One out of eight GCC GN-10 Si_3N_4 rotors was successfully proof spin tested to 80,000 rpm.

Discussion

Review of the 15-airfoil data from the 3-D analyses shown in Table VIII shows that the transient condition for the three Si_3N_4 material systems does not meet the design goal POS of 0.9797.

The 20-airfoil rotor design has a higher POS during the transient condition as shown in Table IX for the Kyocera SN252 Si_3N_4 material. The blade of the 15-airfoil rotor can be identified as the major influence on the overall ceramic rotor POS. During the transient condition, a large bending stress is present in the root of the airfoil caused by an imbalance of stresses on either side of the airfoil. Figure 27 displays a maximum principal stress of over 345 MPa (50 ksi) on the pressure side of the blade, and Figure 28 shows approximately 70 MPa (10 ksi) on the suction surface. This bending stress is further induced by thermal gradients at the rim of the rotor during the transient condition (see Figure 29). The leading and trailing edges of the rim of the rotor are hotter than the central region of the rim and they tend to grow radially outward. This outward growth or bending of the rim is opposed by the airfoil. The radial stresses are shown in Figure 30. At the airfoil/rim interface, the central region of the airfoil is in considerable tension of 415 MPa (60 ksi), while the leading edge is 0 MPa (0 ksi), and the trailing edge is in compression of approximately 207 MPa (30 ksi).

Table VIII.
Calculated probabilities of survival, 15-airfoil ceramic rotor, AGT-5 engine.

GT design POS goal = 0.9797	Room temperature spin 100% N_1 (1)	1371°C (2500°F) BOT (2) Steady-state	 Transient
• Kyocera SN252			
2-D	0.9999	-----	-----
3-D	0.9730	0.9970	0.7010
• GTE PY6			
2-D	0.9999	-----	-----
3-D (3)	0.9850	0.9880	0.8303
• N/TRW NT154			
3-D	1.0000	0.9987	0.9322

Notes:
(1) as-cast tip diameter
(2) finished tip diameter
(3) 0.508 mm (0.020 in.) airfoil root fillet radius (approx. 1/2 dwg. spec.)

Table IX.
Comparison of transient POS values for 15- & 20-airfoil rotors of Kyocera SN252 Si_3N_4.

	15-airfoil	20-airfoil
Airfoil	0.7090	0.9508
Hub	0.9880	0.9417
Total	0.7010	0.8953

Based on this data and the physical understanding of the airfoil/rim interaction, it is seen that low aspect ratio airfoils are adversely affected by rim thermal gradients. This is thought to explain the lower POS value for the 15-bladed rotor under transient conditions versus the 20-bladed rotor. The analyses of the current gasifier turbine rotor design is now complete. No further work is planned.

Proof spin testing is a relatively inexpensive method of checking the analytical 2-D and/or 3-D results and identifying ceramic rotors that have substandard material properties. Proof spin tests for the ceramic components are designed to spin the rotors at room temperature at a speed that is greater than engine design speed. This overspeed condition will increase the CF loading from the blades to approximate both the centrifugal stresses and the thermal stresses imposed on the rotor during actual engine operating conditions. The Si_3N_4 rotor proof test speed was 80,000 rpm, while the proof speed of CBO's α–SiC rotor was initially set at 85,000 rpm. The higher proof speed for the α–SiC rotor was originally deemed necessary in order to simulate the higher stresses resulting from the inherent Eα characteristic of α–SiC. The design proof speed was later set to 80,000 rpm for both α–SiC and Si_3N_4 gasifier rotor material systems.

CBO Rotor Proof Test. Figure 31 represents a 2-D axisymmetric maximum principal stress distribution for the 15-bladed ceramic gasifier rotor modeled using Carborundum's material during a room temperature speed of 100% N_1. The resulting POS for this condition was 0.9903, and

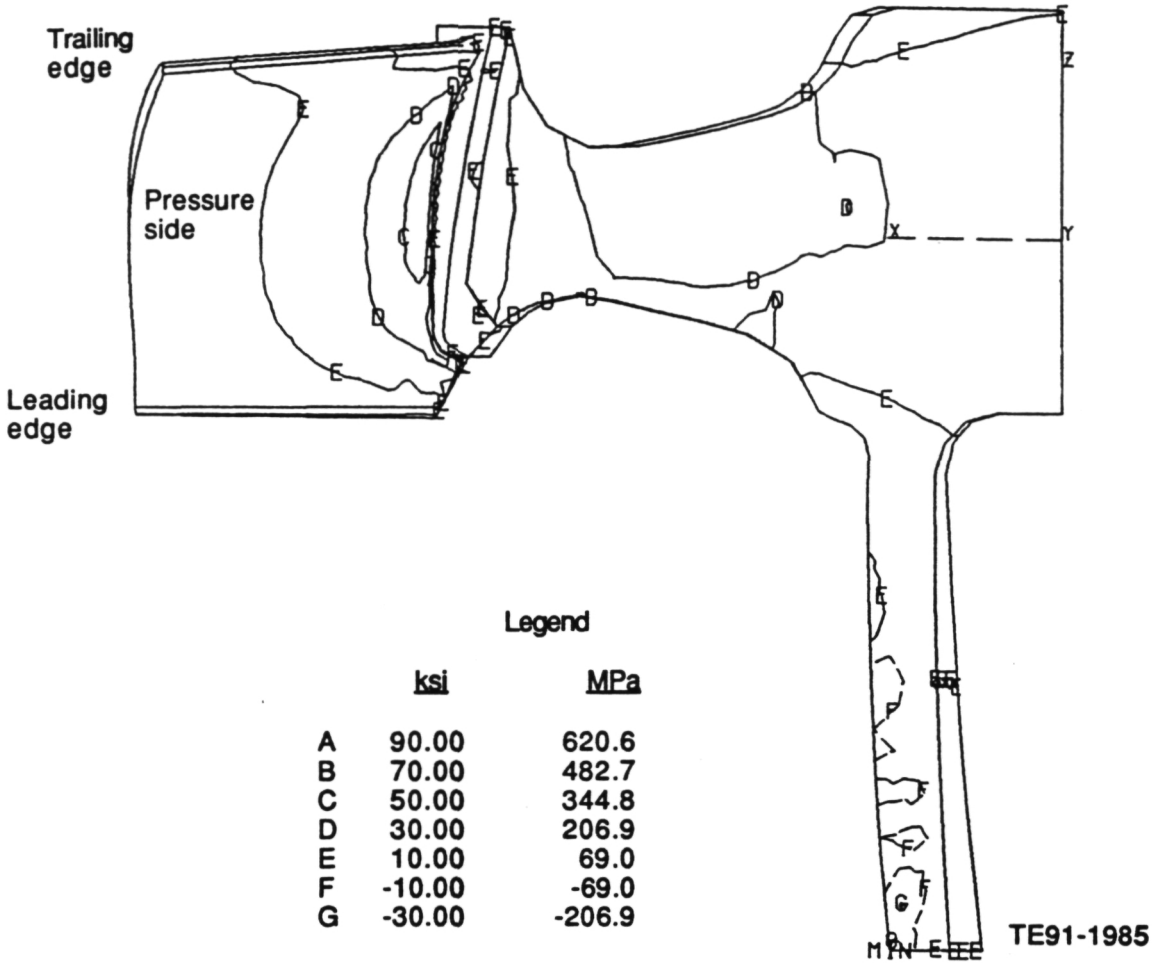

Figure 27. 3-D calculated maximum principal stresses, 15-airfoil rotor, SN252 silicon nitride, transient acceleration condition.

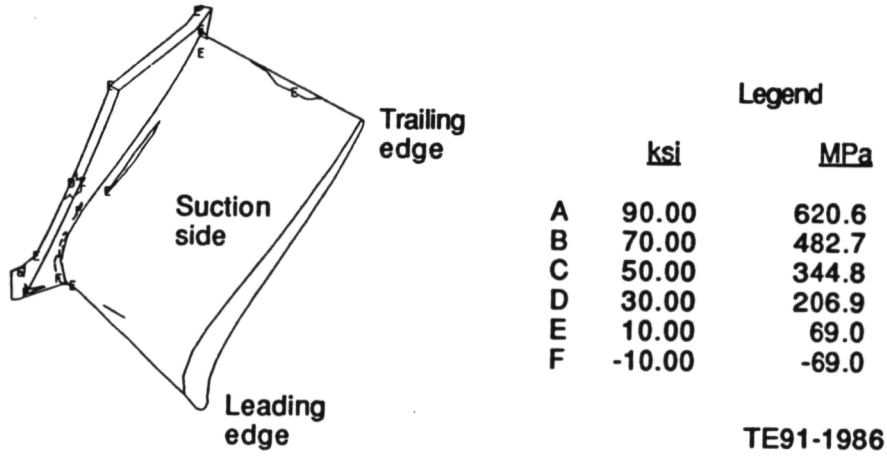

Figure 28. 3-D calculated maximum principal stresses, 15-airfoil rotor, airfoil suction side, SN252 silicon nitride, transient acceleration condition.

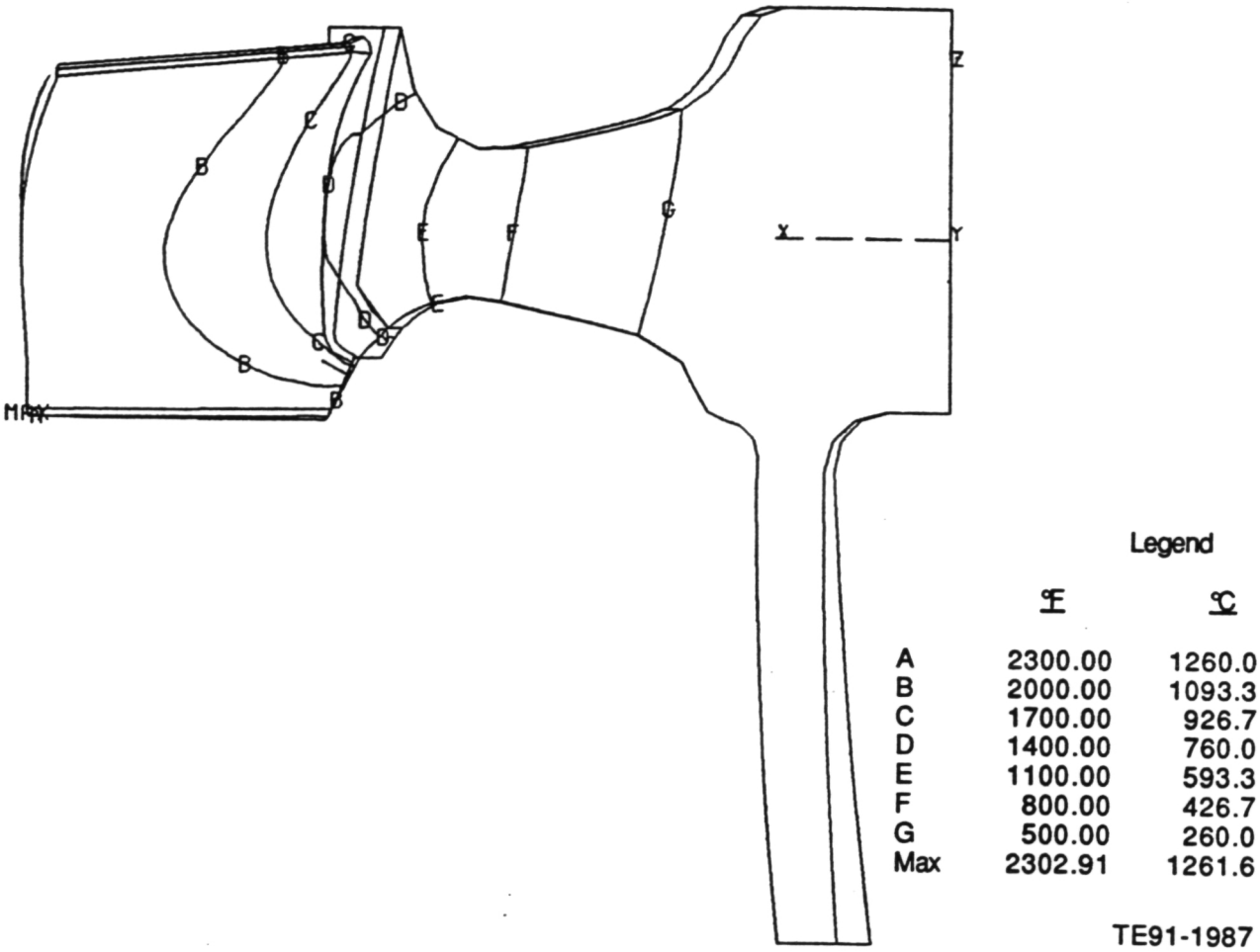

Figure 29. Calculated thermal gradients, 15-airfoil rotor, SN252 silicon nitride, transient acceleration condition.

the rotor exhibited a maximum principal stress of 219 MPa (31.8 ksi) in the forward web of the wheel. Increasing the rotational speed to 85,000 rpm for the proof test will increase the maximum principal stress to 364 MPa (52.8 ksi).

During proof spin testing, a high speed photograph is taken at the instant in time that a failure (burst) occurs. Figure 32 through 34 are pictures of CBO ceramic rotors (serial numbers FX78504, FX78513, and FX78509, respectively) taken at burst. After examination of the photographs and the ceramic remnants, it was determined that these three rotors failed in the balance stock region due to improper machining methods. Small surface cracks were created on the surface of the ceramic rotor when too much material was machined off during one machining pass. These small cracks became potential failure sites when the rotor was loaded during spin testing.

Due to these premature failures, a new balancing method was developed specifically for the spin testing of ceramic rotors. The new balance procedure is shown in Figure 35. For spin testing, the ceramic rotors are epoxied to an aluminum shaft that can be easily removed after testing. This attachment scheme allows the rotor and shaft to become eccentric, therefore requiring balance machining. The new balancing method includes a metal disk which is added to the aluminum shaft. The new assembly is balanced by machining the metal disk on the shaft rather than the ceramic rotor hub. The rotor blade tips are trimmed by a few thousandths of an inch as required to remove moment couple effects. The fourth rotor tested, S/N FX78505, was balanced using the new

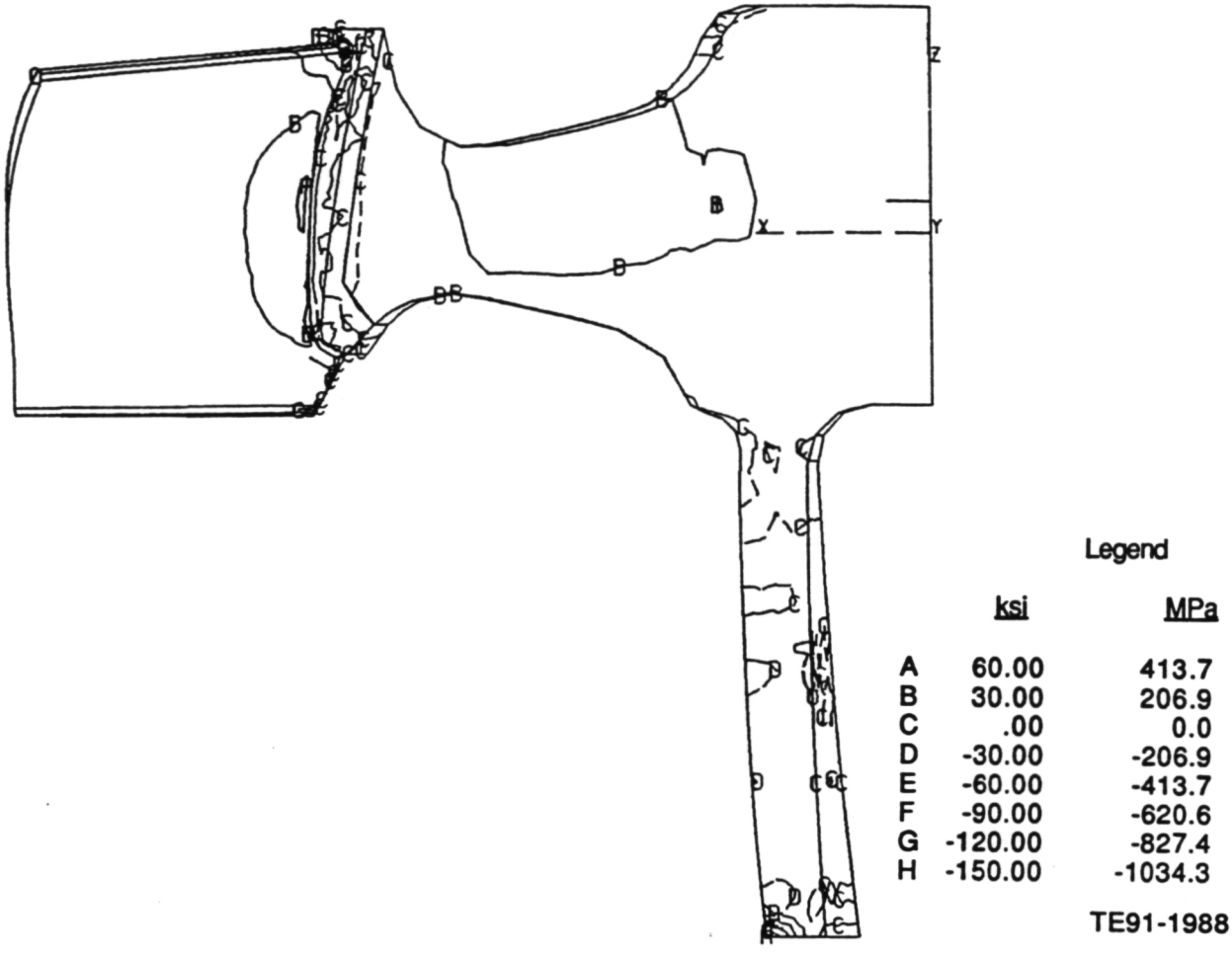

Figure 30. 3-D calculated radial stress components, 15-airfoil rotor, SN252 silicon nitride, transient acceleration condition.

method. It burst at a speed of 78,000 rpm, which was less than the goal. The rotor, however, contained some surface flaws and was selected primarily to evaluate the new balancing procedure. The picture displayed in Figure 36, and the remnants of the rotor after the test, show that spin tests of rotors balanced by the new method will provide a reliable test of a rotor's material integrity.

The next CBO rotor tested, S/N FX78517, burst at 79,900 rpm during a proof spin test. The picture taken at the time of failure was not clear enough to determine a potential failure origin, and the remnants of the rotor were so small that no significant conclusions could be drawn. Following the failure analysis, a 3-D analysis was performed on the α–SiC gasifier rotor simulating a room temperature overspeed condition. The analysis, which considers the rotor airfoils and their associated stresses, showed that the proof speed should be reduced from 85,000 rpm to 80,000 rpm due to blade fillet stresses.

Figure 37 shows the CBO rotor (FX78517) at the moment of burst, which occurred just under the design proof speed of 80,000 rpm. A possible location of the failure origin could be in the thin web area of the wheel or in the blade fillet area. The photo was inconclusive as to the exact location. Figure 38 displays CBO rotor S/N FX78519, which burst at 31,000 rpm. The photograph clearly shows the rotor breaking into two distinct sections (evidence of an internal flaw). A large section of the rotor was recovered and is shown in Figure 39. The defect in the rotor is the circular area (see arrow) in the thick area of the rotor hub. The smaller, lighter colored circle within the outer circle

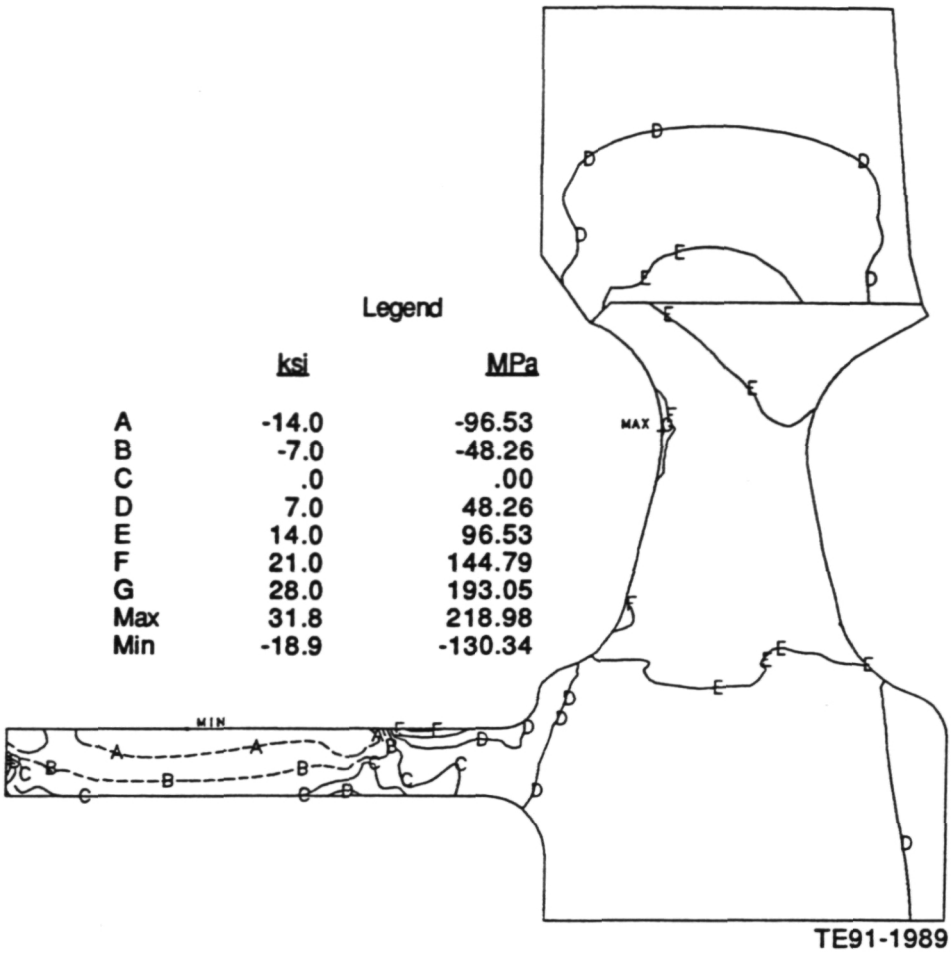

Figure 31. Maximum principal stress profile, 15-bladed CBO GT rotor, room temperature spin, 100% N_1.

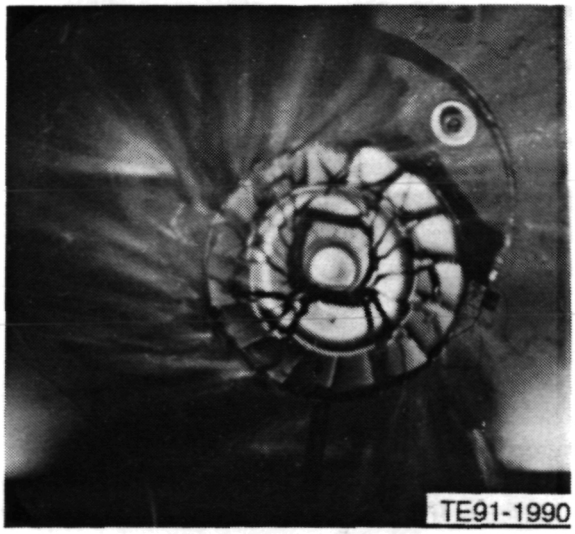

Figure 32. CBO hot isostatic pressed (HIPed) α–SiC rotor (FX78504) burst, N_1 = 68,000 rpm.

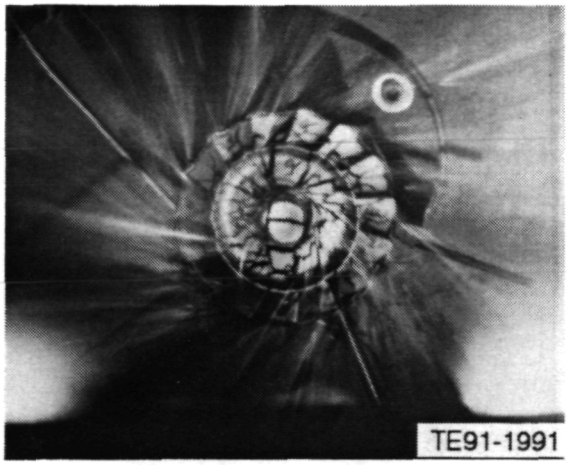

Figure 33. CBO HIPed α–SiC rotor (FX78513) burst, N_1=54,800 rpm.

ORIGINAL PAGE
BLACK AND WHITE PHOTOGRAPH

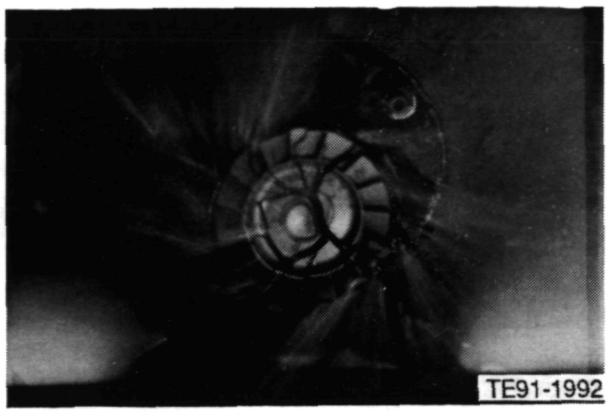

Figure 34. CBO HIPed α-SiC rotor (FX78509) burst, N_1=49,900 rpm.

was probably the initial void which caused the larger circular crack possibly after sintering. The rotor failed at a very low stress level.

CBO rotors FX78518 and FX78527 successfully passed proof spin testing to 80,000 rpm and were prepared (shaft mounting, tip grinding, and spin balancing) for hot gasifier rig testing. Two additional α-SiC rotors from CBO failed during proof testing. FX78522 burst at 78,900 rpm, and FX78528 failed at approximately 79,600 rpm. Due to high speed at the time of both failures, the ceramic remnants that remained after test were too small to draw any conclusions pertaining to the cause or origin of the failures. The photographs taken at the instant of burst for both α-SiC rotors are shown in Figures 40 and 41, respectively.

No further proof spin testing is anticipated for CBO's gasifier rotors, but there are four potential spin candidates remaining. It should be noted that the four spin candidate rotors did pass inspection, but they were not as high in quality as the rotors already tested. Gasifier rotor S/N FX78518 was damaged during the shaft assembly operation. One of the rotor blades has a crack that starts at the trailing edge tip and propagates toward the leading edge rim. The crack renders the rotor as a nonusable ceramic component for engine testing. Table X lists all of the CBO spin test results. A complete breakdown of the status of all of the 15-bladed ceramic rotors produced by CBO is shown in Table XI.

GTE Rotor Proof Test. Figure 42 shows a GTE rotor (S/N 399) bursting during proof spin testing.

ORIGINAL PAGE
BLACK AND WHITE PHOTOGRAPH

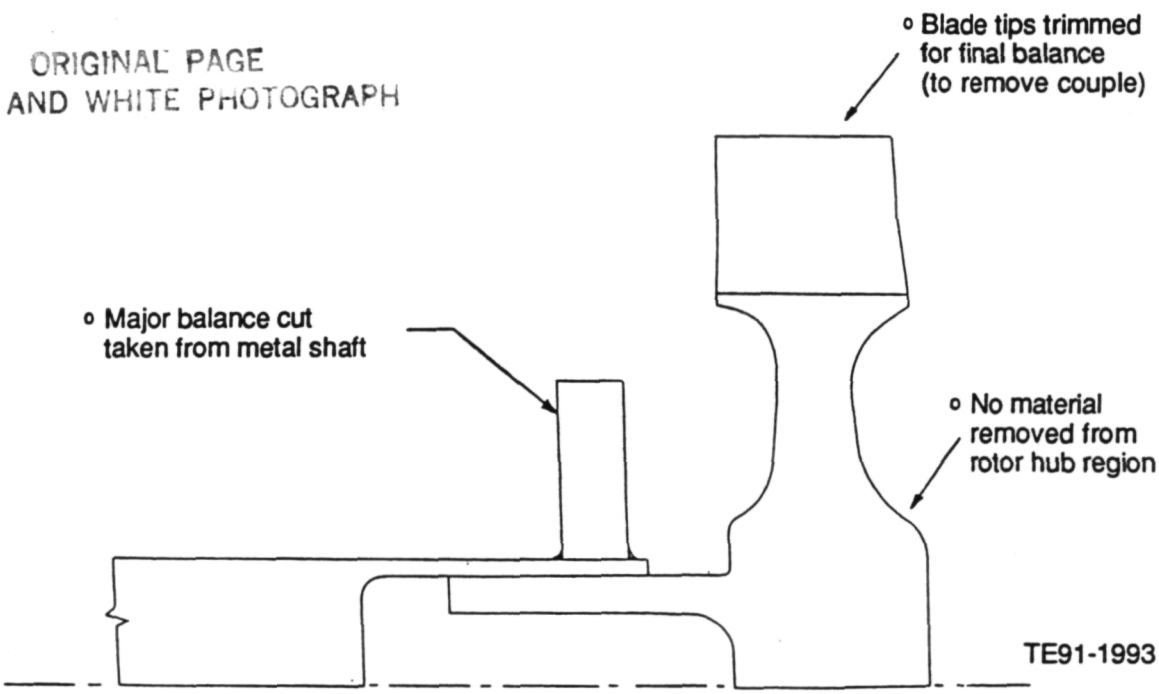

Figure 35. New balance method for spin testing rotors.

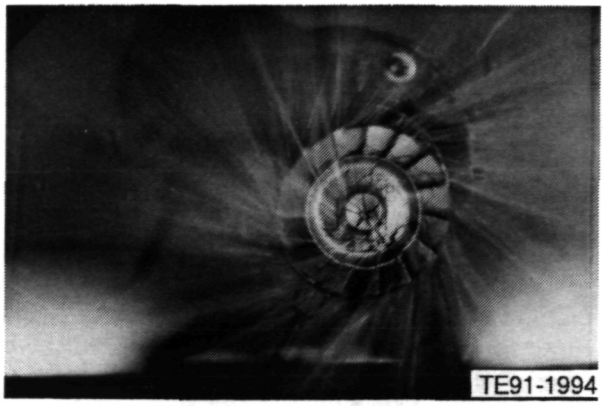

Figure 36. CBO HIPed α–SiC rotor (FX78505) burst, N_1 = 78,000 rpm, new balance method utilized.

The rotor failed at 73,400 rpm with the release of at least two airfoils as the initial failure origin. The large crack that formed was probably due to the rotor being out of balance after airfoil release. This particular rotor had a blade fillet radius of approximately 1.0 mm (0.039 in.) due to a tooling error, instead of the designed fillet of 2.0 mm (0.079 in.). The blade fillet area (blade/wheel interface) is a very highly stressed area, and the decreased fillet radius caused the premature failure of the rotor.

Figure 37. CBO HIPed α–SiC gasifier rotor (FX78517) burst, N_1 = 79,900 rpm.

The next GTE PY6 rotor submitted for cold spin proof testing burst prior to attainment of the 80,000 rpm goal. Rotor S/N 576 failed at 76,400 rpm. Figure 43 shows the rotor at the instant of

Table X.
CBO rotor spin test results.

Date	S/N	Failure speed (krpm)	Proof speed (krpm)
1/22/90	FX78504	68.0 (1), (2)	
1/23/90	FX78513	54.8 (1), (2)	
2/14/90	FX78509	49.9 (1), (2)	
4/26/90	FX78505	78.0 (3), (2)	
5/11/90	FX78515	82.0 (2)	
5/11/90	FX78517	79.9	
6/19/90	FX78519	31.0	
6/19/90	FX78518		80.0
8/15/90	FX78527		80.0
9/06/90	FX78522	78.9	
9/06/90	FX78528	79.6	

Notes: (1) balance stock machining failure
(2) specified proof speed was 85,000 rpm
(3) substandard rotor used to test new balance method

ORIGINAL PAGE
BLACK AND WHITE PHOTOGRAPH

Figure 38. CBO HIPed α–SiC gasifier rotor (FX78519) burst, N_1 = 31,000 rpm.

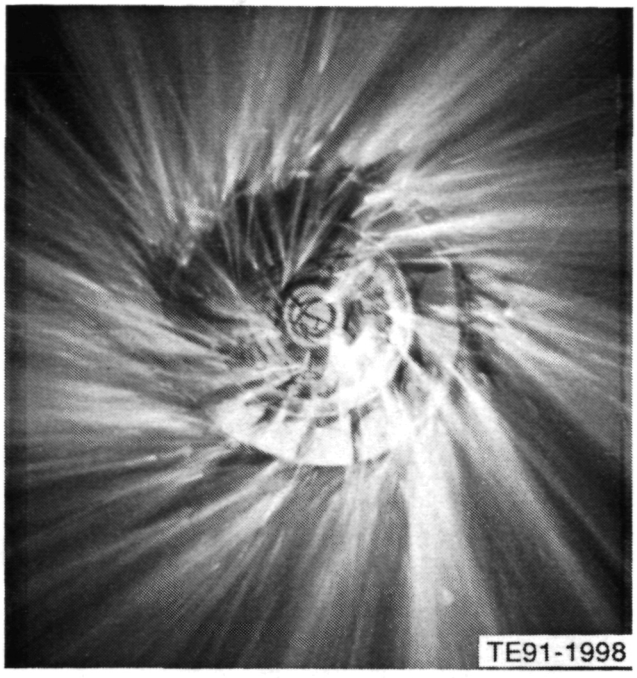

Figure 40. CBO HIPed α–SiC rotor (FX78522) burst, N_1 = 78,900 rpm.

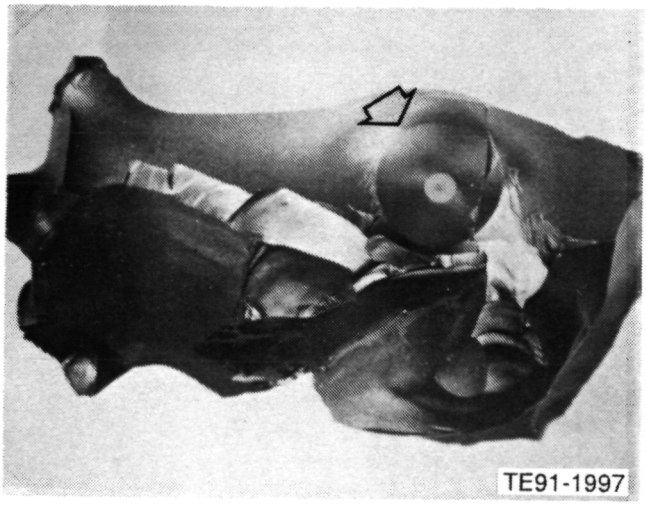

Figure 39. Section of CBO HIPed α–SiC burst rotor (FX78519). Initial failure site is circular crack (see arrow).

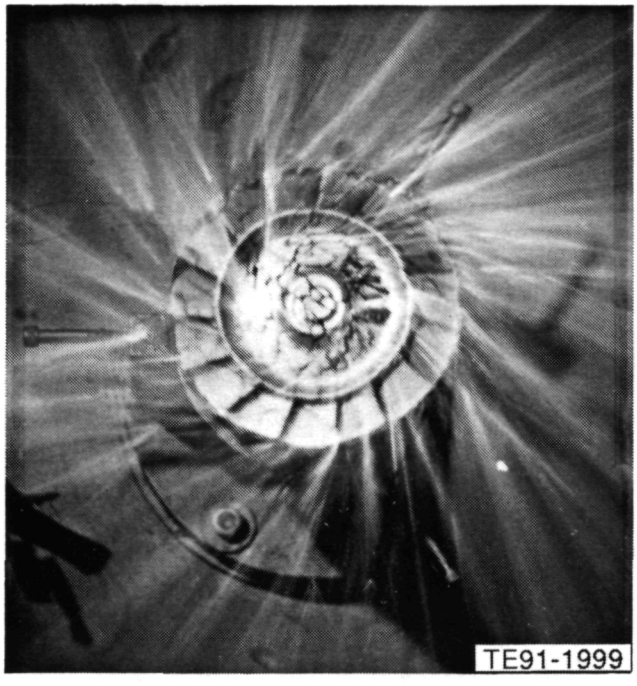

Figure 41. CBO HIPed α–SiC rotor (FX78528) burst, N_1 = 79,600 rpm.

ORIGINAL PAGE
BLACK AND WHITE PHOTOGRAPH

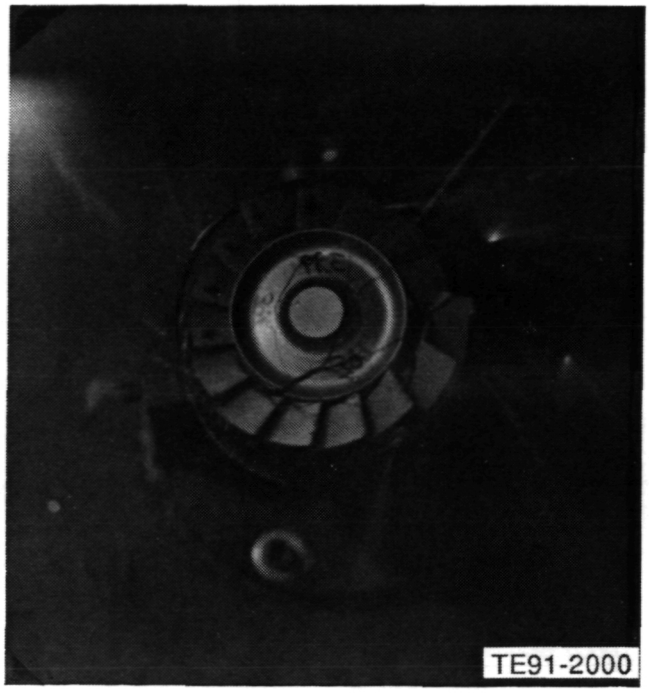

Figure 42. GTE Si_3N_4 gasifier rotor (S/N 399) burst, N_1 = 73,400 rpm.

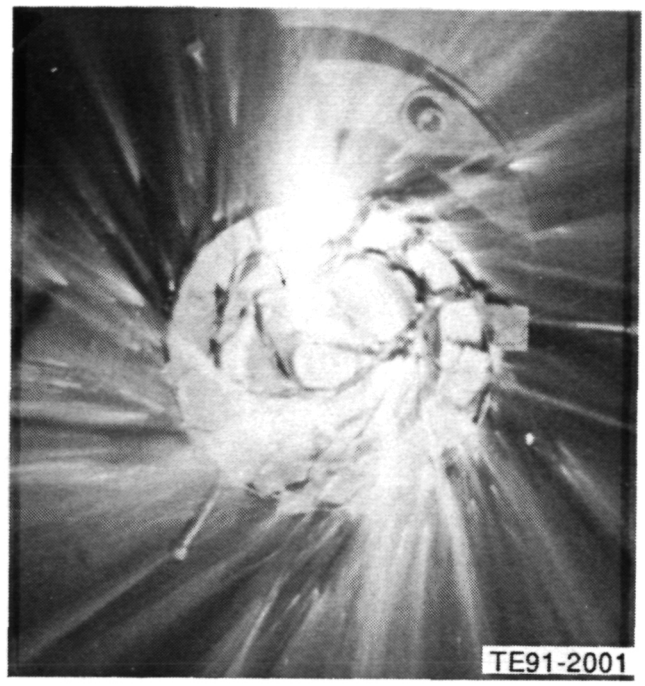

Figure 43. GTE rotor S/N 576 at moment of burst, N_1 = 76,400 rpm.

Table XI.
CBO rotor status.

No. of deliverables scheduled	No. passed spin test (80,000 rpm)	Rotor status
30	2	1 assembled to shaft (FX78527)
		1 damaged during assembly (FX78518)
		9 burst during spin test
		4 spin candidates
		1 not HIPed
		4 subquality rotors
		10 scrap rotors
		30 total

burst. The flaw at which the fracture originated, shown in Figure 44, was located on the aft side of the wheel web (see Figure 45) and had an approximate size of 0.17 mm x 0.066 mm (0.007 in. x 0.0026 in.). A stress of 186.2 MPa (27 ksi) was calculated at the failure origin by measuring the mirror surface area. Figure 46 shows the 3-D calculated maximum principal stress distribution for a room temperature spin condition of 100% N1 and a corresponding stress at the region of failure of 138 MPa (20 ksi). As stress is a direct function of the square of the

ORIGINAL PAGE
BLACK AND WHITE PHOTOGRAPH

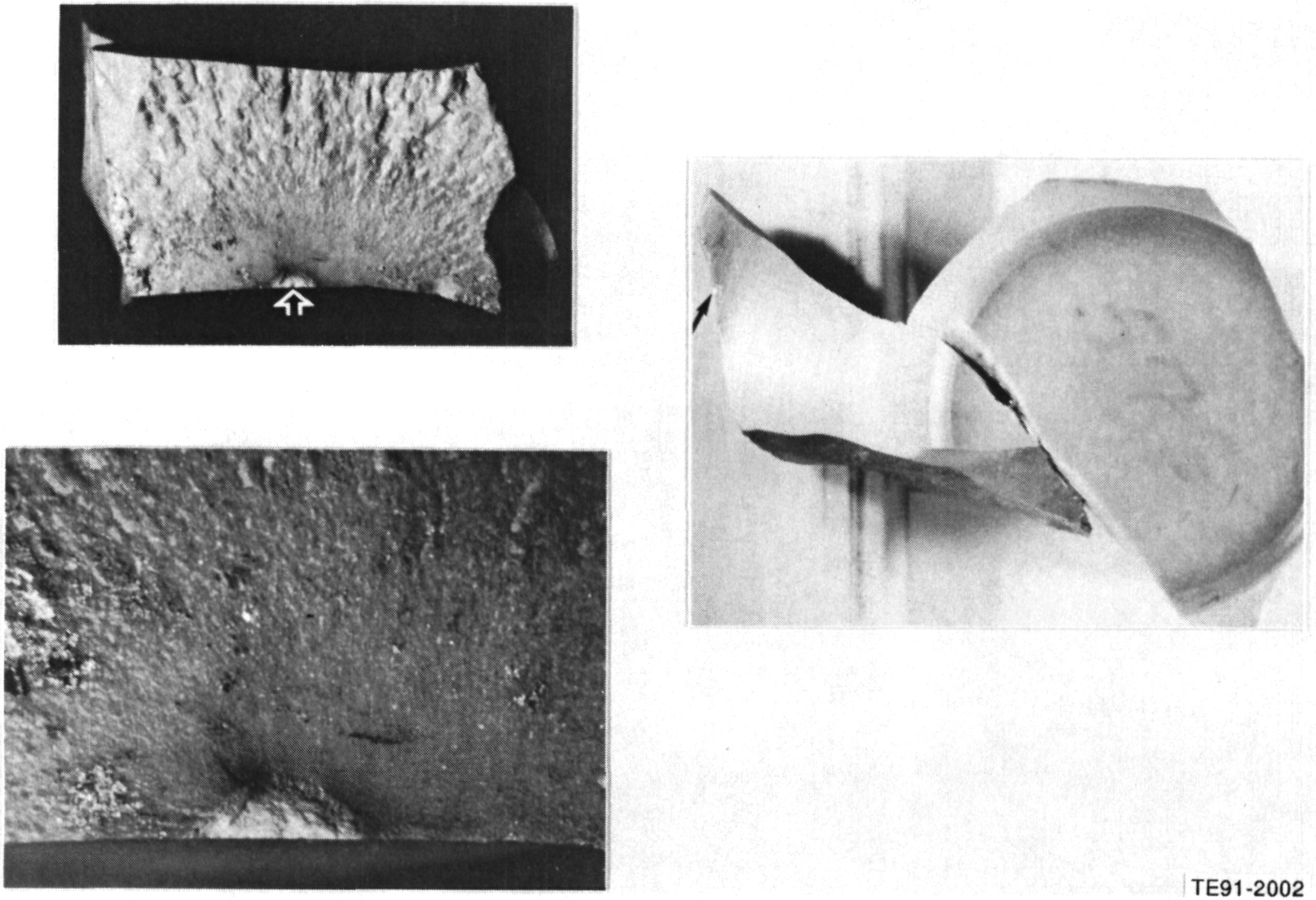

Figure 44. Failure origin of GTE rotor (S/N 576.)

ORIGINAL PAGE
BLACK AND WHITE PHOTOGRAPH

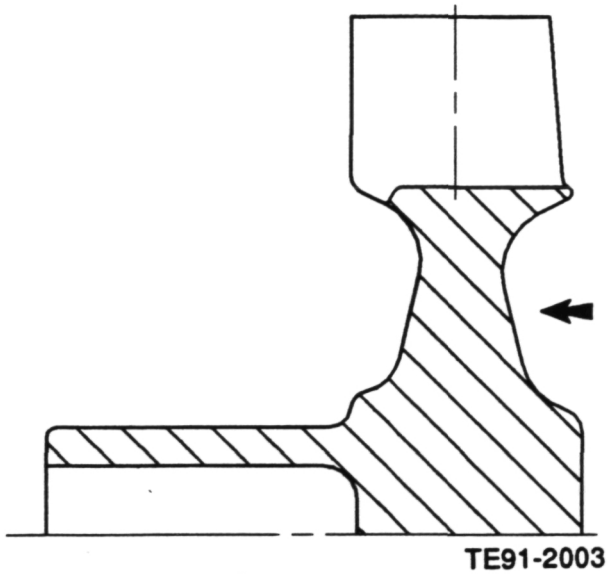

Figure 45. Failure site location of GTE rotor (S/N 576.)

speed, the resulting stress in the failure area at burst speed would be 185 MPa (26.8 ksi), which is consistent with that calculated using the mirror surface area.

GTE's rotor (S/N 656), which failed at 66,800 rpm, is shown in the burst photo in Figure 47. The failure origin, shown in Figure 48, was on the forward face of the wheel in the thin cross section area of the hub (see Figure 49). The flaw is believed to be the result of machining damage. The approximate stress at the failure site was calculated (using the mirror surface) to be 172 MPa (25 ksi). Using Figure 46 as a reference, the resulting stress in the fracture origin location would be approximately 177 MPa (25.6 ksi) when accounting for the rotational speed correction, again consistent with that calculated from the mirror surface area.

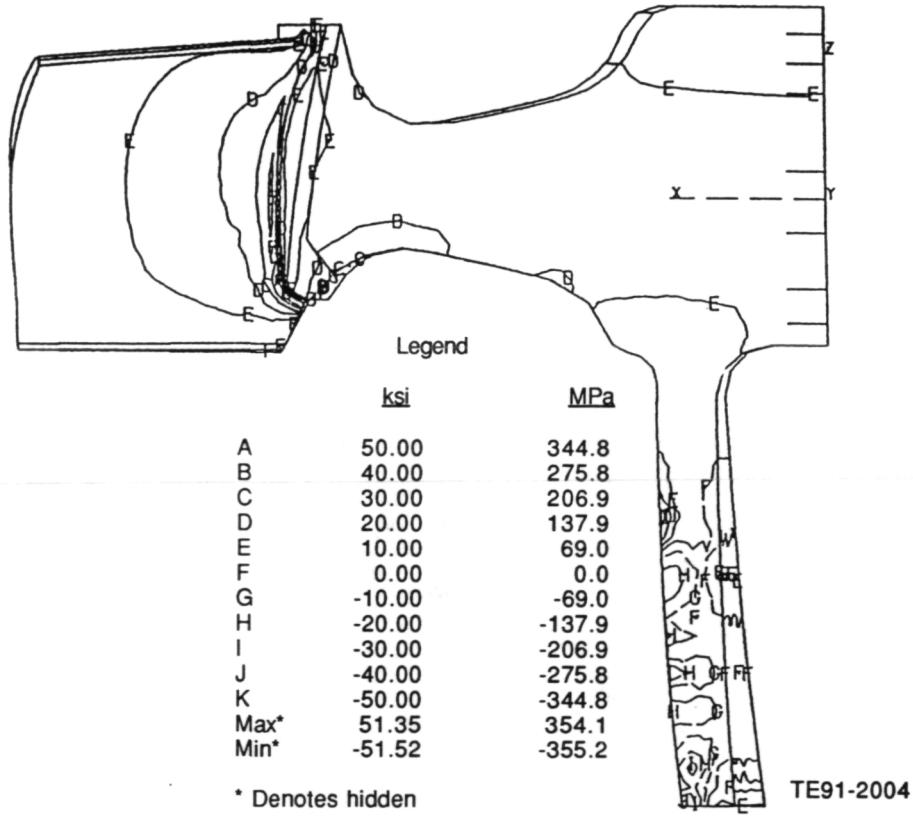

Figure 46. 3-D calculated maximum principal stress distribution for GTE PY6 rotor - room temperature spin condition.

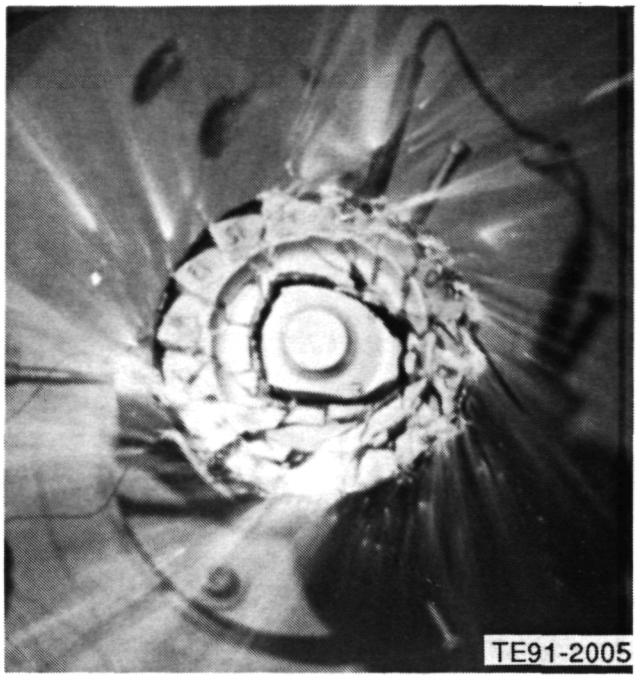

Figure 47. GTE rotor (S/N 656) at moment of burst, N_1 = 66,800 rpm.

GTE's PY6 gasifier rotor S/N 639 burst during spin testing at 63,200 rpm. No photograph was taken at the time of burst due to a malfunction. From the ceramic fragments, the failure was determined to be caused by a machining mark on the forward face of the rotor (see Figure 50). Although this particular rotor was heat treated after final machining at GTE, the machining mark on the rotor face was too deep to be healed by the heat treatment process. The stress at the failure site was calculated to be approximately 120 MPa (17.3 ksi). The stress level was obtained by examination of the fracture mirror surface. Referring back to Figure 46, which is a maximum principal stress profile of the GTE 15-bladed gasifier rotor at room temperature and 100% N1, the plot approximates the stress in the failure region to be 159 MPa (23 ksi). This stress scaled to burst speed would be 146 MPa (21 ksi).

Another heat treated GTE PY6 rotor, S/N 647, is shown at the instant of burst in Figure 51. The rotor attained a speed of 75,500 rpm. From examination of the photo, the failure site is presumed to be in the blade/rim region. The ceramic remnants that were recovered after the test were too small to be conclusive as to the actual failure origin. GTE's PY6 rotor S/N 670 is shown just after failure in Figure 52. It reached a speed of only 56,900 rpm. By examining the fracture mirror surface the stress at the failure site was calculated to be 97 MPa (14.1 ksi). When the analytical FEM results are reduced to 56,920 rpm, the stress in the same area as the failure origin is determined to be 103 MPa (14.9 ksi), which correlates well with the mirror surface stress calculation. The premature rotor failure was caused by a sintering flaw, which could have possibly been a fold line or a pore. The flaw was located on the aft face, and its size was 1.91 mm (0.075 in.) long by 0.41 mm (0.016 in.) deep (see Figure 53). Again, although this rotor had been heat treated after final machining, the flaw was too deep to be healed by the process.

The spin test results summary for the GTE 15-bladed ceramic rotors is displayed in Table XII. A complete breakdown of the status of all of the 15-bladed ceramic rotors produced by GTE is shown in Table XIII.

N/TRW Rotor Proof Test. Table XIV is a list of N/TRW's spin test results for the 20-bladed ceramic gasifier rotors. Rotor S/N 5G is currently being balanced prior to assembly to the metal shaft. A complete breakdown of the status of all of the 20-bladed ceramic rotors produced by N/TRW is shown in Table XV. N/TRW prepared seven rotors for spin test with plans of delivering five to Allison after spin test. As Tables XIV and XV show, 3 rotors failed during spin test. Thus, only 4 rotors were delivered to Allison.

GCC Rotor Proof Test. GCC cast 156 development rotors while changing casting parameters in order to establish a standard casting procedure for fabricating AGT-5 rotors. The mold used to cast the rotors was created by a stereolithography pattern, which produced an extremely rough surface. Fourteen of the 156 rotors were processed by GCC as deliverables. Of these 14 components, 12 rotors were accepted after NDE and subsequently machined in the shaft region only. Fluorescent penetrant inspection (FPI) and visual inspections were performed on the machined rotors, 10 of the 12 were chosen as spin candidates; eight were actually tested.

ORIGINAL PAGE
BLACK AND WHITE PHOTOGRAPH

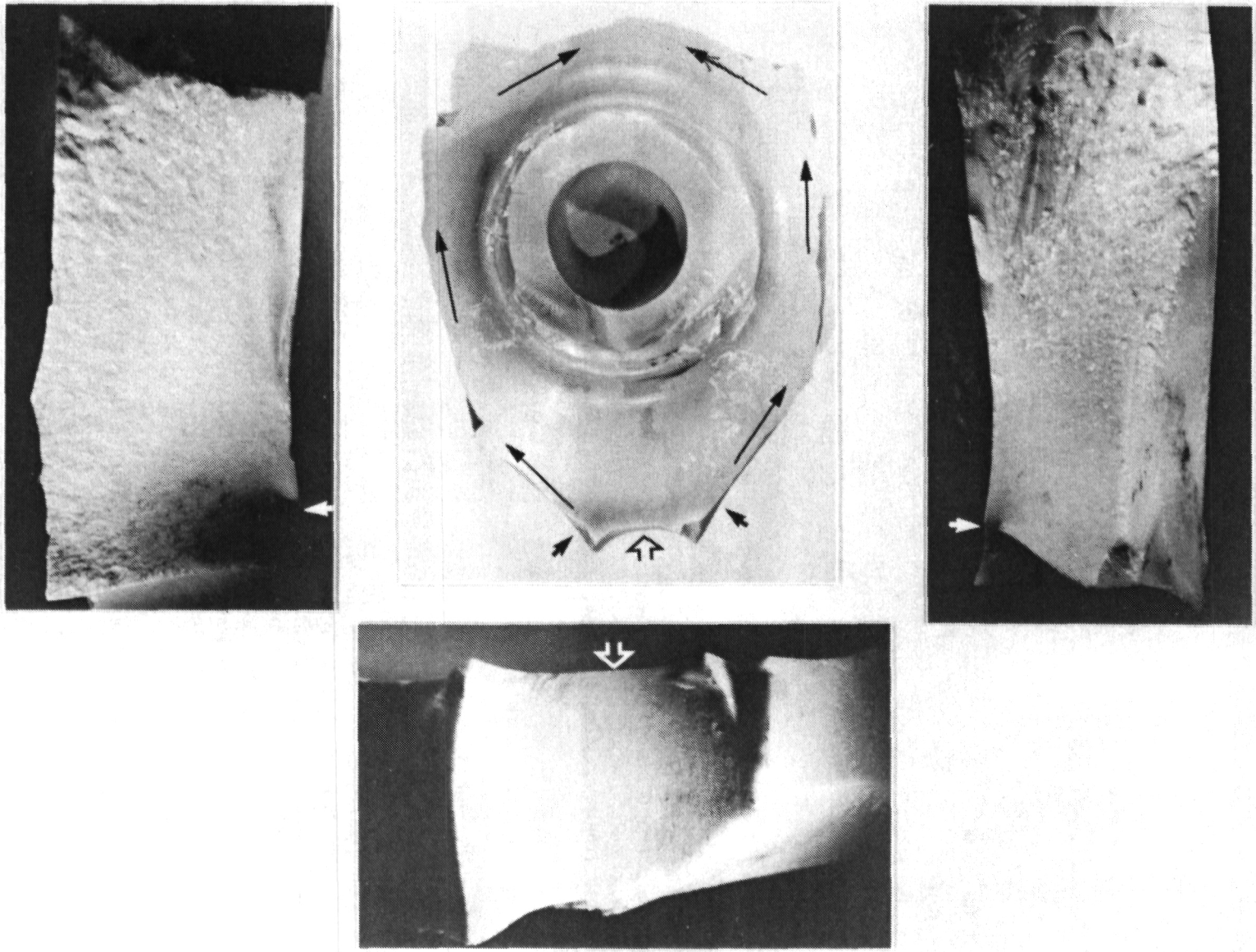

TE91-2006

Figure 48. Failure origin of GTE rotor (S/N 656.)

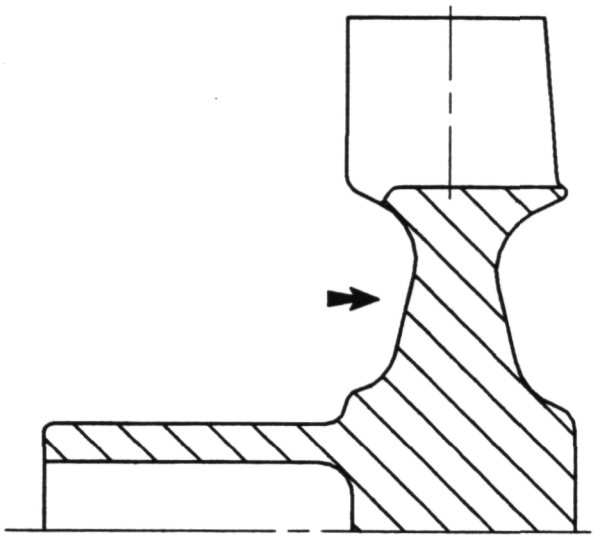

Figure 49. Failure site location of GTE rotor (S/N 656.)

All spin testing was performed in a vacuum at a vendor outside of GCC. The calculated design proof speed for testing was 80,000 rpm. Each rotor was sprayed with an aluminized paint on the aft side of the hub, and any defects present on this face were marked with a magic marker.

A high-speed photograph was taken at the moment of rotor failure. The purpose of the paint was to provide contrast in the photograph between the marked defects and the cracks at the instant of failure with the hub face of the ceramic rotor. In the event of rotor failure during the test, the photograph and ceramic remnants were studied in an attempt to determine the failure origin. Table XVI displays the serial number and the failure speed or proof speed of the rotors tested during this reporting period.

Failure analysis was performed by GCC using the ceramic rotor remnants and the burst photographs, and their results are listed in Table XVII.

For the first set of five rotors that were spun to burst (S/Ns 126, 145, 148, 189, and 191), surface defects, which were found and located prior to testing, correlated well with the indicated failure origin. The surface defects, which were caused primarily by the use of a rough stereolithography pattern and difficulties associated with the casting geometry of the rotor and the unidirectional casting process, acted as the failure origins. The photographs taken at the instant of failure are shown in Figures 54 through 58.

Table XII.
GTE rotor spin test results.

Date	S/N	Failure speed (krpm)	Proof speed (krpm)
6/19/90	399	73.4	
8/15/90	576	76.4	
8/15/90	656	66.8	
10/09/90	639	63.2 (1)	
10/09/90	647	75.5 (1)	
10/09/90	670	56.9 (1)	
3/20/91	232	66.4 (2)	
3/20/91	286	62.8 (2)	

Notes: (1) heat treated subsequent to final machining at GTE
(2) spin tested by GTE. Rotors had 1.00 mm blade fillet

Table XIII.
GTE rotor status.

No. of deliverables scheduled	No. passed spin test (80,000 rpm)	Rotor status
20(1)	0	0 assembled to shaft 8 burst during spin test (2) 2 spin candidates 2 subquality rotors 10 scrap rotors (2) solid shaft (5) heat treated 22 Total (2)

Notes: (1) Two additional rotors were spin tested by GTE
(2) Includes 2 rotors spin tested by GTE

Table XIV.
N/TRW rotor spin test results.

Date	S/N	Failure speed (krpm)	Proof speed (krpm)
8/15/90	5G		80.0
8/15/90	5K	74.5	
8/15/90	4W		80.0
8/15/90	5S		80.0
8/15/90	4H	57.8	
11/12/90	6E	79.1	
11/12/90	6F		80.0

Table XV.
N/TRW rotor status.

No. of deliverables scheduled	No. passed spin test (80,000 rpm)	Rotor status
5 (1)	4	1 assembled to Shaft S/N 5S 1 damaged during assembly S/N 4W 1 being balanced for assembly S/N 5G 1 ready for assembly S/N 6F (3) burst during spin test (2) 4 Total

Notes: (1) 5 rotors scheduled for delivery, only 4 rotors actually delivered
(2) Consumed in spin testing at N/TRW, not delivered to Allison

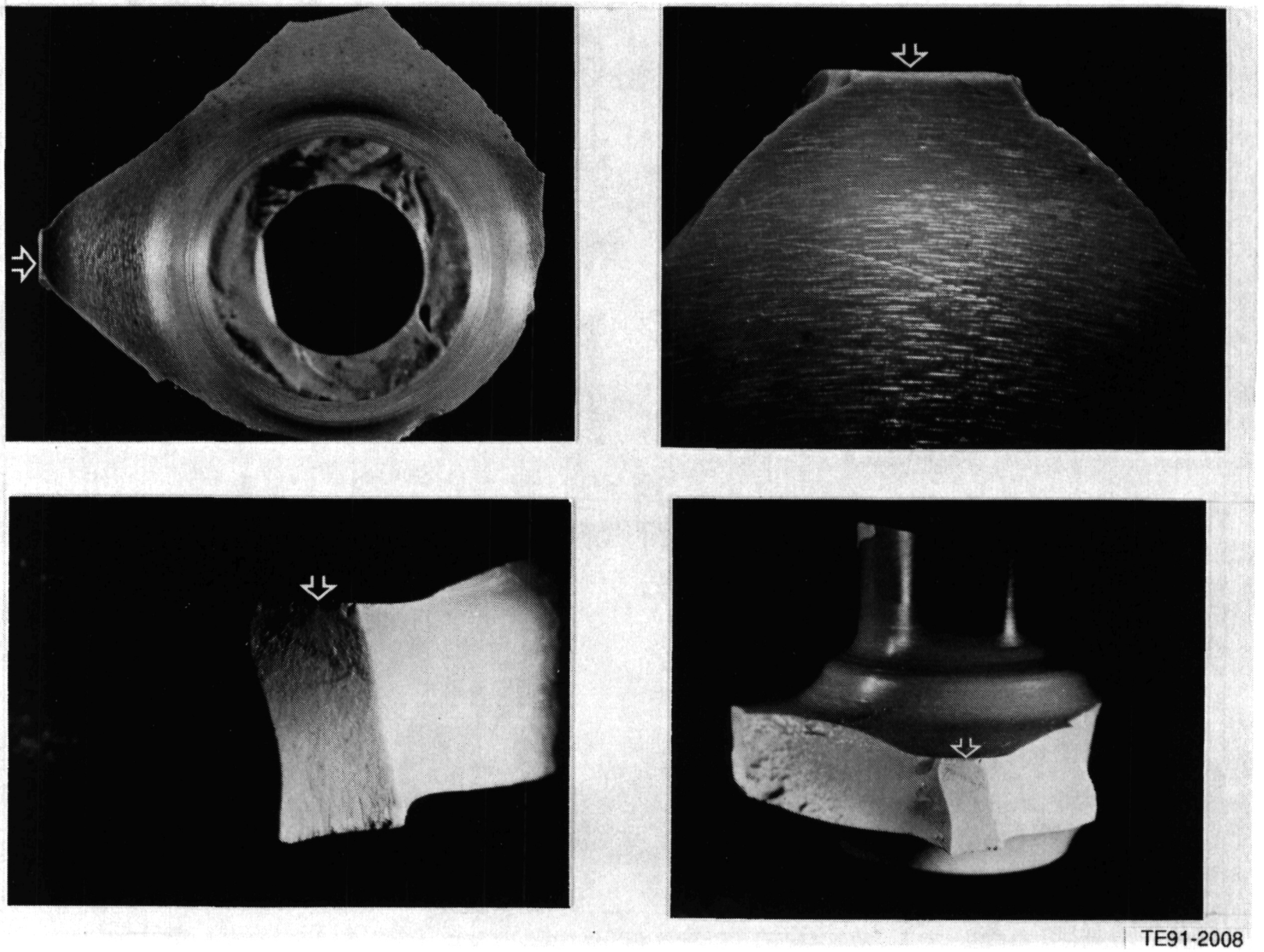

Figure 50. Failure origin of GTE rotor (S/N 639.)

ORIGINAL PAGE
BLACK AND WHITE PHOTOGRAPH

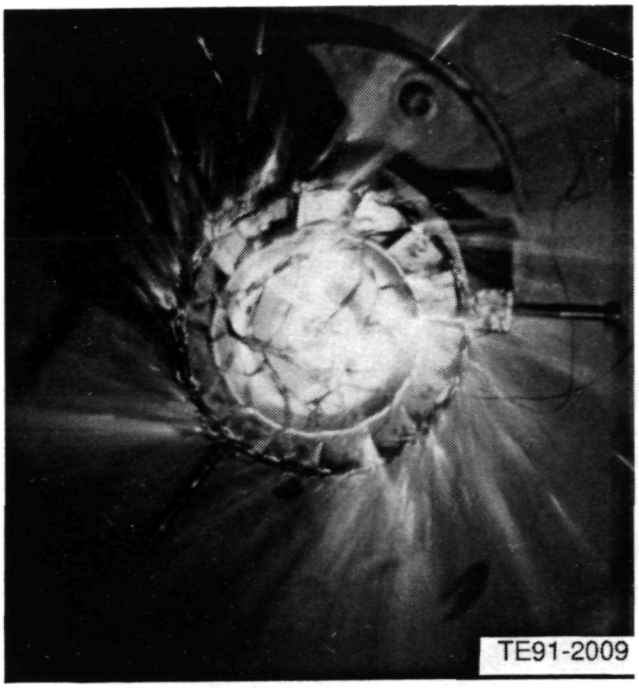

Figure 51. GTE rotor (S/N 647) at moment of burst, N_1 = 75,500.

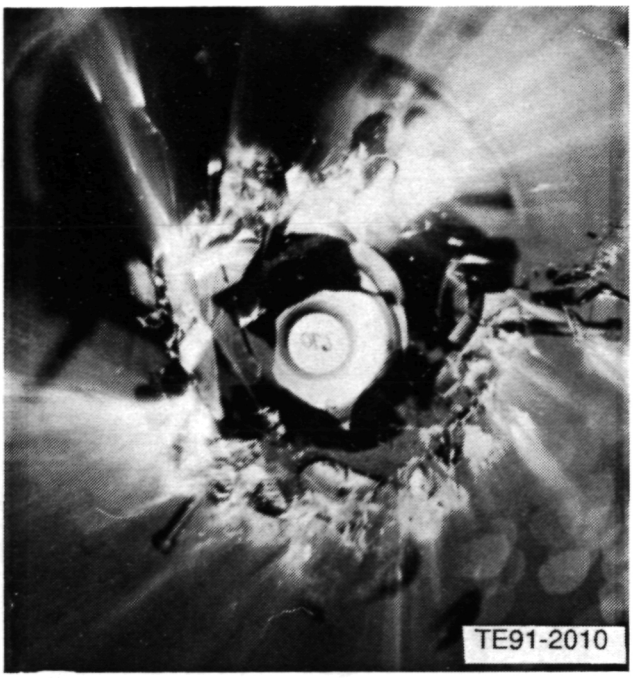

Figure 52. GTE rotor (S/N 670) just after failure, N_1 = 56,900.

Table XVI.
GCC rotor spin test results.

20-bladed rotors
Material: GN-10 Si_3N_4

Date	S/N	Failure speed (krpm)	Proof speed (krpm)
12/05/90	126	78.8	
12/05/90	145	21.5	
12/05/90	148	65.3	
12/05/90	189	79.5	
12/05/90	191	75.6	
12/14/90	149	67.9	
12/14/90	199	78.7	
12/14/90	169		80.0

Table XVII.
GCC spin test data vs. NDE results.

Rotor S/N	Failure speed (rpm)	Preliminary failure origin (NDE results)
126	78,820	hub-rim defect
145	21,480	lost blade
148	65,320	hub-rim defect
189	79,510	machining chip/hub/shaft
191	75,580	hub-rim defect
149	67,850	shaft/hub defect
199	78,660	void on hub surface

ORIGINAL PAGE
BLACK AND WHITE PHOTOGRAPH

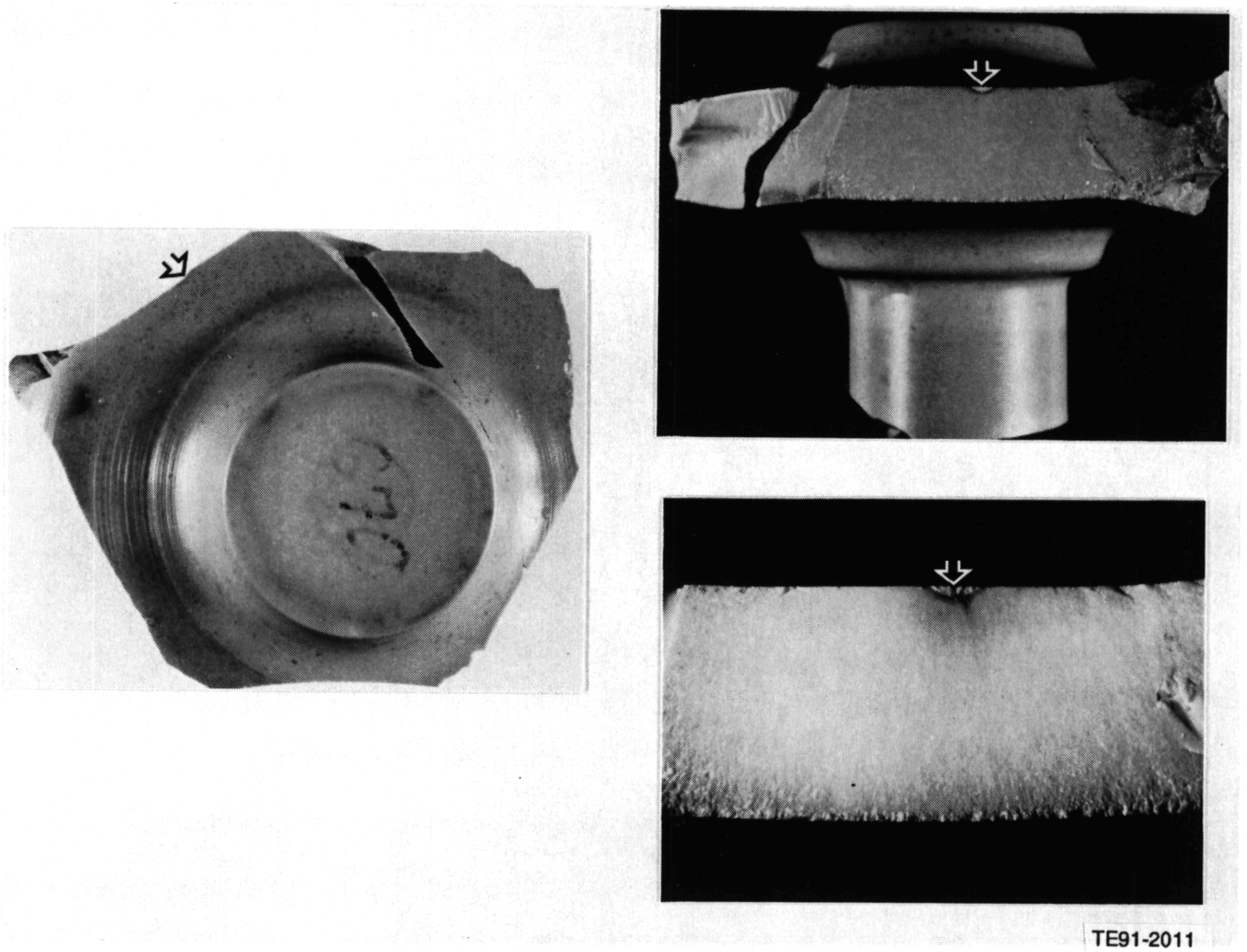

Figure 53. Failure origin of GTE rotor (S/N 670.)

ORIGINAL PAGE
BLACK AND WHITE PHOTOGRAPH

The second set of rotors that were spin tested (S/Ns 149, 199, and 169) had fewer FPI and visual inspection discrepancies than the first set tested. The main flaws in the second set of rotors were surface indications, whereas the first set contained flaws such as missing blades, shaft cracks, and low density. Rotor S/N 169 lost small sections of the blade tips at 48,240 rpm, and the test was stopped. The rotor was then rebalanced and retested, and subsequently survived to 80,000 rpm. The burst photographs for S/Ns 149 and 199 are shown in Figures 59 and 60, respectively.

Table XVIII is a detailed breakdown of GCC's deliverable rotor status.

The majority of the spin testing has been completed for the ceramic gasifier turbine rotors. Table XIX displays the status of the gasifier rotors with respect to being rig/engine ready components.

Table XVIII.
GCC rotor status.

20-bladed rotors
Material: GN-10 Si_3N_4,
P/N 5-80502

No. of deliverables scheduled	No. passed spin test (80,000 rpm)	Rotor status
20(1)	1	1 passed spin test with damaged blade tips, not assembled to shaft 2 delivered and balanced, but not spin tested 7 burst during spin test 10 total

Note: (1) 20 rotors scheduled for delivery, 10 delivered.

Table XIX.
Gasifier rotor status.

Vendor	No. blades	No. of deliverables	No. passed spin test	No. assembled on shaft
CBO	15	30	2	1
GTE	15	20	0	N/A
N/TRW	20	5	4	1
GCC	20	20	1	0
Kyocera	15	13	13	4
Kyocera	20	9	9	5

Setup photograph

Burst photograph

TE91-2012

Figure 54. GCC GN-10 rotor (S/N 126) burst, N_1 = 78,800 rpm.

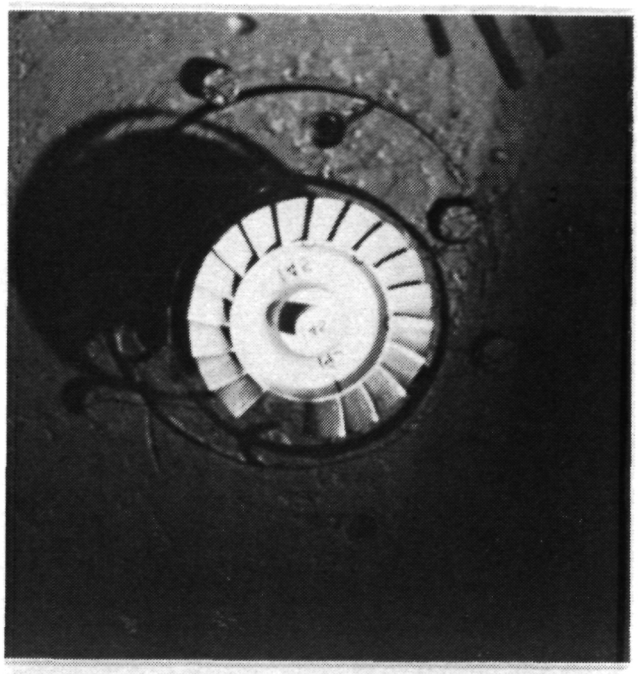

Setup photograph

Burst photograph

TE91-2013

Figure 55. GCC GN-10 rotor (S/N 145) burst, N_1 = 21,500 rpm.

ORIGINAL PAGE
BLACK AND WHITE PHOTOGRAPH

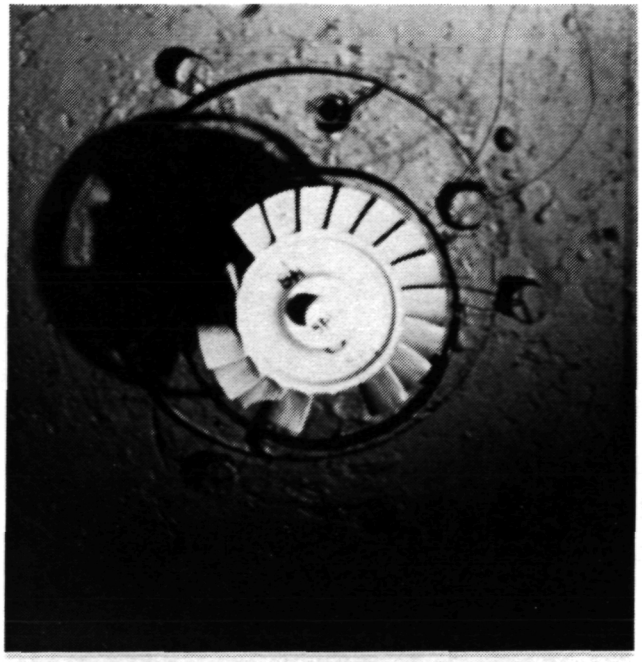

Setup photograph

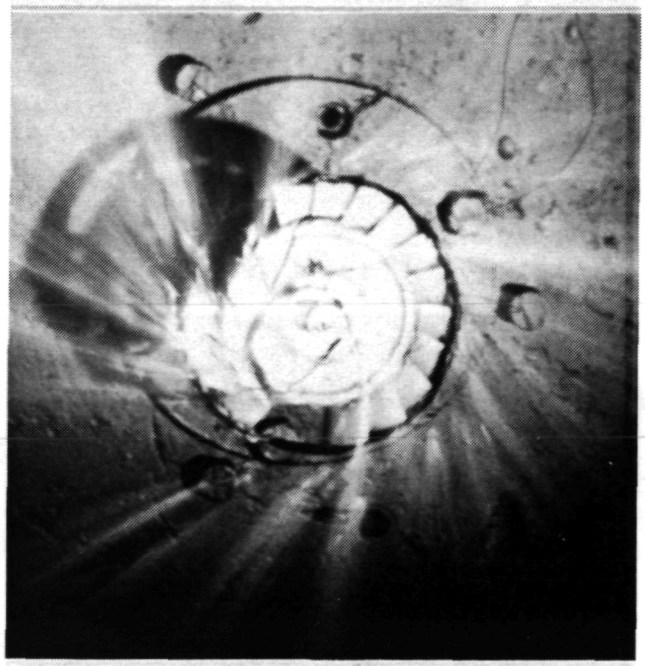

Burst photograph

TE91-2014

Figure 56. GCC GN-10 rotor (S/N 148) burst, N_1 = 65,300 rpm.

Setup photograph

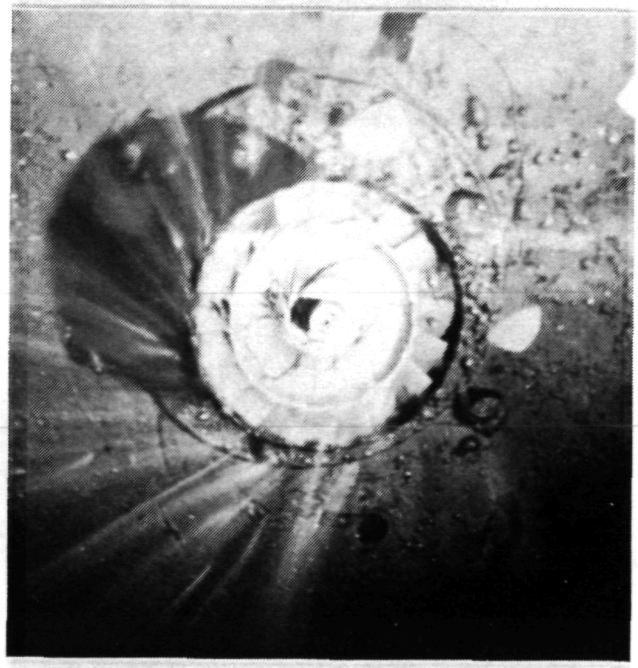

Burst photograph

TE91-2015

Figure 57. GCC GN-10 rotor (S/N 189) burst, N_1 = 79,500 rpm.

ORIGINAL PAGE
BLACK AND WHITE PHOTOGRAPH

Setup photograph

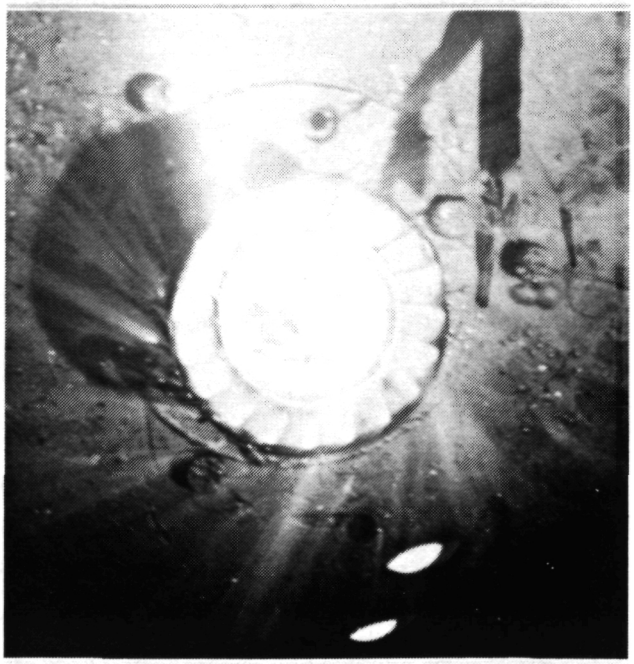

Burst photograph

TE91-2016

Figure 58. GCC GN-10 rotor (S/N 191) burst, N_1 = 75,600 rpm.

Setup photograph

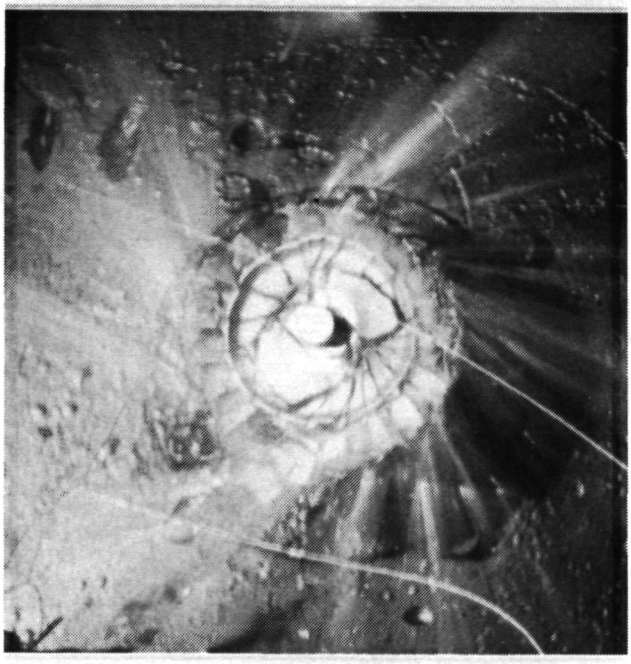

Burst photograph

TE91-2017

Figure 59. GCC GN-10 rotor (S/N 149) burst, N_1 = 67,900 rpm.

ORIGINAL PAGE
BLACK AND WHITE PHOTOGRAPH

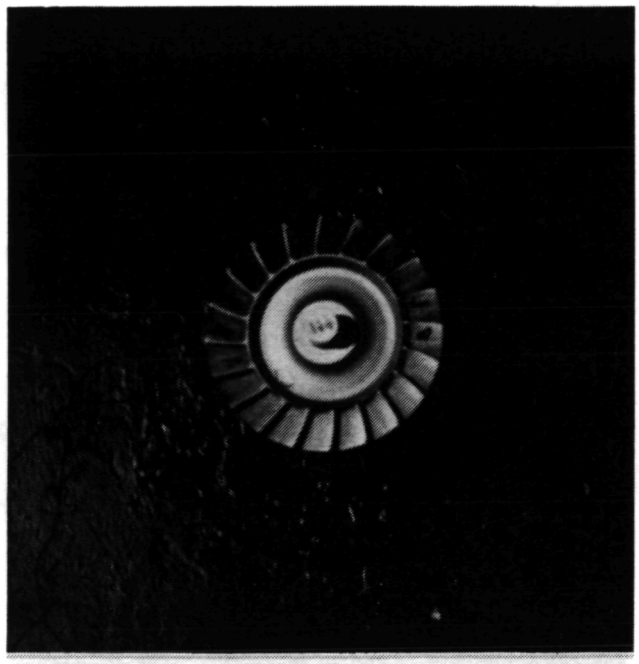

Setup photograph

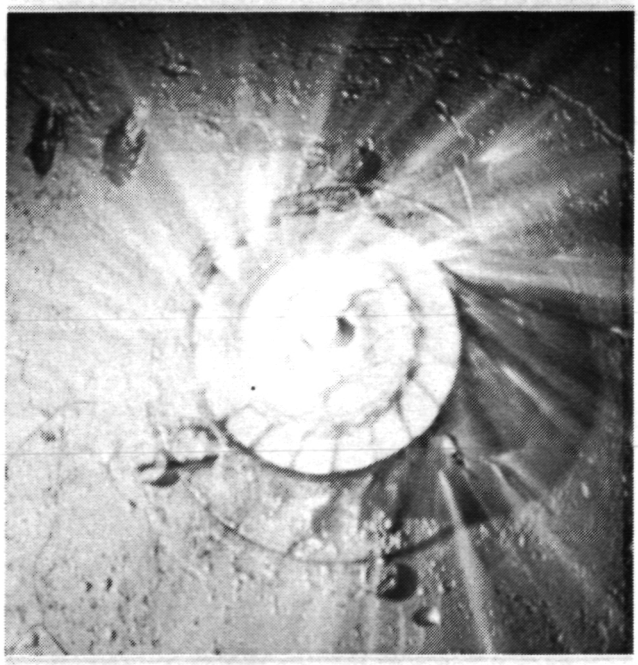

Burst photograph

TE91-2018

Figure 60. GCC GN-10 rotor (S/N 199) burst, N_1 = 78,700 rpm.

2.1.4 Regenerator

Objective/Approach

This activity is focused on the design and analysis of a ceramic regenerator disk matrix that can be extruded initially in segments suitable for cemented modular disks, and perhaps ultimately as one-piece disks. Final matrix geometry will be optimized for cost and manufacturing concerns, as well as for engine performance and fuel economy.

Accomplishments/Results

- 36 different combinations of regenerator matrix wall thickness and cell density were examined. Peak power at 2500°F TIT and lowest BSFC at 25 hp were calculated for each combination. Based solely on a performance/fuel economy trade-off, excluding cost and manufacturing concerns, the following matrix geometries are recommended for a 2 to 1 rectangular cell:

Wall thickness-- mm (in)	Cell Density-- cells/cm^2 (cells/in^2)
0.076 (0.003)	217 (1400)
0.102 (0.004)	202 (1300)
0.127 (0.005)	186 (1200)
0.152 (0.006)	171 (1100)

Discussion

The AGT-5 engine performance was examined for a variety of extruded regenerator core configurations. Earlier studies indicated that a 2 to 1 cell was a good compromise for optimizing heat transfer and cell strength, therefore, each configuration evaluated had a cell aspect ratio of 2 to 1. The cell wall thickness was varied from 0.076 to 0.152 mm (0.003 to 0.006 in.) and the cell density was varied from 62 to 217 cells per square cm (400 to 1400 cells per square inch).

The engine performance was calculated at two operating points: (1) maximum power at 2500°F TIT and (2) lowest brake specific fuel consumption (BSFC) at 19kW (25 hp). Past engine and vehicle studies have indicated that percentage changes in BSFC at the steady-state highway cruise point correlate well with percentage changes in miles per gallon (mpg) for the entire

ORIGINAL PAGE
BLACK AND WHITE PHOTOGRAPH

EPA driving cycle. For a larger passenger car with the AGT-5 engine, this steady-state power requirement is 19kW (25 hp). Percentage changes in peak power correlated with percentage changes in 0 to 97 km/hr (0 to 60 mph) times. To examine vehicle fuel economy versus performance for different cell configurations, the percentage changes in BSFC are plotted against percentage changes in peak power (Figure 61).

A 2 to 1 trade-off of performance for fuel economy might be a logical choice for the AGT-5 in a vehicular application. This implies that a 2% gain in power should be accomplished with only a 1% decrease in fuel economy. This 2 to 1 slope and a line connecting this slope for each wall thickness curve is indicated on Figure 61. The recommended cell density for each wall thickness is as previously listed above.

This selection does not account for pricing or manufacturing input from the vendor. It has been speculated that the price of the core would decrease as the number of cells per square inch is decreased. It should be noted that as the number of cells is decreased, the effectiveness drops and the exhaust temperature increases. A hotter exhaust temperature could eliminate potential cold side wearface material candidates being evaluated.

2.1.5 Power Turbine

Objective/Approach

The AGT-5 test-bed engine, operating at the elevated temperatures associated with the ATTAP program, requires a power turbine capable of delivering increased power while operating at increased rotor speed and inlet gas temperature (versus original 1038°C [1900°F] engine parameters). The objective of this activity is the design and analysis of power turbine structural ceramic components (both rotating and static) which meet performance, material behavior, dimensional criteria, and durability requirements necessary to allow operation of the ceramic gasifier components in the test-bed engine at RPD operating conditions. The resulting power turbine design is a hybrid of metal and ceramic components; the metal components necessary to support the ceramic structures were also designed and analyzed under this task, because extensive system analyses were executed in which all components and their interactive effects were considered. The power turbine design was examined at maximum power steady-state and worst case transient conditions to determine the ceramic components' survivabilities.

Accomplishments/Results

- 2-D axisymmetric finite element stress and probability of survival analyses for first and second stage ceramic power turbine rotors at maximum power steady-state and during the cold start-up transient (baseline transient) were completed using updated temperature data.
- Both power turbine rotors were analyzed using alternate ceramic materials.
- The first four natural frequencies of the first stage ceramic power turbine rotor airfoils were calculated using 3-D FEM analyses.
- The first two natural frequencies of the first stage ceramic power turbine rotor airfoils were determined experimentally.
- Due to the excellent correlation between the calculated and experimentally obtained airfoil frequencies, the ceramic first stage power turbine rotors will be submitted for shaft attachment and final balance in preparation for engine test.
- Both first and second stage ceramic power turbine rotors meet design goal probability of survival during simulated engine operation.
- Completed 2-D axisymmetric finite element thermal and stress analyses of the metal power turbine static structure utilizing a modified or alternate "test stand" transient. The previously proposed "test stand" cold start-to-max power transient was modified by increasing the idle hold to 300 seconds while retaining the baseline idle-to-max power snap.
- Power turbine metal component transient stresses are driven primarily by the idle-to-maximum power acceleration as opposed to the length of time spent at idle.

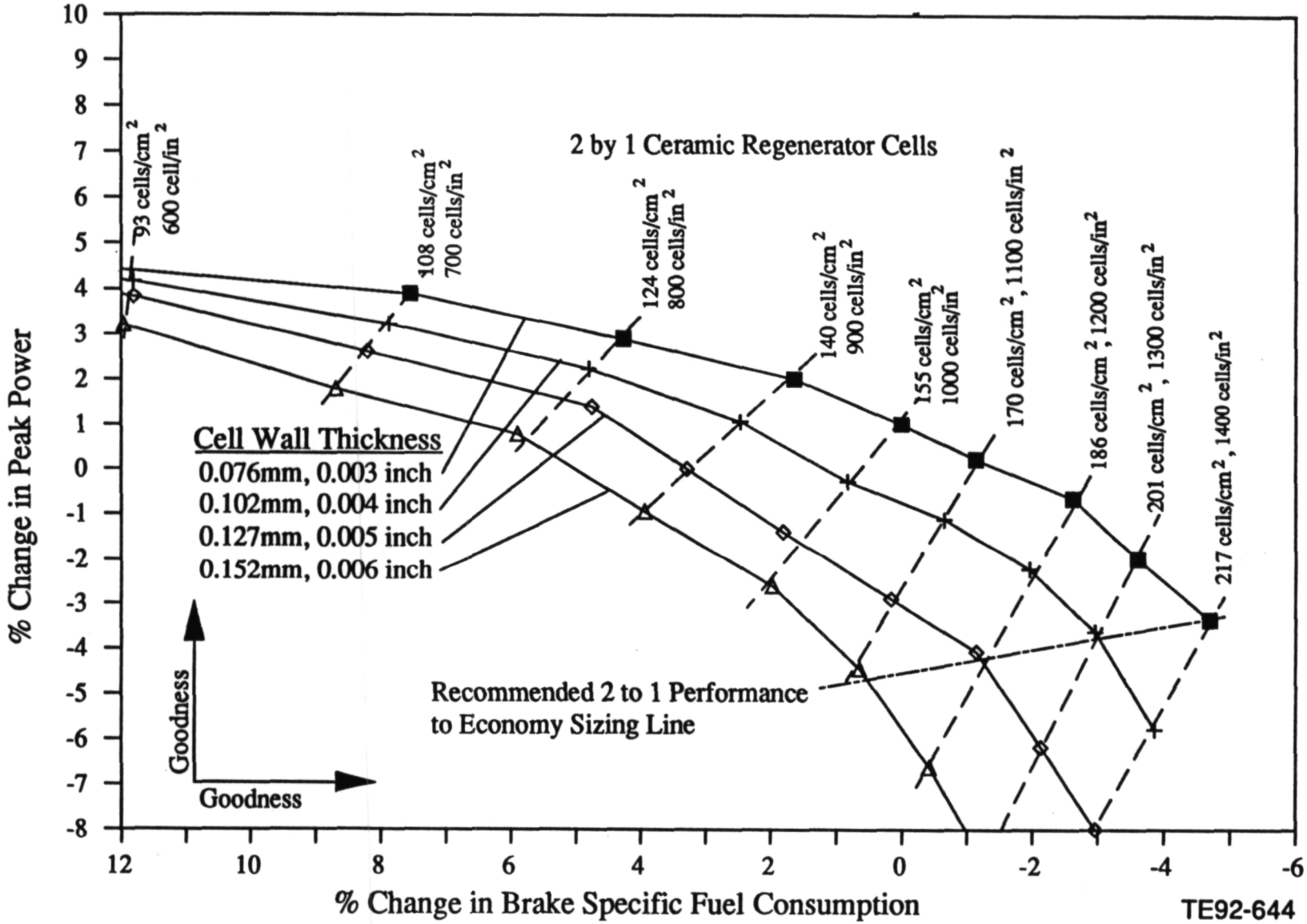

Figure 61. Ceramic regenerator matrix sizing study for recommended 2 to 1 performance to fuel economy trade-off ratio.

- Material yield strength is exceeded locally in the power turbine metal static structure during the engine cold start-up transient. It is recommended that the previous test stand cold start-up transient schedule be utilized during initial engine testing.
- 2-D axisymmetric finite element thermal, stress, and probability of survival analyses of the power turbine ceramic first stage vane configuration at maximum power steady-state and during the cold start-up transient (baseline transient) were completed.
- The ceramic first stage vane probability of survival meets design goals at both steady-state maximum power and throughout the cold start-up transient (baseline acceleration).
- Cold start-up transient metal component stresses for the ceramic vane configuration locally exceed material yield strengths.

Discussion

Rotors. All of the finite element analyses completed to date have been 2-D for the power turbine rotor assembly (Figure 62). Updated temperature data for all of the ceramic and metallic components in the assembly have been obtained via modifications to the analytical model (updated geometry, recalculated leakage flows, etc) to ensure accurate correlation between the mathematical model and the actual engine conditions.

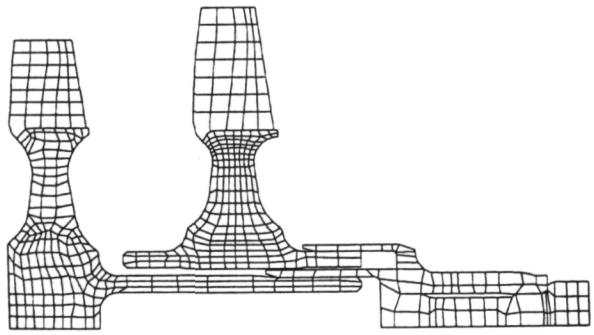

Figure 62. FEM model of ceramic power turbine rotor assembly.

The first-stage power turbine rotor was analyzed as being fabricated using Kyocera's SN252 silicon nitride. The temperature gradients in the ceramic rotor during both steady-state and transient start-up conditions showed consistent trends between the original and updated temperatures. The steady-state temperature profile (Figure 63) displays the effect of the long ceramic shaft as essentially a heat-dam, which creates steep temperature gradients at the base of the shaft. A maximum principal stress of 191 MPa (27.7 ksi) was calculated for the first-stage rotor during steady-state operation with the corresponding POS of 0.9996. The temperature profile for the lowest POS during the start-up transient is shown in Figure 64, and it occurs 36 seconds after a cold start. In this case, temperature gradients are higher in the web region of the rotor than in the base of the shaft. The maximum principal stress produced by these temperatures is 280 MPa (40.6 ksi). The POS is 0.9918, which is greater than the calculated goal for operation of 0.9853.

The second-stage ceramic power turbine rotor was modeled using Kyocera's SN235 silicon nitride material. During max power steady-state operation, a steep thermal gradient exists on the aft side of the rotor where the shaft blends into the rotor hub (Figure 65). This thermal gradient results in a maximum principal stress of 296 MPa (42.9 ksi) in that region of the rotor. A large tangential stress of over 276 MPa (40 ksi) exists in the bore of the rotor. The POS of the rotor during max power steady-state operation is 0.9972.

In the transient operating condition, at a time of 50 seconds after start-up, the highest maximum principal stress occurs in the second-stage power turbine rotor. Temperature and maximum principal stress in the rotor at 50 seconds are shown in Figure 66. In the transient condition, a larger thermal gradient (than at steady-state max power) exists in the web of the rotor and the point of the largest maximum principal stress, 335 MPa (48.6 ksi), is in the bore region of the rotor. The POS of the second-stage rotor is 0.9985 at 50 seconds after start up.

Both stages of the power turbine were examined using alternate ceramic materials. Table XX displays the analytical results for steady-state and transient conditions. POS values for both

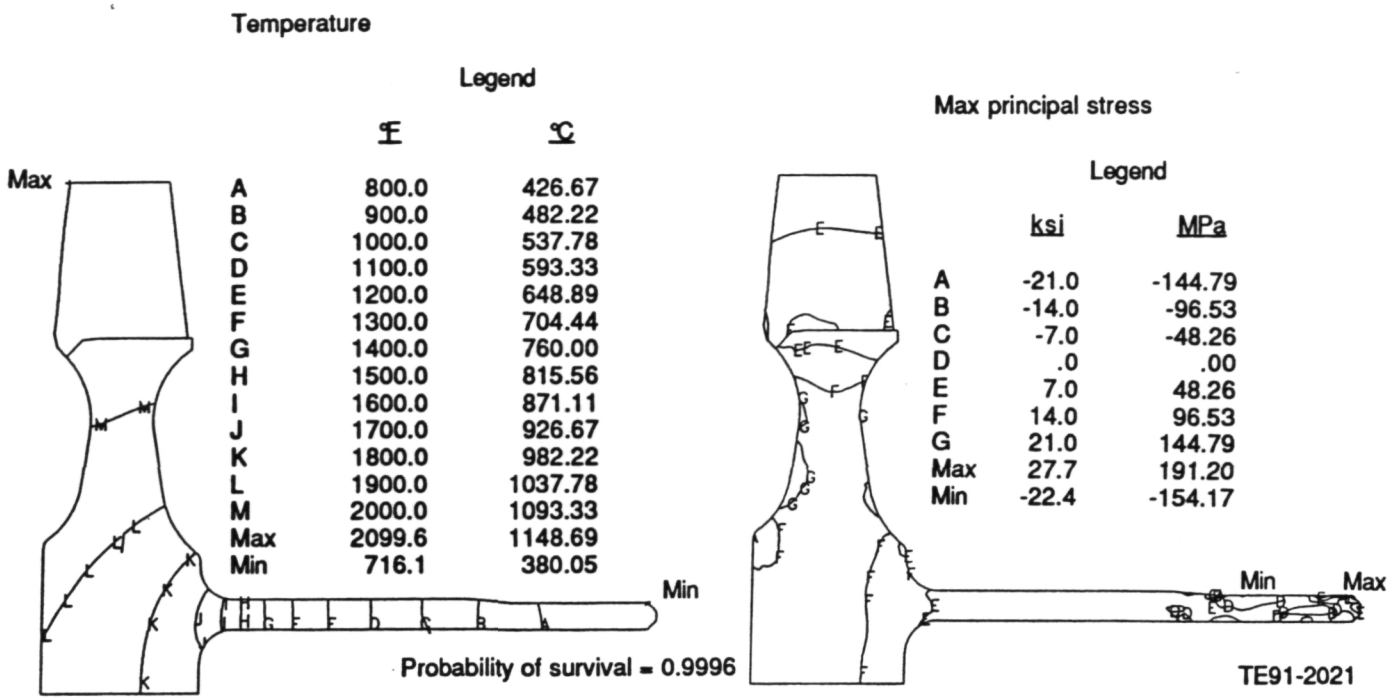

Figure 63. First-stage power turbine rotor temperature and stress distributions - SN252, steady-state.

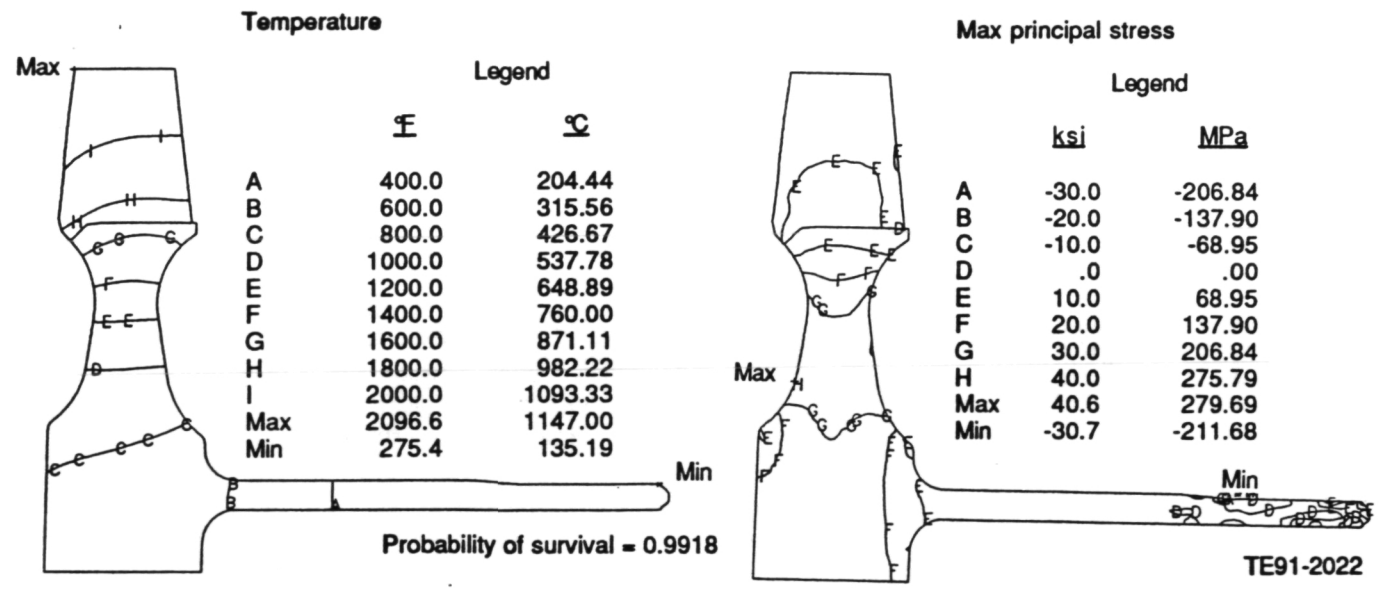

Figure 64. First-stage power turbine rotor temperature and stress distributions - SN252, transient, 36 seconds after start-up.

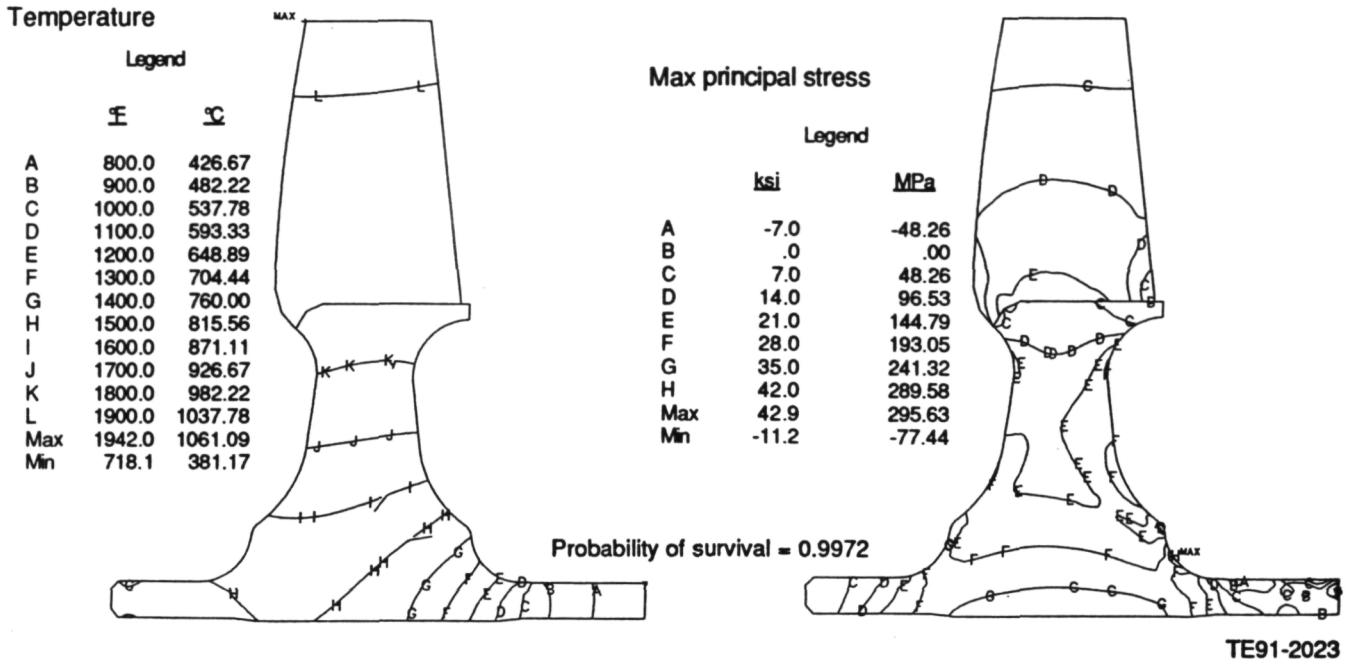

Figure 65. Second-stage power turbine rotor temperature and stress distributions - SN235, steady-state.

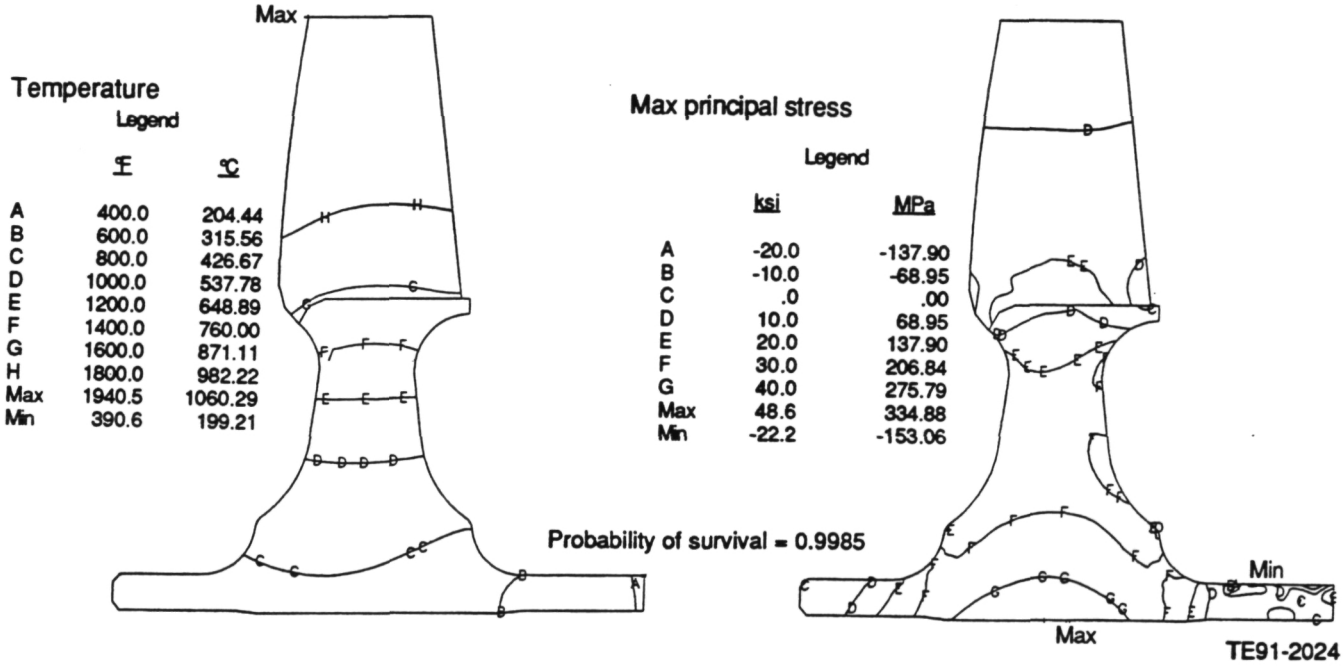

Figure 66. Second-stage power turbine rotor temperature and stress distributions - SN235, transient, 50 seconds after start-up.

Table XX.
Ceramic PT rotor analysis results.

	First stage		Second stage		
Material	SN252	EC-152	SN220M	EC-152	SN235
steady-state					
maximum temperature–°C (°F)	1149 (2100)	1138 (2080)	1050 (1922)	1050 (1922)	1061 (1942)
minimum temperature–°C (°F)	380 (716)	415 (779)	402 (757)	435 (815)	381 (718)
maximum principal stress–MPa (ksi)	191 (27.7)	118 (27.3)	313 (45.4)	302 (43.8)	296 (42.9)
radial expansion–mm (in.)	0.213 (0.0084)	0.221 (0.0087)	0.221 (0.0087)	0.218 (0.0086)	0.229 (0.0090)
POS	0.9996	1.000	0.9742	0.9982	0.9972
start-up transient					
time of P_{max} (sec)	36	30	30	30	50
maximum temperature–°C (°F)	1147 (2097)	1133 (2072)	1048 (1918)	1048 (1918)	1060 (1941)
minimum temperature–°C (°F)	135 (275)	129 (265)	146 (295)	156 (313)	199 (391)
maximum principal stress–MPa (ksi)	280 (40.6)	280 (40.6)	341 (49.4)	336 (48.7)	335 (48.6)
radial expansion–mm (in.)	0.145 (0.0057)	0.152 (0.0060)	0.152 (0.0060)	0.160 (0.0063)	0.168 (0.0066)
POS	0.9918	0.9992	0.9691	0.9969	0.9985
POS goal	0.9853			0.9862	

the first- and second-stage rotors fabricated from NGK Spark Plug's EC-152 exceed design goal. The surface strength properties for the EC-152 material at elevated temperatures of 538°C (1000°F) are approximately 20% higher than those of Kyocera's SN235 silicon nitride at the same temperature. This explains the higher POS for the EC-152 rotors in nearly all cases because the rotor POS is more sensitive to surface stresses than volume stresses in the analyzed rotors. The second-stage rotor has also been modeled with Kyocera's SN220M material. The resultant POS's for this material are slightly lower than goal for steady-state and transient conditions.

A 3-D FEM model was used to analytically calculate the first four natural frequencies of the first stage power turbine rotor airfoil. The calculated frequencies are:

- ω_1 - 11,940 Hz
- ω_2 - 24,990 Hz
- ω_3 - 40,440 Hz
- ω_4 - 50,880 Hz

The model assumed that the blade was grounded at the rotor rim and that the rotor was fabricated of Kyocera's SN252 Si_3N_4.

The frequencies for the airfoils were experimentally determined by using an air siren as the source of excitation. The frequencies had to be measured at very small displacements to keep from fracturing the ceramic airfoils. Limitations of the air siren prevented the acquisition of frequencies above 36 kHz. Thus the third and fourth vibratory modes of the airfoils could not be excited. All 28 blades of the power turbine rotor were tested in order to

observe any scatter in frequencies between airfoils. Table XXI shows the summary of the data collected. There was excellent correlation between the calculated frequencies and the experimentally collected data. Figures 67 and 68 display the normal probability plots for Mode 1 and Mode 2, respectively.

The power turbine rotor that was used for testing had not completed final machining of the forward and aft faces of the wheel hub. Due to the thinness of the airfoils and the extremely close correlation between the analytical and experimental natural frequencies, the unfinished rotor hub did not influence the results.

Static Structure. 2-D axisymmetric finite element thermal and structural analyses of the power turbine assembly (metal nozzles, ceramic shrouds, and ceramic rotors) were previously performed for the baseline cold start-up transient. Stresses and POS values for the ceramic components were within design limits; however, transient stresses for the NX-188 static

Table XXI.
First stage power turbine rotor frequency summary.

Mode	No. of blades tested	Measured frequency –(Hz) Mean	Measured frequency –(Hz) Coefficient of Variable-- (% scatter)	Calculated frequency-- (Hz)	% Dev. (calculated-measured)/ measured
1	28	11,927.3	0.95	11,940.0	0.11
2	28	25,192.0	0.84	24,990.0	-0.08

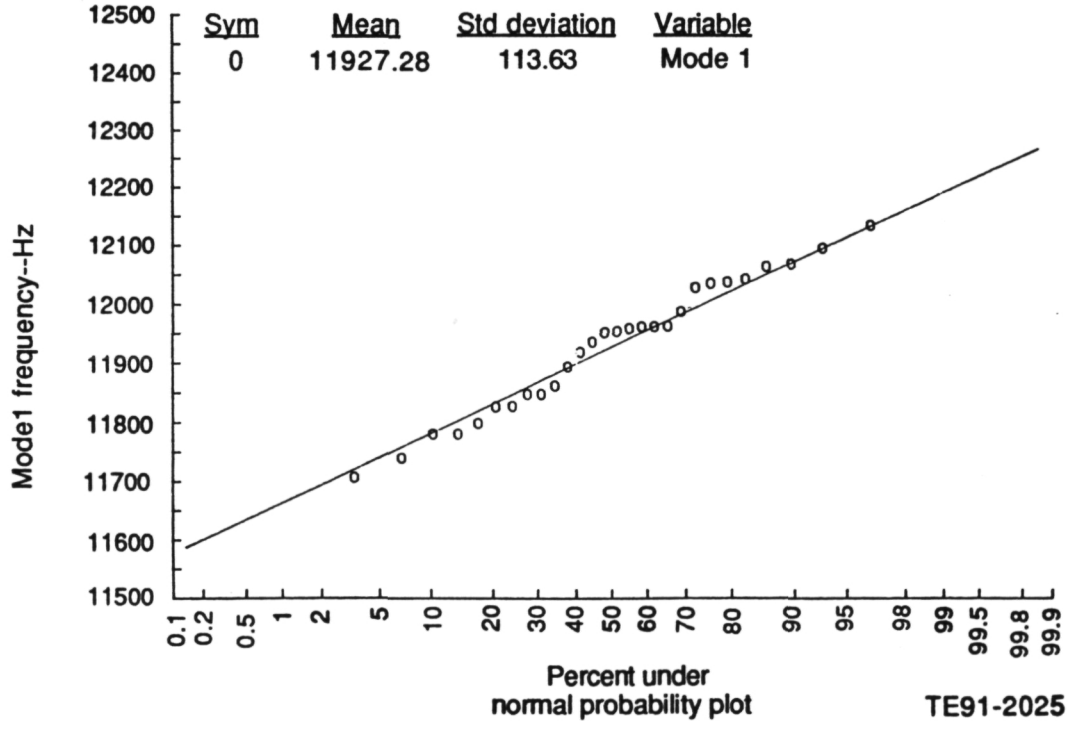

Figure 67. Normal probability plot of Mode 1 frequency for AGT-5 first stage ceramic power turbine rotor airfoils.

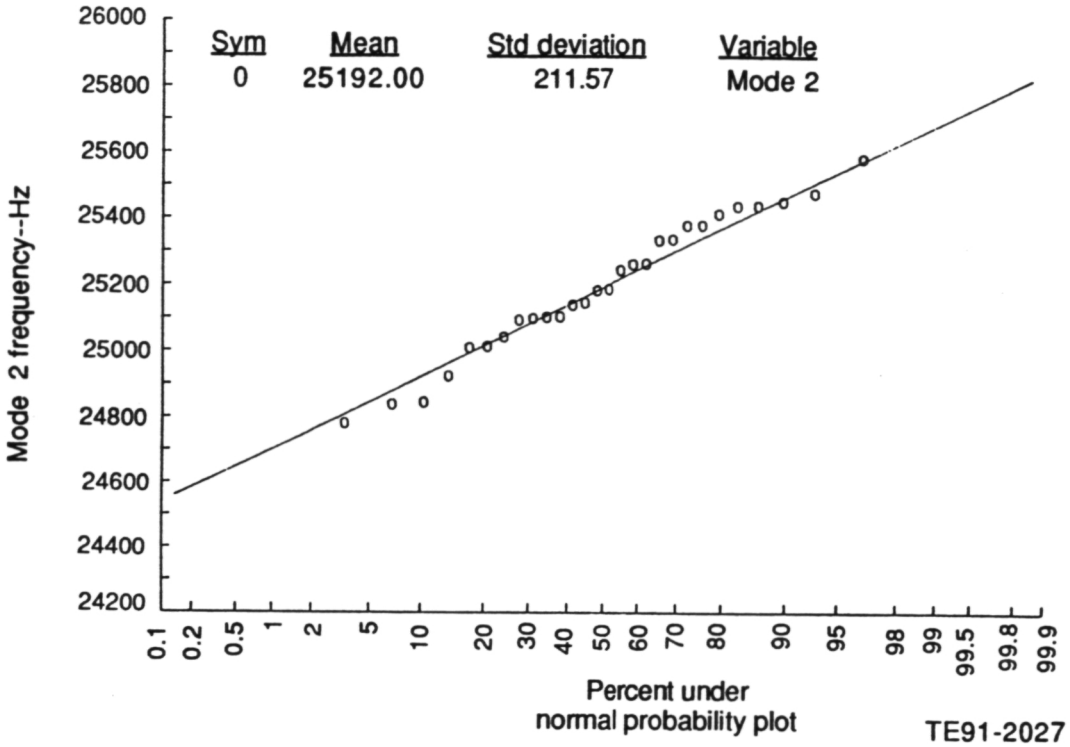

Figure 68. Normal probability plot of Mode 2 frequency for AGT-5 first stage ceramic power turbine rotor airfoils.

components exceeded material capabilities. In order to reduce the thermal stresses, a test stand transient was defined. The test stand transient softened the cold start-up acceleration by increasing the hold at idle to 30 seconds and the idle-to-maximum power snap to 30 seconds. Acceptable ceramic component stresses, POS values, and metal component stresses were predicted for the proposed transient. In an attempt to avoid running a moderated cyclic durability schedule, an alternate test stand transient was investigated. The alternate transient increases the hold at idle to 300 seconds while returning to the baseline idle-to-maximum power snap. Transient temperatures and deflections were generated for the alternate test stand transient using existing 2-D axisymmetric finite element models of the power turbine assembly as shown in Figure 69 and Figure 70. Component transient temperatures and stress predictions at the 340 second time point are illustrated in Figure 71 through Figure 78. POS values for the SN252 Si_3N_4 shrouds were 1.0000 throughout the alternate test stand transient. Figure 79 illustrates metal component maximum equivalent stress normalized by material yield strength during the alternate test stand transient. Based upon material yield strengths, these results indicate that the power turbine static metal component stresses are unacceptable for the alternate test stand transient. Results point out that the driving force behind the high metal component transient stresses is the idle-to-maximum power acceleration as opposed to the length of the idle hold.

Restricting the engine acceleration rate, as in the original test stand transient, is perceived as a short term solution for reducing power turbine metal component stresses. A long term solution entails a redesign of the power turbine static structure and incorporation of a ceramic first-stage vane. The proposed ceramic vane design, shown in Figure 80, is monolithic Si_3N_4 incorporating integral hub and tip platforms which extend to form the interstage turbine duct. The integral tip platform is crosskeyed at the trailing edge using a mount pin common with the

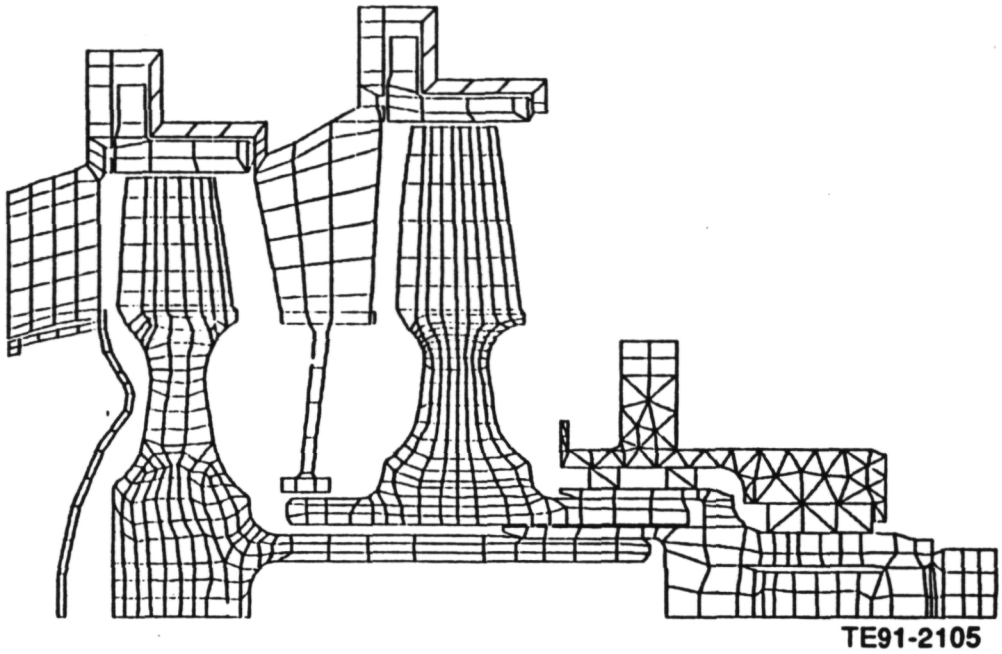

Figure 69. Power turbine FEM heat transfer model.

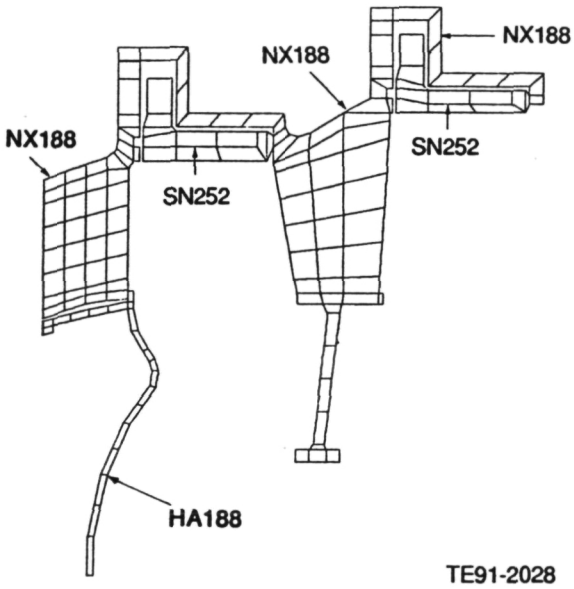

Figure 70. Power turbine FEM stress model.

first stage power turbine rotor shroud. A compliant cushion positions the vane axially against the aft turbine case at assembly. Airloads add an additional seating force to the vane/case interface during engine operation. Additional features of the ceramic vane design are listed in the following:

- The forward turbine case is shielded from the gas path
- The vane is sealable at the inner and outer diameters
- The proposed design fits into the existing vane envelope with only minimal rework to the turbine case
- The design utilizes the existing 20-airfoil geometry

The ceramic vane configuration was analyzed using the 2-D axisymmetric finite element model shown in Figure 81. The analysis utilized SN252 Si_3N_4 as the ceramic vane material. Temperatures, stresses, and ceramic component probabilities of survival were generated for maximum power steady-state and the cold start-up baseline transient. Component temperatures and stresses at the minimum POS time point of 15 seconds are illustrated in Figures 82 through 88. These figures reveal large component thermal gradients and

elevated stresses, characteristics of a rapid acceleration. Transient probabilities of survival for the ceramic vane and rotor shroud are presented in Figure 89. 2-D results indicate that the ceramic first-stage vane minimum POS of 0.99597 exceeds the design goal of 0.9877. The ceramic first stage rotor shroud maintained a POS of 1.0000 throughout the transient and at steady-state. Transient and steady-state stresses for the redesigned forward metal power turbine case were reduced to acceptable levels; however, local thermal stresses in the Ha-230 centerbody and NX-188 aft power turbine case exceed material yield strengths during the cold start-up transient.

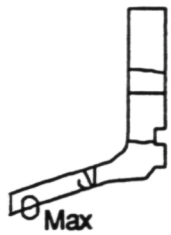

Legend

	°F	°C
A	200.0	93.33
B	400.0	204.44
C	600.0	315.56
D	800.0	426.67
E	1000.0	537.78
F	1200.0	648.89
G	1400.0	760.00
H	1600.0	871.11
I	1800.0	982.22
J	2000.0	1093.33
Max	2063.0	1128.33
Min	161.6	72.00

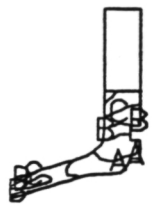

Legend

	ksi	MPa
A	10.0	68.95
B	20.0	137.90
C	30.0	206.84
D	40.0	275.79
E	50.0	344.74
F	60.0	413.69
G	70.0	482.63
Max	73.5	506.56
Min	0.0	0.30

TE91-2029

Figure 71. Transient temperature and stress distribution results at 340 seconds--power turbine first-stage vane shroud.

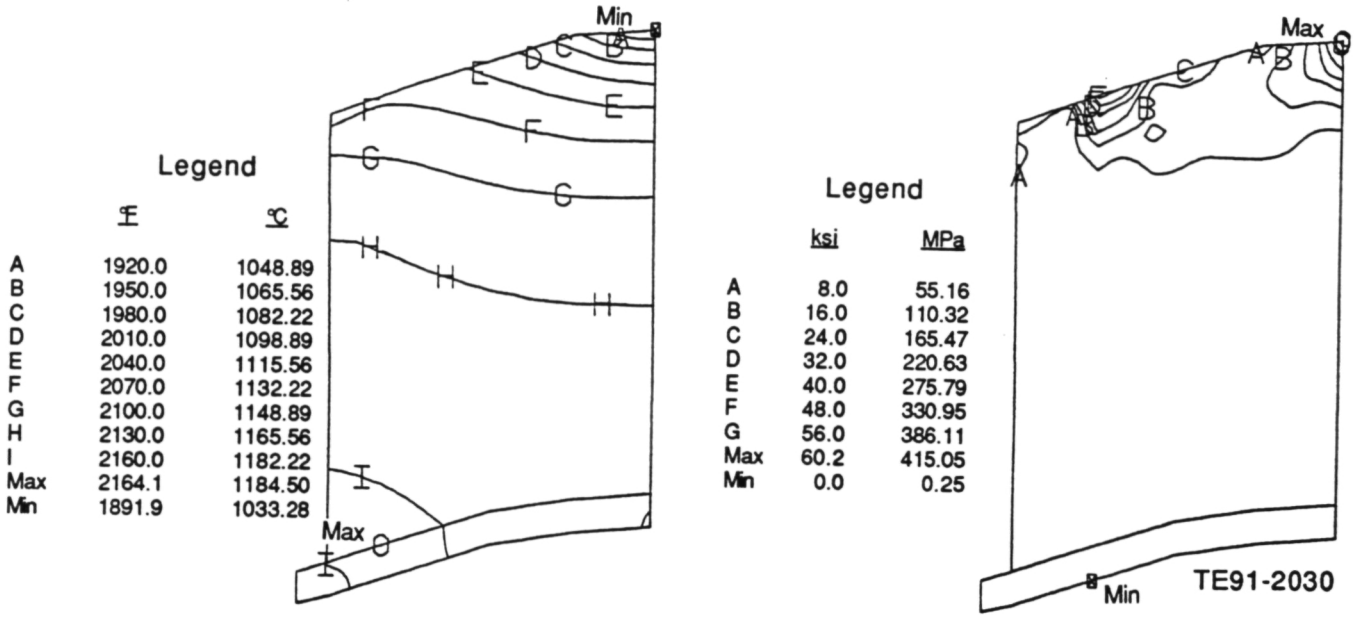

Figure 72. Transient temperature and stress distribution results at 340 seconds--power turbine first-stage vane.

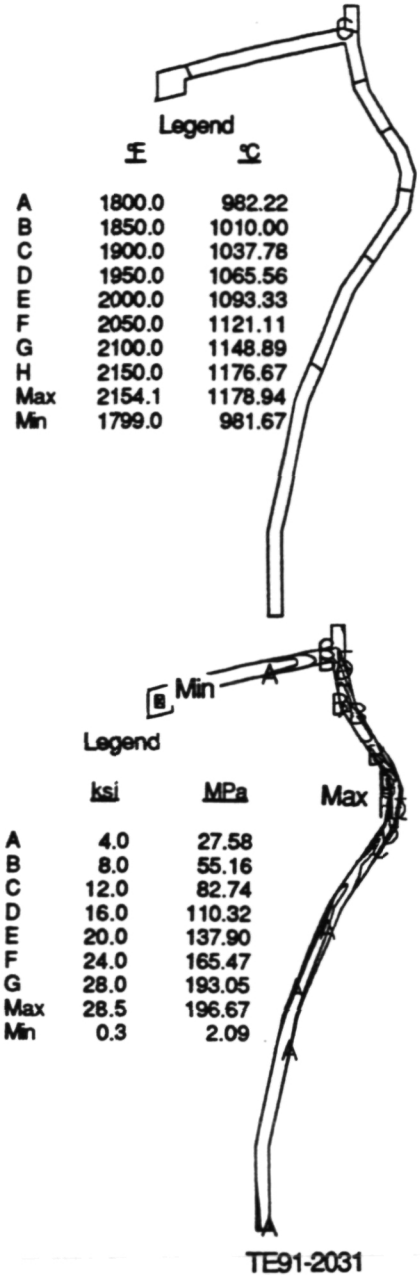

Figure 73. Transient temperature and stress distribution results at 340 seconds--power turbine first-stage vane hub.

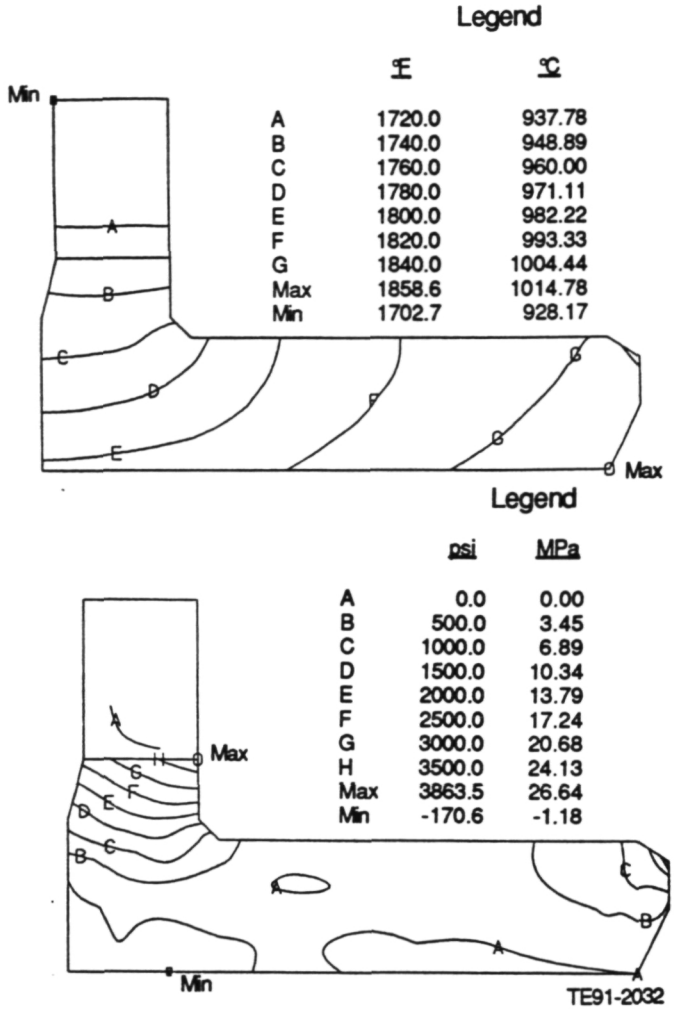

Figure 74. Transient temperature and stress distribution results at 340 seconds--power turbine first-stage rotor shroud.

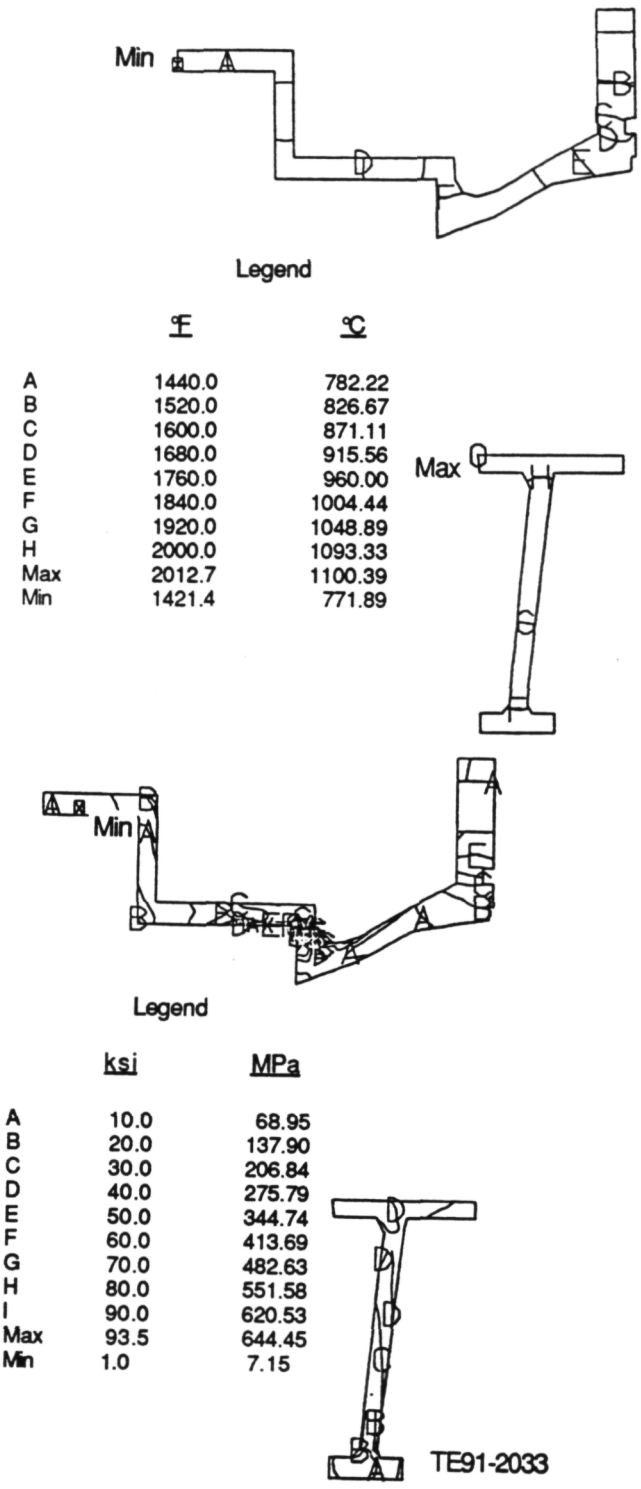

Figure 75. Transient temperature and stress distribution results at 340 seconds--power turbine second-stage vane support.

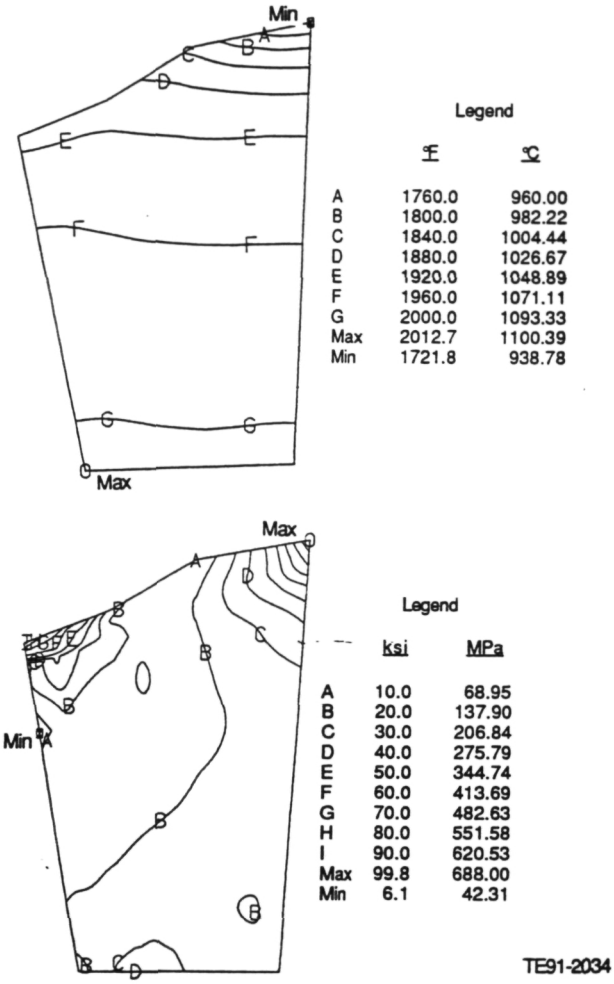

Figure 76. Transient temperature and stress distribution results at 340 seconds--power turbine second-stage vane.

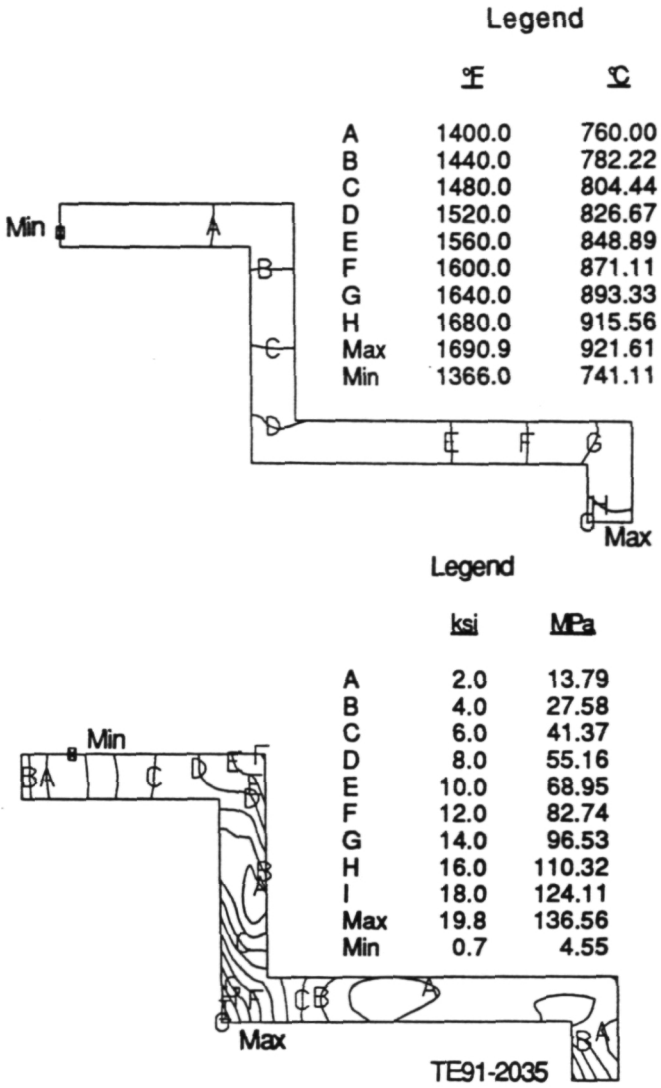

Figure 77. Transient temperature and stress distribution results at 340 seconds--power turbine second-stage shroud clamp.

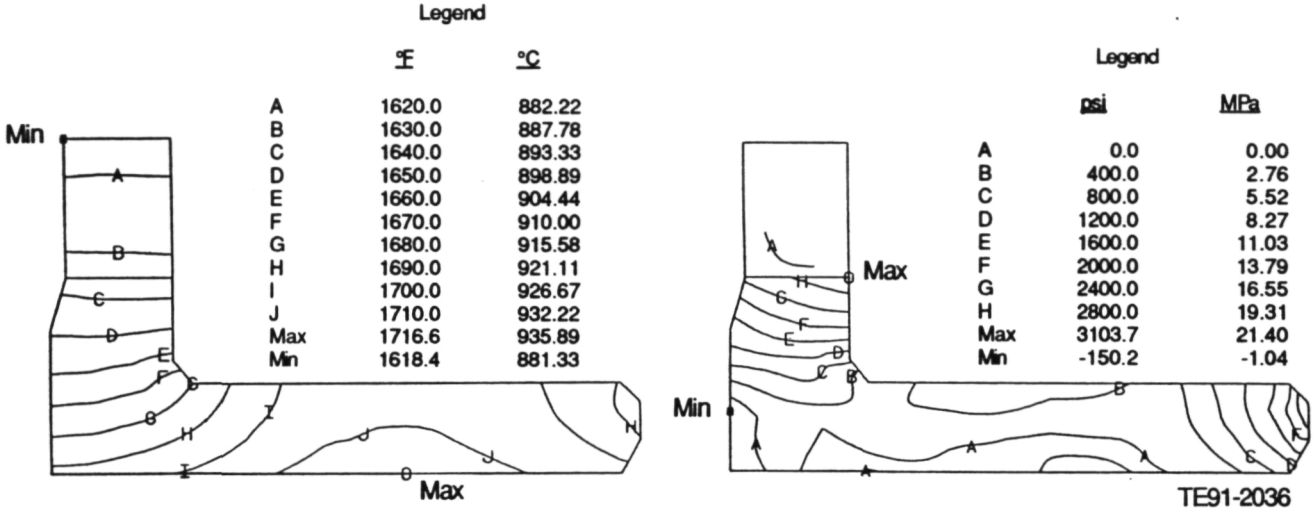

Figure 78. Transient temperature and stress distribution results at 340 seconds--power turbine second-stage rotor shroud.

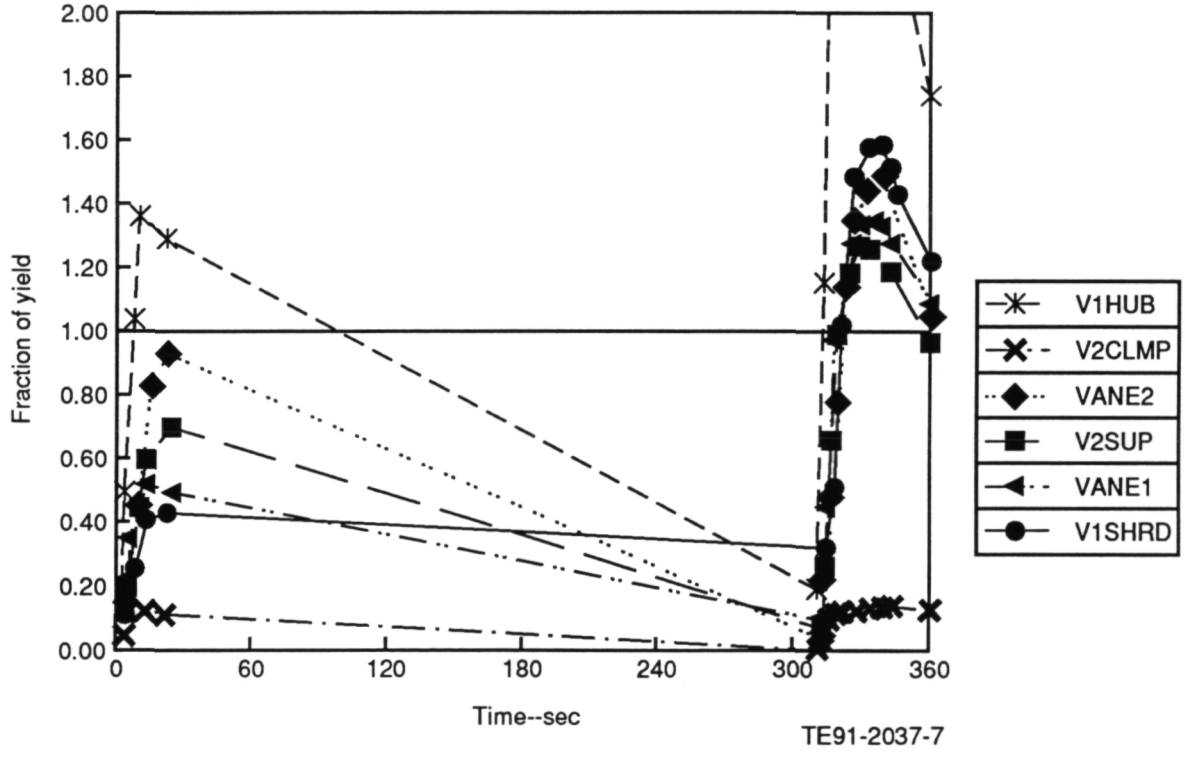

Figure 79. Power turbine metal static component normalized transient stresses: normalized by yield strength for alternate test stand transient.

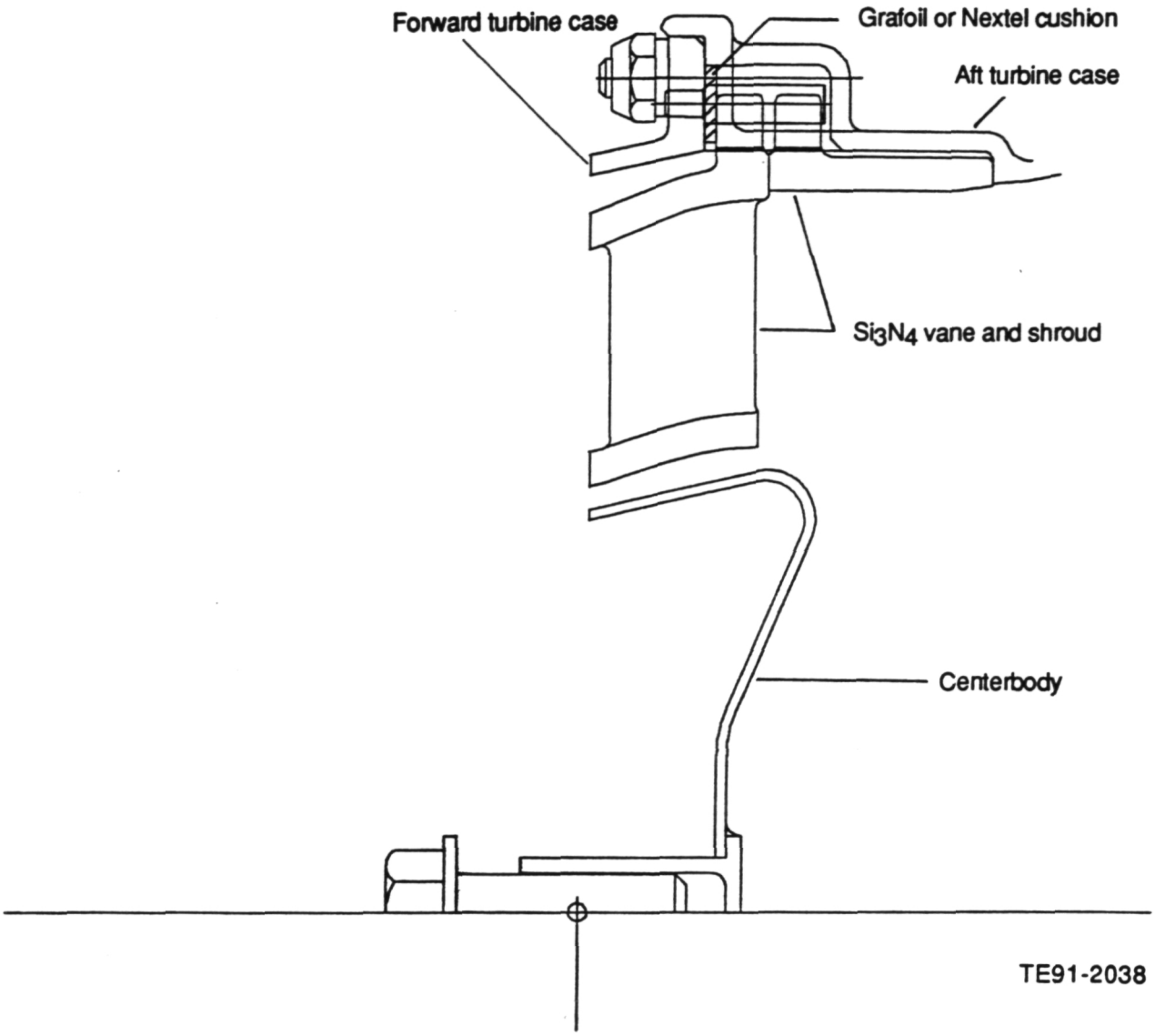

Figure 80. Ceramic first-stage power turbine vane configuration.

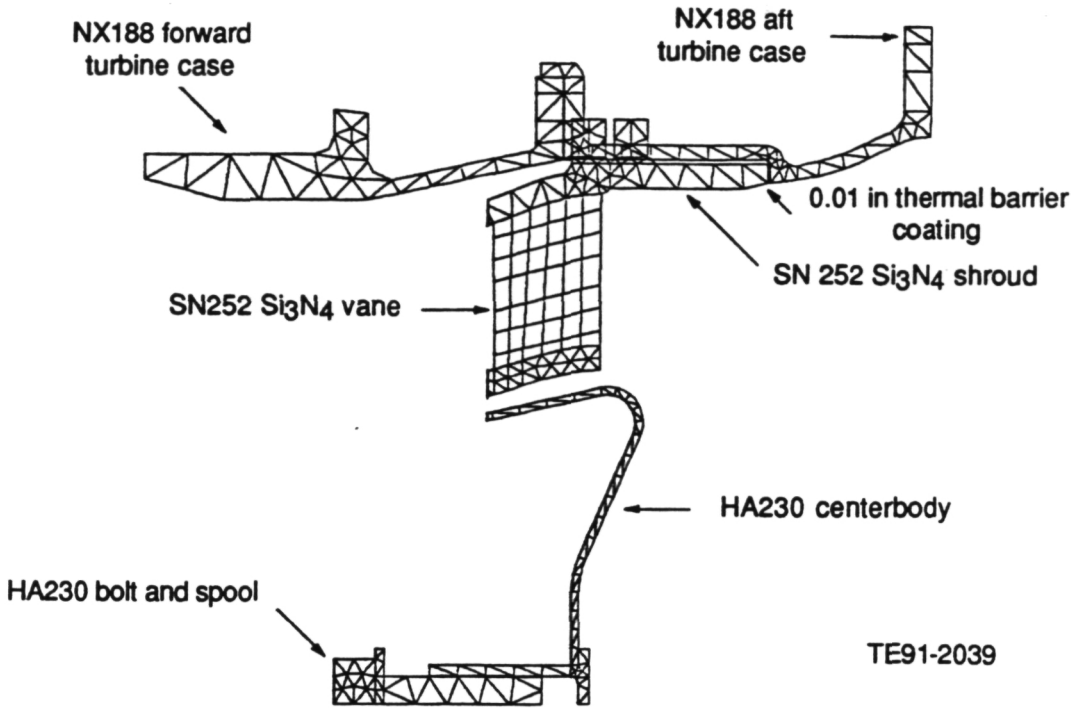

Figure 81. FEM model of ceramic first-stage power turbine vane assembly.

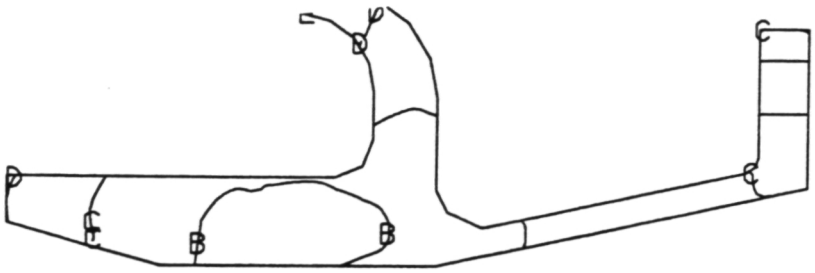

Legend

	°F	°C
A	100.0	37.78
B	120.0	48.89
C	140.0	60.00
D	160.0	71.11
E	180.0	82.22
F	200.0	93.33
G	220.0	104.44
Max	235.8	113.22
Min	93.9	34.39

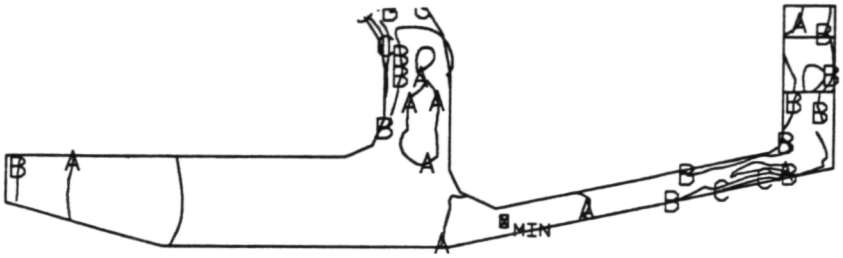

Legend

	ksi	MPa
A	2.0	13.79
B	4.0	27.58
C	6.0	41.37
D	8.0	55.16
E	10.0	68.95
F	12.0	82.74
G	14.0	96.53
Max	14.8	101.94
Min	0.3	1.74

TE91-2040

Figure 82. Temperature and equivalent stress distributions for forward PT case at 15 second transient.

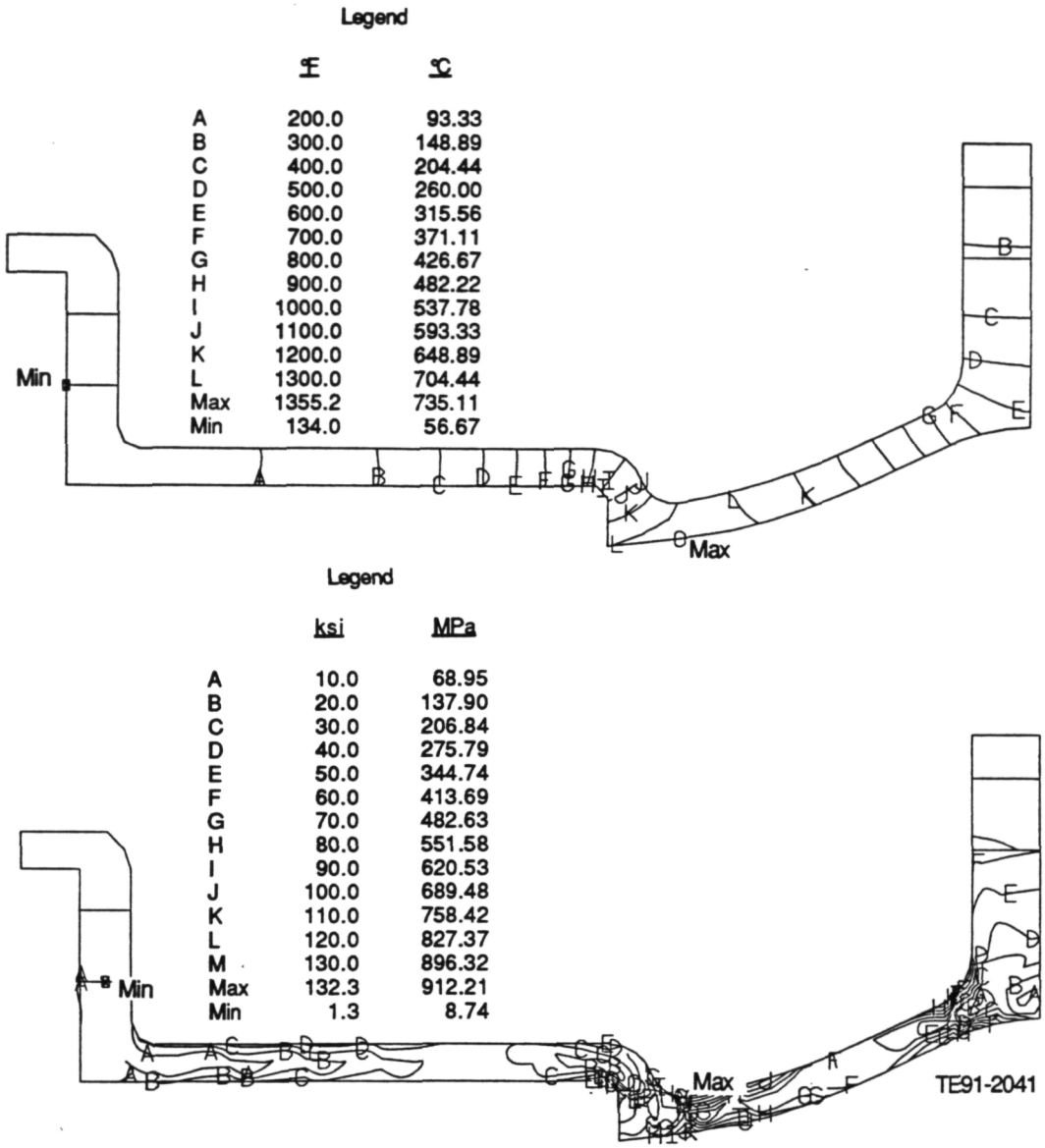

Figure 83. Temperature and equivalent stress distributions for aft PT case at 15 second transient.

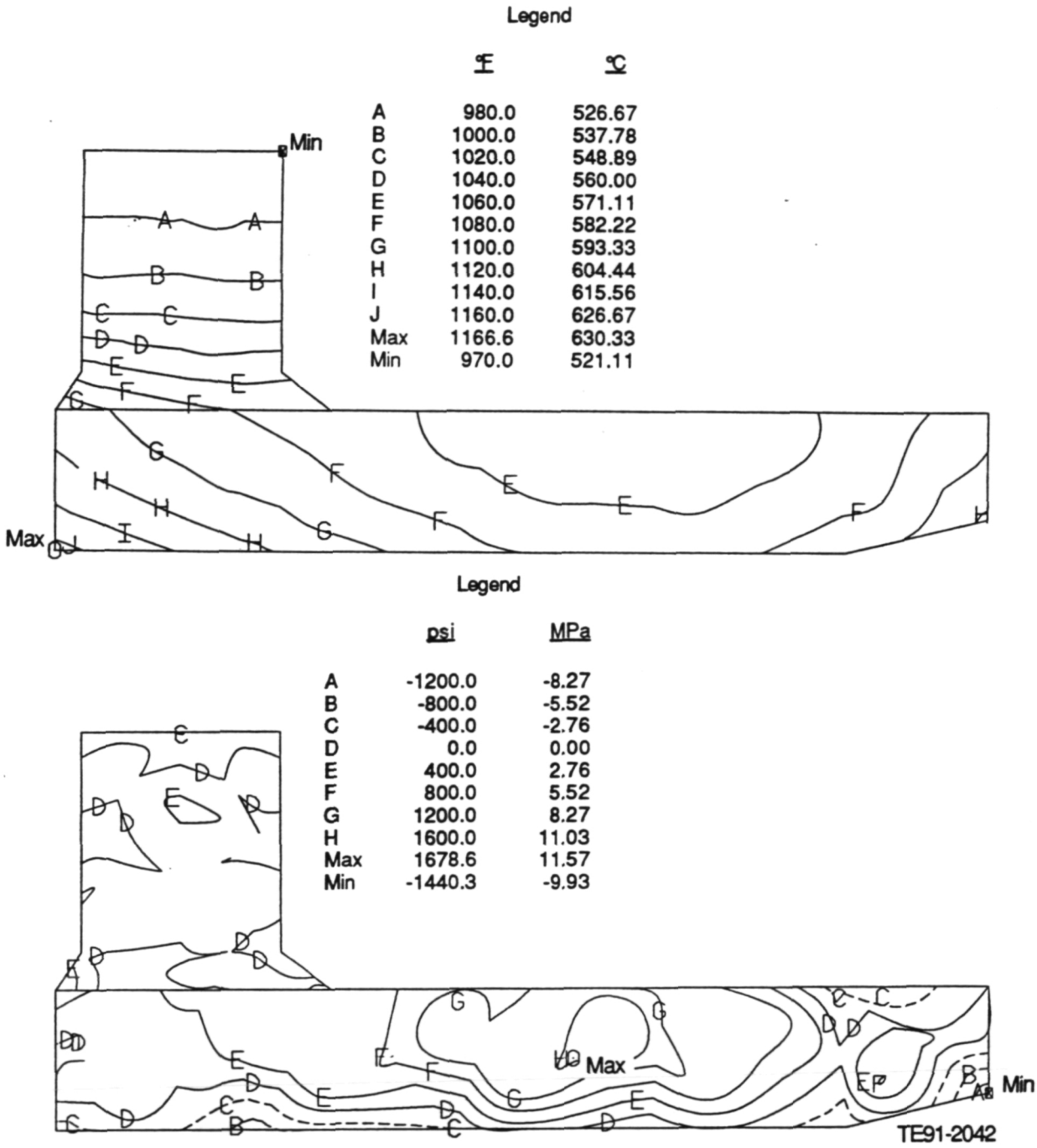

Figure 84. Temperature and equivalent stress distributions for PT first-stage rotor shroud at 15 second transient.

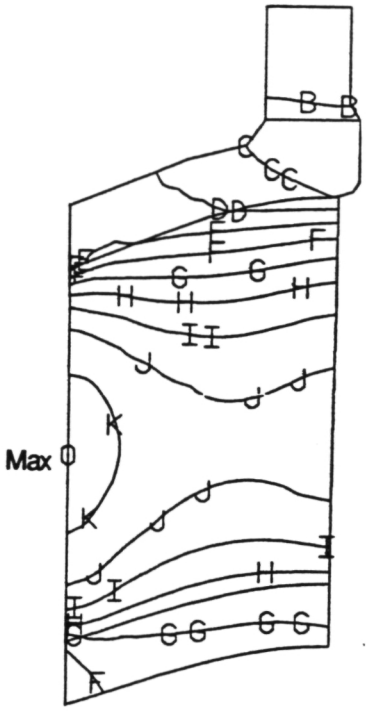

Legend

	°F	°C
A	1000.0	537.78
B	1100.0	593.33
C	1200.0	648.89
D	1300.0	704.44
E	1400.0	760.00
F	1500.0	815.56
G	1600.0	871.11
H	1700.0	926.67
I	1800.0	982.22
J	1900.0	1037.78
K	2000.0	1093.33
Max	2046.6	1119.22
Min	901.3	482.94

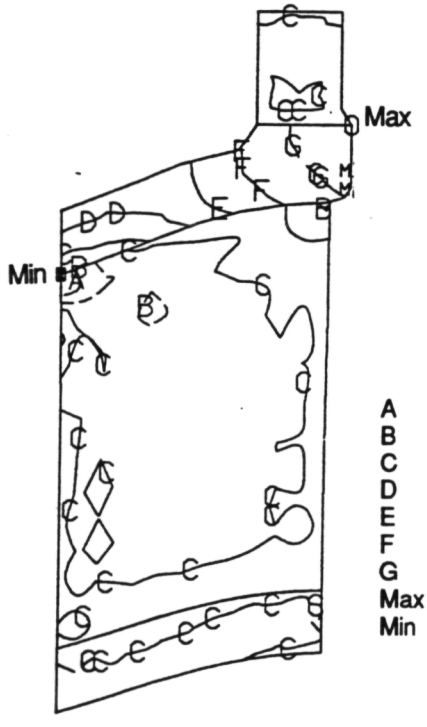

Legend

	ksi	MPa
A	-14.0	-96.53
B	-7.0	-48.26
C	0.0	0.00
D	7.0	48.26
E	14.0	96.53
F	21.0	144.79
G	28.0	193.05
Max	32.9	226.87
Min	-19.0	-130.90

TE91-2043

Figure 85. Temperature and equivalent stress distributions for PT first stage vane at 15 second transient.

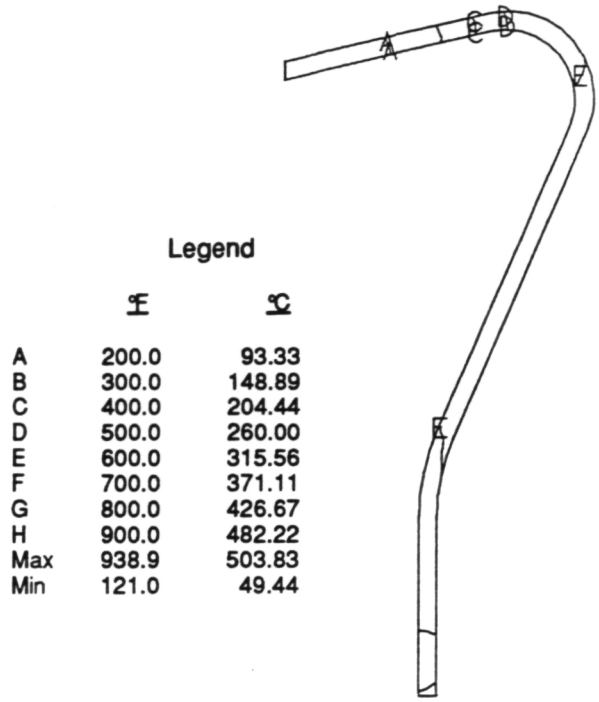

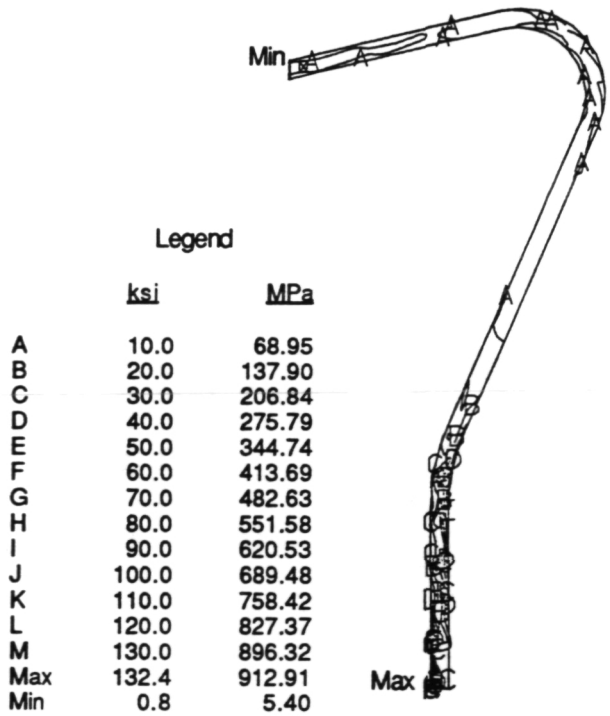

TE91-2044

Figure 86. Temperature and equivalent stress distributions for PT first stage vane centerbody at 15 second transient.

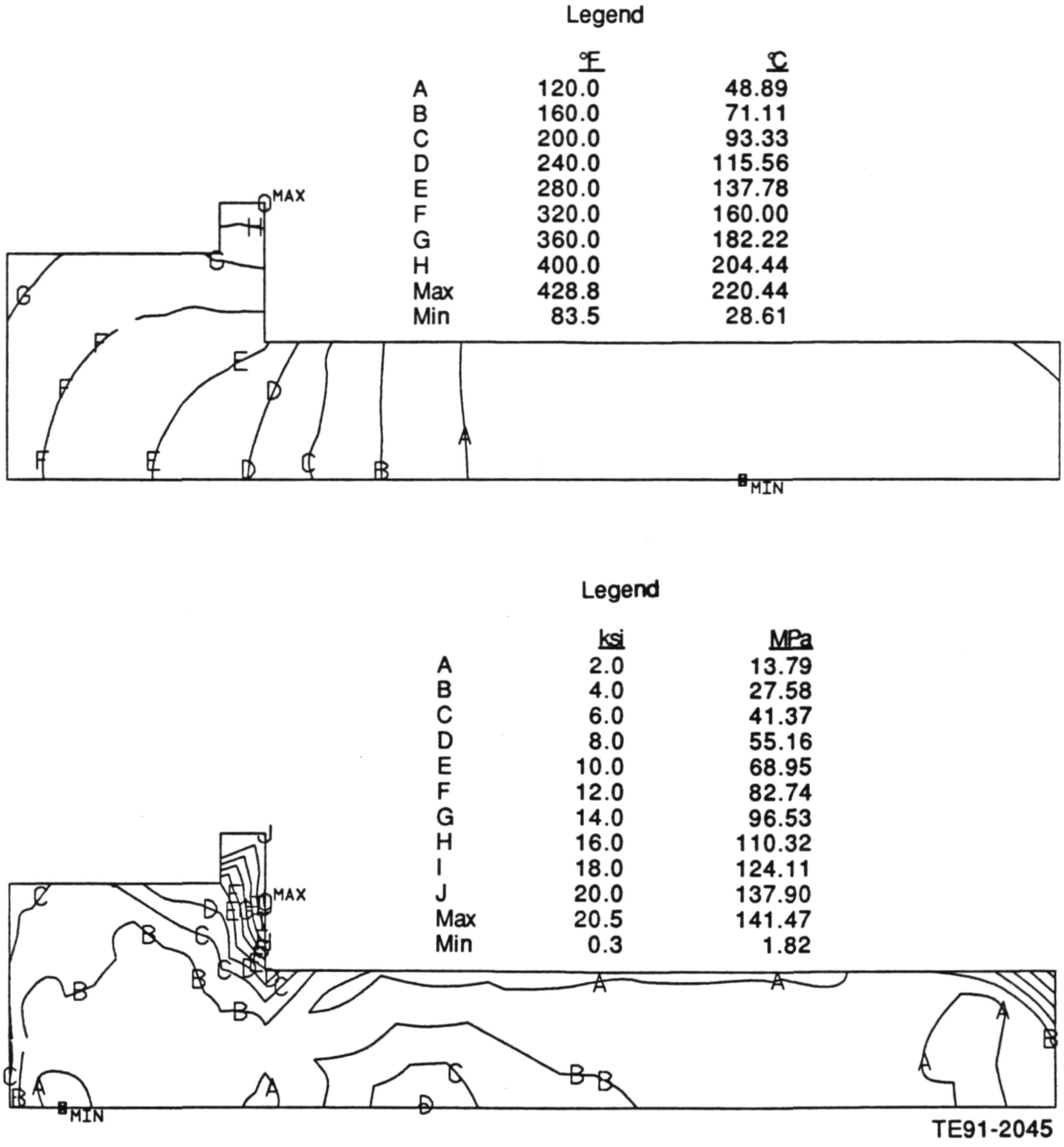

Figure 87. Temperature and equivalent stress distributions for PT centerbody attachment bolt at 15 second transient.

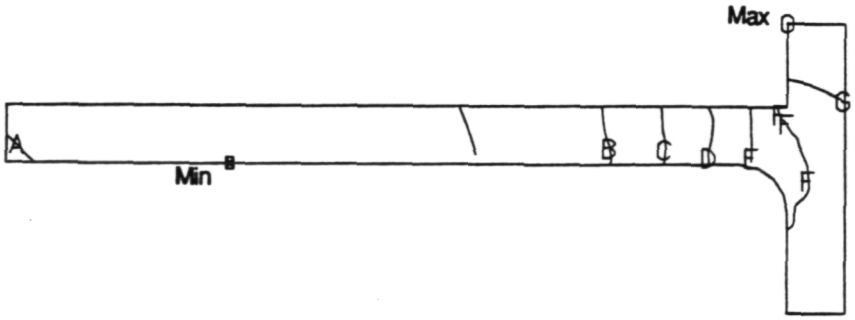

Legend

	°F	°C
A	100.0	37.78
B	150.0	65.56
C	200.0	93.33
D	250.0	121.11
E	300.0	148.89
F	350.0	176.67
G	400.0	204.44
Max	447.2	230.67
Min	85.2	29.56

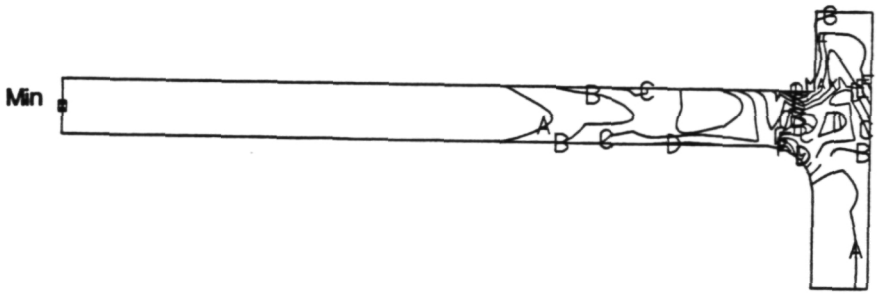

Legend

	ksi	MPa
A	2.0	13.79
B	4.0	27.58
C	6.0	41.37
D	8.0	55.16
E	10.0	68.95
F	12.0	82.74
G	14.0	96.53
H	16.0	110.32
Max	18.0	124.07
Min	0.5	3.25

TE91-2046

Figure 88. Temperature and equivalent stress distributions for PT centerbody attachment spool at 15 second transient.

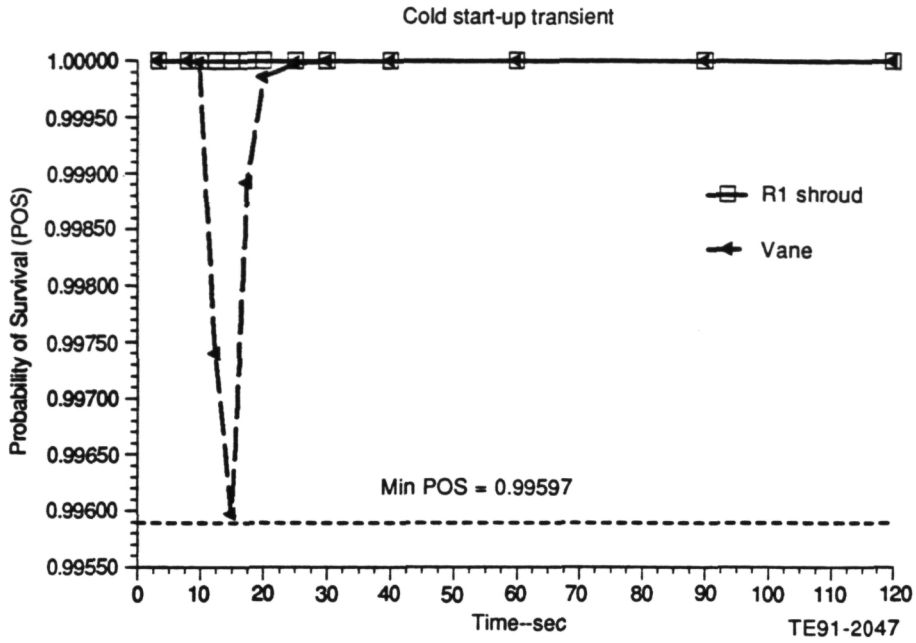

Figure 89. Power turbine ceramic component transient POS; first-stage vane and rotor shroud.

III. MATERIALS CHARACTERIZATION AND CERAMIC COMPONENT FABRICATION

The materials characterization and ceramic component fabrication sections describe the ongoing ceramic material and component fabrication, characterization, and development activities, which are a key focus of the ATTAP program. The ceramic materials subsection documents the results of characterization and qualification of candidate ceramic materials and components being developed for advanced gas turbine engines. This includes characterizations of material properties (e.g., densities, fracture strengths, microstructures, fracture toughnesses), results of failure analyses of rig/engine tested components, and nondestructive evaluation results. The ceramic component fabrication subsection describes the ongoing ceramic component process development activities at the selected ceramic suppliers, including Carborundum, Manville, GTE Laboratories, Corning, Garrett Ceramic Components, Ceramics Process Systems, and Norton/TRW Ceramics. Allison's approach to ceramic component technology development continues to be one of subcontracting process development to the domestic ceramic manufacturing community and working in an iterative development loop with those suppliers in areas of component design, fabrication, characterization, and rig/engine data feedback. While basic ceramic materials development is not a part of the ATTAP program, the program integrates material developments from Oak Ridge programs, supplier in-house activities, and other sources as they become available for component fabrication efforts.

3.1 MATERIALS AND COMPONENT CHARACTERIZATION

3.1.1 Material Properties and Microstructure

Objective/Approach

The materials and component characterization efforts have focused on the testing and evaluation of candidate ceramic materials and components being developed for use in the ATTAP AGT-5 automotive gas turbine engine. The primary objective of this task is to establish a data base of appropriate material characteristics to support the design, development, and testing of hot section ceramic components. A secondary objective is to evaluate new candidate ceramic materials and suppliers and to assess which, if any, should be used in subsequent component development activities. The material characterization activities have focused on microstructural, density, fracture toughness, and flexural strength evaluations of various candidate ceramic materials. Fracture surface analysis is also used to determine the nature and location of the strength-controlling defects. In addition, the time dependent strength characteristics and oxidation resistance are evaluated for select materials.

Accomplishments/Results

The ceramic materials and components that were characterized include the following:

- Garrett Ceramic Components (GCC) GN-10 Si_3N_4
- Norton/TRW Ceramics NT154 Si_3N_4
- Norton/TRW Ceramics NT235 SiC
- Carborundum Hexoloy SX SiC
- Dow Corning β-SiC
- Ethyl unsintered SiC
- Kyocera SN252 Si_3N_4
- GTE Laboratories PY6 Si_3N_4 gasifier turbine rotors
- Carborundum sintered α–SiC gasifier turbine rotors
- Ceramics Process Systems CM200 sialon vane platforms

Discussion

GCC GN-10 Silicon Nitride. Test material was received from GCC and evaluated. These test specimens were supplied by the International Energy Agency (IEA) as part of an international round robin activity involving powder and structural characterization and mechanical strength determination of ceramic materials. A number of laboratories in the US, Germany, Sweden, and Japan are involved in this effort. Initial testing involved conducting 30 room

temperature flexural tests, followed by 15 flexural tests conducted at a temperature of 1250°C (2282°F). Following these activities, it is planned to conduct room temperature tensile tests on 15 specimens at the ORNL High Temperature Materials Laboratory (HTML).

The material evaluated was GCC GN-10 silicon nitride, fabricated by cold isostatic pressing (CIP) and subsequent HIP. The flexural test specimens conformed to MIL-STD-1942 (MR), measuring 3 x 4 x 50 mm (0.118 x 0.157 x 1.969 in.) and were tested in four-point bending with an inner load span of 20 mm (0.787 in.) and an outer span of 40 mm (1.575 in.). All of the specimens were evaluated with a machined tensile surface condition.

The average strength of the 30 specimens tested at room temperature measured 814.47 MPa (118.28 ksi) with a standard deviation of 83.24 MPa (12.07 ksi). The Weibull modulus was 11.39 determined using linear regression and 12.21 using the maximum likelihood approach. The typical strength-controlling defects were observed to be surface flaws, as shown in Figure 90. The second most common fracture origins were surface and internal porosity, as shown in Figure 91.

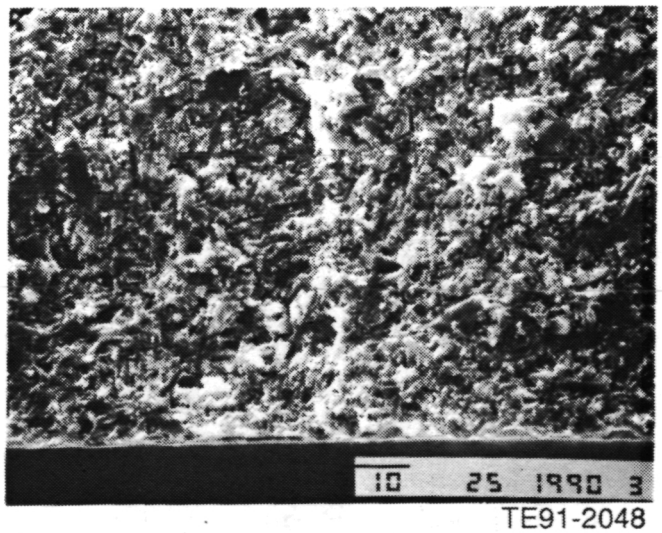

TE91-2048

Figure 90. Typical fracture origin (surface flaw) observed in GCC GN-10 Si_3N_4 IEA test bars.

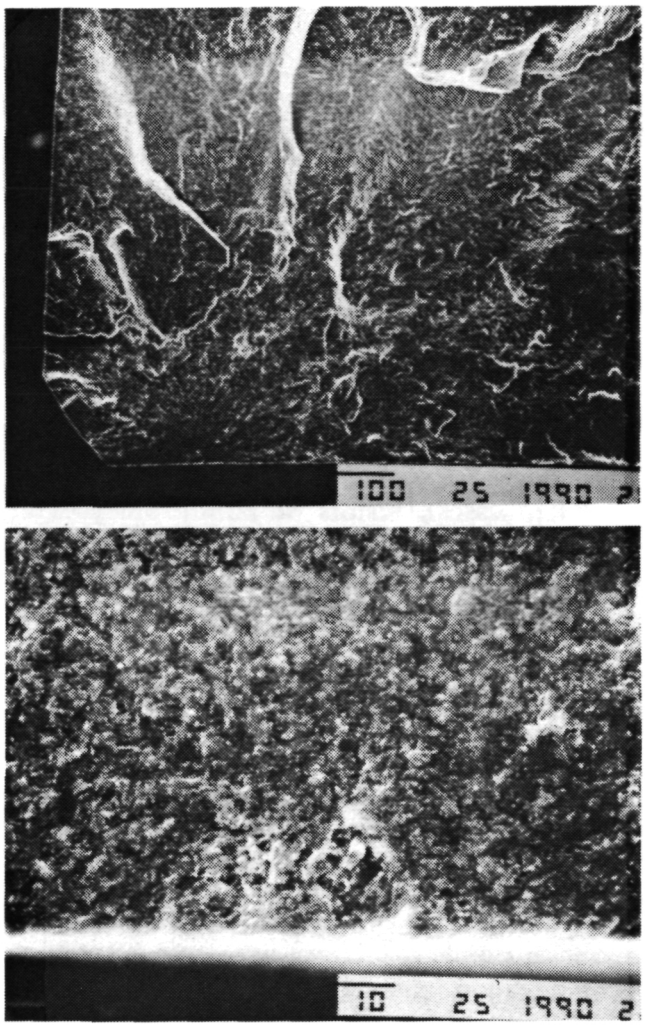

TE91-2049

Figure 91. Fracture origin (surface porosity) observed in GCC GN-10 Si_3N_4.

The average strength of the 15 specimens tested at a temperature of 1250°C (2282°F) was 581.15 MPa (84.29 ksi) with a standard deviation of 48.97 MPa (7.10 ksi). A value of 13.55 for the Weibull modulus was obtained using linear regression analysis, with 13.74 obtained using the maximum likelihood method. The typical fracture origins were again found to be surface flaws observed in a thin layer of oxidation.

Norton/TRW Ceramics NT154 Silicon Nitride. Evaluation of the material strength characteristics of Norton/TRW Ceramics NT154 silicon nitride material was conducted. The test specimens were sectioned from billets, which were fabricated by pressure slip casting and HIPing,

ORIGINAL PAGE
BLACK AND WHITE PHOTOGRAPH

C-2

using process parameters similar to those established for fabrication of the gasifier turbine rotors. A total of 200 test specimens were received, with 100 bars having four sides machined and the remaining 100 bars having an as-HIPed surface for characterization. The microstructure, shown in Figure 92, is typical of advanced Si_3N_4 materials, consisting of a network of interlocking tabular β-Si_3N_4 grains. The average grain size measured 0.7 microns (0.00003 inches). The average density of the test specimens was 3.227 g/cc (0.117 lb/in^3) (99.6% theoretical density).

The strength characteristics of the NT154 Si_3N_4 material are summarized in Table XXII for both machined and as-fired tensile surface conditions. Test specimens evaluated with a machined tensile surface condition had an average room temperature strength of 1070.38 MPa (155.24 ksi) with an associated Weibull modulus of 10.06. The typical strength-controlling defects were observed to be surface flaws, as shown in Figure 93. The primary fracture origins observed in the specimens tested at elevated temperature were internal pores, as shown in Figure 94. Test specimens evaluated with an as-HIPed tensile surface condition had an average room temperature strength of 559.94 MPa (81.21 ksi) with an associated Weibull modulus of 6.19. The typical fracture origins were observed to be small flaws present in the numerous shallow depressions present on the surface of the specimens. A majority of the strength-limiting defects also had shell-type features at the fracture origin. These are typically the result of mechanical impact damage, probably introduced during removal of the glass encapsulation layer used in the ASEA HIP process. Examples of this are shown in Figure 95.

TE91-2050

Figure 92. Microstructure of Norton/TRW NT154 Si_3N_4.

The typical fracture origins observed in the bars tested at elevated temperature were similar to those found in the room temperature tests, i.e., small flaws and pores at the base of shallow surface depressions, as shown in Figure 96.

Norton/TRW Ceramics NT235 Silicon Carbide. Evaluation of the material strength characteristics of Norton/TRW Ceramics NT-235 silicon carbide material was conducted. The test specimens were sectioned from billets, which were fabricated by pressure slip casting using process parameters similar to those employed for scroll fabrication. The NT235 SiC is a reaction bonded SiC material, previously designated NC-430, with a broad bimodal grain size distribution. Large SiC grains, measuring 100-200 microns (0.004 - 0.008 in.), are interspersed with micron-sized SiC grains in a matrix of free silicon (approximately 12%). The microstructure of this material is shown in Figure 97. The average density of the test specimens was 3.131 g/cc (0.114 lb/in.^{3}).

The average strength of machined test bars evaluated at room temperature was 295.24 MPa (42.82 ksi) with an associated Weibull modulus of 16.91. The typical fracture origins in this material are very difficult to distinguish due to the bimodal grain size in conjunction with the free silicon. The fractures appeared to originate on the specimen surface from unidentifiable features. Machined bars tested at a temperature of 1370°C (2500°F) had an average strength of 252.56 MPa (36.63 ksi). The fracture origins were again surface flaws.

No additional characterization efforts are planned for this material, due to the redirection of Norton/TRW's scroll fabrication activities to the NT-230 SiC material. NT230 is also a reaction bonded SiC, but has a much narrower grain size distribution than does NT235 SiC. In addition, the silicon content is slightly higher (15% total). An enhanced carbon treat-

ORIGINAL PAGE
BLACK AND WHITE PHOTOGRAPH

Table XXII.
Strength characteristics of Norton/TRW NT154 silicon nitride.

Temperature--°C (°F)	Strength--MPa (ksi) Machined	As-fired
25 (77)	1070.38 (155.24)	559.94 (81.21)
1000 (1832)	700.05 (101.53)	461.34 (66.91)
1150 (2102)	724.32 (105.05)	405.91 (58.87)
1250 (2282)	729.28 (105.77)	424.80 (61.61)
1370 (2500)	631.86 (91.64)	429.97 (62.36)

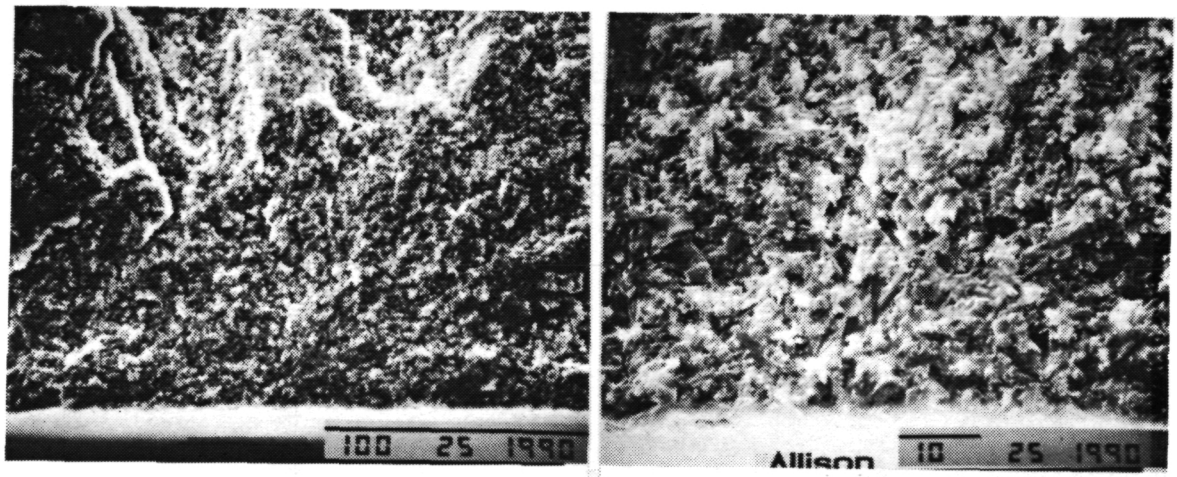

TE91-2051

Figure 93. Typical fracture origin (surface flaw) observed in Norton/TRW NT154 Si_3N_4 machined bars tested at room temperature.

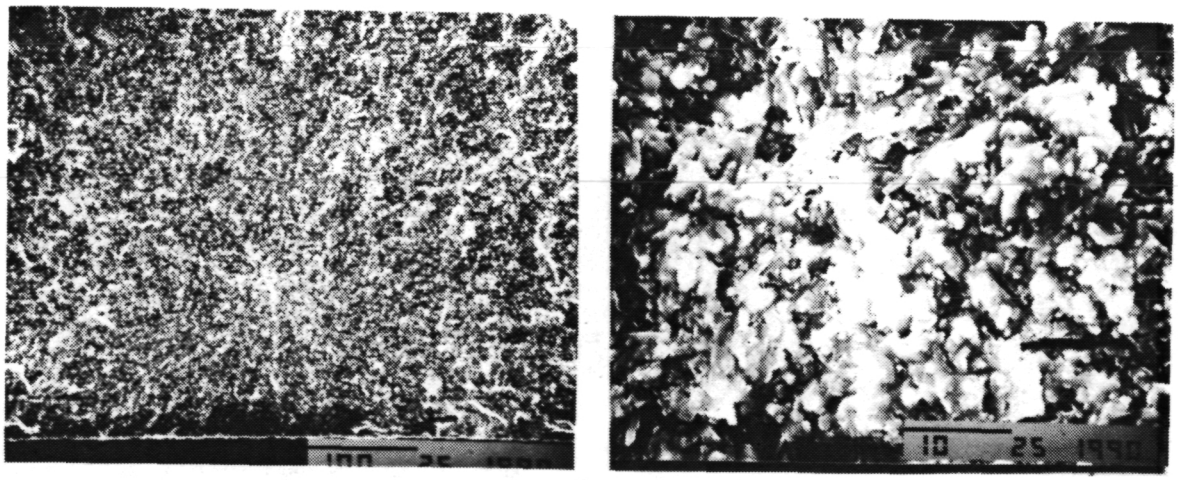

TE91-2052

Figure 94. Typical fracture origin (internal pore) observed in Norton/TRW NT154 Si_3N_4 machined bars tested at 1370°C (2500°F).

ORIGINAL PAGE
BLACK AND WHITE PHOTOGRAPH

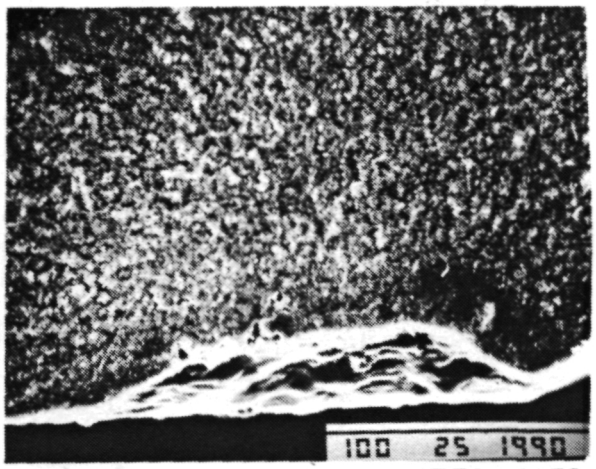

TE91-2053

Figure 95. Typical fracture origin (flaw in shallow surface depression) observed in as-HIPed NT154 bars tested at room temperature.

TE91-2054

Figure 96. Typical fracture origin (surface flaw) observed in as-HIPed NT154 bars tested at 1370°C (2500°F); shell-like feature is indicative of mechanical/impact damage.

ment in conjunction with improved purity in the processing steps results in strengths 50-100% higher than that of the NT-235 SiC. Initial test specimens of the NT-230 material are anticipated in March 1991.

Carborundum Hexoloy SX SiC. Preliminary material characteristics were obtained on Carborundum Hexoloy SX SiC. The Hexoloy SX SiC material is fabricated using the same submicron sized SiC powder as the traditional sin-

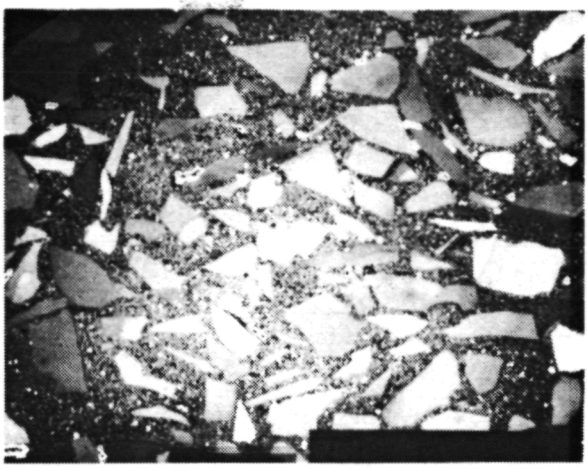

TE91-2055

Figure 97. Microstructure of Norton/TRW NT235 reaction bonded SiC.

tered α–SiC Hexoloy SA SiC, but employs a modified sintering additive. The different sintering additive results in improved fracture toughness and low temperature strength. The test bars received were fabricated by CIP followed by sinter/HIP densification. The microstructure, shown in Figure 98, consists of very fine α–SiC grains, ranging in size between 0.5 to 3 microns (0.00002 to 0.0001 in.). The average density of this material was 3.226 g/cc (0.117 lb/in^3).

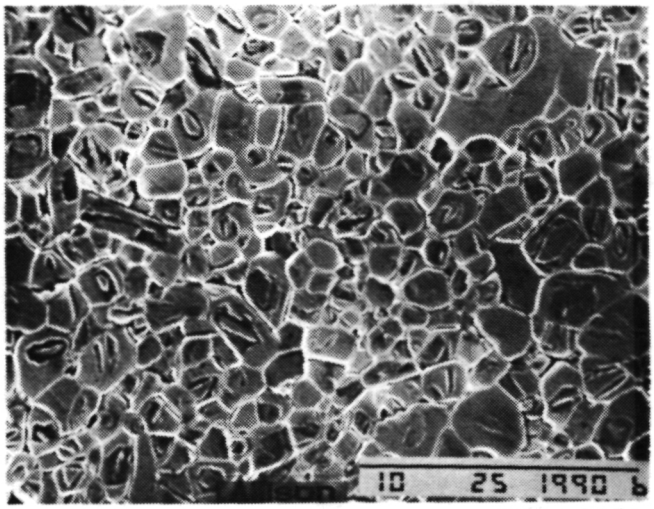

TE91-2056

Figure 98. Microstructure of Carborundum Hexoloy SX SiC.

ORIGINAL PAGE
BLACK AND WHITE PHOTOGRAPH

The preliminary strength characteristics of the Hexoloy SX SiC material are summarized in Table XXIII. The test specimens and test procedure conformed to MIL-STD-1942 (MR). All of the specimens were evaluated with a machined tensile surface condition. The average room temperature flexural strength measured 827.16 MPa (119.97 ksi). The primary strength-controlling flaws were observed to be surface and internal inclusions, consisting of agglomerates of undispersed sintering additive. These fracture origins are shown in Figure 99. The primary fracture origins in the specimens tested at elevated temperature were surface and internal inclusions similar to those observed in the specimens tested at room temperature, with occasional fractures from surface flaws. The fracture toughness of the Hexoloy SX SiC averaged 5.3 MPa-m$^{1/2}$ (4.8 ksi-in.$^{1/2}$) as determined by the single edge notched beam (SENB) method, a significant increase over the value of 3.2 MPa-m$^{1/2}$ (2.9 ksi-in.$^{1/2}$) obtained for sintered α–SiC.

Dow Corning β-SiC. Evaluation of the material characteristics of Dow Corning β-SiC was conducted. This material is produced using β-SiC powder with pre-ceramic polymers used as a nonfugitive binder. The resulting material possesses a high green strength (14 - 70 MPa [2 - 10 ksi]) with the potential for improved dimensional control in the sintered body. The specimens evaluated were produced by CIPing and pressureless sintering. The average density of the SiC measured 3.072 g/cc (0.111 lb/in.^{3}). All specimens were evaluated with a machined tensile surface condition. The average room temperature strength was 436.25 MPa (63.27 ksi) with a Weibull modulus of 8.55. The typical strength-controlling flaws were observed to be surface and internal pores typically ranging from 25 - 50 microns (0.001 - 0.002 in.) in diameter. These features are shown in Figure 100. The strength of bars tested at a temperature of 1370°C (2500°F) was 453.90 MPa (65.83 ksi). The fracture origins were similar to those found in the material tested at ambient temperature, i.e., small pores.

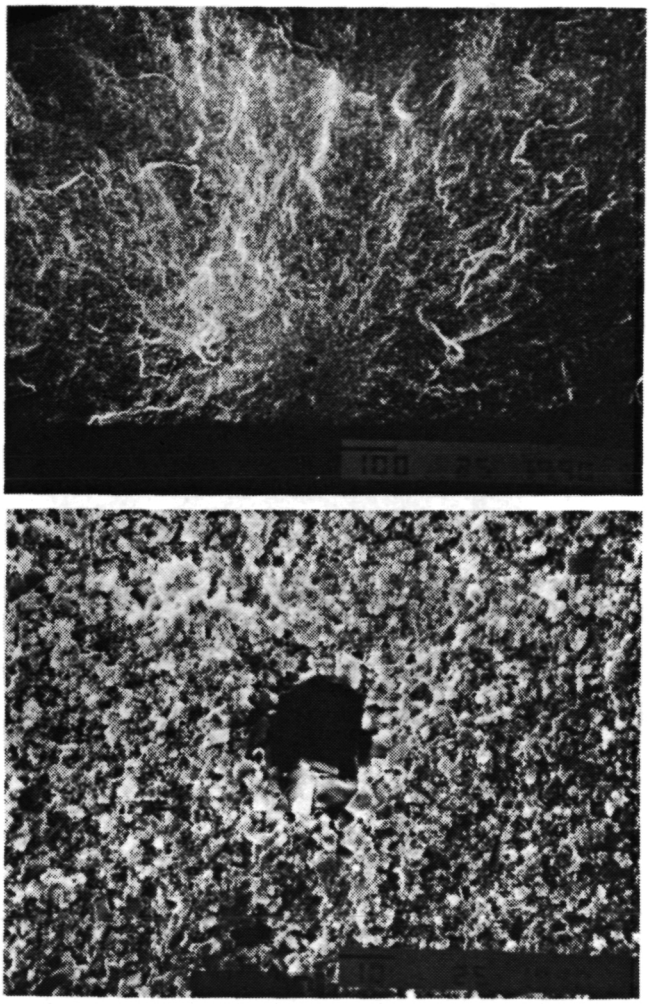

TE91-2057

Figure 99. Typical room temperature fracture origin (internal inclusion/pore) observed in Carborundum Hexoloy SX SiC.

Table XXIII.
Strength characteristics of Carborundum Hexoloy SX SiC.

Temperature--°C (°F)	Strength--MPa (ksi)
25 (77)	827.16 (119.97)
1000 (1832)	577.87 (83.81)
1150 (2102)	505.13 (73.26)
1250 (2282)	445.14 (64.56)
1370 (2500)	351.71 (51.01)

ORIGINAL PAGE
BLACK AND WHITE PHOTOGRAPH

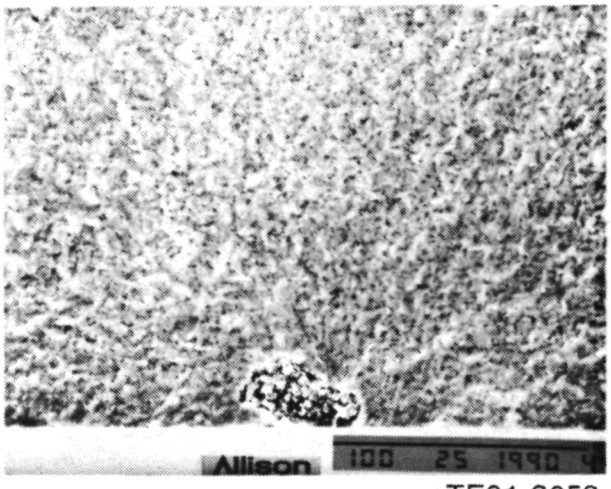

TE91-2058

Figure 100. Typical fracture origin (surface pore) observed in Dow Corning sintered β-SiC test bars.

Ethyl Corporation Silicon Carbide. Characterization of the material strength of Ethyl Corporation's SiC material was conducted this reporting period. The test specimens were fabricated by HIPing of SiC powder derived from polymeric precursors. Ethyl refers to the material as "unsintered" SiC and claims that the material does not undergo a conventional sintering process for densification. A conversion of the polymeric phase to become the matrix joining the SiC particles takes place during the consolidation process, resulting in approximately 3 - 5% volumetric shrinkage. The polymeric conversion process also results in the creation of a large quantity of very small pores in the 1 - 50 angstrom (4×10^{-9} - 2×10^{-7} in.) size range. These pores are small enough to not be the fracture origins in the test bars but do result in a substantially lower density, i.e., 2.444 g/cc (0.088 lb/in.^{3}) versus 3.21 g/cc (0.116 lb/in.^{3}) theoretical density for sintered SiC. The results of the mechanical properties evaluation are summarized in Table XXIV. The average room temperature fracture strength was 216.50 MPa (31.40 ksi) with an associated Weibull modulus of 8.77. The typical fracture origins were pores, located both on the surface and internally, as shown in Figure 101. The primary fracture origins in the specimens tested at elevated temperature were similar to those observed in the room temperature tests, i.e., porosity.

Kyocera SN252 Silicon Nitride. Evaluation of the material characteristics of Kyocera SN252 Si_3N_4 was conducted. The SN252 is a sintered reaction bonded Si_3N_4 and was fabricated using Kyocera's new forming process. This proprietary process is a hybrid of injection molding and slip casting and is intended to address the high volume production of ceramic components. Kyocera's new forming process utilizes a relatively short molding time, low pressure,

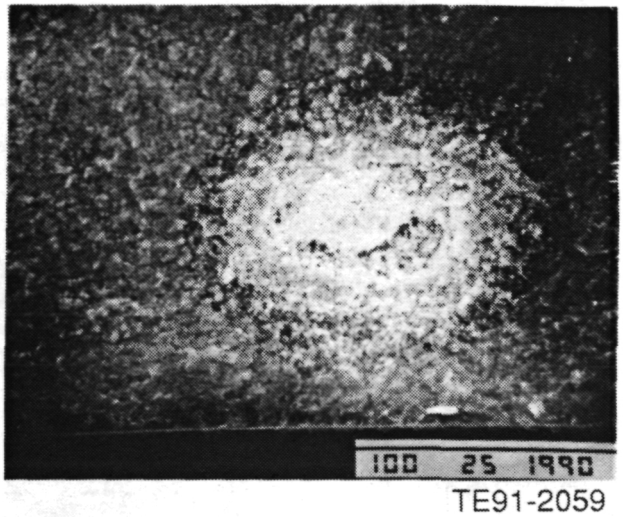

TE91-2059

Figure 101. Typical fracture origin (internal porosity) observed in Ethyl Corporation unsintered SiC test specimens.

Table XXIV.
Strength characteristics of Ethyl Corporation unsintered SiC material.

Temperature--°C (°F)	Strength--MPa (ksi)
25 (77)	216.50 (31.40)
1000 (1832)	294.90 (42.77)
1250 (2282)	274.84 (39.86)
1370 (2500)	293.31 (42.54)

ORIGINAL PAGE
BLACK AND WHITE PHOTOGRAPH

and a low binder level to result in high green density levels. In addition, the new process enables fabrication of components with surface finishes and dimensional tolerances greatly superior to those obtainable with conventional slip casting. The average density of the test specimens measured 3.404 g/cc (0.123 lb/in.^{3}).

The flexural strength characteristics of the SN252 Si_3N_4 material are summarized in Table XXV. Included in the table are the results obtained for SN252 material fabricated by slip casting. All specimens were tested with a machined tensile surface. The average room temperature strength measured 655.23 MPa (95.03 ksi) with a Weibull modulus of 14.3. The primary fracture origins were large tabular β-Si_3N_4 grains at or near the surface, as shown in Figure 102. The primary fracture origins observed in the SN252 Si_3N_4 specimens tested at elevated temperature were large Si_3N_4 grains similar to the room temperature tests.

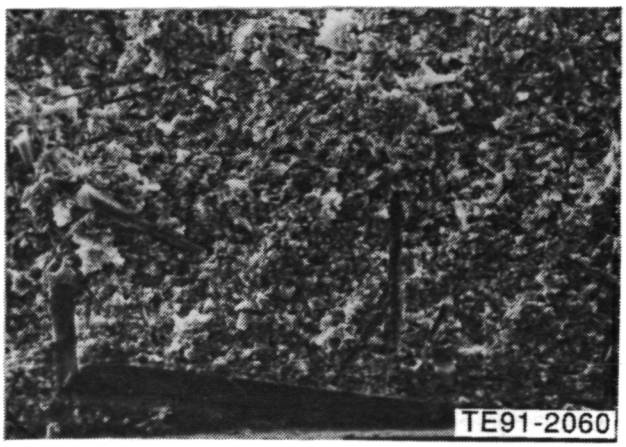

Figure 102. Typical fracture origin (Si_3N_4 grain) observed in Kyocera SN252 Si_3N_4 fabricated by new forming process.

GTE Labs PY6 Silicon Nitride Gasifier Turbine Rotors. Characterization of the material strength characteristics of GTE Laboratories injection molded and HIPed PY6 Si_3N_4 15-bladed gasifier turbine rotors was conducted. The axial turbine rotor evaluated was fabricated using the latest binder burnout aid formulation, which is intended to provide improved structural integrity in the rotor during the binder removal process to minimize cracking.

The rotor evaluated was P/N 5-80503, S/N 420. Test bars sectioned from the rotor had an average density of 3.245 g/cc (0.117 lb/in.^{3}) (99.3% theoretical density). The results of the mechanical strength evaluation are summarized in Table XXVI. The primary fracture origins observed in all of the test specimens were surface flaws, as shown in Figure 103. Secondary strength-controlling defects were found to be surface and internal inclusions. These inclusions, shown in Figure 104, are composed primarily of iron silicides and are believed to be the result of excessive wear of metallic parts in the mixing/compounding step of PY6 rotor fabrication.

Carborundum α–SiC Gasifier Turbine Rotors. Characterization of the material strength characteristics of Carborundum injection molded sintered SiC and sinter/HIPed SiC 15-bladed gasifier turbine rotors was conducted. The axial turbine rotors were fabricated using the latest modifications to the injection molding tool (with high power cartridge heaters) and in-line screens to filter out agglomerates and inclusions.

The pressureless sintered rotor evaluated was P/N 5-80501, S/N FX78523. The rotor was sectioned into standard size test bars (50.8 x 6.35 x 3.18 mm [2 in. x 0.25 in. x 0.125 in.]) according to

Table XXV.
Strength characteristics of Kyocera SN252 silicon nitride.

Temperature--°C (°F)	Strength--MPa (ksi) Slip Cast	New forming process
25 (77)	634.13 (91.97)	655.23 (95.03)
1000 (1832)	538.50 (78.10)	504.23 (73.13)
1250 (2282)	518.30 (75.17)	452.11 (65.57)
1376 (2500)	507.96 (73.667	463.69 (67.25)

ORIGINAL PAGE
BLACK AND WHITE PHOTOGRAPH

Table XXVI.

Strength characteristics of GTE Labs PY6 silicon nitride gasifier turbine rotor (P/N 5-80503, S/N 420).

Temperature--°C (°F)	Strength--MPa (ksi)
25 (77)	771.76 (111.93)
1000 (1832)	617.10 (89.50)
1250 (2282)	594.90 (86.28)
1370 (2500)	545.40 (79.10)

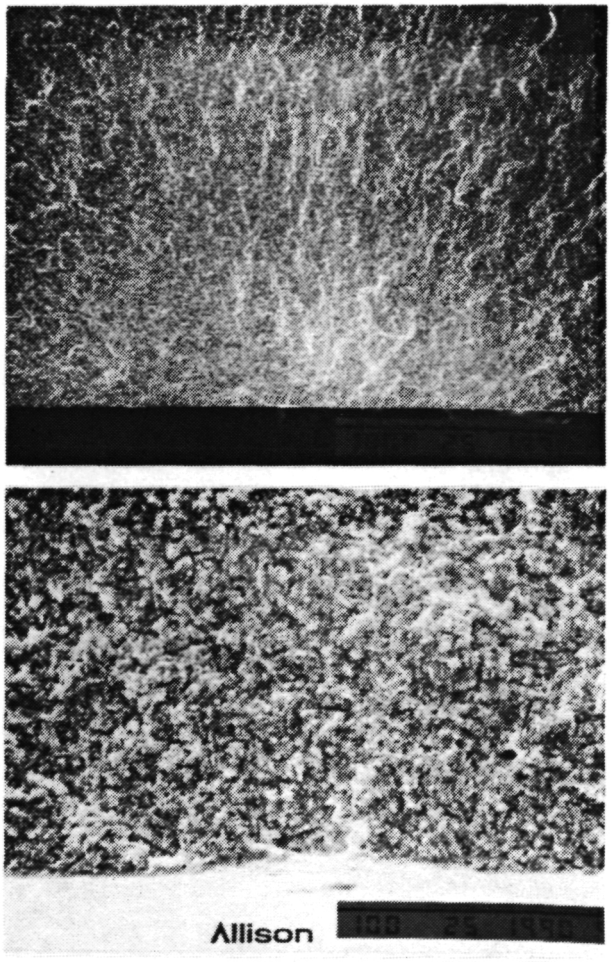

TE91-2062

Figure 103. Primary fracture origin (surface flaw) observed in GTE PY6 Si_3N_4 rotor bars.

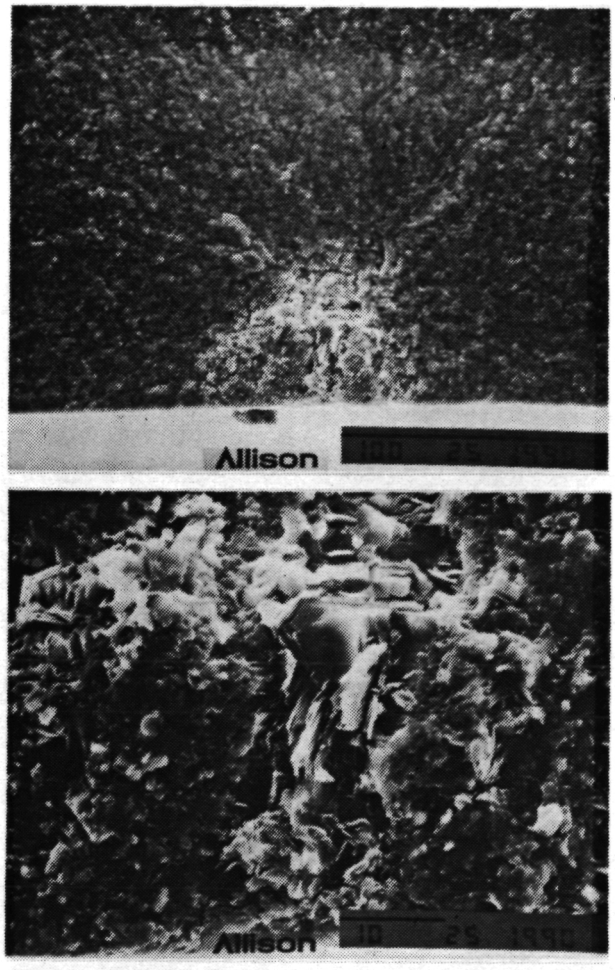

TE91-2061

Figure 104. Fracture origin (metallic inclusion) observed in GTE PY6 Si_3N_4 rotor bars.

ORIGINAL PAGE
BLACK AND WHITE PHOTOGRAPH

the diagram shown in Figure 105. The average density of the test bars measured 3.118 g/cc (0.113 lb/in.^{3}) (97.1% theoretical density), but varied significantly with location of the material within the rotor. Material sectioned from the outer regions of the rotor hub (bars 1-4 and 9-12) had an average density of 3.147 g/cc (0.114 lb/in.^{3}) (98.1% theoretical), while bars sectioned from the thicker core region of the rotor (bars 5-8) had an average density of 3.075 g/cc (0.111 lb/in3) (95.8% theoretical density). Similar variations were observed in the mechanical strength characteristics of the rotor test bars. All bars were evaluated with a machined surface condition. The test bars obtained from the outer portions of the rotor had an average room temperature fracture strength of 394.88 MPa (57.27 ksi), while bars from the central core region had an average strength of 343.44 MPa (49.81 ksi). The typical fracture origins for all specimens were observed to be surface and internal porosity, as shown in Figure 106. The strength-controlling pores observed in the specimens from the central hub portion of the rotor were found to be larger in size than those found in the test bars from the outer section.

The sinter/HIPed rotor sectioned for mechanical evaluation was P/N 5-80501, S/N FX78520. The density of the rotor following pressureless sintering was 3.157 g/cc (0.114 lb/in.^{3}) (98.3% theoretical density). This value increased to a density of 3.174 g/cc (0.115 lb/in.^{3}) [98.9% theoretical density] following HIPing. The average strength of the HIPed rotor material was also significantly higher, with an average strength of 518.02 MPa (75.13 ksi). This value was consistent independent of location within the rotor, indicating greatly improved microstructural homogeneity in the sinter/HIPed rotors. The typical fracture origins were observed to be surface flaws, as shown in Figure 107.

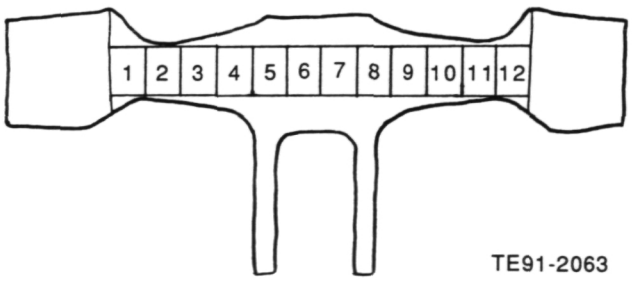

Figure 105. Schematic of test bars cut from Carborundum SiC rotors.

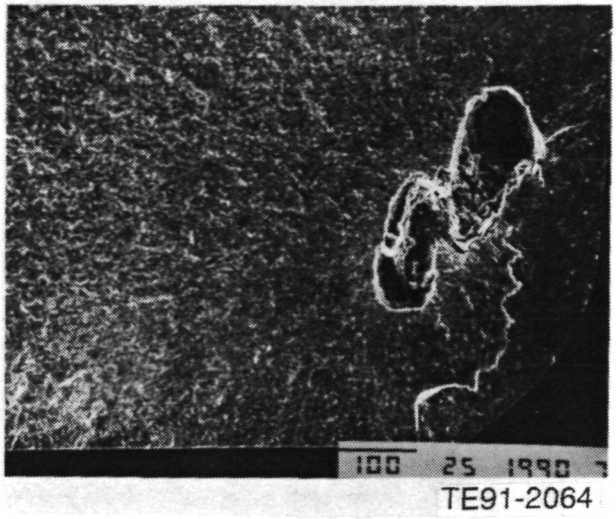

Figure 106. Fracture origin (internal pores) observed in Carborundum sintered SiC rotor S/N FX78523.

Ceramics Process Systems CM200 Sialon Vane Platforms. Evaluation of the material strength characteristics of Ceramics Process Systems (CPS) CM-200 sialon material was conducted.

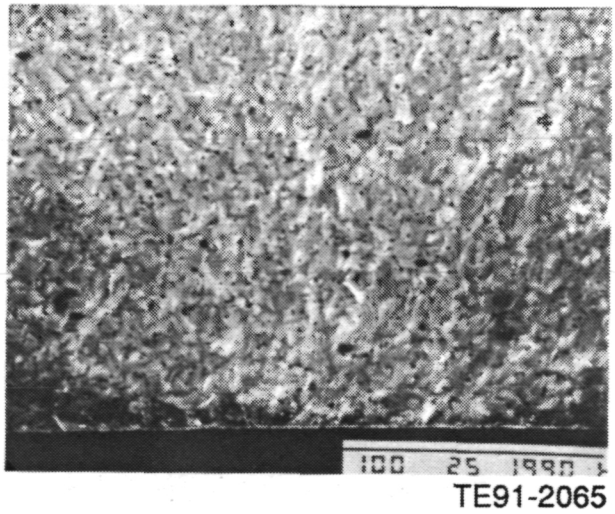

Figure 107. Typical fracture origin (surface flaw) observed in test bars cut from Carborundum sinter/HIPed SiC rotor S/N FX78520.

ORIGINAL PAGE
BLACK AND WHITE PHOTOGRAPH

The test specimens were sectioned from gasifier turbine vane platforms which had been fabricated using the CPS Quickset injection molding process. The CM200 material was densified by pressureless sintering. The average density of this material was 3.222 g/cc (0.116 lb/in.^{3}) (98.9% of theoretical density). The vane platform test bars were tested in accordance with MIL-STD-1942 (MR). The results of the strength characterization are summarized in Table XXVII. The room temperature strength had an average value of 694.74 MPa (100.76 ksi) with an associated Weibull modulus of 8.6. Two types of defects were most commonly observed as the fracture origins in these specimens, surface flaws and internal flaws/pores. Typical examples of these flaws are shown in Figure 108. The typical fracture origin observed in the specimens tested at elevated temperature were surface flaws, as shown in Figure 109. In addition, in the CM200 material tested at 1250°C (2282°F) and 1370°C (2500°F), oxidation was observed on the specimen surfaces, resulting in localized glassy bubbling.

3.1.3 Failure Analysis

Objective/Approach

Failure analysis details the results of fractographic analyses of ceramic components that experienced unscheduled damage during rig/engine testing and evaluation. Fractographic analysis is one of the most powerful tools used in the failure analysis of an engine or rig tested component. A careful study of the general and detailed features of the topography of a fracture by visual assessment and scanning electron microscopy provides a wealth of information concerning the failure origin and the failure mode(s). Analysis of hardware failures allows the separation of design features from material deficiencies, defects, or nonoptimum fabrication procedures and can suggest appropriate corrective measures.

Table XXVII.
Strength characteristics of CPS CM200 sialon.

Temperature--°C (°F)	Strength--MPa (ksi)
25 (77)	694.74 (100.76)
1000 (1832)	527.33 (76.48)
1150 (2102)	488.17 (70.80)
1250 (2282)	440.38 (63.87)
1370 (2500)	384.47 (55.76)

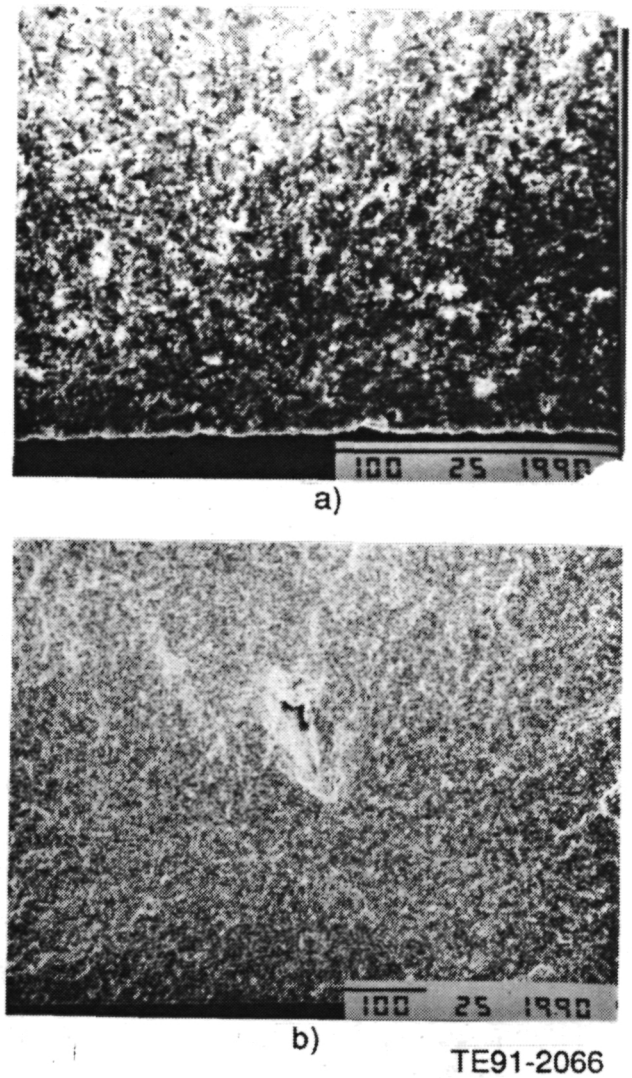

Figure 108. Typical fracture origins observed in CPS CM200 sialon vane platform testbars--(a) surface flaw, (b) internal flaw.

Accomplishments/Results

- Failure investigation of AGT-5 engine, S/N 11, BU22 with a Kyocera SN252 Si_3N_4 gasifier turbine rotor (P/N 5-67200, S/N 0001-4) was conducted. The blades of the silicon nitride rotor and shroud were fractured by foreign object damage (FOD): pieces of the combustor dome melted by an engine oil fire. The

ORIGINAL PAGE
BLACK AND WHITE PHOTOGRAPH

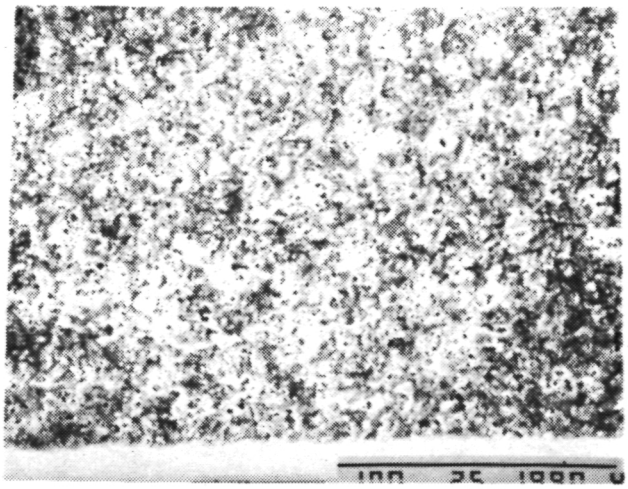

TE91-2067

Figure 109. Typical fracture origin (surface flaw) observed in CPS CM200 sialon tested at 1250°C (2282°F). The bubbles are the result of oxidation.

engine oil fire was caused by an internal oil leak around the oil inlet O-ring at the gasifier housing. The O-ring was 1.19 mm (0.047 in.) shorter than print dimension.

- Fractographic analysis of Kyocera SN252 Si_3N_4 shroud (P/N 5-80510, S/N 005-2) which had been run in the hot gasifier rig BU16 was conducted. The ceramic shroud fracture originated at the O.D. surface. Heavy rub of the shroud occurred after the fracture.

- Failure analyses of ceramic components run in the durability engine (S/N 11, BU25) was conducted following rotor/shroud rub. The Kyocera SN252 rotor had six airfoils fractured with chips originating from the leading and trailing edges. The airfoil fractures resulted from FOD (engine thermal insulation). The Kyocera SN252 Si_3N_4 shroud was undamaged.

Discussion

Durability Engine S/N 11, BU 22. A 20-blade Kyocera SN252 gasifier turbine rotor (P/N 5-67200, S/N 0001-4) and a silicon nitride rotor shroud (P/N 5-80510, S/N 0005-1) were assembled in the AGT-5 durability test-bed engine. In less than a minute after starting a 12 minute test cycle from idle the power turbine speed surged and smoke was observed in the exhaust. The engine was immediately shut down. Total test time for the ceramic rotor and shroud was 7.9 hr. Previously, the rotor had been successfully tested in the hot gasifier rig at 64,000 rpm and 1163°C (2125°F).

The interior of the engine was coated with thick soot, an indication of an oil fire. Figure 110 shows the Lamilloy combustor dome still attached to the engine housing. A small section of the dome was missing, probably due to overtemperature. The insulation immediately adjacent to the damaged section of the dome was melted. Figure 110 also shows the oil inlet O-ring at the gasifier housing where the oil leak occurred. Inspection of the O-ring revealed that it was approximately 1.19 mm (0.047 in.) shorter than the required print dimension.

Figure 111 shows the rotor (S/N 0001-4) after being cleaned in the laboratory. All airfoils were broken at the root and most of the broken roots exhibited impact fracture at the suction side without any dominant fracture origin. The broken airfoils exhibited two types of metallic impact marks. The first type of mark, which occurred exclusively at the leading edge of the airfoil roots, was a cluster of fine dark spots as shown in Figure 112. The second type of metallic impact mark was a larger shiny golden color streak which occurred at the crown of the roots and at the fractured surface of the airfoils, Figure 113.

Semi-quantitative X-ray Energy Dispersive Analysis (XEDA) of the two metallic impact marks showed that the dark type matched to INCONEL 601 type dome base material. The golden color metal was identified as NX-188 type power turbine vane material. The results coincided with the locations of these metallic impact marks. The dome material, coming from upstream, struck the rotor leading edges only. The debris of the downstream power turbine vane bounced upstream and struck the middle section of the rotor airfoils.

All remaining shroud fragments exhibited heavy foreign deposits at the I.D. adjacent to

ORIGINAL PAGE
BLACK AND WHITE PHOTOGRAPH

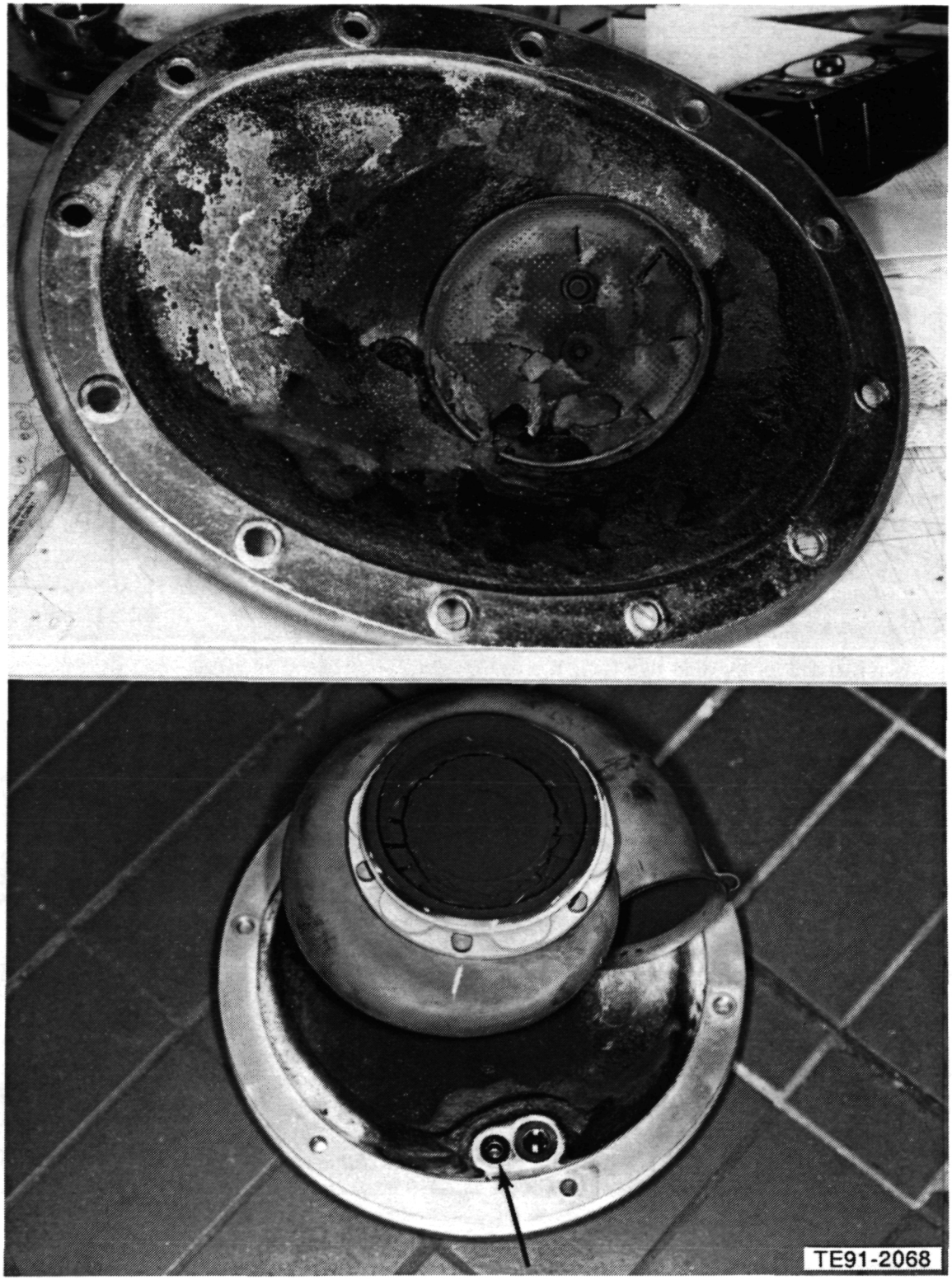

Figure 110. As-disassembled condition of combustor dome and burner cover insulation (top); black O-ring (pointed out by arrow in bottom photo).

ORIGINAL PAGE
BLACK AND WHITE PHOTOGRAPH

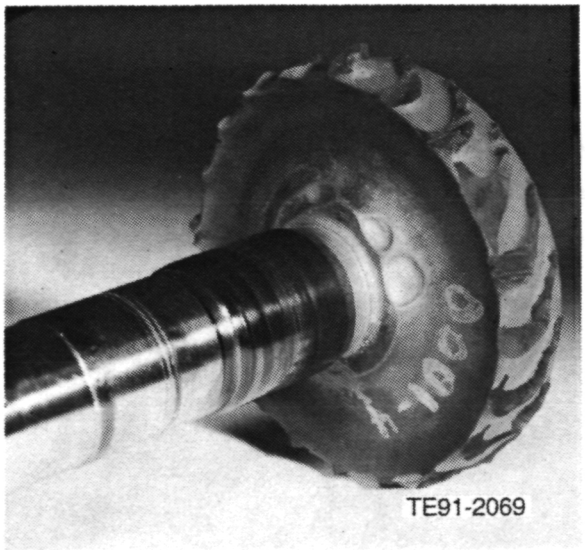

Figure 111. Gasifier turbine rotor (P/N 5-67200, S/N 0001-4) after laboratory cleaning.

the aft edge. XEDA results indicated these deposits were INCONEL 601 dome material. Five out of six crosskey slots were found. None of the slots fractured at the loading point against the pin, indicating the shroud was not the primary cause of the engine failure.

Tear-down inspection revealed two large pieces of metal (12.7 x 25.4 mm [0.5 x 1 in.]) welded on the inlet inside diameter of the metallic scroll (Figure 114). Another equivalent size piece of metal was found stuck between gasifier vanes. XEDA of these metallic debris indicated they were of INCONEL 601 type material.

Hot Gasifier Rig, BU16. A Kyocera slip cast SN252 gasifier turbine rotor (P/N 5-67200, S/N 5K22), was run in the hot gasifier rig (BU16) in conjunction with a Kyocera isopressed SN252 Si_3N_4 gasifier turbine shroud. While the rig was running at 59,000 rpm and 1290°C (2354°F) rotor inlet temperature (RIT), a bright light was visually observed through the quartz viewing window. The rig was then disassembled. The shroud was found to have sustained multiple fractures while the rotor was basically undamaged.

The shroud, shown in Figure 115, fractured at the 10 o'clock position viewed from the aft side. The shroud was lightly rubbed all way around except for a region of heavy rub measuring 58.42 x 5.08 mm (2.3 x 0.2 in.) where the fracture occurred. The crack measured 78.7 mm (3.1 in.) in length. Figure 116 shows the reduced cross-section of the shroud at the region of heavy rub.

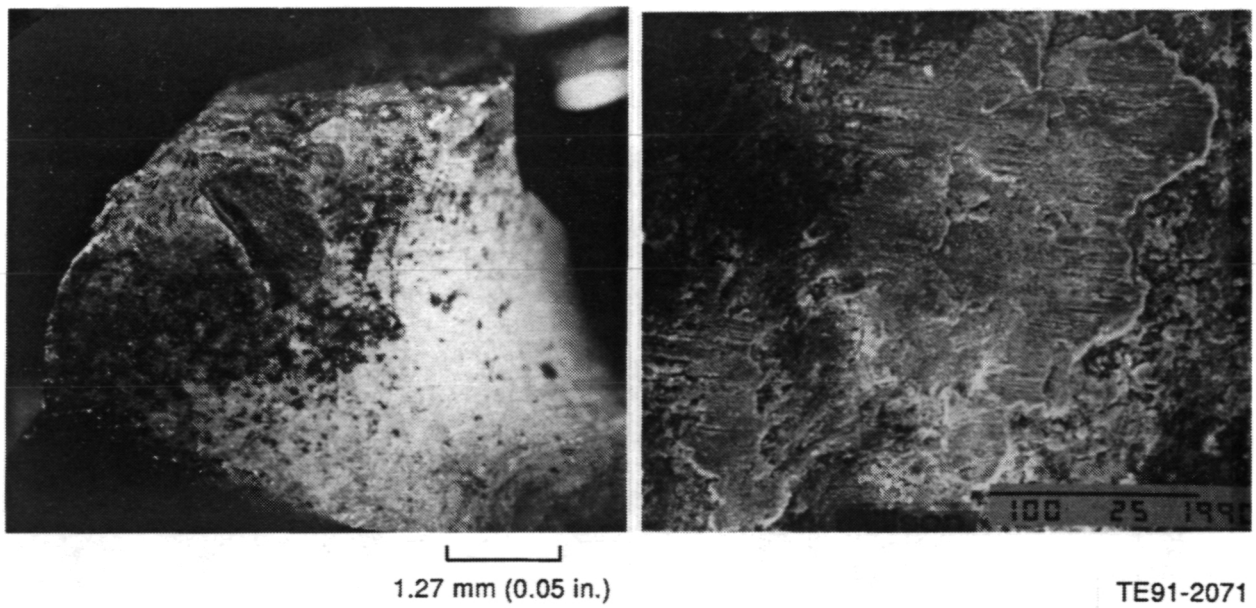

Figure 112. A representative rotor airfoil exhibited dark metallic deposits at leading edge root. This is the same airfoil shown in Figure 113.

ORIGINAL PAGE
BLACK AND WHITE PHOTOGRAPH

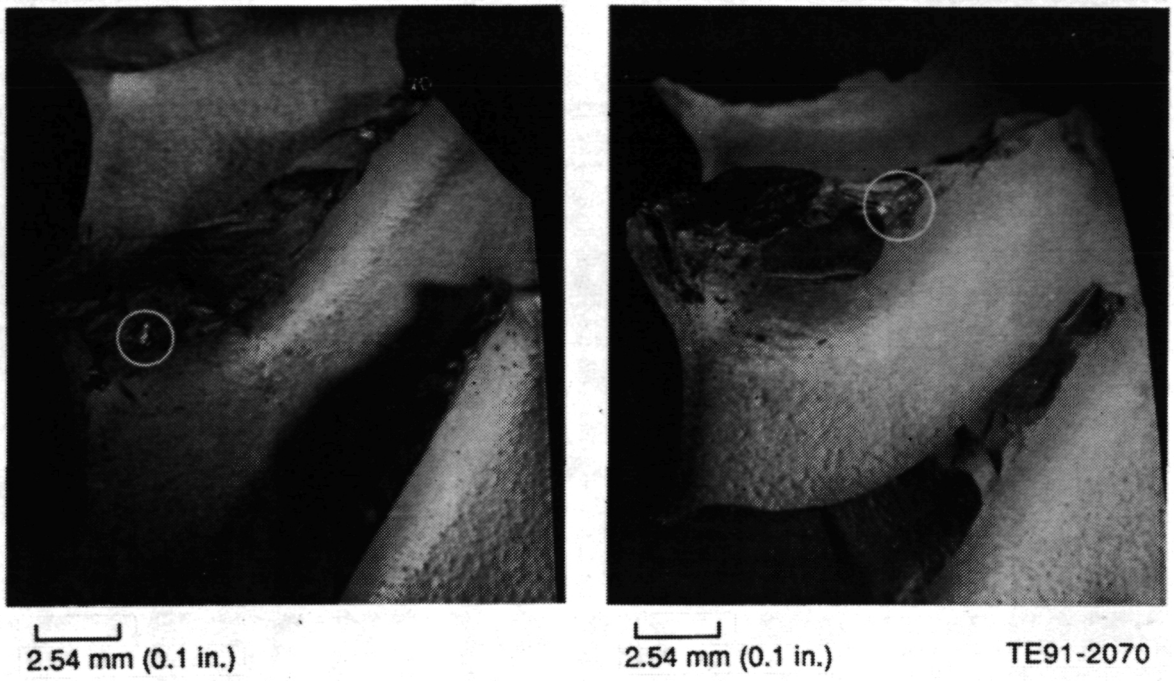

Figure 113. Representative gasifier rotor airfoil impact fracture. Golden metallic marks (circles) were found on suction surface of airfoil. Magnification = 5X.

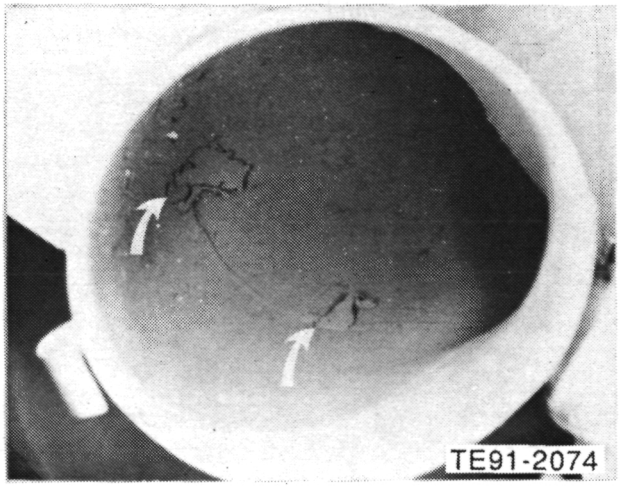

Figure 114. Two pieces of combustor dome welded to I.D. of scroll inlet.

A fracture origin was observed at the O.D. of the shroud for the longitudinal crack in the location shown in Figures 117 and 118.

The fracture surface on the aft section was oxidized adjacent to the I.D. due to the high temperature generated during the heavy rub. This fact indicated that the heavy rub occurred after the fracture. Scanning electron microscope (SEM) examination of the fracture origin indicated that the fracture initiated at the longitudinal grinding marks, shown in Figure 119. Calculation of the fracture stress based on the radius of the fracture mirror indicated a stress of 443.3 MPa (64.3 ksi), which was somewhat lower than the baseline modulus of rupture (MOR) test bar data of 559.9 MPa (81.2 ksi) at 1250°C (2282°F) and 526.8 MPa (76.4 ksi) at a temperature of 1370°C (2500°F).

Durability Engine, S/N 11, BU25. A Kyocera slip cast SN252 Si_3N_4 20-bladed gasifier turbine rotor (P/N 5-67200, S/N 5K25) was run in the AGT-5 durability engine (S/N 11, BU25) in conjunction with a Kyocera isopressed SN252 gasifier turbine shroud. Both components had been previously tested in the hot gasifier rig for 2.8 hr and had run for 1.1 hr in the engine. After a total of 5.0 hr of engine testing (including one previous engine test) at a maximum temperature of 1160°C (2120°F), a rotor/shroud rub was observed at 90% N_1 (55,000 rpm).

Figure 120 shows the as-disassembled condition of the rotor. Chipping and fracture of the airfoils was observed in six blades: two from

ORIGINAL PAGE
BLACK AND WHITE PHOTOGRAPH

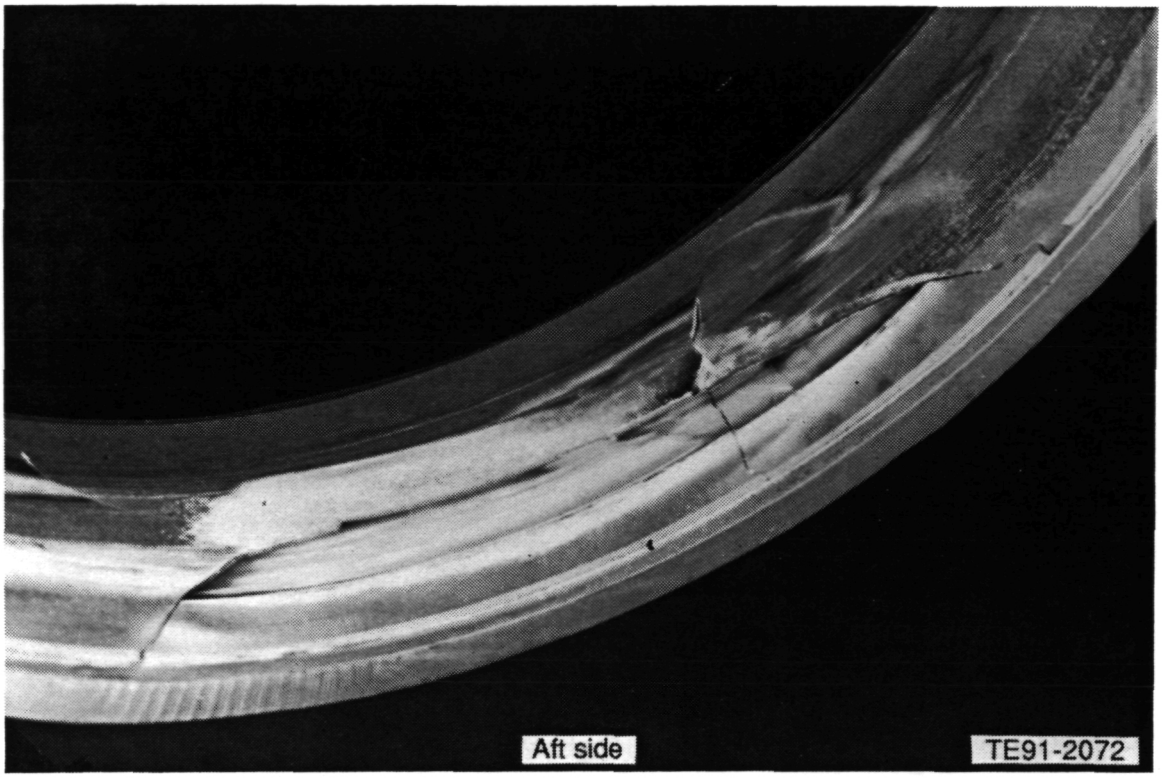

Figure 115. As-disassembled condition of the shroud.

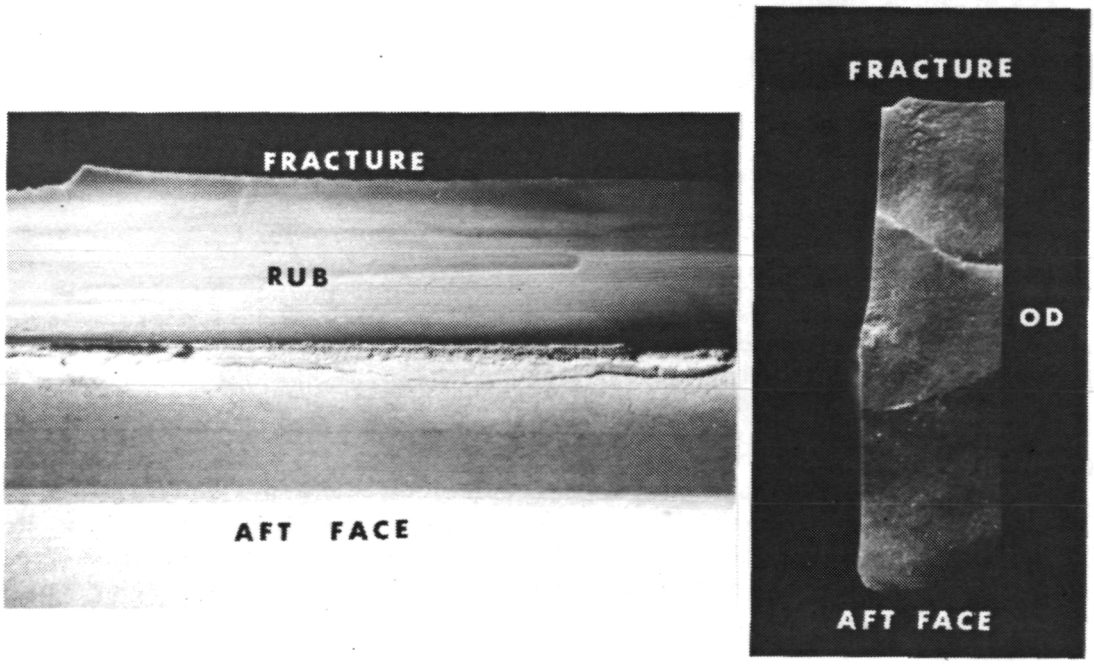

TE91-2073

Figure 116. Rubbed I.D. surface on the aft side (left) and the cross-section of the piece (right).

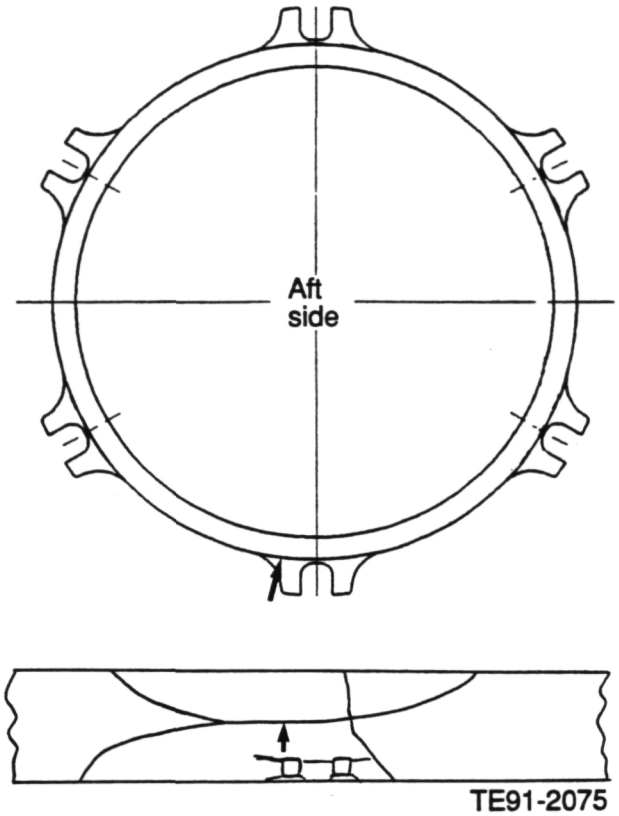

Figure 117. Schematic diagram of the fracture of the gasifier shroud. Arrows point to the fracture origin at the O.D. of the shroud.

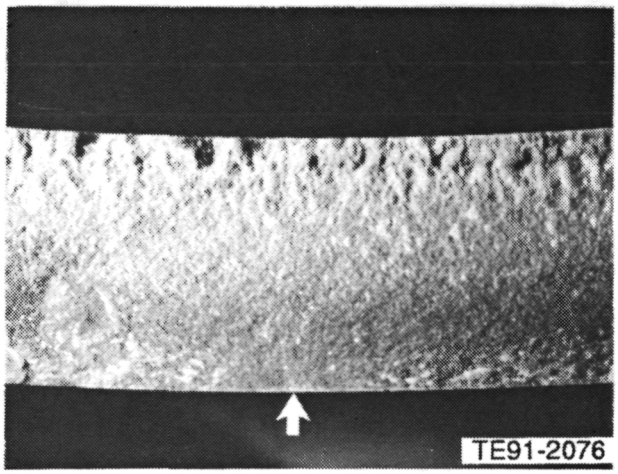

Figure 118. Fractographs of the shroud on the forward side. The fracture origin is pointed out by the arrow.

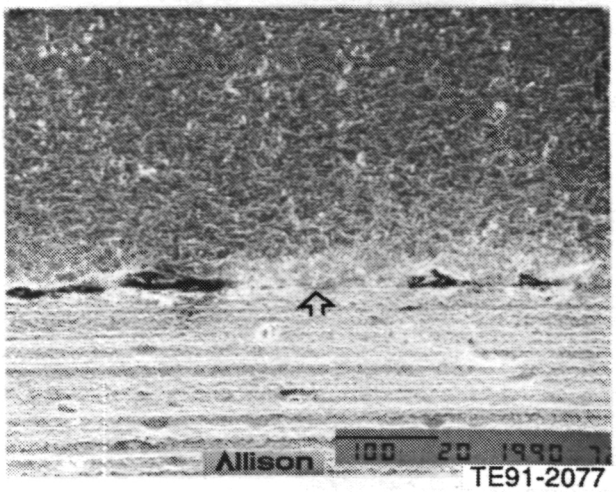

Figure 119. The O.D. surface condition at the fracture origin (arrow).

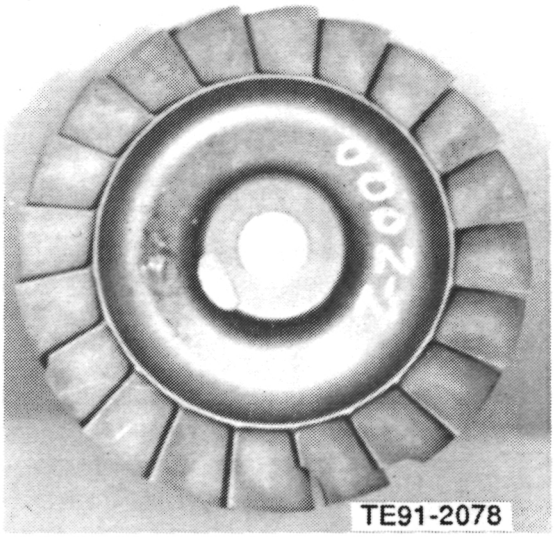

Figure 120. Kyocera SN252 Si_3N_4 gasifier rotor (P/N 5-67200, S/N 5K25) after testing in engine S/N 11, BU25.

the leading edge and four from the trailing edge. In addition, rub marks on the middle and trailing edges of the blades were observed on 10 additional blades. The fractures in blades 3, 7, 9, 10, and 13 (see Figure 121) originated from the blade tips. The fracture origins in these blades, shown in Figure 122, are basically featureless and indicative of fracture from impact damage. Additionally, witness marks of insulating material were observed on the suction side of the leading edge of blade 10 (Figure 123). Blade 8 had a fracture initiating

ORIGINAL PAGE
BLACK AND WHITE PHOTOGRAPH

Blade damage survey

3: Small chip at trailing edge (TE) tip

7: Large chip at TE tip

8: Large chip at TE tip

9: Large chip at leading edge (LE)

10: Small chip at TE tip

13: Small chip at LE

11 - 20: Rub marks on middle and TE tips

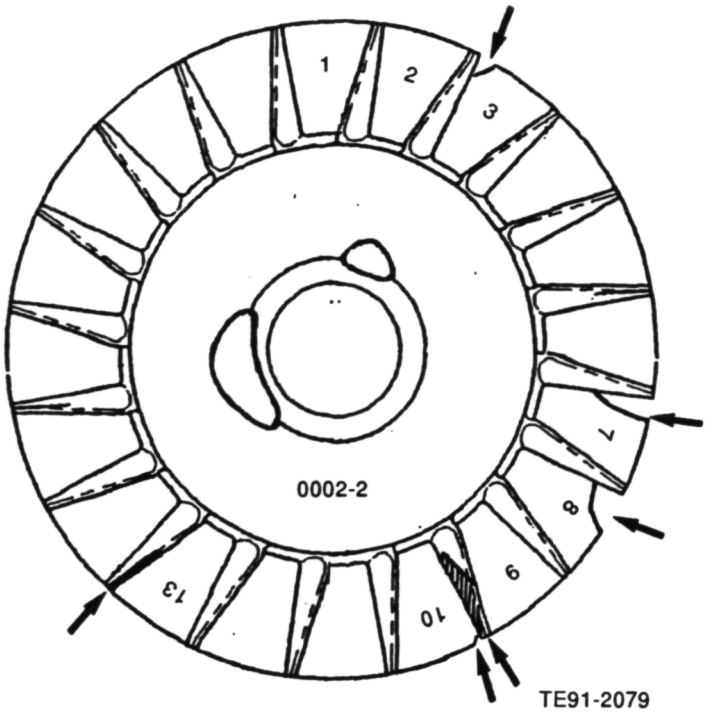

Figure 121. Schematic of damage to Kyocera gasifier rotor S/N 5K25.

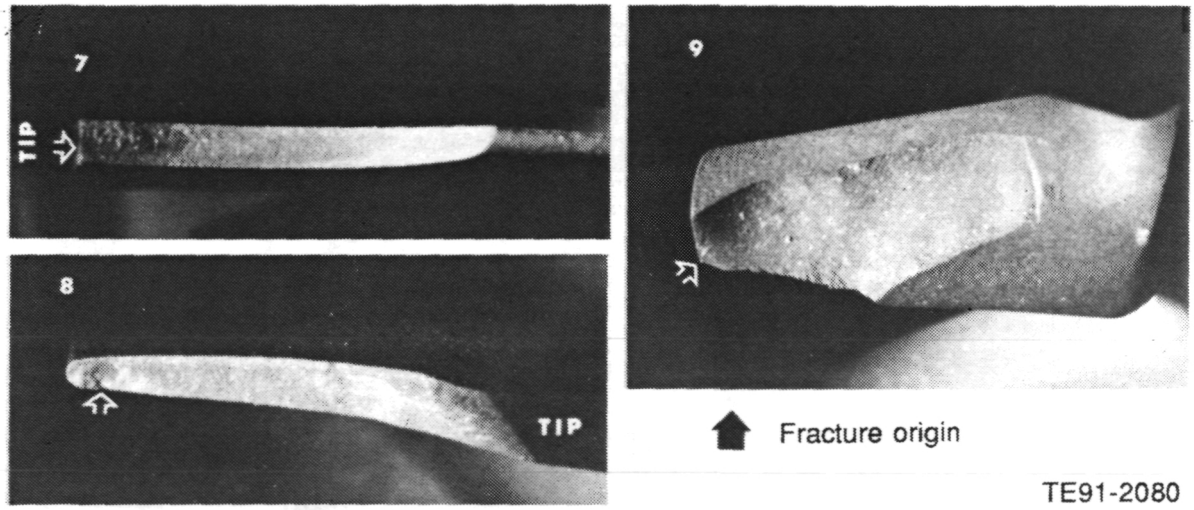

Figure 122. Fracture origins in Kyocera rotor S/N 5K25 airfoils.

from the pressure side of the airfoil near the trailing edge.

The gasifier shroud was basically undamaged, although witness marks on the I.D. were observed indicating that a rub with the rotor had occurred.

3.2 CERAMIC COMPONENT PROCESS DEVELOPMENT AND FABRICATION

This subsection details the ongoing ceramic component process development and fabrication activities at the selected ceramic component

ORIGINAL PAGE
BLACK AND WHITE PHOTOGRAPH

TE91-2081

Figure 123. Suction side of blade 10 (per Figure 121). White areas are engine insulation.

developers, including Carborundum, Manville, GTE Laboratories, Corning, Garrett Ceramic Components, Ceramics Process Systems, and Norton/TRW Ceramics. Allison's approach to ceramic component development continues to be one of subcontracting process development to the domestic ceramic manufacturing community and working in an iterative development loop with those suppliers in areas of component design, characterization, and rig/engine test data feedback.

The major focus of the component development activities at Carborundum included injection molded SiC gasifier turbine rotors, vane set development, and slip cast SiC scrolls. Manville's efforts concentrated on development and fabrication of ceramic thermal insulation for test rigs and engines. The development activities at GTE Laboratories focused on injection molded Si_3N_4 gasifier turbine rotors and vanes, as well as studies addressing toughened Si_3N_4 material systems using both microstructural and SiC whisker reinforcements. Corning was involved in development and fabrication of extruded aluminosilicate regenerator disk specimens. Garrett Ceramic Components' efforts were focused on the development and fabrication of gasifier turbine rotors using pressure slip cast GN-10 Si_3N_4. The efforts at Ceramics Process Systems addressed fabrication of CM200 sialon gasifier turbine vane platforms using their Quickset injection molding process. Norton/TRW Ceramics' efforts were directed towards development of both gasifier turbine rotors fabricated by pressure slip casting NT154 Si_3N_4 and turbine scrolls fabricated of slip cast NT235 and NT230 SiC.

3.2.1 Carborundum

Objective/Approach

The ceramic component development efforts conducted during 1990 with CBO consisted of three major tasks: improved SiC rotor processing, vane set development, and slip casting. The rotor processing and vane set development tasks focused on injection molding of sintered α–SiC while the scroll fabrication development efforts have focused on slip cast sintered α–SiC.

Accomplishments/Results

- Optimized sintering and HIPing parameters of α–SiC rotors to obtain small grain, high density, and improved strength rotor material; received 3 sintered and 12 HIPed rotors
- 113 defect-free α–SiC vanes were received.
- Six scrolls of α–SiC were successfully slip cast and sintered. One scroll was qualified for engine testing.

Discussion

Improved Rotor Processing. The improved rotor processing activities consisted of sintering and HIPing rotors fabricated in the heated mold in CY89, characterization of the rotor material, and feasibility assessment of CBO's new SX silicon carbide material for axial rotor fabrication.

The 15 rotors produced using the heated mold in CY89 were baked, sintered, and HIPed during CY90. No flow lines were visible on the surface of the green rotors fabricated in the heated mold. However, some porous inclusion-type sites were observed on the surface. The rotor compound was further screen packed to remove large inclusions. Upon completion of the compounding, a total of 18 particles were extracted from the screen pack which included 15 large SiC particulates originating from the silicon carbide milling media. Only one of the particulates contained stainless steel media.

ORIGINAL PAGE
BLACK AND WHITE PHOTOGRAPH

Sintering cycles of complex shapes such as the axial rotor with varying cross-sections must be optimized to obtain uniform density and microstructure which translate into improved strength of the material. A typical as-sintered α silicon carbide rotor was sectioned. Photomicrographs revealed that the hub region had the highest porosity. Typical grain size was 13 microns, with the smaller grains at 4 microns and the larger grains ranging from 40 to 56 microns. In order to reduce the range of grain size and maintain a reasonable density, experimental rotors were sintered at three temperatures: the standard sintering temperature of X°C, (X-15)°C, and (X-40)°C. The photomicrographs of the three rotors are shown in Figure 124. The density of the rotors and a microstructural summary are listed in Table XXVIII.

The primary reason for investigating the effects of sintering temperature, prior to HIPing, on rotor characteristics is that Uematsu demonstrated that lower presintered temperatures in alumina resulted in a finer grain size which, upon post-HIPing, ultimately produced a finer grain size and higher density. In addition, Druschitz and Schroth found that HIPing below the sintering temperature to minimize grain growth of presintered material which contained no open porosity led to a significant increase in strength. Results in Table XXVIII show that the material sintered at X-15°C exhibited the highest density and the smallest grain size.

Several rotors processed at the three sintering temperatures were also HIPed and sectioned into MOR test bars to evaluate the material strength characteristics as a function of sintering temperature. Results are summarized in Table XXIX. Post-HIPing of axial turbine rotors resulted in an increase in strength of between 44 and 82% depending on the initial sintering temperature. The average grain size of the rotors sintered at X°C (the standard sintering temperature) was 8 microns and that for (X-15)°C and (X-40)°C was 5 microns. The lower strengths of the as-sintered rotor test bars are probably due to the low density core region as previously identified by computed tomography. Based on these results, all the rotors were sintered at (X-15)°C temperature. Three of the 15 rotors were only sintered and the remaining 12 were sintered and HIPed.

Table XXVIII.
Carborundum SiC rotor sintering matrix.

Rotor No.	Sintering temperature--°C	Density--g/cc	Grain size--microns		
			Average	Small	Large
261	X	3.150	8	4	19
412	X-15	3.156	5	2	11
417	X-40	3.137	5	2	14

Table XXIX.
Properties of CBO sintered and sinter/HIPed α-SiC rotors.

	Sinter temperature		
	X°C	(X-15)°C	(X-40)°C
Density--g/cc			
as-sintered	3.147	3.152	3.150
post-HIPed	3.173	3.175	3.184
Strength--MPa (ksi)			
as-sintered	376.5 (54.6)	385.4 (55.9)	327.5 (47.5)
post-HIPed	561.3 (81.4)	556.4 (80.7)	595.7 (86.4)

ORIGINAL PAGE
BLACK AND WHITE PHOTOGRAPH

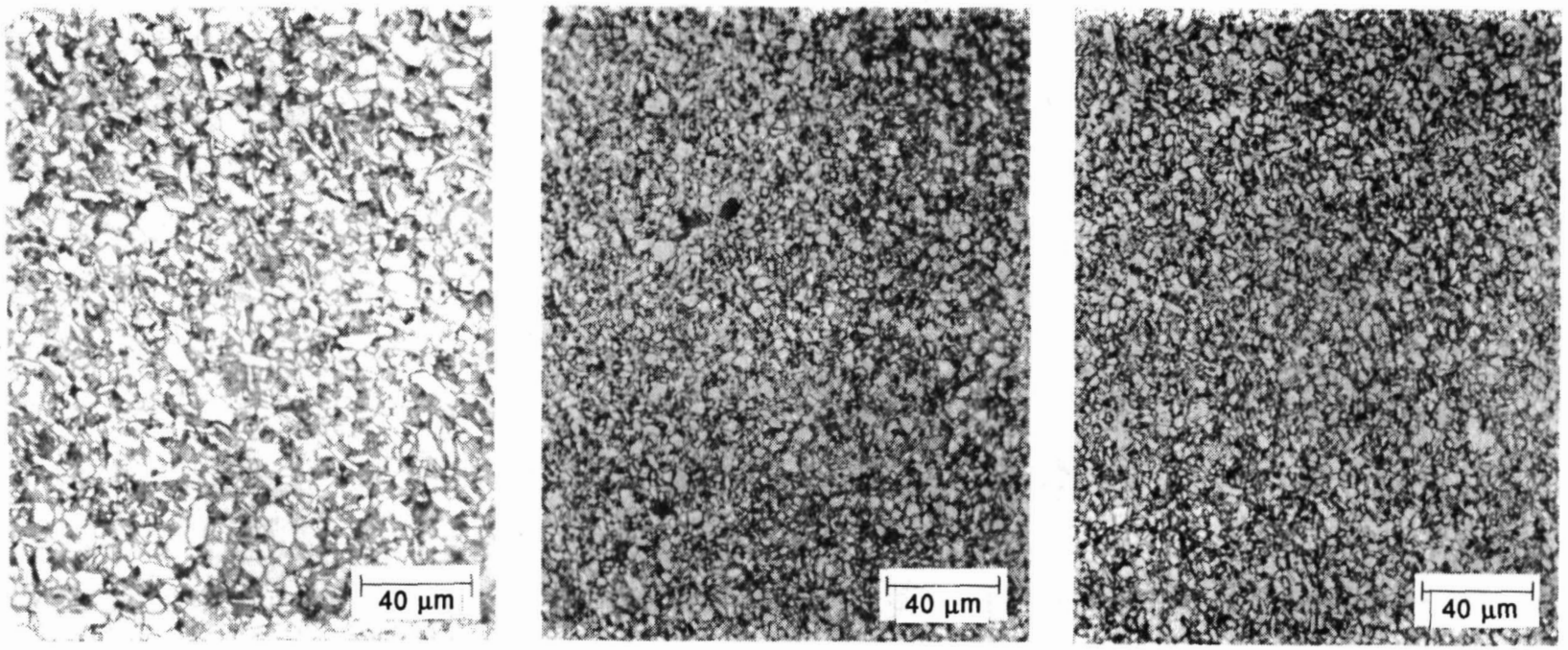

a. X°C

b. (X - 15)°C

c. (X - 40)°C

TE91-2082

Figure 124. CBO sintered α–SiC microstructures. X°C is the standard sintering temperature.

During July 1990, the α–SiC rotor activity was redirected to focus on CBO's sintered SX material for rotor fabrication. The α–SiC material does not possess the mechanical properties to meet the transient loading conditions of the gasifier rotor. The baseline properties of the SX material are discussed in subsection 3.1.1. Preliminary powder processing and compound development activities on this material proceeded slowly and the work on this task was discontinued in October 1990. The development of this material is currently in progress under a DOE/ORNL funded program at CBO.

Vane Set Development. Development activities were conducted to address the fabrication of injection molded sintered α–SiC vanes for the gasifier turbine. Inspection of the vanes delivered during 1989 revealed small indications on the leading and trailing edges of the vanes which were caused by the diamond tools used to remove excess flash. The vane injection molding tool was modified in 1990 to eliminate the extra flash with the injection gate moved to the end of the platform and made 0.15875 cm (1/16 in.) round and radiused into the part. The original design used a rectangular gate fully radiused and entering the platform at a 45 deg angle (as shown in the top left photo of Figure 125) so that the melt stream impinges a wall and a flow front is created. The sintered part, however, had a slight undulation in the platform surface, as shown in Figure 125 (top right). A 0.15875 cm (1/16 in.) round and radiused gate into the platform end (shown in Figure 125 bottom left photo) produced a continuous sintered platform radius, as shown in the photo at the lower right of Figure 125.

Over 300 vanes were injection molded. A total of 170 vanes were subsequently sintered and subjected to FPI and X-ray after grit blasting. A total of 113 defect-free vanes were delivered to Allison in June 1990, completing the deliverable requirements.

Slip Casting. The objective of the slip casting development task involves fabrication of slip cast scrolls to be evaluated in rig and engine test activities, optimization of slip properties, and low pressure casting studies for scroll fabrication.

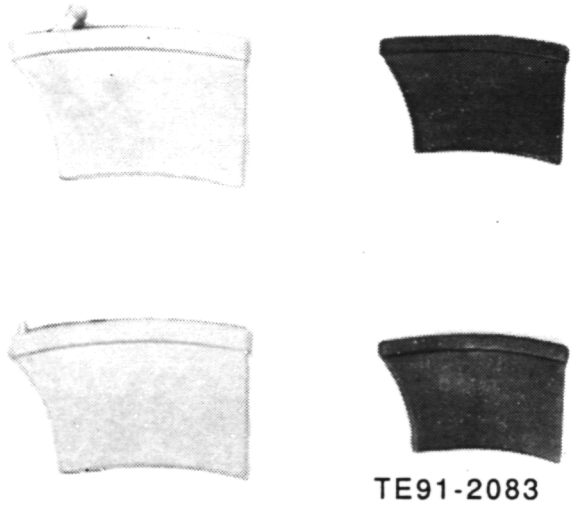

Figure 125. CBO molded and sintered vane iterations.

Several different scroll mold configurations were tested in 1990 in an effort to fabricate crack-free engine-quality scrolls. The majority of the scrolls failed during casting from a crack in the throat area. The first change was the introduction of a disposable piece of soft plaster to form the throat intersection. This piece was not removed during demolding to avoid any stressing of the part in that region. Several scrolls were slip cast and sintered, and all had small hairline cracks in the throat region. The second mold modification was to split the top half of the mold into two sections. The mold half covering the neck and the throat area was clamped in place while the other mold pieces were removed. This approach also led to cracks in the throat.

The third configuration involved changes to the center core sections of the original mold design. The first change involved making the five core pieces without the interlocking notches normally used to align the mold sections. Eight scrolls with different throat geometries were cast from this mold type with no notable problems. The fourth mold design incorporated the noninterlocking core region in conjunction with relocating a parting line away from the throat area. The number of mold core sections was also reduced from five to four pieces. All molds previous to this design had one core seam located 0.635 cm (0.25 in.) to 1.27 cm (0.5 in.) from the throat base. The core

ORIGINAL PAGE
BLACK AND WHITE PHOTOGRAPH

pieces were redesigned so that the nearest seam was 3.81 cm (1.5 in.) from the throat area.

Throat area radii and shape were changed to ascertain their effect on throat cracking of the scroll. A noninterlocking core-type mold and a disposable insert mold were used to test the three model changes. Figure 126(a) shows a sintered scroll with the original throat shape. Figure 126(b) shows a sintered scroll with increased throat area radii blended into the rest of the part. The small change in the throat from Figure 126(a) to 126(b) resulted in a significant decrease in casting yield with all scrolls cracking during sintering. In the second model the junction was moved forward approximately 0.635 cm (0.25 in.) Figure 126(c) shows a sintered scroll with the forward throat design. The casting yields for this throat configuration were higher than for 126(b); however, the casting and sintering yields were no better than the original model design. A final change was made by moving the throat forward approximately 2.54 cm (1 in.) from the original design. This change is shown in the sintered scroll in Figure 126. This radial change from the original shape resulted in a casting yield for this configuration at about 80%, and one out of three parts sintered passed dimensional and FPI inspections.

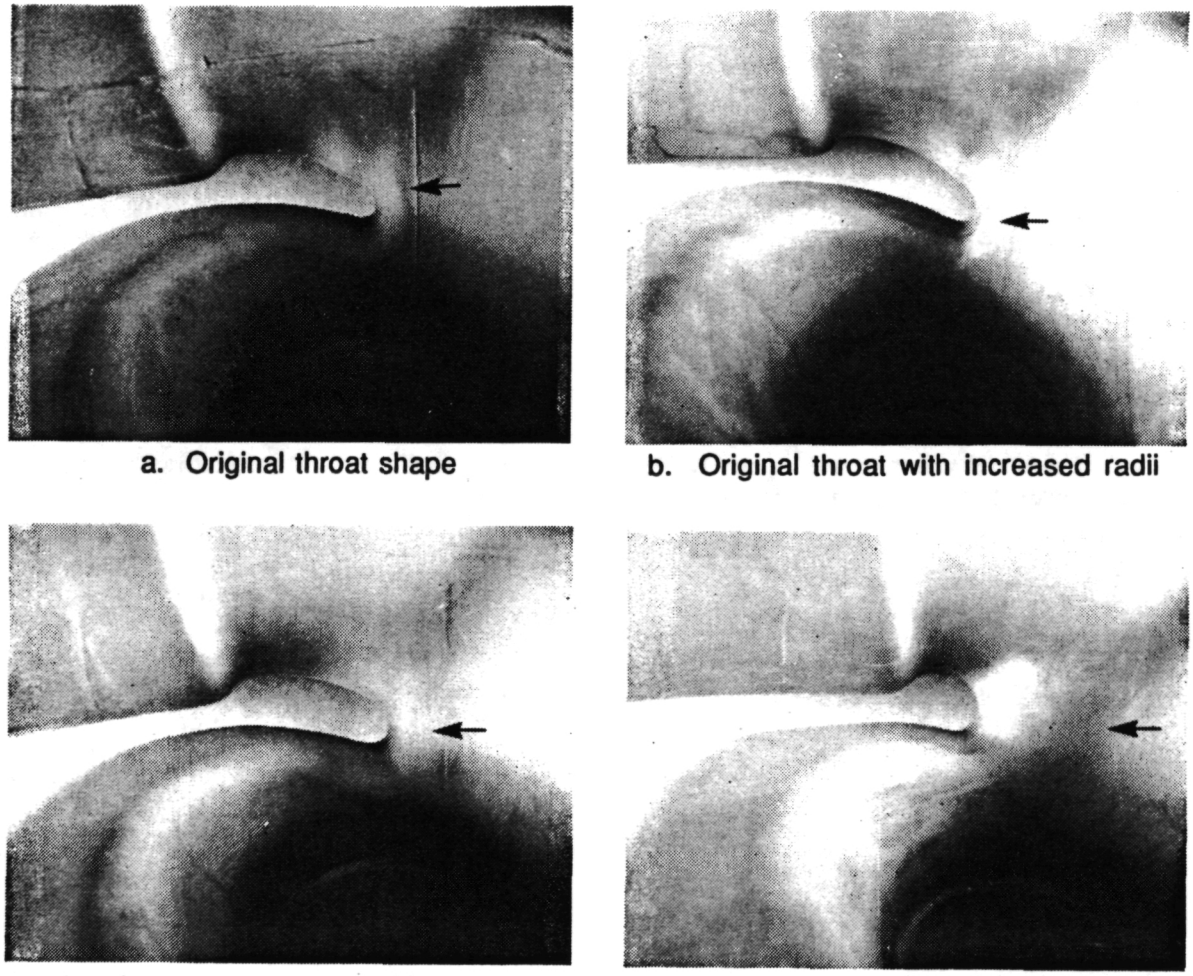

a. Original throat shape

b. Original throat with increased radii

c. Junction moved forward 0.635 cm (1/4 in.)

d. Junction moved forward 2.54 cm (1 in.)

TE91-2084

Figure 126. CBO scroll configurations.

ORIGINAL PAGE
BLACK AND WHITE PHOTOGRAPH

Casting and mold filling procedures were also varied to assess their impact on the throat area cracks. The first change was to cover the scroll opening while the part dried in the mold. During drying, the combustor end of the scroll is directly open to the atmosphere and dries faster than interior sections. Only one of the eight scrolls cast and dried in this manner demolded without cracking in the throat and it cracked after sintering. The second procedural change involved casting the part at a different angle. Normally the mold is filled through the combustor end opening with that end facing up. Angular casting did not fill the molds completely and large air pockets were observed on two of the inner walls when scrolls were cast with the molds upside down or on their sides. This inadequate filling and venting was attributed to the scroll mold design. The third casting procedure change entailed smoothing the casting along the seams and throat with a diluted slip. The seams and the throat were blended with the rest of the part while the part was still somewhat wet after casting. This procedure eliminated the need for presinter cleaning and filled and/or blended surface flaws that later would show as FPI indications.

Based on the above experimental results, a final scroll casting process was established which included several mold and processing changes. The model was not altered and maintained the original throat geometry. The optimum mold for the scroll was the disposable insert type with a four-piece, instead of the previously used five-piece, core section. This configuration was the easiest to work with for demolding and provided the highest casting yield. A change to the demolding procedure was also found to be an important factor. The disposable insert was cut from the cast part while it was still somewhat wet to eliminate or minimize any crack producing stresses in the throat area.

A combination of processing changes was also implemented. The seams and the throat were wiped down with a dilute slip when the part was still wet after demolding. This procedure eliminated the need for the more time consuming sanding after the part dried, and also filled in the seams and throat with additional submicron-sized material. A presintering step was added to the process which increased the processing time but reduced the probability of stressing the part.

Six scrolls were fabricated and selected for machining according to the above process to yield structurally, dimensionally, and NDE acceptable parts. Three scrolls were delivered in September 1990. One scroll had no machined vane pockets, whereas the other two scrolls had machined vane pockets. One scroll with vane pockets had an open pore adjacent to the cross-key area. The pore was blended and the scroll was qualified to be tested in the rig/engine. The other scroll cracked in the shroud area and was rejected for rig/engine testing. A fourth machined scroll was received in November 1990 and qualified for rig/engine testing. Two additional scrolls are currently unmachined. Further machining efforts are on hold pending rig/engine test results of the scrolls already qualified.

The slip and low pressure casting efforts were initiated in July of 1990 to further understand slip rheological behavior and its effect on cast properties. The factors for both the experiments were as follows:

Slip optimization	Cast variables
Grit concentration	Casting time
Slip pH	Casting pressure
Percent solid	Casting attempt

The slip rheology and pressure casting parameters were optimized using a rectangular one-piece crucible plaster mold. The various relationships of pH, grit concentration, and percent solids loading were found to be no different than normal drain casting parameters. When the slip pH was high, the casting stuck in the mold because the dispersed fines locked into the pores, thus complicating demolding. When the pH was low, the green and sintered densities decreased due to the increased flocculation of the system.

The effects of grit concentration and solids loading were less pronounced than pH. It was found that as the grit concentration is decreased, the green densities also decrease but the sintered densities improve. This was consistent with past observation where finer particle size distributions that do not pack well showed higher sintered densities due to the

better sintering kinetics associated with high surface area/small sized powders. The solids loading had essentially no effect on the properties monitored.

Parametric studies were conducted to determine the effect of slip rheology on the low pressure casting behavior and properties. The cast wall thickness increased with increasing casting pressure (see Figure 127) with a substantial decrease in casting time as expected. The increase in casting rate substantially reduced the total cycle time for a casting. For example, a scroll that typically takes 20-25 min. could be reduced to 5-6 min. with the application of pressure. Another interesting result, shown in Figure 127 is that wall thickness of over 1.27 cm (1/2 in.) are possible with the application of pressure. The maximum wall thickness for drain casting typically levels off at about 0.953 cm (3/8 in.) However, the 1.27 cm (1/2 in.) part only sintered to 93% theoretical density due to inadequate distribution of the presintering aid. Uniform dispersion of the aid is very desirable. Another observed advantage of low pressure casting is that four or more castings could be fabricated from a given mold, compared to one or two by drain casting, before the mold saturates, thereby decreasing the casting rate and requiring drying before reuse.

Experiments conducted under low pressure casting conditions (207 Pa (30 psi) for 20 min) indicated that as the slip pH was increased, the wall thickness and the casting rate both decreased because the highly dispersed slip plugs the mold rapidly. The casting pressure had very little or no effect on green and sintered densities of the cast. Green densities increased with broader particle size distribution as expected. Surprisingly, the sintered density increased with a decrease in green density. The reason for this trend was that finer particles (low grit) sintered more readily than coarser particles even though they do not pack as well. The mold release became poorer as the pH increased because the higher concentration of dispersed fine particles closed the mold porosity and caused sticking.

Powder beneficiation and dispersion studies were conducted using three dispersants. They were dispersed individually in the slip or as a suitable mixture. It was observed that the beneficiated powder required less dispersant and possibly one or two dispersants to achieve the state of dispersion that is required by the normal slip. Low pressure casting experiments revealed that beneficiated powder does not adversely affect the casting process. The average

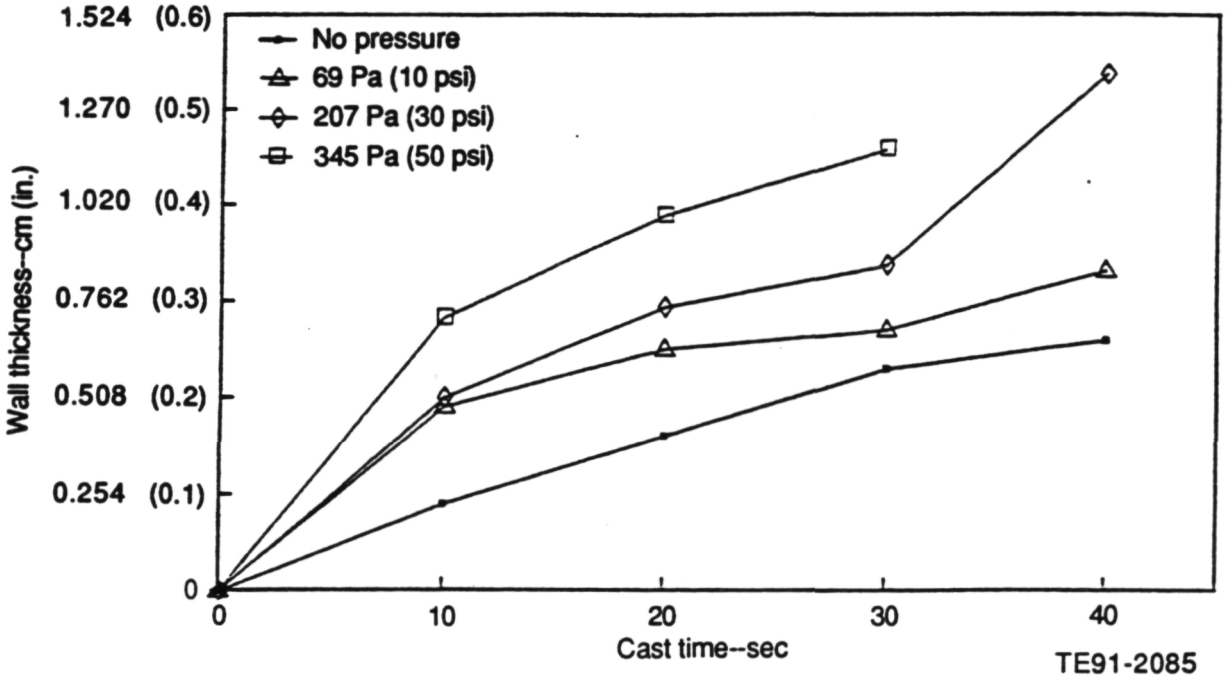

Figure 127. Effect of casting time and pressure on wall thickness; CBO low pressure slip casting.

sintered density of the cast material was 3.08 g/cc which is comparable to the normal slip. Powder milling studies, which began in late 1990, will continue to ascertain the optimum particle size distribution for slip casting.

3.2.2 Manville

Objective/Approach

Efforts at Manville are aimed at developing an injection moldable insulation capable of low-cost high-volume production for automotive gas turbines. The approach is to modify the insulation material system for improved injection molding properties while developing the injection molding process for both simple and complex engine components. In addition to the development of the molding process, several other developmental items are being addressed including: insulation/metal hardware bondability, erosion resistance, and nonhazardous nonrespirable materials.

Accomplishments/Results

- Completed initial molding of gasifier housing utilizing a mold release agent
- Completed initial molding of engine block with wax inserts and machined polyurethane foam inserts
- Designed removable metal inserts for injection molding trials of the engine block
- Molding trials indicate that the engine block can potentially be insulated using removable inserts
- Performed mixing experiments to eliminate drying shrinkage and water "bleeding"
- Initial application of two-part surface layer hardening agent for erosion resistance has been tested
- A simple fiber washing with water appears to provide the benefits of fiber milling without the increased shrinkage seen with the very fine opening screen on the hammermill

Discussion

Release agents were evaluated and optimized during insulation injections into the gasifier housing mold. The optimized release agents allowed the gasifier housing mold to be easily removed without disturbing the insulation surface. The injectability of the insulation was compromised by water "bleeding" from the material.

The drying shrinkage and water bleeding appear to be related to the dispersion, solution, and amount of one of the organic polymers in the insulation formula. Mixing sequence, time, and speed experiments indicated that these parameters have significant impact on the molding and drying characteristics of the insulation. Additionally, the ratio of several components of the inorganic binder system appears to have an impact on the drying characteristics. Batches of insulation were prepared with varied ratios of the colloidal silicas. The length, width, and thickness drying shrinkages are shown plotted versus colloidal silica ratio in Figures 128 through 130, respectively. Dry density of the molded insulation is plotted versus colloidal silica ratio in Figure 131.

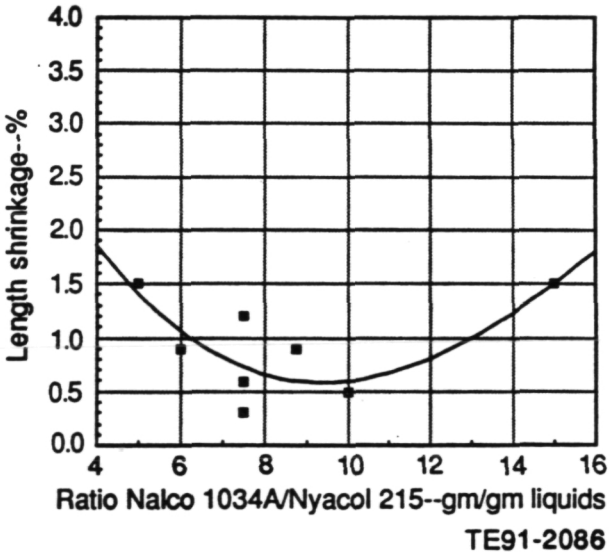

Figure 128. Length shrinkage versus colloidal silica ratio: Manville insulation.

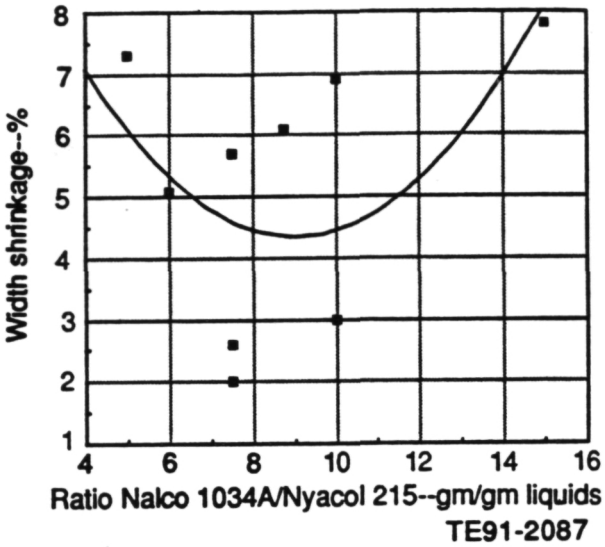

Figure 129. Width shrinkage versus colloidal silica ratio: Manville insulation.

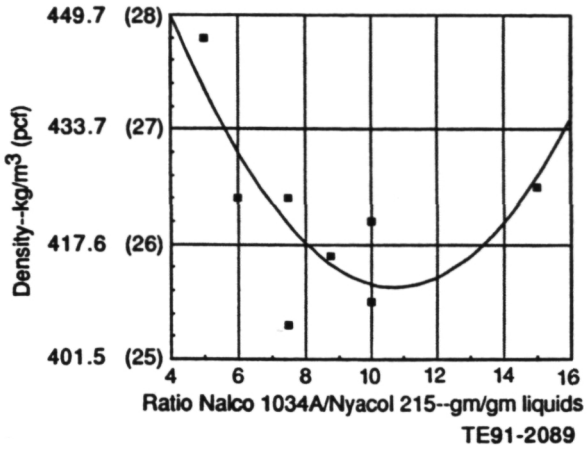

Figure 131. Dry density versus colloidal silica ratio: Manville insulation.

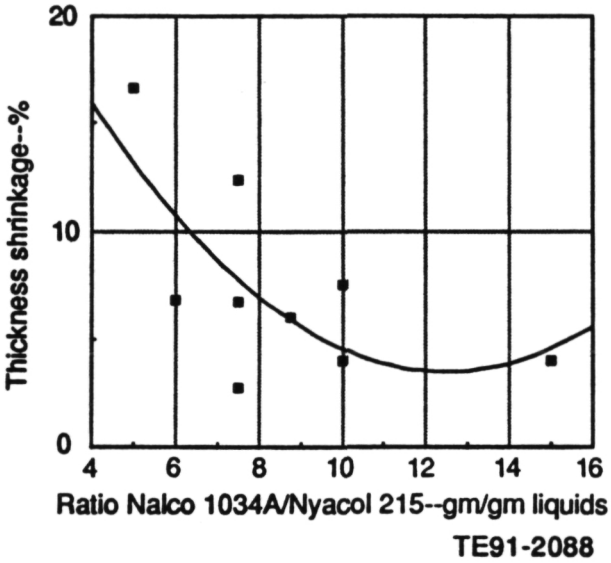

Figure 130. Thickness shrinkage versus colloidal silica ratio: Manville insulation.

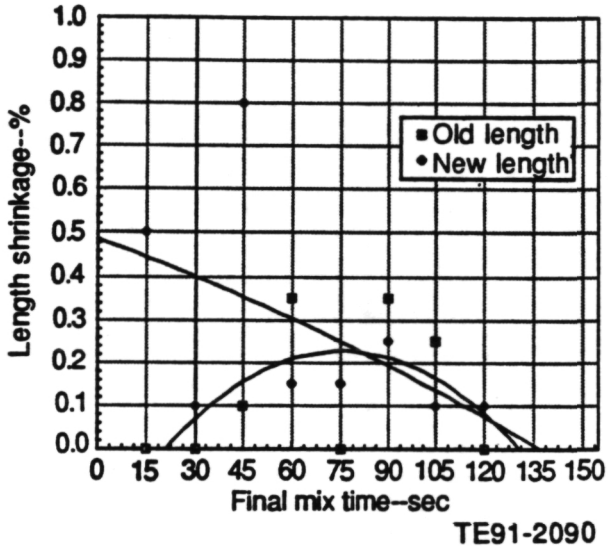

Figure 132. Length shrinkage versus mixing time for both old and new polyox batches: Manville insulation.

Additional batches have been prepared to identify the formulation parameters which affect the performance of the polyox. The length, width, and thickness drying shrinkage and dry density of the molded insulation are plotted respectively against mixing time for both old and new polyox batches in the Figures 132 through 135. Enough variation appears between lots/batches of polyox such that the insulation formulation must be adjusted for each batch to balance the moldability, water retention, and drying shrinkage characteristics. Revised formulation amounts and mixing procedures have been established for molding experiments and hot gasifier rig evaluation.

Additional injection molding trials were performed with the insulation formulation modified to control shrinkage and water bleeding and utilize hammer-milled high temperature fibers. Use of hammer-milled fibers yields

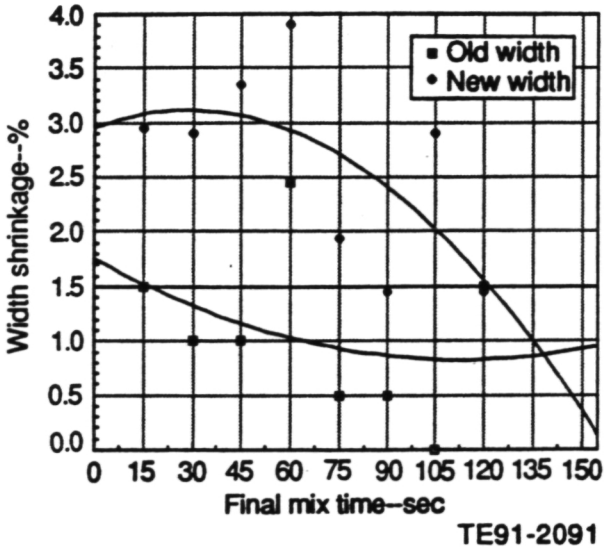

Figure 133. Width shrinkage versus mixing time for both old and new polyox batches: Manville insulation.

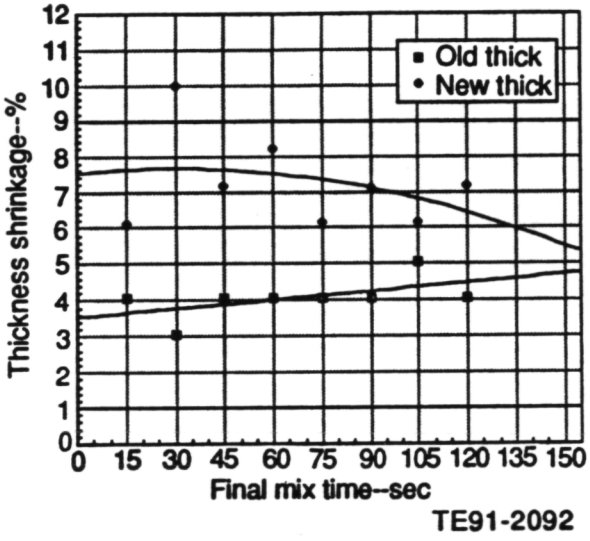

Figure 134. Thickness shrinkage versus mixing time for both old and new polyox batches: Manville insulation.

wet insulation with a smoother consistency than raw unprocessed fiber. Injection molding with the smoother consistency resulted in the best gasifier housing mold fill-out and the best surface finish of all the molding trials performed to date.

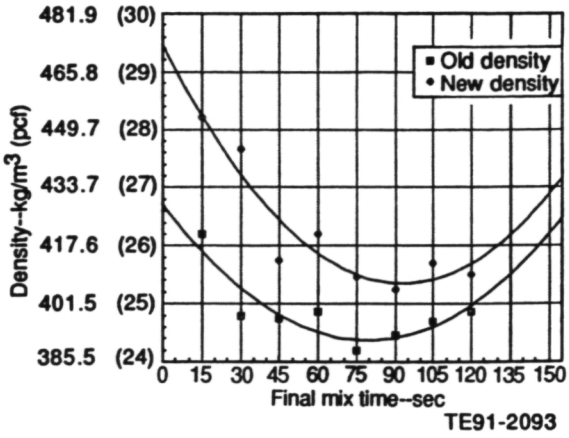

Figure 135. Dry density versus mixing time for both old and new polyox batches: Manville insulation.

Batches of insulation prepared with formulation modifications to control shrinkage and water bleeding and to include hammer-milled high temperature fibers were evaluated for drying shrinkage. The shrinkage increased to higher than desired values. Table XXX compares the desired and measured shrinkage values.

A storage-life limit for one of the colloidal silicas was thought to be a potential cause for the increased shrinkage. Fresh colloidal silica was obtained and eight new batches of insulation were formulated and evaluated. Drying shrinkage remained high throughout all batches as shown in Table XXXI.

A review of the shrinkage performance indicates that the degree of fiber milling may have an impact on the drying shrinkage. Preliminary batches of insulation prepared with fiber processed through different hammermill screen sizes indicate that a lower limit of screen size opening exists at about 12.7 mm (0.5 in.) Figures 136 and 137, respectively, show the effects of fiber milling on drying shrinkage and dry density.

Table XXX.
Drying shrinkage comparison: desired versus measured.

	Desired	Measured
Drying shrinkage		
Length	<0.5%	1%
Width	<1%	3-10%
Thickness	<2%	5-10%
Dry density--kg/m^3 (lbm/ft^3)	<353.4 (<22)	401.5-465.8 (25-29)

Table XXXI.
Evaluation of fresh colloidal silica impact on drying shrinkage.

	Measured range (8 batches)
Drying shrinkage	
Length	1-2.6%
Width	4-11%
Thickness	5-20%
Dry density--kg/m^3 (lbm/ft^3)	401.5-497.9 (25-31)

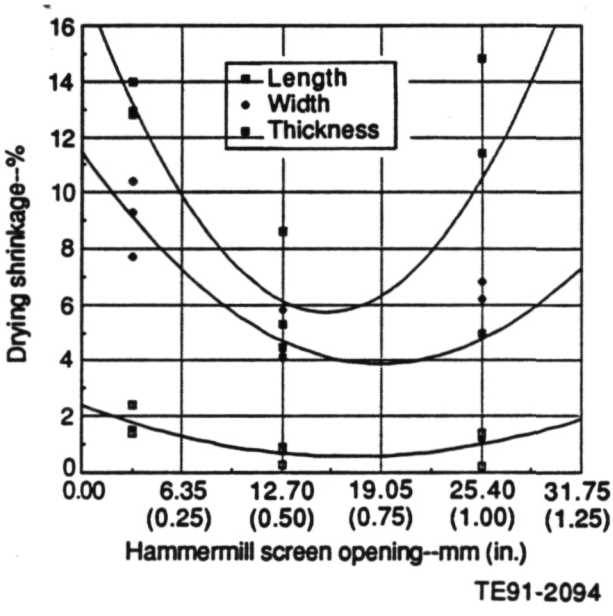

Figure 136. Effect of fiber milling on insulation drying shrinkage: Manville insulation.

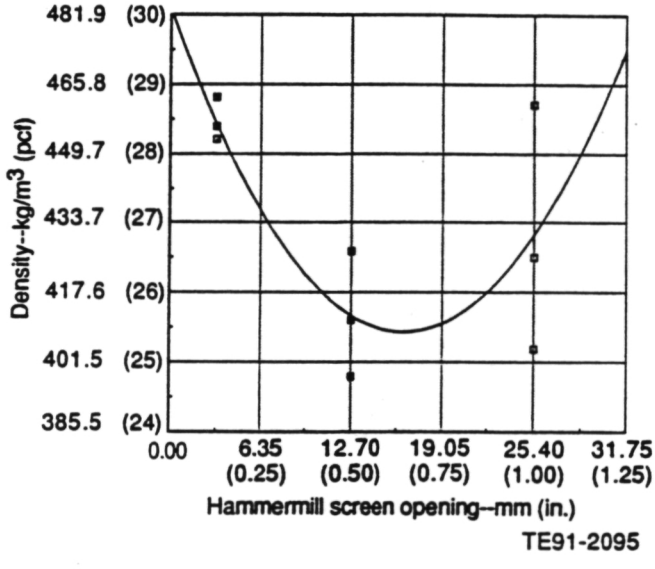

Figure 137. Effect of fiber milling on insulation dry density: Manville insulation.

The second attempt at insulation injection into the complex gas turbine housing has shown some promise. Machinable wax cores were used. The cavities filled completely and the wax cores were not dislocated as with previous attempts utilizing Styrofoam cores. After drying, the wax cores were removed by heating the housing to 93.3°C (200°F), which allowed the wax to melt and run out of the housing. The surface of the insulation was not contaminated by the wax.

The engine block was successfully injection molded with machined polyurethane foam inserts. Indications are that the block can potentially be insulated via injection molding with removable inserts.

A two-part surface layer hardening system of alumina and silica has been applied to the dried, unfired insulation on several engine pieces and subjected to the high temperature environment of the test rigs. The surface appears to be harder than the untreated surface, but is not as hard as a dense ceramic coating. The development of a one-part combined alumina-silica hardening agent is being explored.

An alumina hard-coating was flame sprayed onto a cured insulation sample for evaluation of erosion resistance. The coating appears to be a significant improvement over the previous surface hardening system and may potentially provide adequate erosion resistance in the engine environment.

Alumina was plasma spray applied to the insulation. The coating was characterized as having undesirable microcracks and several blisters. Modification of the plasma to impart less heat to the powder, increased spray transverse speed, and an insulation preheat resulted in coatings with little porosity and no microcracks. The plasma sprayed alumina coating appears to be an improvement over the flame spray applied coating.

3.2.3 GTE Laboratories

Objective/Approach

The ceramic component development activities at GTE have been focused on three main objectives: (1) to develop PY6 Si_3N_4 fabrication technology for axial turbine rotors and vanes, (2) to improve monolithic PY6 Si_3N_4 toughness using microstructural modifications, and (3) to improve the toughness of PY6 Si_3N_4 using SiC whisker reinforcement.

Accomplishments/Results

- Process established for fabrication of PY6 Si_3N_4 gasifier turbine rotors
- 20 PY6 Si_3N_4 turbine rotors fabricated and delivered
- HIP test matrix designed and conducted
- The final batch of PY6 Si_3N_4 turbine rotors with 30 v/o SiC whiskers were fabricated

Discussion

Task I--Rotor Shapemaking Development for AY6/PY6 Rotors. The Task I effort in rotor shapemaking development has primarily focused on fabrication of PY6 Si_3N_4 AGT-5 gasifier turbine rotors. As a result of the change to Ube silicon nitride powder from the prior SN502 powder, the cracking tendency of large cross-section parts, such as the rotor, during the binder removal step has increased significantly. The cracking was most commonly observed at the junction of the rotor shaft and hub.

Initial activities were directed towards the refinement of an alternate injection molding procedure which utilizes small additions of a binder removal aid. This procedure was developed during GTE in-house research and showed potential for greatly improving resistance to crack formation during binder removal without compromising final mechanical properties. The rotors were fabricated and observed to be consistently free of typical binder removal cracks. The process initially resulted in residual rough areas of both hub faces and the blades. Although not yet optimized, a relatively simple adjustment to the normal HIP cycle was able to produce an acceptable as-HIPed surface.

Preliminary material evaluation indicates that the burnout aid approach did not appreciably degrade the material strength characteristics. Two PY6 Si_3N_4 rotors (Nos. 398 and 428), which were processed with burnout aids,

were sectioned after HIPing into test specimens measuring 25.4 x 2.54 x 1.27 mm (1 x 0.1 x 0.05 in.). The strength results are summarized in Table XXXII. The strength measurements, particularly for rotor No. 428, show the potential of the current process. The reduced room temperature strength values observed in rotor No. 398 were attributed to the 5 to 10% residual alpha Si_3N_4 remaining in the rotor after densification. The presence of the alpha Si_3N_4 may indicate a need for additional time at temperature to achieve full alpha-to-beta conversion. Also of note is the fact that both rotors showed higher 1370°C (2500°F) strength levels relative to earlier PY6 Si_3N_4 rotors.

Concurrent with the binder related activities, the injection molding tool was modified to improve its performance for fabricating deliverable components. The modifications which were made are as follows:

- Increase the 1 mm (0.04 in.) radius at the base of each blade to the correct value of 2 mm (0.08 in.) as specified in the rotor drawing.
- Revise the tool to achieve a cavity vacuum of 254 mm (10 in.) of mercury or better, measured by a gage placed at the sprue bushing.
- Tighten the blade inserts against the scroll plate to minimize stresses created by the motion of the inserts during mold opening.
- Fabricate a new hub insert for the side opposite the shaft, allowing for 0.75 mm (0.03 in.) of additional grind stock for a total of 1.14 mm (0.045 in.).
- Machine the existing hub insert for the shaft side, increasing the stock an additional 0.5 mm (0.02 in.). The additional stock will begin where the blade overhang meets the hub and continue through the radius into the shaft.

Initial molding trials with the modified tool were very successful. The cavity evacuation capability coincided with the disappearance of surface blisters on the molded parts. Based on the quality of the initial molded parts, a decision was made to discontinue efforts with the binder removal aid process and concentrate on the original monolithic PY6 Si_3N_4 process. The first series of binder removal runs with the rotors fabricated using the modified injection molding tool were encouraging. The burned out parts did not exhibit the large hub and shaft cracks that were frequently observed in monolithic rotors processed prior to the recent tooling modification.

The tooling changes did not resolve the problem with fold lines on the backface of the rotor. Although these fold lines are present in an area of generous grinding stock, they frequently open up during HIPing and allow HIP glass penetration into regions deeper than the allowable machining depth. These fold lines result from the freezing of the material first injected into the mold cavity. Also, since mold release is applied at the entrance of the cavity (sprue), the freezing material carries along some of the mold release, which then becomes entrapped as the cooling material folds back upon itself. It appears that the mold release prohibits intimate mating of the folded surfaces with each other, and thereby establishes a precursor to crack development during binder removal and HIPing.

The mold release used for the initial rotors was a traditional liquid spray and applied every few moldings. An alternate "permanent" release agent was then evaluated. It is applied to the mold cavity surface and allowed to completely dry before material injection. Thus far it appears that approximately 20-30 rotors can be molded with a single application of the new mold release without significant degradation.

Table XXXII.
Strength characteristics of GTE PY6 Si_3N_4 gasifier turbine rotors.

	Strength–MPa (ksi)		
Rotor S/N	25°C (77°F)	1200°C (2192°F)	1370°C (2500°F)
398	775.7 (112.5)	679.8 (98.6)	570.9 (82.8)
428	975.6 (141.5)	–	708.8 (102.8)

This coating allows the cavity to be operated at a higher temperature, and more importantly, does not trap liquid mold release within the green molded part. The surface quality of parts molded using this release agent is significantly better than prior pieces with respect to flow indications, but the occurrence of knit lines on the rotor hub face opposite the shaft has not been completely eliminated.

Delivery of the required 20 AGT-5 gasifier turbine rotors of injection molded and HIPed PY6 Si_3N_4 was completed in October. One final molding change was performed for several parts to reduce the frequency and severity of knit lines. A hot sprue was adapted to the molding tool to keep the injected material molten up to the end of the shaft. This was expected to reduce knit lines in the balancing stock area opposite the rotor shaft by decreasing the freezing of the initial material entering the cavity. An improvement in the overall packing quality of molded rotors was observed using the hot sprue. In particular, the hub perimeter regions between the blades were packed out more completely. However, some indications of knit lines did persist in the balance stock opposite the shaft.

Both the semipermanent mold release and the hot sprue modifications were incorporated into the rotor fabrication process during the final three months of GTE's six month program extension. The final set of 20 AGT-5 rotor deliverables were parts fabricated with the following set of processing conditions:

- 6 made with traditional liquid mold release and cold sprue
- 12 made with new permanent mold release and cold sprue
- 2 made with new permanent mold release and hot sprue

In addition, two vendors were used for hub profile grinding. The majority of rotors were machined by a lapping process using diamond paste and iron contoured laps. Several other rotors were machined by computer numerically controlled (CNC) diamond grinding at a second vendor.

The results of proof spin testing of the GTE PY6 Si_3N_4 rotors is summarized in subsection 2.1.3 of this report.

Task II – Toughened Monolithic Rotors. The objective of this task was to identify process conditions for increasing the fracture toughness of monolithic PY6 Si_3N_4 . The basic mechanism for achieving improved fracture toughness has involved microstructural modifications, specifically focusing on increasing the average grain size. By increasing the grain size of Si_3N_4 , resistance to crack growth increases because the crack is deflected more by propagation around the grains.

To study the effect of different densification times, pressures, and temperatures on microstructure and material properties, a test matrix of the hot isostatic pressing process for PY6 silicon nitride was conducted. The initial three cycles were designed to scope out general relationships of HIP conditions and resultant microstructures prior to a more complete HIP parametric study. SEM examination indicated different microstructures resulting from each of the HIP cycles, indicating that sufficient flexibility exists in the process variability to warrant a study of toughness adjustment via process modifications. However, no significant differences were measured in the fracture toughness. Similar to the hot pressed billets, all HIPed materials exhibited high values for the Weibull moduli. Compared to hot pressed PY6 Si_3N_4, however, the HIPed PY6 showed higher room temperature strength but lower retention of strength at elevated temperatures. The hot pressed PY6 Si_3N_4 billets retained 60-70% of their room temperature strength at 1400°F (2552°F), while the HIPed PY6 Si_3N_4 material retained only 50% of the room temperature strength at 1400°C (2552°F). In addition, almost all of the HIPed bars tested at 1400°C (2552°F) exhibited minor deflection before failure, while the bars machined from hot pressed billets failed without yielding. SEM examination of hot pressed and HIPed microstructures revealed a significantly larger average grain size (approximately five times larger) in the hot pressed material compared to the HIPed material. It is possible that this large difference in grain size may account for

the different strength and toughness behavior between hot pressed and HIPed material.

The materials produced from the final three experimental HIP runs were characterized for fracture toughness, strength, and alpha-to-beta silicon nitride conversion. The combined outcome of the investigations conducted for Task II has been the identification of the factors which are most important to controlling the PY6 microstructure during HIP. The useful range of values for such HIP parameters has been determined. Improved strength, fracture toughness, and control of the reactions between the PY6 Si_3N_4 and the HIP encapsulation glass have been observed for several experimental HIP cycles.

The factors which were tested included the initial silicon nitride powder size distribution, HIP peak temperature, HIP hold time, and HIP peak pressure. Material evaluations indicate that the initial powder size distribution is important for controlling the densification rate, alpha-to-beta Si_3N_4 transformation rate, fast fracture strength, and final grain size. HIP hold temperature has a strong influence on alpha-to-beta transformation rate and final grain size. HIP hold time has a strong effect on fracture strength and on grain size. However, grain growth in HIPed PY6 does not proceed to the same extent as that of material hot pressed for similar times. The level at which HIP pressure is held is less critical in terms of material properties, provided that it is kept within the acceptable range identified previously.

For all of the combinations of the various parameters evaluated, it is apparent that indentation fracture toughness is limited to approximately 5.4 MPa-m$^{1/2}$ (4.9 ksi-in.$^{1/2}$) for the PY6 composition. This is a 20% improvement over the current level; however, it indicates that, unlike hot pressed PY6, HIPed PY6 does not follow the simple model which shows that fracture toughness increases with grain size. Other factors which contribute to toughness improvement, such as grain boundary composition and distribution, will be examined in the future under the ORNL CTAHE-funded Advanced Processing Program to determine the means to further increase PY6 fracture toughness.

Strength improvements were achieved by altering the standard HIP cycle and initial powder type. By ending the HIP cycle at the point when full density was reached and alpha-to-beta transformation was near completion, strength increases of 15% at both room temperature and 1370°C (2500°F) were achieved while maintaining the current level of toughness for selected initial powder size distributions. Strength at 1370°C (2500°F) increased up to 40% for some samples; however, fracture toughness did not increase concurrently.

Task III – Toughened Composite Rotors. The objective of this task was to evaluate the densification kinetics, material properties, and fabricability of PY6 Si_3N_4 containing 30 v/o SiC whiskers. Improvements in fracture toughness, strength, and creep resistance were demonstrated in the CTAHE project for additions of SiC whiskers in an AY6 Si_3N_4 matrix. At 30 v/o whisker additions, a 40% increase in fracture toughness and a 25% increase in fracture strength were observed. However, whisker reinforcement also decreased the densification rate of the composite material by limiting particle rearrangement. To extend the concept of whisker reinforcement of the PY6 Si_3N_4 matrix containing less densification additives than the AY6 Si_3N_4, the feasibility of attaining near theoretical density must first be demonstrated. If densification is possible, notable improvements in material properties must then be determined to establish the benefit of utilizing whisker-reinforced PY6 material for ATTAP rotors.

Several thick cross-section test samples of PY6 Si_3N_4 with 30 v/o SiC whiskers were successfully injection molded. Two of these samples were processed through binder removal and HIPing. Both samples were over 99% theoretical density after HIP, and exhibited only slight distortion during densification. Test specimens sectioned from the sample pieces were characterized by GTE and had an average room temperature strength of 807 MPa (117 ksi) and an average strength of 552 MPa (80 ksi) obtained at a test temperature of 1400°C (2552°F). The fracture toughness of the whisker reinforced material measured 5.8 MPa-m$^{1/2}$ (5.3 ksi-in.$^{1/2}$) as determined using the controlled surface flaw technique.

A larger batch of PY6 Si_3N_4 + 30% SiC whisker material was then compounded for preliminary AGT-5 gasifier rotor fabrication trials. The solids loading and final viscosity of the compounded mix were approximately the same as those used for monolithic PY6 batches. A total of 12 rotors were injection molded. The material filled the mold easily, but the molded parts tended to show more flow lines and were not as well packed as rotors made using monolithic PY6. Two of the rotors were processed through binder removal. Both rotors showed numerous cracks on the outside contour of the rotor shaft after binder removal, but appeared acceptable in the hub and airfoil sections. The cracked shafts were removed from the rotors prior to densification. One rotor made from the PY6 Si_3N_4 reinforced with 30% SiC whiskers was densified by HIPing. The component densified fully, but showed considerable airfoil distortion, as shown in Figure 138, presumably due to whisker alignment during the injection molding step, which has been demonstrated to cause such distortion in whisker-containing injection molded test bars.

The distortion findings were such that work in the whisker-reinforced rotor fabrication efforts was discontinued and no further fabrication and/or testing of whisker composites was conducted.

3.2.4 Corning

Objective/Approach

Efforts at Corning continue for the purpose of developing a reliable, low cost, extruded ceramic regenerator disk capable of operating at RPD conditions. Initial effort is focused on a segmented disk formed from multiple extruded pieces cemented together.

Accomplishments/Results

- Corning delivered samples of a new 20% porous MAS extruded regenerator matrix. The thermal expansion of 20% porous MAS was found to be 62% higher than the typical expansion of Corning 26% porous MAS.
- Corning confirms excessive projected production cost for AS regenerator disk material with current process.
- Corning has submitted a proposal outline for material, extrusion, and cementing development.

Discussion

The 20% porous MAS material tested under cyclic thermal conditions as reported in subsection 4.2.4 has proven to be 1.3 times stronger than the previously tested 26% porous material initially, but loses more strength from thermal cycling. The 62% higher thermal expansion of 20% porous MAS may explain why it suffered a higher loss of strength during thermal cyclic testing than did 26% porous MAS. Both materials were expected to have similar expansion; however, similar and larger variations are being seen between different batches of the same material.

A cost study by Corning has shown that the previously favored AS regenerator disk material made with the current process will be too expensive for production automotive use. This material has been favored for the regenerator for years because of ultra-low expansion, high strength, and less loss in strength due to thermal cyclic cracking when compared to current MAS. Corning's latest MAS materials, as well as NGK's, have shown excessive loss in strength due to thermal cyclic crack growth. Based on their experience in developing ceramics, Corning believes the required properties can be achieved either in MAS or a new glass ceramic. Variations in batch formulation and mixing, binder, drying, and sintering schemes would be tried to produce the required properties. Extrusion experiments would involve material flow and forming strategies, die fabrication techniques, and die size. Development of segment cementing would follow.

3.2.5 Garrett Ceramic Components

Objective/Approach

A technical development effort with Garrett Ceramic Components (GCC) was completed.

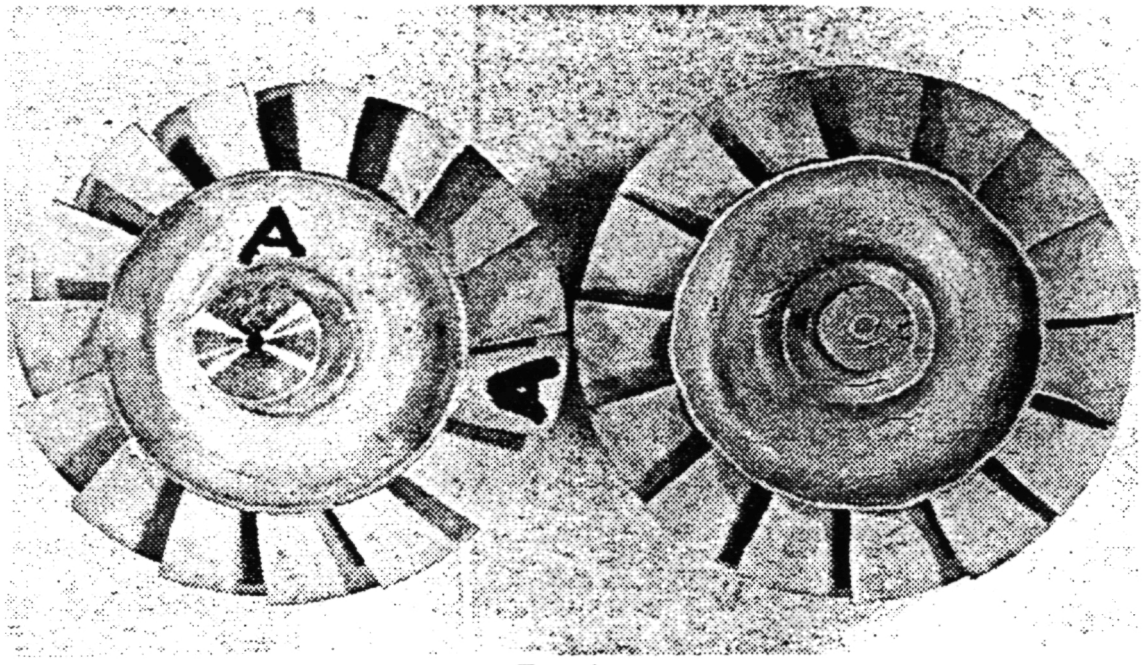

Top view

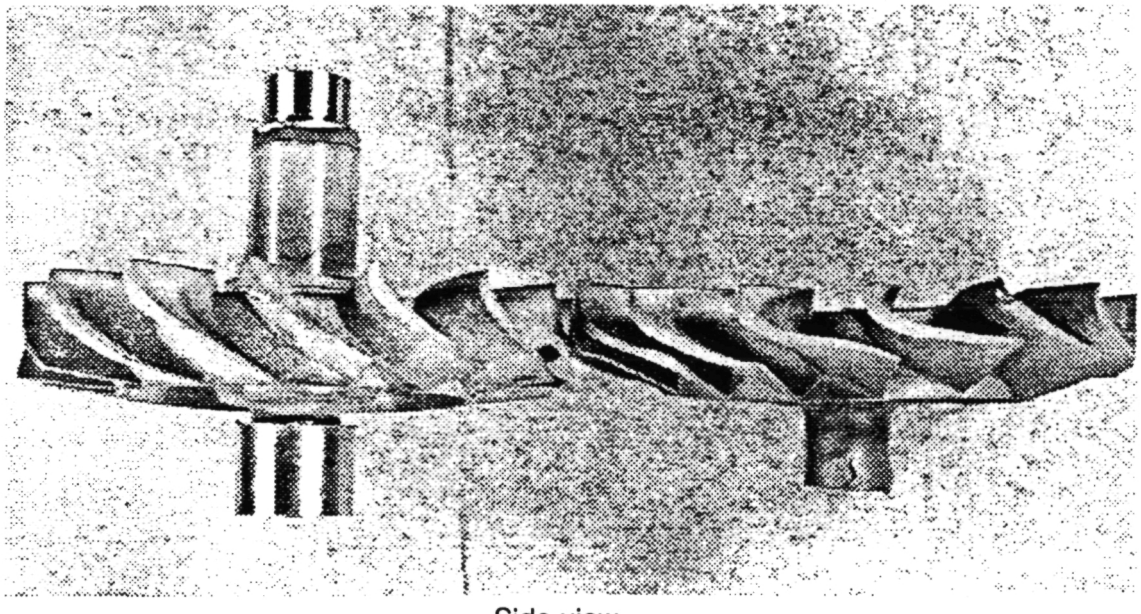

Side view

TE91-2096

Figure 138. Injection molded and HIPed GTE AGT-5 rotors made using monolithic PY6 (left) and PY6 +30% SiC whiskers (right).

The objective of this activity was to develop and deliver silicon nitride AGT-5 gasifier turbine rotors for test and evaluation. GCC tailored its pressure slip casting techniques and proprietary mold technology to develop and fabricate GN-10 Si_3N_4 rotors. In Phase I, subscale GN-10 Si_3N_4 rotors were produced to establish a processing and properties baseline for axial turbine rotors. In Phase II, the techniques developed in Phase I were scaled-up to produce full-scale GN-10 Si_3N_4 AGT-5 rotors.

Accomplishments/Results

- 156 full-scale GN-10 Si_3N_4 rotors cast to date
- Blades are casting fully
- Eight rotors spin tested
- One rotor passed proof spin test to 80,000 rpm (after blade release)

Discussion

Full-Scale AGT-5 Rotor Fabrication. The processing procedures and NDE techniques established in the subscale rotor fabrication effort were expanded to fabricate full-scale AGT-5 gasifier turbine rotors with 20 blades. A total of 156 development rotors were cast while changing a variety of casting parameters. These experiments were designed to establish a standard casting procedure by which full-scale AGT-5 turbine rotors could be fabricated. Revision No. 15 slip procedures have been used for the rotor casting activities.

Processing activities have concentrated on developing a standard casting procedure to fabricate defect-free rotors by equilibrating the casting rates in all portions of the rotor to eliminate stresses that develop due to nonuniform drying shrinkage during the casting process. Internal hub cracks have been eliminated and the blade detail is similar to that of the stereolithography pattern. The cause of inconsistent surface cracking in the shaft and intermittent blade detachment have not been determined. The process parameters were closely monitored and all rotors carefully inspected using microfocus X-ray after removal from the mold and after drying.

There was concern that the rotor blade roughness, caused by the use of the stereolithography pattern as the master for the molds, would adversely affect the proof spin test results. The roughness was such that these inherent surface discontinuities may act as stress concentrators. The effect of blade roughness was monitored closely during the proof spin testing.

A total of 14 rotors were processed through HIPing to satisfy the deliverable requirements. After NDE inspection, 12 rotors were deemed acceptable for further processing. Two of the rotors were subsequently rejected due to large shaft cracks which appeared after shaft machining. A total of eight of the remaining ten rotors were subjected to proof spin testing. The spin testing was conducted at the Balancing Company (BALCO) to Allison specifications. A metal arbor was glued onto the O.D. of the shaft using a high temperature epoxy. All balancing of the rotors was done with two-plane balancing on the metal arbor to eliminate any removal of material from the rotors. High-speed photography was used to document the burst failures.

The results of the proof spin testing are summarized in Table XXXIII. In general, each rotor tested had a substantial number of surface defects, cracks, blade spalling, and blade surface roughness. Some of the surface defects noted

Table XXXIII.
GCC GN-10 silicon nitride gasifier turbine rotor spin test results.

Rotor No.	Burst speed--rpm
126	78,820
145	21,480
148	65,320
189	79,510
191	75,580
149	67,850
199	78,660
169	80,000*

*Rotor lost a blade tip at 48,240 rpm. After rebalance, the rotor reached the proof speed of 80,000 rpm without failure.

were in the 0.5-1.0 mm (0.02-0.04 in.) size range. Five of the rotors (Nos. 126, 145, 148, 189, and 191) were spin tested to develop baseline data since each rotor had significant defects as noted by the prior nondestructive evaluation. Three of the remaining five rotors were also spin tested to attempt to qualify rotors for subsequent rig/engine testing. Photographs of the rotors at the moment of burst may be found in subsection 2.1.3 (Gasifier Turbine Rotor) of this report.

The five rotors in the first set were all tested to failure. The results of preliminary failure analysis indicate that the observed surface defects correlated well with the indicated failure origins. Even rotor No. 191, which had a density of only 3.15 g/cc (0.114 lb/in.^{3}) (95% theoretical density), failed at a missing section on the rotor rim. This indicates that the bulk material properties were not the primary cause of failure, and that the surface defects caused by the use of the rough stereolithography pattern and difficulties experienced due to the casting geometry of the AGT-5 rotor with GCC's unidirectional casting process acted as the failure origins. There appeared to be no correlation between either density and internal defects and burst speed for these rotors.

Since the remaining five rotors all had similar surface defects to those observed in the initial set of rotors, only three were spin tested. Two of the three rotors burst, with the remaining rotor (No. 169) surviving the spin test to the proof spin of 80,000 rpm. Rotor No. 169 had lost small sections of the blade tips at a speed of 48,240 rpm. The test was stopped, and the rotor was rebalanced and retested. Rotor No. 149 had a large pore (approximately 1 mm [0.04 in.] diameter) in the hub rim area and failed at 67,850 rpm. Rotor No. 199, which burst at 78,660 rpm, had indications on the hub and a missing area at the hub platform edge. Photographs of the bursts indicate that the fracture origins were surface defects.

Overall, the burst speed results were considered promising considering the roughness of the blades and blade/hub interface and the problems experienced with casting this geometry, which resulted in a significant number of surface defects. The lowest speed failure (Rotor No. 145 at 21,480 rpm) correlated directly to a blade release which was a result of the surface roughness. The majority of the other failures occurred at the hub rim, concentrated at the blade/hub interface.

Standard-size test bars, measuring 50.8 x 6.35 x 3.18 mm (2 x 0.25 x 0.125 in.), were machined from the hub sections of four additional GN-10 Si_3N_4 gasifier turbine rotors. The fast fracture strength characteristics of the specimens were evaluated at room temperature, 1204°C (2200°F), and 1370°C (2500°F). The results of the mechanical strength assessments of these test bars are summarized in Table XXXIV. In general, the properties of the rotor test bars were comparable to those of test bars cut from slip cast plates for GN-10 Si_3N_4 for the revision No. 15 slip process and the revision No. 17 HIP process.

Fractography was conducted by GCC on all test bars. In general, the room temperature failure origins were primarily small inclusions, while the specimens tested at elevated temperature failed from chamfers, inclusions, and agglomerates.

This effort completes the initial technical program with GCC.

Table XXXIV.
Strength characteristics of GN-10 silicon nitride test bars cut from AGT-5 rotors.

Temperature --°C (°F)	Strength --MPa (ksi)	No. specimens	Weibull modulus
25 (77)	702.6 (101.9)	29	9.9
1204 (2200)	548.8 (79.6)	7	15.6
1370 (2500)	379.2 (55.0)	9	5.3

3.2.6 Ceramics Process Systems

Objective/Approach

A development program with Ceramics Process Systems (CPS) was initiated in April 1989 for fabrication of gasifier turbine vane platforms. The platforms are being fabricated using the Quickset injection molding process for CM200 sialon material. The vane platform configuration incorporates a center section with approximately the same cross section as the gasifier turbine rotor, which is subsequently cored out of the final part to provide test specimens for material characterization activities. The vane pockets are molded integrally with the vane platform, eliminating the requirement for ultrasonic machining.

Accomplishments/Results

- Fabrication of Quickset injection molded vane platforms with integral vane pockets completed
- Tool modifications completed to eliminate vane pocket cracking
- Finish machining of vane platforms active
- Characterization of CM200 sialon material conducted

Discussion

The effort with CPS has concentrated on the fabrication of Quickset injection molded gasifier vane platforms. This configuration, shown in Figure 139, incorporates a center section with approximately the same cross section as the gasifier turbine rotor. The injection molding tool was ordered in August 1989 and was delivered in October.

An initial set of ten vane seat platforms was fabricated using the VSP-2 final configuration injection molding tool. The molded parts were analyzed using an optical microscope. Small cracks, approximately 0.025 mm (0.001 in.) in length, were observed at the base of each vane pocket. The vane pockets also had linear scratches, indicating that the tool inserts were dragging on the pocket base during vane insert withdrawal. A second set of ten vane seat platforms was fabricated using the VSP-2 tool,

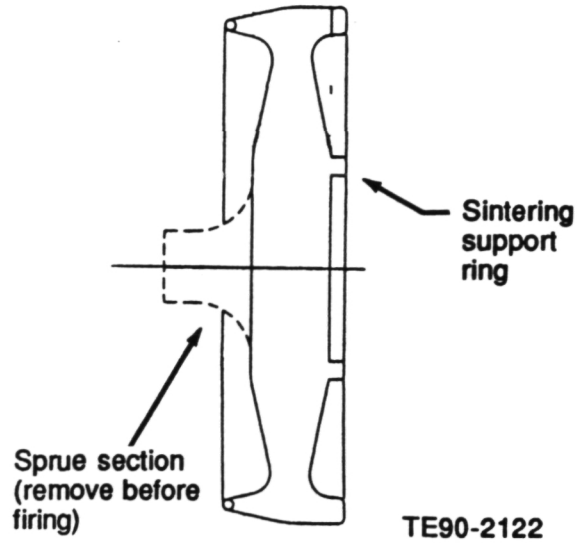

Figure 139. CPS vane platform configuration.

with the vane pocket inserts being retracted from the molded parts manually. After injection, the mold was disassembled and the vane inserts were individually pulled out prior to the lifter plate ejecting the part. Visual examination of the molded parts revealed that only 1 of the 14 vane pockets was cracked. The vane insert which caused the singular crack was examined and found to be galling in the vane guide. The injection molding tool is designed such that the vane inserts should pull out of the pockets prior to the lifter plate ejecting the part. Examination of the current tool revealed that the articulated vane retraction mechanism operates simultaneously with the ejector plate. This causes the vane inserts to be levered onto the vane pocket bases, resulting in crack formation. To correct this problem, stronger springs were fitted into the tool to prevent the ejector plate from lifting the part out of the tool before all of the vane inserts are retracted. Additionally, the vane guide was remachined to open up the positioning channel to prevent galling of the vane inserts during retraction.

Concurrent with the tool modification efforts, a drying study was conducted to assess the effect of drying shrinkage on any further vane pocket cracking. During drying, the Quickset molded parts undergo a drying shrinkage of approximately 0.5%. Although this shrinkage is uniform and small in extent, shrinkage stress can cause cracking at sharp corners as the part dries from the outside toward the middle of the part.

The cracking can be eliminated through drying rate control, as the outer shell particles shrink onto a solid core. Also, settering in the dryer was examined to ensure no constrained drying occurs as the vane platform rests on the dryer shelf during drying.

To address the cracking observed at the base of the vane pockets, the vane platform injection molding tool was modified in accordance with GM design changes. The major modification was to extend the axial length of the vane platform an additional 3.81 mm (0.15 in.) from the trailing edge of the vane pocket to minimize the potential for cracking at this location during processing. Following sintering, this additional material was machined off. The tooling was modified and part fabrication commenced in mid-April.

A total of 70 CM200 sialon solid hub vane platforms were Quickset injection molded using the modified tool. Of these 70 platforms, 35 were sintered and annealed, completing the fabrication activities to satisfy the deliverable requirements. Thirty-eight unmachined solid hub platforms were delivered in September for microstructural and mechanical property evaluations. The total number of deliverable vane platforms with the cross-key features machined was reduced from 12 to 6. The platforms, being finish machined at Bullen Ultrasonics, are scheduled for delivery in early 1991.

Dimensional evaluations were conducted on the sintered vane platforms to verify the component dimensional conformance and to establish the as-fired tolerances. Three areas of the vane platforms were evaluated: the platform outside diameter, the axial height, and the vane pocket chord length. The results of the dimensional evaluations are summarized in Table XXXV. All of the dimensions were within print tolerance, with most of the deviations varying between 0.2-1.0% from the specified dimensions.

To assess the mechanical properties of the CM200 vane platforms, a number of test bars (corresponding to MIL-STD-1942(MR), B-size) were machined by BOMAS from the hub sections of the vane platforms. CPS delivered 90 bars in June for material characterization. The results are summarized in subsection 3.1.1 (Material Properties and Microstructure) of this report. Concurrent with this activity, additional characterization of the CM200 sialon material was conducted at CPS. Four point flexural testing was conducted on test material sectioned from the hub region of the vane platforms. The average room temperature fracture strength was 752 MPa (109 ksi) with a Weibull modulus of 7.8. Additional testing, including high temperature creep testing, is ongoing on the CM200 material at the ORNL HTML.

3.2.9 Norton/TRW Ceramics

Objective/Approach

A development program with Norton/TRW Ceramics (N/TRW) was initiated in October 1989 for fabrication of gasifier turbine rotors and scrolls. The gasifier turbine rotor is being fabricated by pressure slip casting NT154 Si_3N_4. The scroll activities have been focused on NT235 siliconized SiC and the drain casting process.

Table XXXV.
CPS CM200 sialon vane platform dimensions.

Area	Tolerance–mm (in.) Specified	Measured	Percent
Platform diameter	±0.3 (0.012)	±0.11 (0.004)	0.15
Platform height	±0.3 (0.012)	±0.20 (0.008)	1.04
Vane pocket chord length	±0.3 (0.012)	±0.03 (0.001)	0.12 (in part)
	±0.3 (0.012)	±0.09 (0.004)	0.41 (part to part)

Accomplishments/Results

- Processes established for fabrication of NT154 rotors and NT235 scrolls
- Four rotors achieved proof spin test goal of 80,000 rpm
- Total of 26 scrolls cast with an overall process yield of 60%
- Scrolls are fracturing in the shroud area during finish machining

Discussion

Gasifier Turbine Rotor. The development activities at N/TRW for the gasifier turbine rotor have focused on four main areas: process verification, tooling design and fabrication, component production and deliverables, and quality assurance.

The process verification task focused on the development of casting process parameters and optimization of the NT154 Si_3N_4 slip system. Work was performed using a combination of exploratory screening experiments, including a Taguchi L8 experiment. Initially, screening tests were conducted in molds prepared from a 15-bladed rotor model. In most cases, these experiments were component specific and combined mold design issues as factors with slip casting parameters. The result of these experiments and subsequent component casting trials was the definition of a suitable slip preparation and casting process.

Problems which were identified in initial casting trials using the 15-bladed rotor included radial cracks in the shaft region during drying and cracking of blades on removal of blade inserts. In an attempt to eliminate drying cracks, modifications to the slip system (additive types and levels) and slip preparation techniques were performed. A very stable and workable slip was developed. Verification of the mechanical properties was conducted and is summarized in Table XXXVI. Although drying cracks were minimized, they still persisted in the shaft region. A Taguchi L8 experiment was conducted in which mold design, drying condition, powder treatment, and powder blend were included as experimental factors. Mold design was found to be the most significant factor for elimination of cracks. Within this experiment drying cracks were absent in all rotors cast with the preferred mold design. Throughout the remainder of this program, drying cracks were rarely observed in rotors.

Removal of mold inserts between blades proved to be a difficult problem to overcome. A large number of blade insert materials and insert coatings to aid release were screened. Limited success resulted from applying a release agent. However, the use of RTV rubber inserts significantly aided insert removal. To further ease the process of insert removal, components were frozen after removing the outer mold sections. Residual water in the cast components acted as a binder when frozen and gave the green rotors considerable strength. This technique was used to produce rotors for proof spin testing.

Upon verification of the proper shrinkage factor, a master pattern for the 20-bladed rotor configuration was procured. On receipt of the master pattern, casting molds were constructed and evaluated. Using concepts concerning mold design and materials developed in the prior 15-bladed rotor efforts, rotors were successfully cast after several mold design iterations. One of the iterations involved the addition of an insert to the shaft side of the pattern to prevent the hub section of the rotor from casting solid before the blades were fully cast. A second area of concern was the parting line where the hub insert, blade inserts, and aluminum pattern

Table XXXVI.
Mechanical properties of slip cast NT154 Si_3N_4.

Property	Average	No. of specimens
Density	3.224 g/cc (0.116 lb/in.^{3})	10
25°C (77°F) strength	937 $\pm$117 MPa (136 $\pm$17 ksi)	20
1370°C (2500°F) strength	662 $\pm$28 MPa (96 $\pm$4 ksi)	10

all mated. This region was found to be critical for successful removal of blade inserts. Poor alignment could lead to defects in dense castings. Originally, these defects were not revealed until final component machining. Upon further investigation, the source of these defects was found to be the mold design in this region. Changes in insert design were incorporated, but these defects continued to appear in castings throughout the program.

Development in the slip system, casting progress, and mold design led to fabrication of rotors for spin testing. Early in this production task, problems were encountered with a loss of components in HIPing and final dense machining. On start-up of the production task, a dense component packing arrangement in the HIP was implemented. Unfortunately, this led to breakage of rotor blades during HIPing and several engine-quality castings were lost. The loading arrangement was corrected by reducing the packing density and no additional blade cracking occurred during HIPing.

In final machining, several iterations were required before a first article component could be produced which met all dimensional requirements. The most difficult task involved achieving proper radii on the hub profiles. A secondary operation using smaller diameter grinding wheels was required to obtain these features. Another region which was time consuming and somewhat difficult was the machining of the shaft hole. A near-net shape hole was green machined into the shaft and then final grinding was performed on the dense casting. Design changes to the shaft cavity would yield a component which could be produced much easier.

Using information from final inspection of machined rotors, an investigation into the source of casting defects was conducted. Several of the defects were traced to specific features of the molds and/or pattern. These defects included poor surface finish of blades, cracks in the blades, and pores or cracks in the transition region from the blades to the rotor hub. Corrective actions included hand polishing the aluminum master pattern to improve the surface finish of the blades. An alternate rubber mold material was used to fabricate new blade inserts to aid removal. Concurrent screening trials in other component development programs had shown that cracking of blades was reduced by utilizing this alternate material. Finally, the blade insert design was modified in the transition region.

A total of seven pressure slip cast NT154 Si_3N_4 rotors were densified, finish machined, inspected, and shipped to BALCO for proof spin testing. The results of the proof spin testing are summarized in Table XXXVII. Three of the rotors failed at speeds below the proof spin speed of 80,000 rpm, bursting at 74,500 rpm, 57,800 rpm, and 79,100 rpm, respectively. A total of four rotors (S/N 5G, 4W, 5S, and 6F) passed the proof test and were forwarded for assembly to metal shafts for subsequent rig/engine test evaluation.

Table XXXVII.
Spin test results for N/TRW NT154 silicon nitride gasifier turbine rotors.

Rotor No.	Spin speed--rpm
5G	80,000*
5K	74,500-burst
4W	80,000*
5S	80,000*
4H	57,800-burst
6E	79,100-burst
6F	80,000*

* Rotor passed proof spin speed of 80,000 rpm without failure.

Five rotors which were judged to be nonengine quality after densification were delivered for material assessment prior to machining or spin testing. In addition, NT154 test tiles were cast and processed, from which 200 test specimens were machined and delivered.

This effort completes the initial activities with N/TRW involving rotor fabrication.

Turbine Scroll. The development activities at N/TRW for the turbine scroll have focused on three main areas: process verification, tooling design and fabrication, and component production and deliverables.

Verification of the slip casting process for NT235 reaction bonded SiC included development of an enhanced slip system and carbon impregnation treatment. Using baseline Norton Co. casting technology, development was initiated to address some of the component specific requirements of the AGT-5 scroll. One of these requirements was that the casting slip maintain a low viscosity during the dwell time in the plaster mold so that excess slip could be drained uniformly. Simple dispersion tests were conducted to screen several additives to test for improvements, followed by casting trials of candidate slip systems as a final evaluation. A suitable slip system was identified and was given the designation NT235.

An additional concern with respect to the AGT-5 scroll design was the radius between the scroll inlet and the vortex. Past efforts in the AGT100 program had revealed the tendency for castings to crack in that region upon removal of the mold insert. To strengthen the material and minimize this problem, several emulsion binders were evaluated. A final selection was made based on slip rheology, material green strength, and success of scroll castings.

A carbon impregnation process previously developed by Norton Co., and subsequently discontinued, was reestablished for scroll fabrication efforts. This process introduces carbon into the porous green microstructure. During furnacing operations, the carbon is reacted with silicon metal to form SiC and increase the overall SiC phase content. This increase in SiC has been shown to enhance the high temperature mechanical properties of the material. This process was successfully implemented, enabling material densities of $\geq$3.07 g/cc^3 (0.111 lb/in.^{3}) to be obtained. Later in the program a pressure assisted process was developed and resulted in consistent densities of greater than 3.10 g/cc^3 (0.112 lb/in.^{3}) being obtained for scrolls.

Properties verification was performed on this newly developed slip system and is reported in Table XXXVIII. This was conducted by machining MIL-STD-1942(B) test specimens from test tile. This verification exercise also validated component forming and densification processes used for scrolls.

Upon defining an appropriate shrinkage factor for slip cast NT235 SiC, a tooling shop was selected for fabrication of a master pattern and mold set-up forms. Plaster casting molds were formed in-house at N/TRW using the fabricated tooling. The first tooling iteration was successful in producing crack-free castings. Modifications to simplify the molds by combining subsections into common sections were performed. A total of three molds were produced for utilization in casting of engine-quality components.

Table XXXVIII.
Mechanical properties of NT235 SiC.

Property	Average	No. of specimens
Density	3.12 g/cc (0.113 lb/in.^{3})	9
25°C (77°F) strength	203 MPa (29.5 ksi)	8
1260°C (2300°F) strength	241 MPa (34.9 ksi)	10

Utilizing the slip system and molds developed in previous tasks, a total of 26 NT235 siliconized SiC AGT-5 scrolls were cast to satisfy the deliverable requirements. A process yield of 60% after densification was achieved. Several dense components from an initial siliconization run were sectioned for evaluation. The remaining components were inspected and qualified via mechanical properties testing of coprocessed test specimens.

Seven engine-quality candidate components were delivered to an outside shop for final machining in early January 1990. After numerous delays in the machining schedule, a first article component was completed to the point of ultrasonic machining of airfoil pockets in May. On shipping this component to Bullen for airfoil machining, it was destroyed. N/TRW subsequently decided to complete component machining in-house.

In June 1990, the existing machining fixture was modified to conform to requirements of N/TRW's grinding equipment. The fixture was also improved to provide accurate location of the casting to ensure dimensional conformance. Machining was performed on a set-up component to validate the machine tool program and machining process. A crack was generated in the shroud section of this scroll on the final grinding pass of the outside diameter. Corrective action was taken and based on the success of machining all other aspects of this set-up component, including the cross-keys, machining was initiated on an engine quality component. However, cracking again occurred in the shroud region on grinding the shroud to final dimensions.

This operation was critically reviewed and several conditions were considered the cause for continued machining problems in this region. These included: (1) thin walls in the shroud section of <2.54 mm (0.10 in.) due to design limitations, (2) low material strength of the NT235 SiC, and (3) the CNC grinding equipment is very rigid and is capable of applying undue stress to the component on wheel loading or other nonoptimum grinding conditions. A decision was made to drop CNC grinding of this section of the scroll and use a tool-post grinder mounted on a lathe. A tool-post grinding set-up should minimize the stress imposed on the scroll as the setup is more flexible and allows for continuous control by the operator. Despite modifications to the grinding operation, all of the scrolls being finish machined have fractured in the shroud region during I.D./O.D. grinding. A decision was made to terminate machining of the NT235 SiC scrolls in this program and to include an initial deliverable requirement for additional machined scrolls in the 1991 workplan. In addition to minor geometric modifications, the use of NT230 SiC for scroll fabrication will be employed. Changing materials will increase the machinability of these components, as the room temperature strength of NT230 SiC is approximately 150% that of NT235 SiC.

IV. COMPONENT RIG DEVELOPMENT AND TEST

4.1 COMPONENT RIG DEVELOPMENT

The objective of this activity is the design, fabrication, and development of rigs required to test ATTAP development ceramic components and assemblies. In addition, these rigs are utilized to develop nonceramic hardware/systems as necessary to evolve the AGT-5 to a high temperature test-bed. Currently, five component rigs are being developed: (1) two rotor/shafting system rigs, (2) two hot gasifier rigs, and (3) a regenerator sample pressure rig.

4.1.3.1 Rotor/Shafting System Rig Development

Objective/Approach

The objective of this activity is the development of rotor/shafting system rigs capable of evaluating seals, bearings, rotor shaft dynamics, and lubrication systems as necessary to evolve the AGT-5 hot gasifier rig and engine to high temperature test-beds. In addition, the rigs are to be capable of room temperature high speed proof testing of candidate ceramic turbine rotors prior to AGT-5 hot gasifier rig or test-bed engine evaluation.

Accomplishments/Results

Gasifier rotor/shafting system rig:

- Oil pump problems resolved
- Vibration problem traced to dynamometer propshaft
- Vacuum source added to rotor spin chamber
- Rig is fully operational

Power turbine rotor/shafting system rig:

- Completed design of new rig and initiated hardware procurement

Discussion

Gasifier Rotor/Shafting System Rig. Attempts to bring the gasifier rotor/shafting system rig up to the desired speed were originally thwarted by three problems: lube pump failure, excessive vibration, and insufficient dynamometer power. Lube pump problems stemmed from galling of the pump housing side surfaces by the gears. Corrective action consisted of adding a thin wear plate to the pump housing. Axial chucking of the pump's driven shaft is being addressed.

The vibration problem appeared when the gearbox speed was brought to a value in excess of its design speed while moving toward the 130% point. Initially, a gear or chain imbalance within the gearbox was thought to be causing the vibration, and a series of tests was run to isolate the contributing component. The dynamometer propshaft was found to be the problem, having developed a severe wobble.

The dynamometer power limitation was corrected when the chamber that surrounds the ceramic wheel was sealed and a vacuum drawn to reduce the pumping losses.

Corrective actions were implemented and verified, and the rig is fully operational. Shaft dynamics and bearing development work may require additional instrumentation.

Power Turbine Rotor/Shafting System Rig. A new rig has been designed to develop the rotor/shafting system of the AGT-5 power turbine. The rig will be capable of cold spin testing as well as the evaluation of seals, bearings, rotor shaft dynamics, and lubrication systems. Drawings, utilizing metal dummy power turbine rotors for initial rig evaluation and checkout, have been detailed and released. Rig instrumentation has been ordered, and rig components are being procured.

4.1.3.3 Hot Gasifier Rig Development

Objective/Approach

Development efforts focus on improving the durability of the rig particularly while operating under conditions prescribed by the cyclic durability schedule at temperatures up to 1371°C (2500°F.) Increased thermal data are being gathered from critical areas of the rig to

assist in design modifications of rig specific, as well as engine turbomachinery and hardware. To handle the increased amount of data, resources are being applied to the integration of a new pressure/temperature data acquisition system in the appropriate test facilities.

Accomplishments/Results

- Redesigned the quartz window mounting system for improved high temperature retention
- Fabricated, installed, and completed shakedown of a second hot gasifier rig
- Procured and installed an auxiliary air compressor to supply additional cooling air to the gasifier rigs
- Installed a high speed pressure and temperature scanning system, and wrote required software for data acquisition

Discussion

Frequently when the gasifier rig is operated at high temperatures the clamp force retaining the quartz window is lost. The loss of retention causes the window to vibrate and chip the circumferential edge of the window, resulting in substantial hot gas leakage. To remedy this, the mounting system was redesigned utilizing a large wave spring to maintain loading on the gasket during thermal cycling. The mounting system redesign is illustrated in Figure 140.

A second hot gasifier rig was assembled and brought on-line. The objective of this rig is to maximize available ceramic component development evaluation time. Following shakedown testing, the rig accumulated over 120 hr of ceramic component test time.

Makeup air is utilized by the gasifier rigs to reduce exhaust temperatures to tolerable levels for the ceramic regenerator cores. Available air in the various test cells was marginal, so an Atlas Copco rotary screw compressor was procured and installed as background data to ATTAP to provide additional cooling air for the two rigs. Increased pressure and temperature scanning capability has also been added to the dynamometer test cells (as background data to ATTAP) with the installation of Pressure System's 8400 data acquisition equipment. The necessary software for communication between the 8400 system and the host computer has been completed. Completion of plumbing and wiring is expected in the first quarter of next year. This system will provide over 100 additional pressure and 100 additional temperature measurements to the current data acquisition capability.

4.2 COMPONENT RIG TESTING

The objective of this activity is to develop the necessary test procedures and to conduct rig testing of the ATTAP development ceramic components and assemblies. A secondary objective is to conduct tests of nonceramic hardware/systems related to the evolution of the AGT-5 engine into a high-temperature test-bed. All ceramic components are rig proof tested prior to AGT-5 test-bed engine testing. Rig tests of the ceramic components are generally conducted with more instrumentation than normally available within a test-bed engine. Critical data provided by rig testing are used in the development and verification of the ceramic design methodology. Currently, a gasifier rotor/shafting system rig, two hot gasifier rigs, a regenerator cyclic sample rig, and a regenerator sample pressure rig are being utilized.

4.2.3.1 Rotor/Shafting System Rig Test

Objective/Approach

The objective of this activity is the room temperature performance evaluation testing of seals, bearings, rotor shaft dynamics, and lubrication systems as necessary to evolve the AGT-5 hot gasifier rig and engine to high temperature test-beds. In addition, both the gasifier and power turbine spin rigs are capable of room temperature, high-speed proof testing of candidate ceramic turbine rotors prior to AGT-5 hot gasifier rig or test-bed engine evaluation.

Accomplishments/Results

- Four candidate shaft seal ring materials were evaluated, with one appearing worthy of additional testing in the hot gasifier rig.

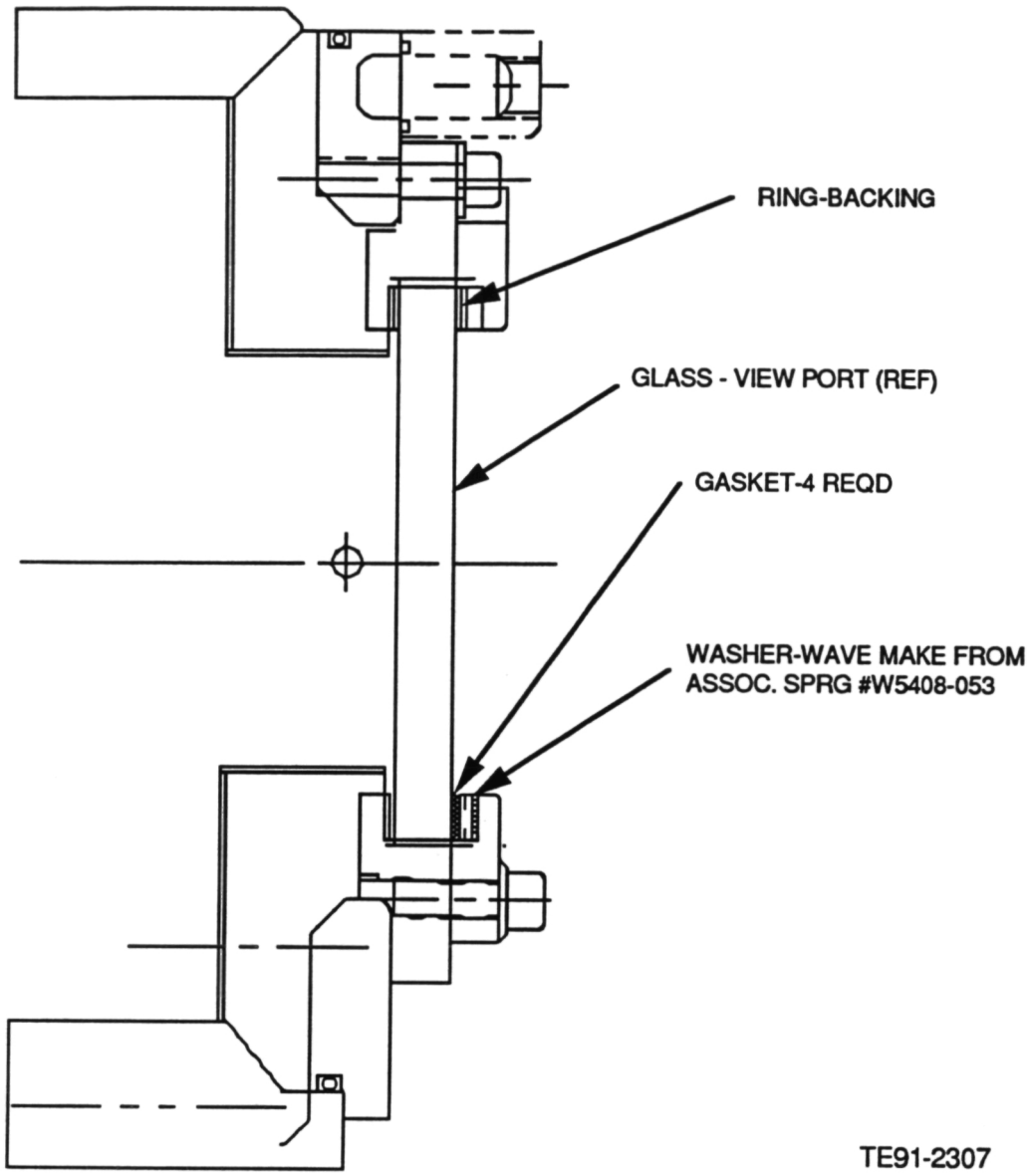

Figure 140. Redesigned mounting system of hot gasifier rig viewing window.

Discussion

Wear tests were performed on the gasifier shaft air seals using powdered metal, silicon carbide, and two versions of carbon-carbon as seal ring materials. The tests were performed at 50% or 100% speed for a given length of time. The seals were running against a dummy rotor with a shaft of 4140 steel.

The powdered metal seals wore over 0.0254 mm (0.001 in.) after only 12 min. at 100% speed. After 2 hr of additional testing it was found that one of the seals had developed a hairline fracture at its pressure balance groove. The unit was rebuilt with new seals and run for an additional 2 hr. Upon examination, both seals were found to be fractured. In both cases, the pressure balance groove was the sight of the fracture origin. The shaft was worn extensively under both seals. Grooves of 0.07112 mm (0.0028 in.)

and 0.02032 mm (0.0008 in.) were found. It is believed that when the seals broke they became wedged to one side and started acting like a cutting tool. Because of its low fracture toughness, powdered metal is no longer considered an acceptable seal ring material, especially when pressure balance grooves are used.

Sintered alpha silicon carbide seals were also evaluated. Testing was performed for 15 min. at 50% speed. Wear on the seal rings was less than 0.0127 mm (0.0005 in.); however, the shaft material under the ring was worn over 0.0254 mm (0.001 in.)

K-Karb carbon-carbon seals were run against a shaft that had been chrome plated. An initial diametral clearance of 0.0381 mm (0.0015 in.) was established between the shaft and the seals. After 2 hr at 100% speed, the seals were inspected and found to be worn by 0.02032 mm (0.0008 in.) The test was then repeated using the same seals. No additional seal wear was evident, and the chrome plated shaft had no measurable wear.

A change to a higher strength F210 carbon-carbon seal material permitted simplifying the design to eliminate the use of the seal ring spacer. Testing began with 0.0635 mm (0.0025 in.) diametral clearance established between the chrome plated shaft and the seals. This configuration was tested for 2 hr at 50% speed and for 1 hr at 100% speed. Inspection revealed no measurable wear on the seals or on the shaft. This design is considered suitable for further testing in the hot rig.

4.2.3.3 Hot Gasifier Rig Test

Objective/Approach

Hot gasifier rig testing is used to screen/proof test and evaluate structural ceramic components (namely combustors, gasifier turbine components, and regenerators) prior to introduction into the AGT-5 test-bed engine(s). The rig has build-time, accessibility, instrumentation, and cost benefit advantages compared to the full engine test-bed. The rig has been designed to simulate the engine environment so that ceramic components are subjected to nearly the same operating conditions as if they were installed within the test-bed engine. Developmental rig evaluation is continuing while domestic ceramic components are being fabricated for testing.

Accomplishments/Results

- Achieved 1366°C (2491°F) @ 90% N_1, with an experimental air-cooled metal gasifier scroll and a 15-bladed Si_3N_4 ceramic rotor
- Achieved 1395°C (2543°F) @ 98% N_1, with an experimental air-cooled metal gasifier scroll and a 20-bladed Si_3N_4 ceramic rotor. This specific rotor also accumulated 311.9 test hours during the year, including 210.3 hr on the GM Automotive Gas Turbine Durability Test Cycle. The rotor endured tip rubs due to both shroud movement and compressor impeller failure
- Achieved 1401°C (2554°F) @ 100% N_1, with an experimental ceramic gasifier scroll and a 20-bladed Si_3N_4 ceramic rotor
- Conducted tests to compare the aerodynamic performance of 20-bladed ceramic gasifier rotors to 38-bladed metal gasifier rotors
- Ran the GM Automotive Gas Turbine Durability Test Cycle on unattended computer control

Discussion

Ceramic Rotor/Scroll Design Evaluation and Rig Development. Three hundred thirty-seven hours of rig testing of two ceramic gasifier turbine rotor designs (15- and 20-bladed) have been accumulated on four different rotors during the third year of ATTAP as outlined in Table XXXIX. Evaluation of these rotor designs added valuable information to the program by verifying design parameters and FOD-survivability, as well as providing material evaluation in components. These rotors simultaneously served as workhorse components for rig shakedown and development to high temperature capability.

A Si_3N_4 rotor shroud band (Kyocera SN252), AS wrapped regenerator disks, and an experimental air cooled metal gasifier scroll were utilized in evaluating/developing hot gasifier rig operation at temperatures at and exceeding the ATTAP RPD goal of 1371°C (2500°F) TIT.

Table XXXIX.
Hot gasifier rig accumulated test time.

Rotor	No. of blades	Material	Hours on test 1990	Hours on test Total	Peak temperature--°C/ peak speed--%N_1
5K12	15	SN252	14.9	26.4	1366/98
5K22	20	SN252	311.9	660.5	1395/100
5K25	20	SN252	7.2	7.2	1130/90
5K26	20	SN252	3.9	3.9	1401/99

Initial testing revealed excessively high regenerator inlet temperatures in the rig at turbine inlet temperatures above 1287°C (2349°F). An air compressor was installed to provide increased regenerator inlet cavity dilution air and a 15-bladed design Si_3N_4 ceramic rotor (Kyocera SN252, S/N 5K12) was utilized for a run to TIT = 1366°C (2491°F) at 98% gasifier speed. Inspection revealed no damage to the rotor; however, the insulation in the regenerator inlet cavity had eroded due to the extremely high dilution air velocity and flow rate. Kaowool blanket-type insulation was incorporated into the rig and selected dilution air cooling tower jets were blocked to prevent direct jet impingement on the insulation.

Evaluation of the 20-bladed design at high TIT was carried out by installing a Si_3N_4 ceramic rotor (Kyocera SN252, S/N 5K22) into the rig. The rotor survived a major rotor tip/shroud rub while operating at 93% speed and TIT = 1302°C (2376°F). While operating at the above condition, a sudden brightness occurred on the remote video monitor. Viewing the rotor directly, by looking through the rig's quartz window, it was observed that the blade tips were a bright white color. The gasifier speed was reduced to 80% and since no damage was apparent, the speed was increased to 87% where the bright white light reappeared. The gasifier module was then removed for inspection. See subsection 3.1.3 for a detailed analysis of the rub. The rotor was reinstalled into the rig with a new shroud band, having increased tip clearance, and run to 1395°C (2543°F) TIT at 100% speed (exceeding RPD conditions). Fifteen minutes were spent at TIT greater than 1371°C (2500°F). Inspection following the test revealed no damage to either the rotor or the shroud.

An experimental advanced concept ceramic (Si_3N_4) scroll was built and installed into the gasifier rig for the purpose of evaluating the ceramic scroll type geometry, the scroll mounting system, and the ceramic rotor at high temperature. A Si_3N_4 20-blade rotor (5K26) was used for this test. At 100.5% speed, a TIT of 1367°C (2493°F) was reached. An inlet throttle was used to decrease the airflow through the rig and raise the TIT to 1401°C (2554°F) at 99% speed. Total time above 1300°C (2372°F) was approximately 38 minutes. Figure 141 illustrates the peak temperature versus percent speed characteristic.

In addition to the above high temperature run, rotor 5K22 was operated on the durability schedule. The rotor accumulated a total of 311.9 hr running during 1990 for a total of 660.5 hr and 2331 starts. 210.3 of the hours have been run on the durability schedule. The rotor ran to a TIT = 1395°C (2543°F) as described above. At 320 hr into the test history of the rotor, an emergency rig shutdown occurred at 86% gasifier speed and 1300°C (2372°F) TIT due to rig overtemperature and high vibration conditions. Inspection revealed that a large piece of hard carbon was lodged between rotor airfoils. The rotor was returned to service after carbon removal and inspection. At 556.5 hr, during a cyclic acceleration, a compressor impeller failure occurred causing a rig shutdown. This particular impeller had accumulated well over 1000 hr of operational test time and appeared to have suffered fatigue failure. The compressor shaft bent 0.508 mm (0.02 in.) (total indi-

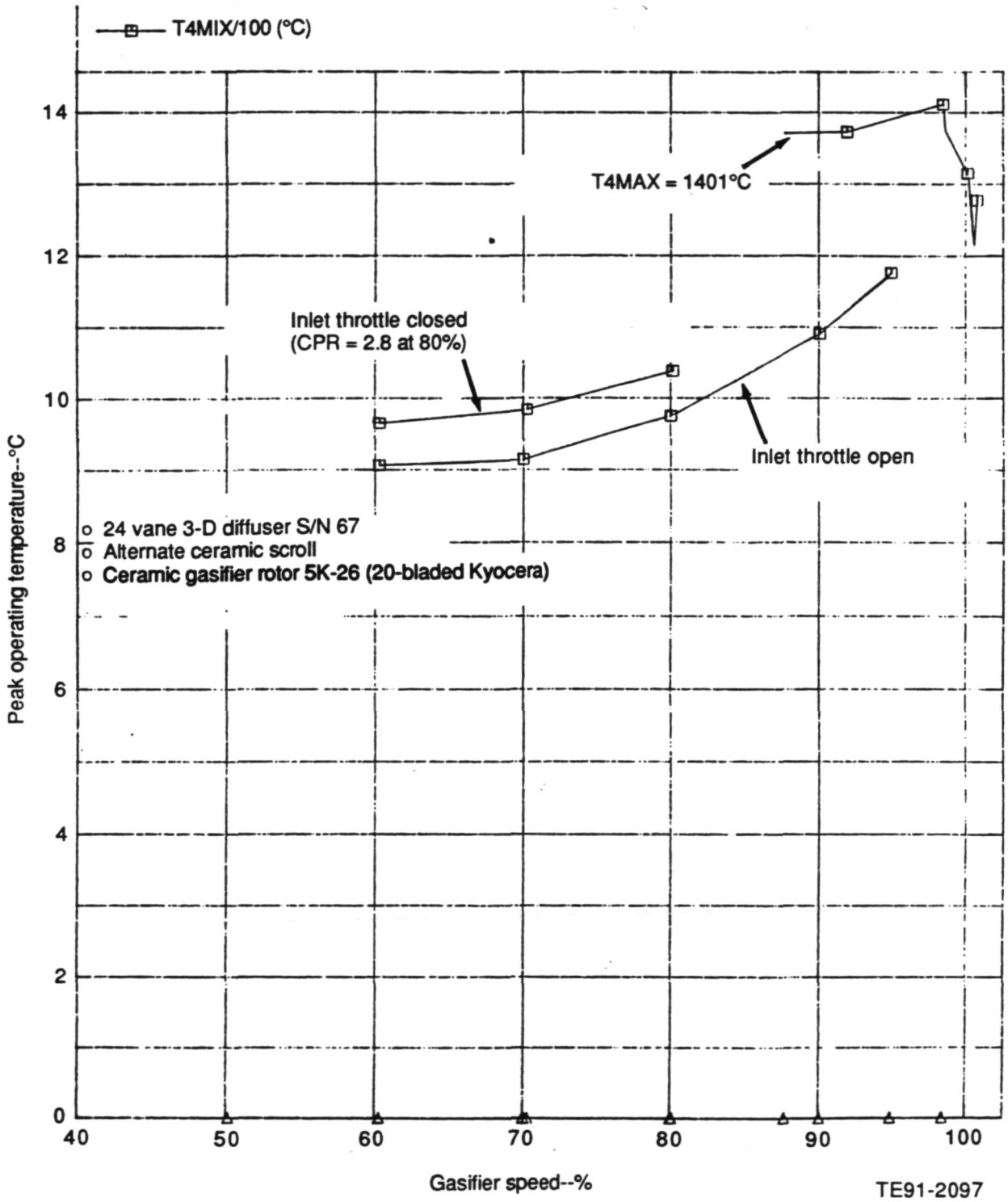

Figure 141. Peak operating temperature versus speed: advanced concept ceramic scroll test.

cated runout) and the ceramic rotor shroud cracked, but the ceramic rotor was not damaged. After straightening the compressor shaft, the rotor returned to test for continued rig evaluation/testing with a new ceramic shroud. A summary of this rotor test history is shown in Table XL.

A 20-bladed Si_3N_4 rotor (SN252, 5K25) was run with a ceramic shroud to provide data for the metal to ceramic gasifier aerodynamic comparison discussed below. This build was limited to a TIT = 1130°C (2066°F) at 90% speed due to the metal components in the gasifier build. The rotor ran for a total of 7.2 hr.

Table XL.
History of AGT-5 ceramic gasifier rotor; 20-bladed design, Kyocera SN252, S/N 5K22.

Period	Hours/ starts	Maximum speed/temp.	Comments
March-April 1989	34.5/150	100%N_1 at 1030°C (1886°F)	• Sustained fracture damage • Failure of particle containment screen or shroud rub • Minor chips in blade leading edge tips
May-June 1989	188.3/134	100%N_1 at 1204°C (2200°F)	• Rotor condition unchanged
July-August 1989	79.3/279	100%N_1 at 1204°C (2200°F)	• Successfully ingested FOD • Insulation broken away from engine block • No additional rotor damage
September-October 1989	46.5/161	100%N_1 at 1204°C (2200°F)	• Converted rig from air start to mechanical start • Burner dome degradation-metal FOD through rotor • No additional rotor damage
March 1990	7.5/112	93%N_1 at 1302°C (2376°F)	• Introduced ceramic shroud • Ceramic shroud fractured and rubbed rotor • Rotor intact and in engine-ready condition
April 1990	9.0/42	100%N_1 at 1395°C (2543°F)	• Rotor run to full RPD conditions
May 1990	64.9/92	95%N_1 at 1250°C (2282°F)	• Hard carbon lodged between rotor airfoils • No additional rotor damage
June-August 1990	126.5/407	100%N_1 at 1250°C (2282°F)	• Cyclic durability • Compressor failure • Shaft bent, shroud broken, rotor rubbed shroud • No additional rotor damage
September-December 1990	104.0/954	100%N_1 at 1200°C (2192°F)	• Shaft straightened, rotor returned to test • Unattended cyclic durability
Total	660.5/2331		• Continuing cyclic durability testing

Note: All testing since March 1990 with ceramic shroud. All testing in hot gasifier rig.

Ceramic Gasifier Rotor Aerodynamic Performance. Tests were run to compare the aerodynamic performance of a ceramic 20-bladed rotor (5K25) running with a ceramic shroud to the baseline 38-bladed design metal gasifier rotor. Data were obtained from back-to-back hot gasifier rig tests in which only the gasifier rotor section hardware was changed. Only absolute efficiency deltas were considered as the rig had considerable regenerator leakage, making any absolute efficiency calculations difficult. The ceramic rotor seems to perform better at higher speeds and work levels. At 90% speed, it is comparable to, or better than, the 38-bladed metal rotor. Conversely, at lower speeds and work levels (e.g., 70%), stage efficiency is down approximately 0.6% (with tip clearance accounted for). Considering the lower aspect ratio of the 20-bladed rotor compared to the 38-bladed metal rotor, the results are encouraging.

Durability Schedule Computer Control. A second hot gasifier test rig was brought on-line this year; initial evaluation was carried out utilizing rotor 5K22. Computer controlled unattended operation was demonstrated. Having the computer controlled mechanism available will allow accumulation of test hours on the many ceramic components that will require testing in the ATTAP. The computer control monitors all pertinent rig parameters to ensure rig shutdown if any improper signals are noted, as well as storing and displaying a full set of rig parameters at shutdown.

4.2.4 Regenerator Rigs Test

Objective/Approach

The objective of this activity is to evaluate the durability of candidate ceramic and metal regenerator matrix samples by exposing them to pressures and/or temperatures simulating engine conditions. Rigs include a compressive pressure failure rig and a cyclic temperature burner rig. The burner rig simulates full-throttle AGT-5 engine accelerations/decelerations.

Accomplishments/Results

- Hot face of 26% porous Corning MAS retained 35% of original strength after 10,000 cycles, leaving it too weak to withstand expected stresses.
- SEM examination of NGK MAS after 10,000 cycles failed to reveal any cracking or other damage to explain over 93% loss of original strength (porosity made the search for cracks difficult).
- Hot face MOR strength of 20% porous Corning MAS was reduced to an average of 22% of original strength after 10,000 thermal cycles. This retained strength is inadequate for use in the regenerator disk.
- Hot face MOR strength of Corning AS was reduced to 54% of original strength after 10,000 thermal cycles. This retained strength is more than adequate for usage in the regenerator disk.
- Haynes 230 nickel alloy thermal cyclic testing was terminated after 5000 cycles due to unacceptable oxidation, cracking, cell distortion, and surface bulging.
- The cause of the abnormally low 29% strength retention for a second sample of Corning AS after only 5000 cycles is presently unknown. While the 29% strength retention is by far the lowest ever seen for the AS material, the retained strength probably should be adequate.
- A single temperature scan across the width of the regenerator matrix thermal cyclic rig showed very small variations in transient peak temperatures of $T_{max}/T_{avg} = 1.02$ and in maximum power temperatures of $T_{max}/T_{avg} = 1.03$ (burner pattern does not appear to be the cause of high strength variation in one sample).
- The ability of a relatively weak rectangular ceramic matrix to withstand 6.2 MPa (900 psi) pressure loading has relieved concern for the low (0.41-0.48 MPa [60-70 psi]) cross-corner uniaxial compressive strength of the matrix to some extent.

Discussion

Allison's experience has shown that engine accelerations are the most damaging operating condition to both ceramic and metal regenerators. Thermal cyclic tests, which simulate engine accelerations, are therefore utilized to evaluate candidate regenerator materials.

Thermal cycles cause progressive strength loss in ceramic (believed to be due to crack growth), and oxidation, embrittlement, cracking, cell distortion, and surface bulging in metal materials. A 10,000 cycle run represents the full-throttle accelerations made in the life of a vehicle by a 98 percentile driver. The cycles were defined in the 1989 ATTAP Annual Report and have a peak temperature of 1110°C (2030°F).

Ceramic Candidates. Table XLI shows MOR strengths of 18 bars cut from a Corning 26% porous MAS sample after 10,000 cycles. The samples are cut into six slices in the flow direction, and three MOR bars are cut from each slice as shown in the 1989 report. The first three bars (11, 12, and 13) represent the first slice or hot face and so forth. The three hot face bars show retention of 35% of MOR strength when compared to an as-received sample shown in Table XLII. The second slice bars show a 13% loss and the cold end bars show 9% loss while the third, fourth, and fifth slices show little effect. An NGK MAS sample showed over 93% loss of hot face strength and 35% on the cold end. As-received strength of this 26% porous Corning material is only about half that of the NGK, so the 65% loss is intolerable. A 20% porous Corning MAS is 1.3 times stronger than the 26% porous MAS.

After 10,000 cycles, three bars cut from the hot face of a new 20% porous Corning MAS showed 4, 18, and 43% of original strength, an average of 22% of original strength. Original strength of 2.16 MPa (313 psi) was taken as the average for three bars at the 3.8 cm (1.5 in.) depth which is relatively unaffected by cycling. These low retained strengths are unacceptable and raise a question of why the loss was greater than that for the Corning 26% porous MAS. Original strength was 1.3 times that of the 26% porous material. A 4.13 MPa (600 psi) original strength (which should result with 12% porosity) will be required, together with a low thermal expansion, to retain adequate strength after cyclic testing.

After 10,000 cycles, two bars from the hot face of Corning extruded AS showed 54% retention of original strength. Results of a third bar were invalidated by a load cell failure. Original strength of 6.39 MPa (928 psi) was taken as the average for three bars at the 5 cm (2 in.) depth. The retained strength of 3.3 MPa (479 psi) is quite adequate.

The retained strength of a Corning extruded AS rectangular regenerator matrix sample was measured after 5000 simulated full-throttle accelerations in the cyclic temperature regenerator rig. The retained strength (as measured from the average of the three hot face bars: 2.7, 1.7 and 1.3 MPa [399, 247, and 192 psi]) was only 29% of its initial strength (6.6 MPa [956 psi]). The sample came from a lot which had average values of MOR strength, modulus of elasticity, and thermal coefficient of expansion when compared to samples from three other lots. A previously tested sample had retained 54% after 10,000 cycles, and tests of wrapped AS in 1983 consistently showed decreasing strength with increasing cycles. The reason for less retained strength after fewer cycles is presently unknown. While the 29% strength retention is by far the lowest ever seen for the AS material, the retained strength probably should be adequate due to AS's high initial MOR strength. Regenerator disk stress for the AS material in engine service is not likely to exceed 0.69 MPa (100 psi), as thermal stresses are low due to the material's low thermal coefficient of expansion.

A large variation in strength of three hot face test bars following exposure in the thermal cyclic test rig raised concern for possible variation in the rig temperature pattern. A scan across the width has been completed with very encouraging results. Transient peaks produced a smooth curve within 11°C (20°F) while full-power points produced a smooth curve with no significant variation as shown in Figure 142. These results provide adequate proof of an acceptable pattern.

A pressure test was conceived as a potentially better way to characterize ceramic regenerator compressive strength than uniaxial compressive tests. The foreseen advantages of the pressure test were:

- gas pressure would apply loading evenly to the walls of the matrix eliminating the need for accurately ground surfaces and bonding of metal plates to those surfaces for load transfer

Table XLI.
Corning MAS regenerator matrix MOR strength following cyclic testing.

Date:	February 20, 1990
Vendor:	Corning
Material:	MAS (26% porous)
Fabrication:	Extruded
Part:	Test bars
Temperature:	Room temperature
Surface:	10,000 cycles

Bar No.	Width –cm (in.)	Thickness –cm (in.)	Load --Kg (lb)	Stress –MPa (psi)	Average of three –MPa (psi)	
11	1.0947 (0.4310)	1.2293 (0.4840)	3.63 (8)	0.61 (89.1)		
12	1.1087 (0.4365)	1.2433 (0.4895)	3.18 (7)	0.52 (75.3)		
13	1.3487 (0.5310)	1.2611 (0.4965)	5.44 (12)	0.71 (103.1)	0.61 (89.2)	35% of original 1.75MPa (253.7 psi) avg
21	1.1798 (0.4645)	1.0490 (0.4130)	6.35 (14)	1.37 (198.8)		
22	1.2674 (0.4990)	1.0757 (0.4235)	8.16 (18)	1.56 (226.3)		
23	1.0744 (0.4230)	1.0732 (0.4225)	7.26 (16)	1.64 (238.4)	1.52 (221.1)	
31	1.1582 (0.4560)	1.2586 (0.4955)	11.34 (25)	1.73(251.2)		
32	1.2865 (0.5065)	1.2421 (0.4890)	11.34 (25)	1.60(232.2)		
33	1.0706 (0.4215)	1.2332 (0.4855)	10.89 (24)	1.87(271.8)	1.73 (251.7)	
41	1.2420 (0.4890)	1.1176 (0.4400)	8.16 (18)	1.47 (213.9)		
42	1.1506 (0.4530)	1.1125 (0.4380)	7.26 (16)	1.43 (207.1)		
43	1.1409 (0.4490)	1.1007 (0.4365)	9.07 (20)	1.81 (263.0)	1.57 (228.0)	
51	1.2090 (0.4760)	1.1493 (0.4525)	9.07 (20)	1.59 (230.9)		
52	1.1316 (0.4455)	1.1303 (0.4450)	9.52 (21)	1.85 (267.8)		
53	1.1620 (0.4575)	1.1620 (0.4575)	10.89 (24)	1.94 (282.0)	1.79 (260.2)	
61	1.3665 (0.5380)	1.1900 (0.4685)	10.43 (23)	1.51 (219.1)		
62	1.1849 (0.4665)	1.1938 (0.4700)	9.98 (22)	1.66 (240.2)		
63	1.0668 (0.4200)	1.1934 (0.4700)	8.62 (19)	1.59 (230.4)	1.58 (229.9)	
		Avg		1.47 (213.4)		
		Std dev		(65.2)		

- gas pressure loads would be applied to the sample in the same manner as in an engine thereby directly measuring the pressure load capability

The test fixture shown in Figure 143 had "D" shaped ports exposing the interior of the sample to atmospheric pressure, just as the exhaust ports do in an actual engine. In addition, the end plates leave a 0.025 mm (0.001 in.) clearance with the sample, closely resembling regenerator seals in the engine. Thus the sample is not loaded in the flow direction. It was believed that the gas pressure, fully surrounding the sample except for its ends, would disclose any susceptibility of the rectangular matrix to cross-corner loading. Since the sample has a uniaxial cross-corner, compressive strength of only 0.41-0.48 MPa (60-70 psi) yet withstood 6.17 MPa (900 psi) gas pressure without failure,

Table XLII.
Corning regenerator samples (MOR) extruded MAS (26% porous) as received.

Sample number	b, width --cm (in.)	d, thick --cm (in.)	p, --kg (lb)	s strength --MPa (psi)	Average of three MPa (psi)
11	1.2014 (0.4730)	1.1506 (0.4530)	8.62 (19)	1.52 (220.2)	
12	1.1265 (0.4435)	1.1354 (0.4470)	10.21 (22.5)	1.97 (285.6)	
13	1.1951 (0.4705)	1.1265 (0.4435)	10.89 (24)	2.01 (291.8)	1.83 (265.9)
21	1.2814 (0.5045)	1.1443 (0.4505)	10.21 (22.5)	1.70 (247.2)	
22	1.0346 (0.3990)	1.1722 (0.4615)	8.39 (18.5)	1.69 (244.9)	
23	1.2306 (0.4845)	1.1836 (0.4660)	11.11 (24.5)	1.80 (262.0)	1.73 (251.4)
31	1.2014 (0.4730)	1.1900 (0.4685)	10.89 (24)	1.79 (260.1)	
32	1.1405 (0.4490)	1.1824 (0.4655)	10.43 (23)	1.83 (265.9)	
33	1.1874 (0.4675)	1.1887 (0.4680)	10.43 (23)	1.74 (252.7)	1.79 (259.6)
41	1.1316 (0.4455)	1.2078 (0.4755)	10.66 (23.5)	1.81 (262.5)	
42	1.2789 (0.5035)	1.1836 (0.4660)	11.79 (26)	1.84 (267.5)	
43	1.1824 (0.4655)	1.1646 (0.4585)	9.53 (21)	1.66 (241.4)	1.77 (257.1)
51	1.1278 (0.4440)	1.1278 (0.4440)	8.39 (18.5)	1.64 (237.8)	
52	1.1684 (0.4600)	1.1405 (0.4490)	9.07 (20)	1.67 (242.6)	
53	1.2725 (0.5010)	1.1519 (0.4535)	10.66 (23.5)	1.77 (256.6)	1.69 (245.7)
61	1.1316 (0.4455)	1.2433 (0.4895)	9.98 (22)	1.60 (231.9)	
62	1.2802 (0.5040)	1.2357 (0.4865)	13.15 (29)	1.88 (273.5)	
63	1.1646 (0.4585)	1.2205 (0.4805)	9.53 (21)	1.54 (223.3)	1.67 (242.9)

s = 1.75 MPa (253.7 psi)
s = 0.21 MPa (31.2 psi)
n = 18

it is concluded that the rectangular matrix is not subjected to cross-corner compressive weakness by pressure loading. In addition, a compressive failure due to pressure is highly unlikely, barring defects. The 6.17 MPa (900 psi) test pressure was limited by depletion of the single nitrogen cylinder used.

Metal Candidates. After 5000 cycles, testing was terminated on the Haynes 230 nickel alloy due to unacceptable oxidation, cracking, cell distortion, and surface bulging. Oxidation had resulted in complete embrittlement so that the surface could be scraped away to a 0.127 cm (0.05 in.) depth with negligible effort. Interconnected cracks spanned 12 to 14 layers in two locations in addition to individual cracks 1.27 cm (0.5 in.) deep in most cells (see Figure 144). Cell distortion in large areas was too great to allow proper flow distribution. The surface had bulged about 0.08 cm (0.03 in.) above the surrounding surface in one area of about 1.27 cm (0.5 in.) diameter.

Since Haynes 214 was marginally successful, as reported in the 1989 ATTAP Annual Report, Allison is searching for other metal candidates.

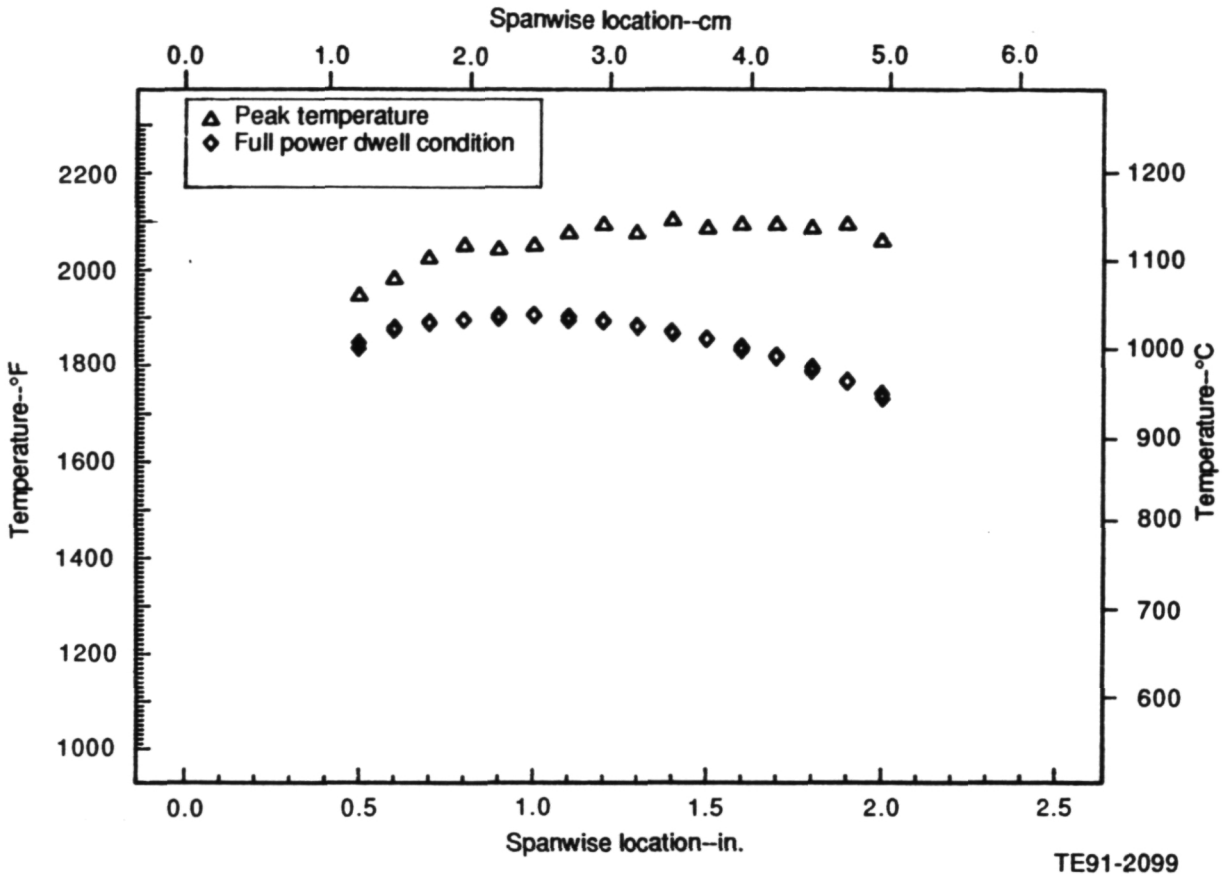

Figure 142. Temperature survey of regenerator matrix sample thermal cyclic rig (note: radial location = center of sample).

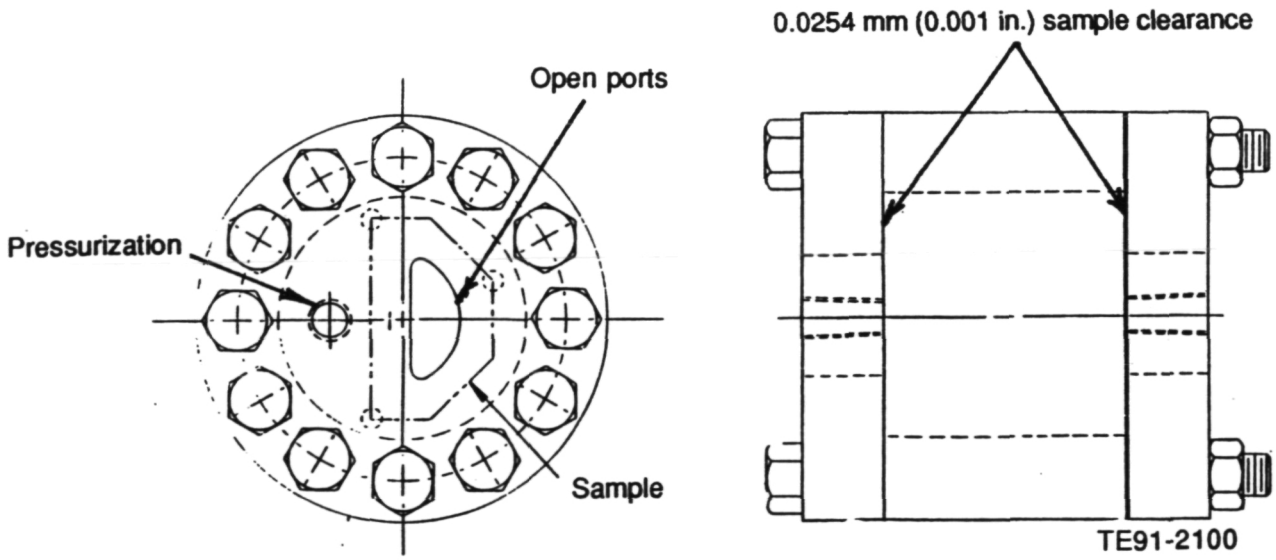

Figure 143. Regenerator test sample pressure rig.

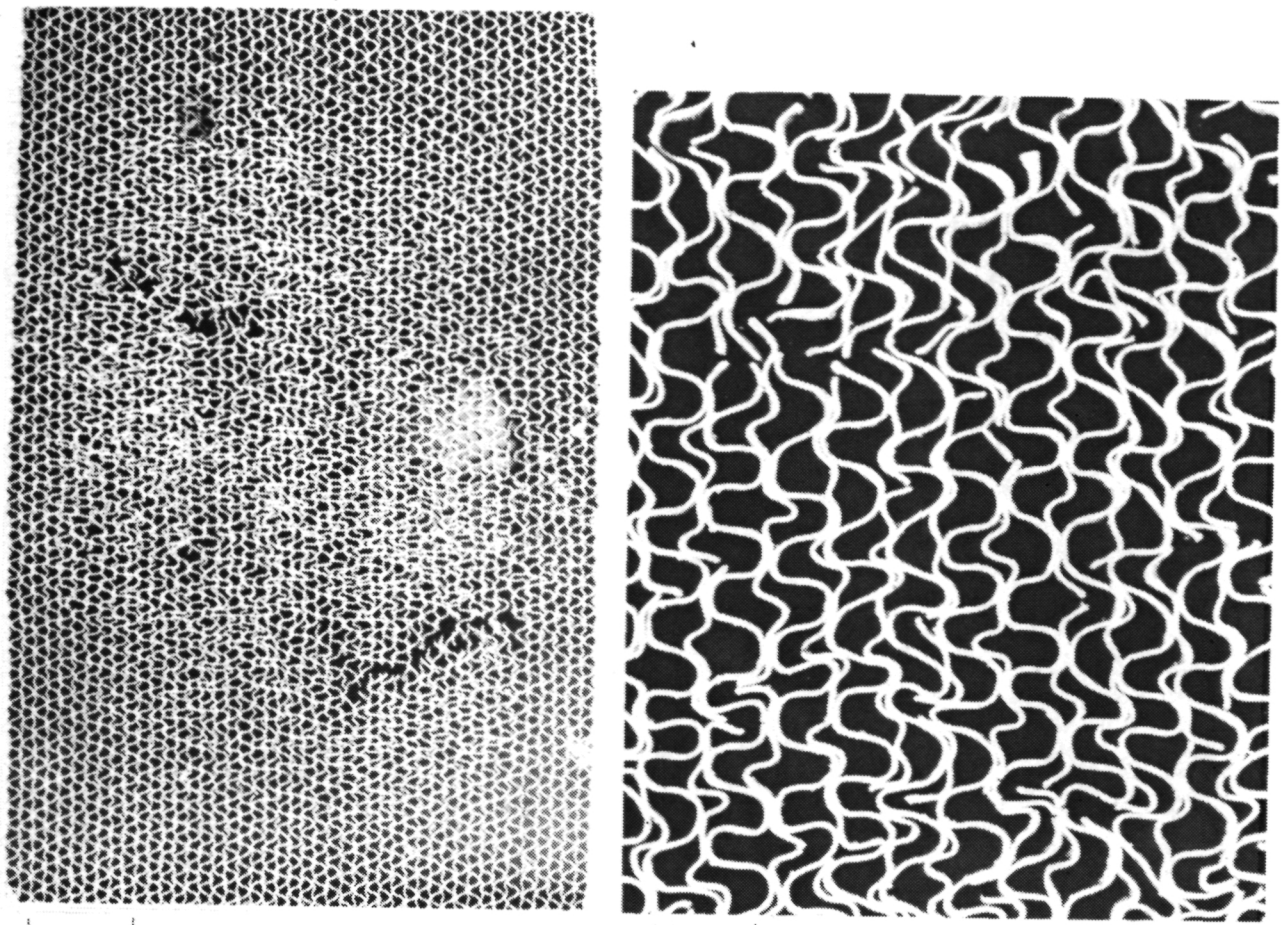

6.35 mm (0.25 in.)

1.27 mm (0.05 in.)

TE91-2101

Figure 144. Haynes 230 nickel alloy after 5000 thermal cycles.

V. PERFORMANCE AND DURABILITY TESTING--TEST-BED ENGINES

5.2 DURABILITY TESTING

The objective of this activity is to conduct test-bed engine fabrication and testing in order to verify those advancements in ceramic component technology that address the achievement of program performance and durability goals. Ceramic component designs and integrity are to be ultimately verified at maximum engine steady-state and cyclic durability conditions. As the ceramic component technology improves, the test-bed engines are being modified to allow operation up to Reference Powertrain Design (RPD) conditions. Test efforts continue to be conducted that develop and demonstrate the durability and reliability of the test-bed engines, as well as of the ceramic components and designs. Both long-term cyclic and steady-state tests are being performed. Cyclic tests simulate the GM automotive gas turbine driving cycle while steady-state tests are being performed at idle, cruise, and full-power conditions.

5.2.3 Test-Bed Engine Fabrication and Test

5.2.3.1 Test-Bed Engine Fabrication

Objective/Approach

Test-bed engine fabrication activities support all engine test activities through instrumentation, build, and repair where necessary (see subsection 5.2.3.2). New engine component fabrication activities support the design/development efforts to evolve the AGT-5 to a high temperature durability test-bed engine.

Accomplishments/Results

- Supported 33 engine builds/tests
- Performed initial assembly of the 'upgraded' gearbox

Discussion

During 1990, all phases of test-bed engine fabrication were supported for both test stand and vehicular engine testing. Fabrication efforts include everything from high temperature combustion components to instrumentation and simple brackets. Thirty-three engine builds were supported including teardown for inspection and reassembly. The new 'upgraded' gearbox design was assembled for the first time. See subsection 5.2.3.2 for details of specific engine tests.

5.2.3.2 Test-Bed Engine Testing

Objective/Approach

The objective of this activity is to perform shakedown durability testing of the AGT-5 durability test-bed engine, high temperature durability verification of the test-bed, and evaluation of ceramic hot flow path components and engine insulation. This is accomplished through operation using the General Motors' gas turbine durability schedule and conduction of tests at steady-state idle, cruise, and full-power conditions.

Accomplishments/Results

- A total of 1591.9 hr of test and development time have been accumulated on the test-bed engines in 1990
- The designated durability engine has accumulated 730.6 hr (371.3 hr in 1990), 485.6 of which were on the durability schedule
- 438 engine test hours have been accumulated with ceramic regenerator cores
- Successfully tested the first upgraded power turbine gearbox
- Engine tested a ceramic gasifier rotor
- Conducted tests to determine the optimum gasifier turbine diameter
- Intake system and compressor diffuser tests were completed to determine the optimum combination
- Ceramic regenerator core pressure drop was measured
- Block skin temperatures were measured

Discussion

Ceramic Gasifier Rotor Testing. Several engine modifications were required to run the ceramic gasifier rotor in an otherwise all-metal flow-path engine.

First, the metal turbine shroud thermally grows away from the ceramic turbine blades causing excess clearance and low efficiency operation. To remedy this condition, a cross-keyed ceramic shroud was utilized. Additionally, the ceramic rotor axial length is greater than the original metal rotor, thereby requiring a shorter interstage duct. A new interstage duct hub section was designed and fabricated, but the outer wall was not redesigned as the outer wall is part of a major complex casting which would take too long to procure for this intermediate evaluation. The result is a major step in the flow path which causes large total pressure losses, attenuating performance levels. Although the scroll was metal, it was estimated that the engine could be operated at 1200°C (2192°F) without a material related failure. This higher temperature capability would provide some additional information related to operating the complete engine at increased temperatures.

An engine was built using the ceramic-to-metal transition parts described above and installed in a dynamometer test cell. The ceramic rotor (S/N 5K24) had previously run for 7.2 hr in the hot rig to 100% speed and 1163°C (2125°F) TIT. Unfortunately, an oil pressure feed O-ring was out of specification (1.2 mm short), allowing oil to leak into the burner cavity. A subsequent fire in this cavity melted several metallic combustor components sending a barrage of metallic FOD at the ceramic rotor, causing its failure. The engine had been running for 0.7 hr before the problem resulted in a computer shutdown. Subsection 3.1.3 details the failure analyses of this test.

Ceramic Regenerator Disk Pressure Drop Test. Back-to-back tests were performed to ascertain the increase in pressure drop (P_{23}) across the ceramic regenerator compared to the drop incurred across metal cores. The results shown in Figure 145 indicate an increase in pressure drop of 0.75% for the ceramic cores.

Block Skin Temperatures and Evaluation of Upgraded Gearbox. A new upgraded gearbox was assembled and operated incident free. This gearbox was designed to handle the increased power anticipated at 1371°C (2500°F) TIT.

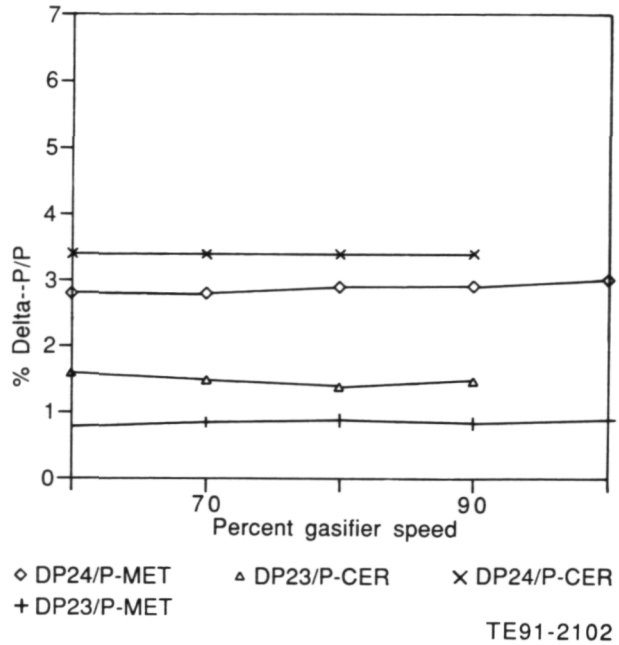

Figure 145. Comparison of ceramic regenerator versus metal regenerator: pressure drop.

Skin temperature measurements were made on the engine block. The physical locations of the thermocouples are indicated in Figures 146 and 147. Temperatures were measured at 100% gasifier speed and peak power. These data are used to aid heat transfer analysis.

Engine Configuration Optimization. Testing has been performed to determine the optimum parameters desirable for ceramic component operation such as the best available gasifier rotor tip diameter (reaction), compressor diffuser geometry, and the most acceptable intake housing configuration. These tests were not exhaustive but were designed to help select the best of the available hardware in many cases.

In order to determine the inlet geometry effects on engine operation and compressor surge characteristics, standard power runs were made with a test-bed engine with various inlet configurations. Inlets tested were: a bifurcated engine inlet with air bell plenum and air filters; an axial inlet with a plenum and filters; and an axial inlet without plenum or filters. The conclusion reached from these series of tests was that the bifurcated inlet does not increase the

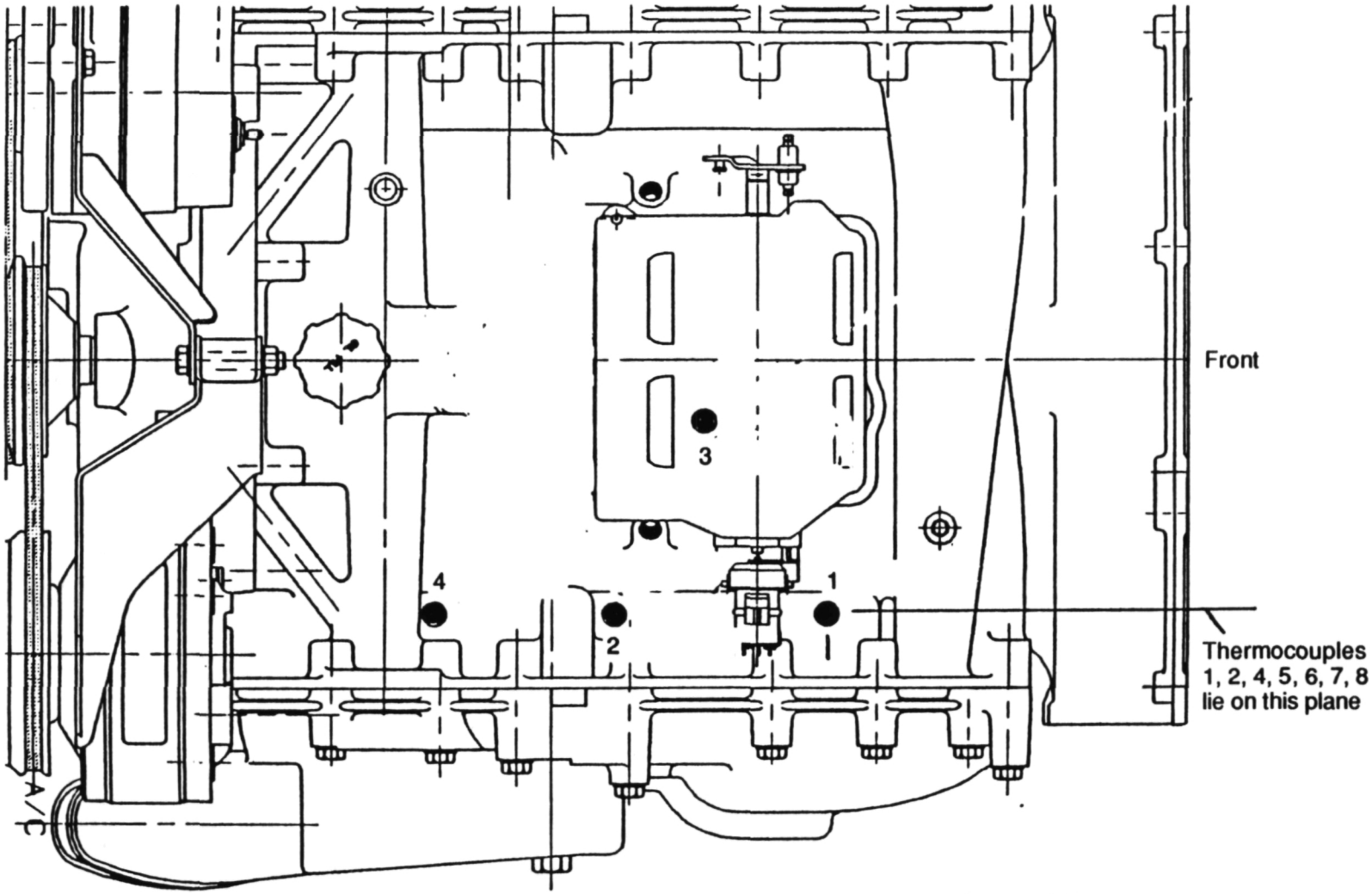

S/N 11, BU29, run 388

Note: All 8 thermocouples are mounted on the surface of the engine block

TE91-2103

Figure 146. AGT-5 engine--external thermocouple locations (top view).

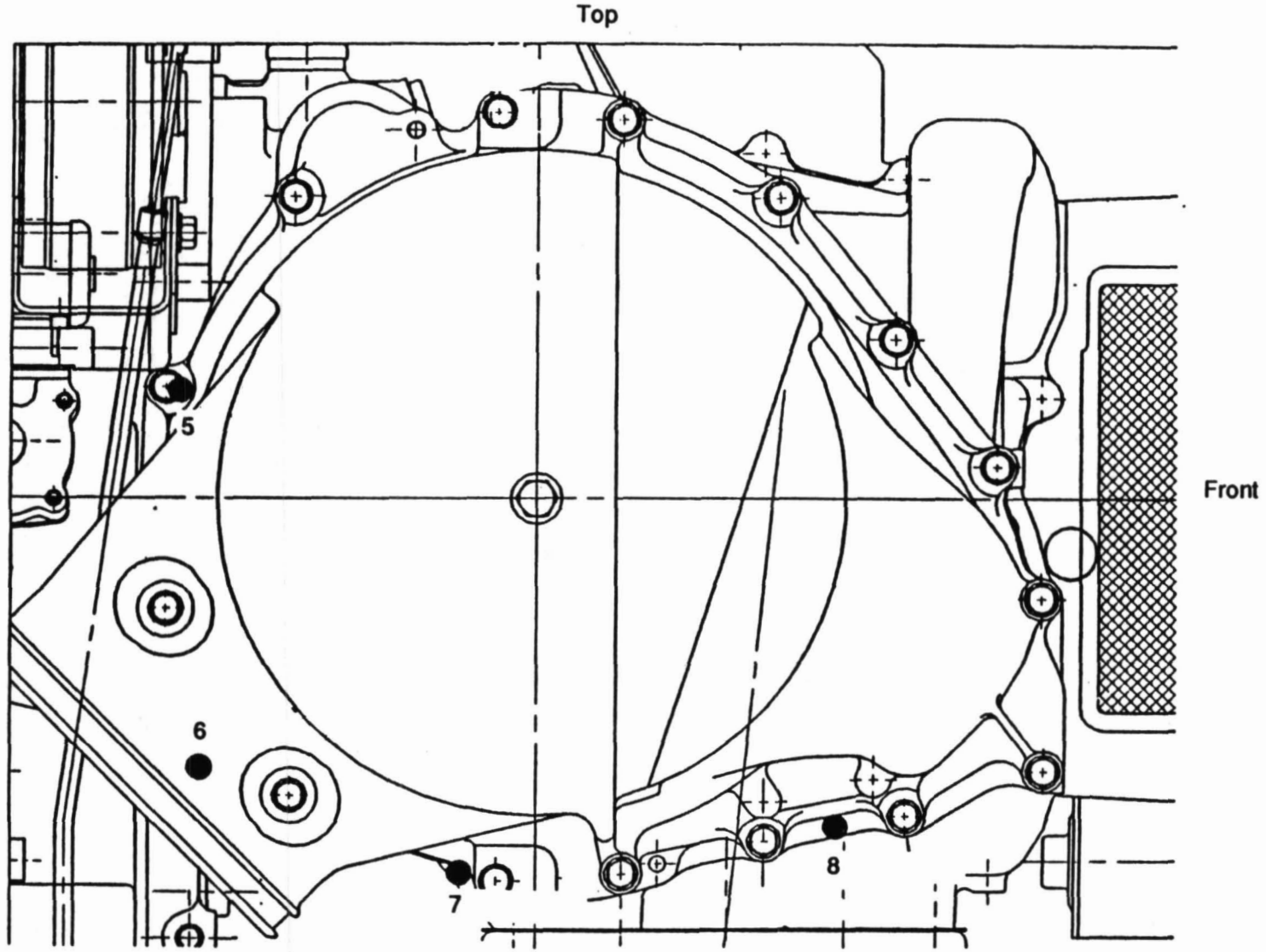

Note: See top view for lateral location of thermocouples 5, 6, 7, 8

S/N 11, BU29, run 388

TE91-2104

Figure 147. AGT-5 engine--external thermocouple locations (side view).

likelihood of compressor surge, but that it does raise the engine operating temperature somewhat. Using an axial inlet with a plenum and filters causes the compressor to surge at lower gasifier speeds than with either of the other two inlet configurations.

Engine tests were conducted to determine the best area for the compressor diffuser, and two diffuser vane geometries were evaluated: one with 18 vanes and the other with 24 vanes. The required diffuser area for surge-free operation was determined for all diffusers. Only a slight improvement (slightly cooler TIT) was found at lower speeds with the 24-channel diffuser, and virtually no difference at the design speed. Tests were also conducted on several gasifier rotors to ascertain the optimum rotor diameter for this existing stage. A detailed discussion may be found in subsection 1.4.3.

Total engine test time in 1990 is approximately 1591.9 hr for a total cumulative ATTAP time of 2444 hr. The designated durability engine has accumulated 730.6 hr (371.3 hr in 1990), 485.6 of which were conducted on the durability schedule. Engine test time with ceramic regenerator cores reached 438 hr. No major problems were encountered with the ceramic regenerator cores.

APPENDIX

TERMS AND DEFINITIONS

AES	Advanced Engineering Staff
AGT	automotive gas turbine/Advanced Gas Turbine
α	alpha
AS	aluminum silicate
ATTAP	Advanced Turbine Technology Applications Project
BALCO	The Balancing Company
BOT	burner outlet temperature
BSFC	brake specific fuel consumption
BU	build up
CBO	The Carborundum Company
CF	centrifugal force
CIP	cold isostatic pressing
CNC	computer numerical control
CO	carbon monoxide
CPS	Ceramics Process Systems
CTAHE	Ceramic Technology for Advanced Heat Engines
CY	calendar year
dwg	drawing
DOE	U.S. Department of Energy
E	elastic modulus
EDM	electronic development module (engine controller)
EPA	Environmental Protection Agency
FCM	function control module
FEM	finite element method
FOD	foreign object damage
FPI	fluorescent penetrant inspection
GCC	Garrett Ceramic Components
GM	General Motors
gm/mi	grams per mile
GT	gasifier turbine
GTE	GTE Laboratories Inc.
HC	hydrocarbon
HIP	hot isostatic pressing
hp	horsepower
HP	Hewlett Packard
HTML	High Temperature Materials Laboratory
Hz	Hertz (cycle/second)
I.D.	inner diameter
IEA	International EnergyAgency
I/O	input/output
krpm	thousands of revolutions per minute
ksi	kilopounds per square inch
kW	kilowatt
LeRC	NASA Lewis Research Center
ℓ	liter
MAS	magnesium aluminum silicate
MOR	modulus of rupture
MPa	megapascal
MR	magneto-resistive
NDE	nondestructive evaluation
NGK	NGK-Locke, Inc.
N_1	gasifier speed
NO_x	oxides of nitrogen
N/TRW	Norton/TRW Ceramics
O.D.	outer diameter
ORNL	Oak Ridge National Laboratory
POS	probability of survival
ppm	parts per million
psi	pounds per square inch
RDS	see VMS
RIT	room inlet temperature
RPD	reference powertrain design
rpm	revolutions per minute
SiC	silicon carbide
Si_3N_4	silicon nitride
SEM	scanning electron microscope
SENB	single edge notched beam
S/N	serial number
Spec	specification
3-D	three-dimensional
TIT	turbine inlet temperature
2-D	two-dimensional
UHC	unburned hydrocarbons
ULEV	ultra low emissions vehicle
VMS	Vehicular Electronic Controller Instrumentation System
v/o	volume percent
V/Vc	surface velocity/critical velocity
ω	omega, frequency
x/Cs	blade axial distance/blade axial chord
XEDA	X-ray Energy Dispersive Analysis